Department Chemie und Pharmazie

FAU Friedrich-Alexander-Universität
Naturwissenschaftliche Fakultät

Adsorption, Growth, Stability and Thermal Evolution of Protic and Aprotic Ionic Liquid Films on Non-Reactive and Reactive Metal Surfaces

Adsorption, Wachstum, Stabilität und thermische Entwicklung protischer und aprotischer Ionischer Flüssigkeiten auf unterschiedlich reaktiven Metalloberflächen

Der Naturwissenschaftlichen Fakultät der
Friedrich-Alexander-Universität Erlangen-Nürnberg
zur Erlangung des Doktorgrades

Dr. rer. nat.

vorgelegt von
Stephen Massicot
aus Schoelcher/Martinique

Als Dissertation genehmigt von der Naturwissenschaftlichen Fakultät
der Friedrich-Alexander-Universität Erlangen-Nürnberg

Tag der mündlichen Prüfung: 01.12.2023

Vorsitzender des Promotionsorgans: Prof. Dr. Wolfgang Achtziger

Gutachter: Prof. Dr. Hans-Peter Steinrück
Prof. Dr. Jörg Libuda

Contents

List of Papers [P1-P4] in the Appendix

[P1] S. Massicot, T. Sasaki, M. Lexow, S. Shin, F. Maier, S. Kuwabata, H.-P. Steinrück:

Adsorption, Wetting, Growth and Thermal Stability of the Protic Ionic Liquid Diethylmethylammonium Trifluoromethanesulfonate on Ag(111) and Au(111).

Langmuir **2021**, *37*, 11552-11560

The author's contribution are the ARXPS measurements, data analysis and interpretation, and preparation of the manuscript.

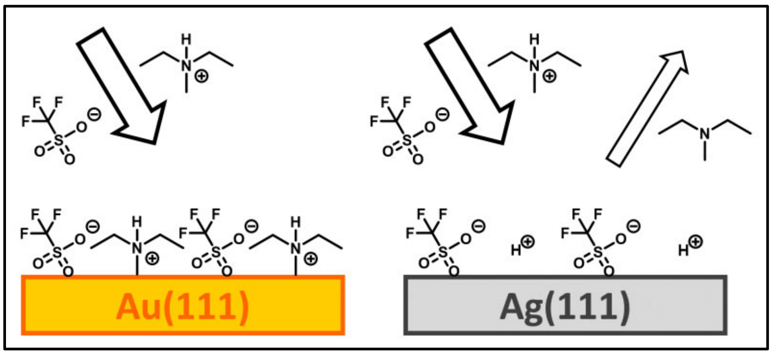

[P2] S. Massicot, T. Sasaki, M. Lexow, F. Maier, S. Kuwabata, H.-P. Steinrück:

On-Surface Metathesis of an Ionic Liquid on Ag(111).

Chem. Eur. J. **2022**, e202200167

The author's contribution are the ARXPS measurements, data analysis and interpretation, and preparation of the manuscript.

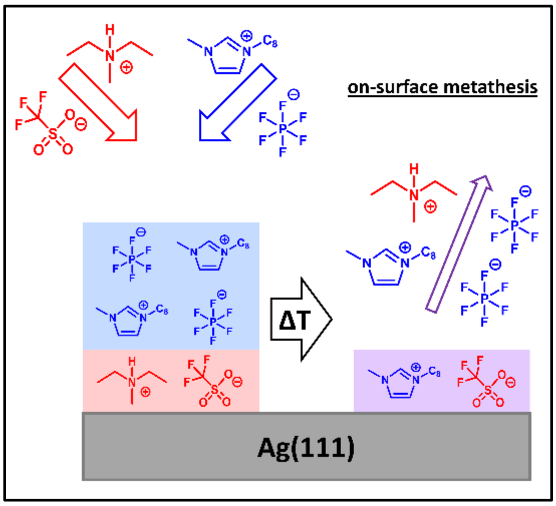

[P3] R. Adhikari*, S. Massicot*, L. Fromm, A. Gezmis, M. Meusel, A. Bayer, S. Jaekel, F. Maier, A. Görling, H.-P. Steinrück:

Structure and Reactivity of the Ionic Liquid [C_1C_1Im][Tf_2N] on Cu(111).

Top Catal **2023**, 66, 1178-1195

The author's contribution are the ARXPS measurements, data analysis and interpretation, and preparation of the manuscript. The nc-AFM and DFT investigations were performed by Rajan Adihkari and Lukas Fromm, respectively.

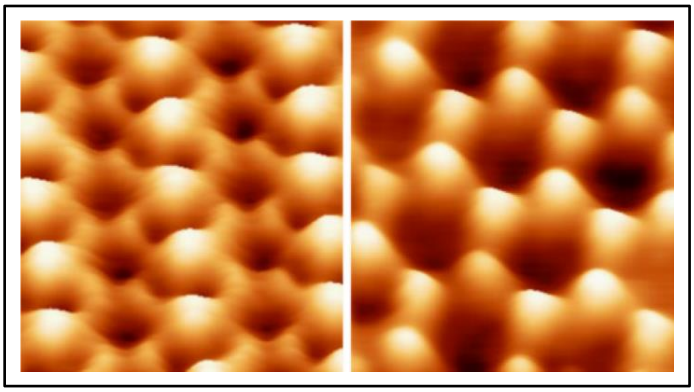

[P4] S. Massicot, A. Gezmis, T. Talwar, M. Meusel, S. Jaekel, R. Adhikari, L. Winter, C. C. Fernández, A. Bayer, F. Maier, H.-P. Steinrück:

Adsorption and Thermal Evolution of [C_1C_1Im][Tf_2N] on Pt(111).

Phys. Chem. Chem. Phys. **2023**, 25, 27953-27966

The author's contribution are the ARXPS measurements, data analysis and interpretation, and preparation of the manuscript. The STM investigations were performed by Afra Gezmis.

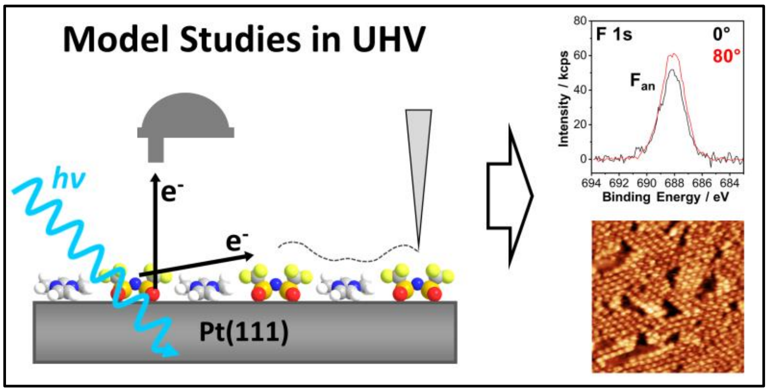

---

*shared first-authorship.

List of Abbreviations

$[C_1C_1Im][Tf_2N]$	1,3-dimethylimidazolium bis(trifluoromethylsulfonyl)imide
$[C_8C_1Im][PF_6]$	1-methyl-3-octylimidazolium hexafluorophosphate
[dema][TfO]	Diethylmethylammonium trifluoromethanesulfonate
ARXPS	Angle-Resolved X-ray Photoelectron Spectroscopy
ASF	Atomic sensitivity factor
BE	Binding energy
IL	Ionic Liquid
IP	Inflection point
ML	Monolayer
Nc-AFM	Non-contact Atomic Force Microscopy
PIL	Protic Ionic Liquid
PVD	Physical Vapor Deposition
RT	Room temperature
TPXPS	Temperature-Programmed X-ray Photoelectron Spectroscopy
STM	Scanning Tunneling Microscopy
SCILL	Solid Catalyst with Ionic Liquid Layer
UHV	Ultra high vacuum
WL	Wetting layer
XPS	X-ray Photoelectron Spectroscopy

1. Introduction

Ionic Liquids (ILs) are salts with melting points typically well below 100 °C, and are composed of poorly coordinating organic cations and organic or inorganic anions. A delocalized charge distribution and steric effects lead to the low melting point of ILs with a majority even being liquid at room temperature (RT), in contrast to "classical" salts such as sodium chloride (NaCl), which is solid up to ~800 °C (illustrated in Figure 1).[1]

Figure 1: Ionic Liquid (left) and sodium chloride (right), both at RT.

In the last three decades, ILs received a lot of attention due to their unusual properties, such as a low melting point,[2] extremely low vapor pressure,[3-4] thermal stability,[5-8] wide liquid range,[9] non-flammability,[10] viscosity[11] and large electrochemical window.[12] This behavior is the result of a complex interplay of Coulomb, hydrogen bonding, dipole and Van der Waals interactions, which rarely occurs in other materials.[13] The class of ILs exhibits a wide structural diversity based on the nearly unlimited possibilities to combine various cations and anions. Moreover, the possibility of implementing functional groups to the chemical structure or applying mixtures allows for further adjusting their properties for specific demands. Besides green chemistry,[14-15] lubrication[16-17] and electrochemical applications,[18-20] ILs are of particular interest in the field of catalysis[21-25] due to their low vapor pressure[3-4] and high thermal stability.[5-8] The first industial and still highly important application of ILs in catalysis is the BASIL^{TM} (Biphasic Acid Scavening using Ionic Liquids) process for the production of alkoxyphenylphosphines in 2002.[26-27] Compared to the conventional process, the BASIL process resulted in a substantial 80,000-fold increase in productivity (in terms of space-time yield).[28]

Since then, different novel catalytic concepts based on ILs were developed, like the SCILL (Solid Catalyst with Ionic Liquid Layer) approach.[29-32] Thereby, a solid catalyst material – often metal nanoparticles dispersed on porous supports – is covered by a thin IL layer that modifies the behavior of the catalyst. In the course of the catalytic turnover, the reactants have to pass through the gas/IL interface of the IL film in order to reach the active sites of the solid catalyst, where the actual chemical conversion takes place (see Figure 2). The IL film fulfills several main functions: Differences in the solubility and diffusion rate of competing reactants (and products) can be exploited to tune the concentration and reactivity close to the active metal sites. Furthermore, the IL can modify sites by ligand-like interactions or block less selective sites of the solid catalyst and thus increase the yield and selectivity of the catalytic process.[33-35] Such SCILL systems are already commercially available by Clariant and are used for the selective hydrogenation of unsaturated hydrocarbons.[36] Based on this SCILL systems, the Dow Chemical Company started up a new world scale production site in 2017 for the ultra-selective hydrogenation of acetylene to form ethylene, which is a crucial feedstock for the production of a variety of polymers.[37]

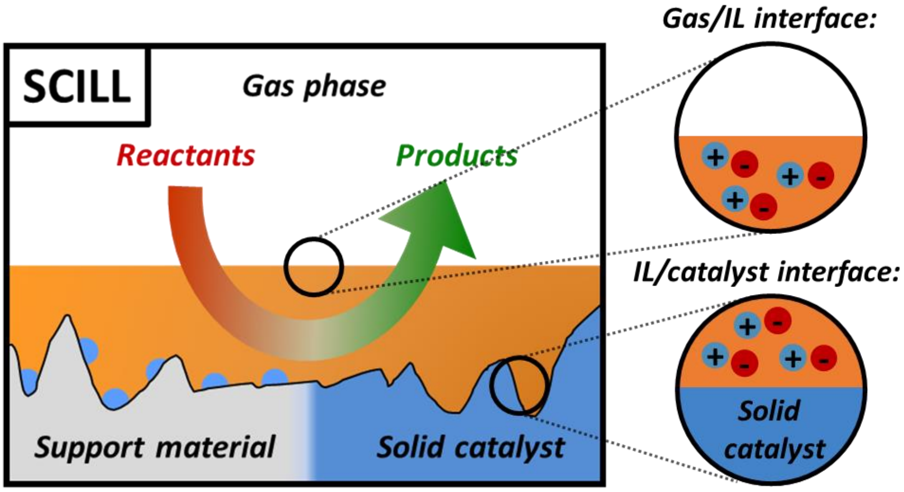

Figure 2: Illustration of the SCILL process. Adapted from Ref.[38]

To obtain the desired catalytic behaviour of a SCILL system, it is crucial to choose a suitable IL/catalyst combination. Solid catalysts are well known and were studied in-depth for several decades, if not centuries.[39-40] In comparison, ILs are a comparable novel class of material and have only been studied for a few decades.[41-42] In particular, surface science studies on thin IL films on metallic supports as model catalysts have only been addressed for a limited number of systems.[43] To break down the complexity of the IL/metal systems making them more accessible for surface science investigations, many studies in the past were limited to comparatively unreactive surfaces (*e.g.* Au(111) and Ag(111)) or ILs with a simple chemical structure (*e.g.* [C_8C_1Im][PF_6] and [C_1C_1Im][Tf_2N], see Table 1 on page 7) which are chemically more stable and abundant on the market and in science.[43]

However, these conditions differ considerably from real industrial applications where more reactive metals are involved and more "complex" ILs with additional functionalities are used, *e.g.* with proton availability. This complexity leads to a mismatch between real applications and surface science.[30, 44] Based on previous studies of less complex systems,[43] the thesis at hand directs towards bridging this gap. For this purpose, metal substrates with different degree of reactivity and/or an IL with an intrinsic functionality are chosen in order to investigate model systems that are more relevant for real SCILL systems.

The performance of SCILL systems is governed by the interplay of the reactants with the gas/IL interface, the bulk film and most importantly, the IL/metal interface. The properties of the gas/IL interface and the bulk of thin macroscopic films have been under intensive investigation for over two decades.[45-49] In case of macroscopic films of several µm up to mm thickness, however, the IL/metal interface is buried under the bulk and therefore not accessible for most surface science techniques.[50] Thus, information on the IL/metal interface is scarce. The surface science community had to wait impatiently until 2008 when the cornerstone for investigations of the IL/metal interface was laid by Cremer *et. al*.[51] For the first time, ILs were successfully deposited via Physical Vapor Deposition (PVD) onto a substrate and subsequently analyzed by Angle-Resolved X-ray Photoelectron Spectroscopy (ARXPS) under ultra-high vacuum (UHV) conditions. Since then, PVD of ILs evolved to an established *in-situ* deposition method of well-defined ultra-thin IL films under extremely clean conditions. Furthermore, the coverage can precisely be controlled ranging from the Ångström regime to several nanometers. XPS on the other hand, is an established surface science technique and allows for the analysis of the chemical composition of the near-surface region of a condensed sample. Due to the XPS information depth up to ~10 nm in ILs, which is in the order of the applied film thicknesses, ARXPS is indeed a powerful technique for investigating the properties of the IL/metal interface.[38, 43]

The following four IL/metal systems were investigated as SCILL model catalysts in this thesis and the results are published in four individual journal articles; the chemical structures of all investigated ILs are shown in Table 1 on page 7.

[P1] [dema][TfO] on Au(111).
[P2] Mixtures of [dema][TfO] and [C_8C_1Im][PF_6] on Ag(111).
[P3] [C_1C_1Im][Tf_2N] on Cu(111).
[P4] [C_1C_1Im][Tf_2N] on Pt(111).

The main results are summarized in four chapters that address important aspects of these model SCILL systems. The first intact deposition of a protic IL by PVD *in vacuo* is presented in Chapter 3.1 ([P1]). The protic IL (PIL) [dema][TfO] was chosen because of its melting point below RT (260-267 K),[52-53] its high thermal stability (decomposition at ~630 K),[52-53] and most important by its proton availability with the equilibrium far on the ionic side (ΔpK_a well above 17).[52, 54-55] Ultra-thin films that remain chemically intact were investigated on an Au(111) surface that showed no reactivity towards ILs in the past. In SCILL catalysis, a good wettability is a crucial requirement for the performance of the system. In this context, the arrangement of the ions at the IL/metal interface, the film growth and most importantly, the wetting behavior are discussed for all systems (except [C_8C_1Im][PF_6]) in Chapter 3.2 ([P1, P3, P4]). Thereafter, the thermal stability of ultra-thin films of [dema][TfO] on the moderately reactive Ag(111) surface, and of the aprotic IL [C_1C_1Im][Tf_2N] on the more reactive Cu(111) and Pt(111) surfaces are summarized in Chapter 3.3 ([P1, P3, P4]). Indeed, both ILs undergo decomposition already well below RT on the respective surfaces. Finally, a novel synthesis approach of ILs is presented in Chapter 3.4 ([P2]). By applying a second aprotic IL to [dema][TfO] films on Ag(111), a new IL can be formed by on-surface metathesis at the IL/metal interface.

2. Fundamentals and Techniques

This chapter introduces the main methods, materials and experimental approaches used for the investigations in the work at hand.

2.1 Angle-resolved X-Ray Photoelectron Spectroscopy (ARXPS)

In this thesis, X-ray Photoelectron Spectroscopy (XPS) is the central spectroscopic technique, which probes the elemental composition of the surface of condensed material.

XPS is based on the photoelectric effect discovered by Hertz[56] and Hallwachs[57] at the end of the 19th century, and finally explained by Einstein in 1905.[58] A sample is irradiated with photons of defined energy ($h\nu$) and hereby photoelectrons are excited to the continuum. The kinetic energy (E_{kin}) of the electrons is detected by an electron analyzer and their binding energy (E_b) can be calculated. For this purpose, the spectrometer is typically calibrated to the Fermi Level of the (metallic) sample taking into account the work function of the spectrometer (ϕ_{sp}):

$$E_b = h\nu - E_{kin} - \phi_{sp}$$

The binding energy of the photoelectrons is element specific and contains further qualitative information on the chemical/physical environment and the oxidation state. Moreover, XPS is a quantitative technique with distinct cross sections for the photoemission process of each electron level.[59]

The information depth (ID) of XPS signals is dependent on the mean free path of the emitted electrons (λ) and the emission angle (ϑ), and is defined as:

$$ID\ (\lambda) = 3\lambda \cdot \cos\vartheta$$

with 96% of the total signal originating within this depth.[60] In Angle-Resolved XPS (ARXPS), the ID varies with the emission angle of the electrons (see Figure 3). Probing organic materials such as polymers or ILs with Al Kα-radiation ($h\nu$ = 1486.6 eV), the ID is typically 7 to 9 nm in normal emission (0°, bulk sensitive) and reduces to 1 to 1.5 nm in grazing emission (80°, surface sensitive).[43]

Auger signals occur as side effect in XPS. Thereby, an excited core hole created in the photoemission process undergoes an Auger decay resulting in the emission of an Auger electron. Auger electrons have characteristic kinetic energy independent of the incident photon energy. Further signals in XP-spectra are *e.g.* plasmon loss peaks or satellites. For a more detailed description of XPS, literature of van der Heide,[60] Hüfner,[61] Seah and Briggs[62] is recommended.

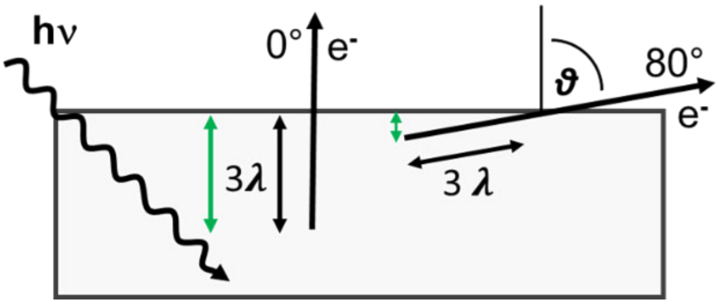

Figure 3: In ARXPS photoelectrons (e^-) are emitted upon X-ray irradiation (*hν*). In 0° and 80° emission the emitted electrons are referred as bulk and surface sensitive, respectively.

2.2 Single Crystals & Polycrystalline Foil

For the experiments in this thesis, round Pt(111), Au(111), Ag(111) and Cu(111) single crystals with a diameter of 15 mm and a thickness of 2 mm were used. They were purchased from MaTeck with a purity of ≥ 99.999 %. The polished front side is aligned to the (111)-plane with an accuracy better than 0.1°. Furthermore, on the small side two pinholes in opposing position allow for inserting (K-type) thermocouples for temperature measurements and notches enable fixation on the sample holders. The crystals were mounted to tantalum sample holders and fixed with Ta wires. The polycrystalline Ag-foil was spot-welded with the help of tantalum foil to the sampleholder. The sample holders, all mounted crystals and the mounted Ag-foil are depicted in Figure 4.

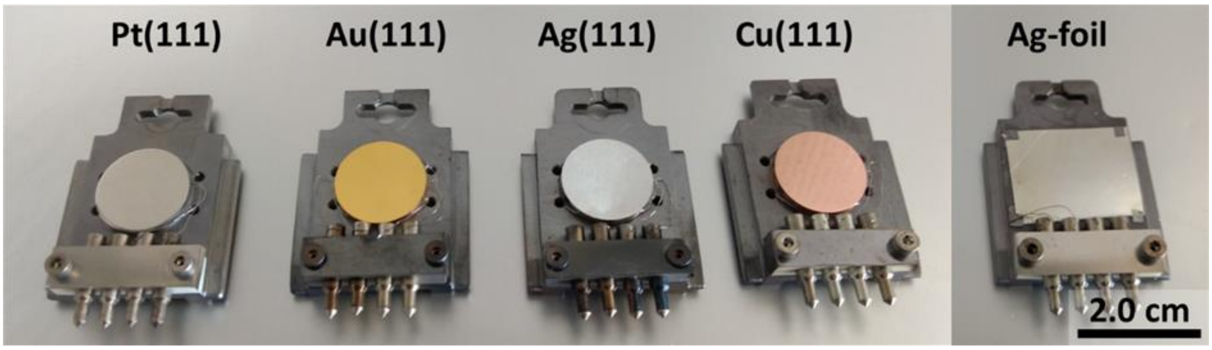

Figure 4: Pt(111), Au(111), Ag(111) and Cu(111) single crystals, and a polycrystalline Ag-foil sample mounted on standard Tantalum sample holders of the ESCA system.

2.3 Ionic Liquids

The Ionic Liquids (ILs) used in this work are summarized in Table 1 along with several relevant physical properties. [dema][TfO] was provided and synthesized by Tomoya Sasaki from the group of Prof. Kuwabata (Osaka University).[63] $[C_8C_1Im][PF_6]$ was purchased from Sigma-Aldrich (purity > 95 %) and $[C_1C_1Im][Tf_2N]$ was purchased from Iolitec (purity ≥ 99 %).

Table 1: Overview of all investigated ILs: name, chemical structure, glass transition temperature (T_g), melting point (T_m) and molecular mass (M).

Ionic Liquid	**Chemical structure**	**T_g (K)**	**T_m (K)**	**M (g/mol)**
[dema][TfO] **Diethylmethylammonium trifluoromethanesulfonate**	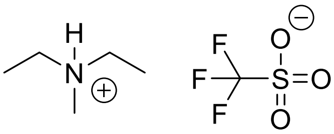	-	260[53]	237.24
$[C_8C_1Im][PF_6]$ **1-methyl-3-octylimidazolium hexafluorophosphate**	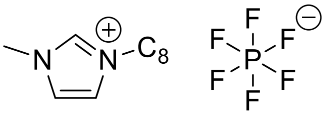	191[64] 194[65] 202[66]	203[67]	340.29
$[C_1C_1Im][Tf_2N]$ **1,3-dimethylimidazolium bis(trifluoromethylsulfonyl)imide**	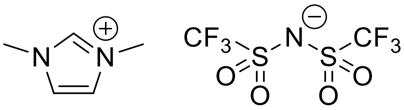		295[22] 299[68]	377.28

2.4 Experimental Aspects

ESCA laboratory: For the work at hand, all experiments were performed using an ultra-high vacuum (UHV) system entitled “ESCA”, which is an alternative and historical acronym for XPS: Electron Spectroscopy for Chemical Analysis (see Figure 5). The ESCA system is composed of a Preparation Chamber (sputtering, annealing, LEED, QMS, PVD of ILs), an Analysis Chamber (ARXPS) with a base pressure in the 10^{-11} mbar range and a Load Lock Chamber (transfer system, through which samples can be introduced into the UHV system). XP-spectra were acquired with a non-monochromatic Al Kα X-ray source (SPECS XR 50, 1486.6 eV, 240 W) and a hemispherical electron analyzer (VG SCIENTA R3000). For more details on the ESCA laboratory, the reader is referred to the theses of Cremer[69] and of Rietzler[70].

Data acquisition: All spectra on Au(111), Ag(111), Cu(111) were measured with a pass energy of 100 eV, resulting in an overall energy resolution of about 0.9 eV (for more details see Refs[69-70]). To improved statistics, the pass energy was increased to 200 eV for measurements on Pt(111) resulting in an overall energy resolution of about ~1 eV.[P4] The raw

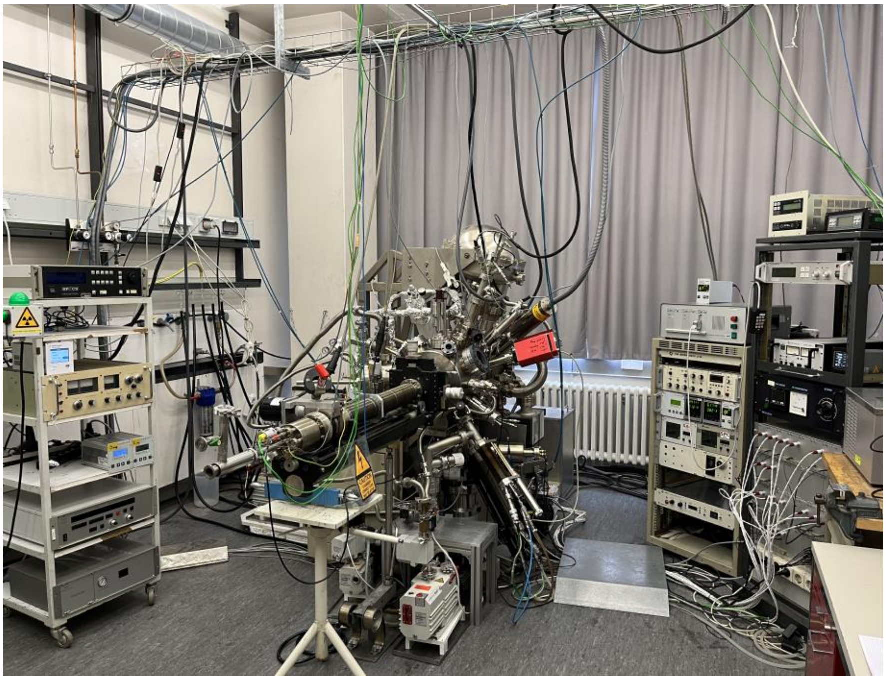

Figure 5: ESCA laboratory with UHV system.

data were quantitatively evaluated in CasaXPS V2.3.16Dev16. Shirley backgrounds were subtracted for the Au 4f, Ag 3d and Cu 2p core levels.[71] For Pt 4f, a constant background was subtracted between 77 and 66 eV. Linear backgrounds were subtracted for the IL related S 2p, C 1s, N 1s, C 1s and F 1s regions, and fitted with Voigt profiles (30% Lorenzian contribution). The Au $4f_{7/2}$, Ag $3d_{5/2}$, Cu $2p_{3/2}$ and Pt $4f_{7/2}$ substrate related core levels were referenced to the Fermi edge yielding 83.85, 368.2, 932.5 and 71.1 eV, respectively. The atomic sensitivity factors (ASF) used for the quantitative analysis of the IL related S 2p, C 1s, N 1s, O 1s and F 1s regions are 0.41, 0.21, 0.36, 0.60 and 1.0, respectively.[72]

Sample preparation: Prior to the deposition of ultra-thin IL films, all single crystals were cleaned by short heating to 500 K and subsequent Ar^+ sputtering (600 V, 8 μA) for 30 mins at RT. The Au(111), Ag(111) and Cu(111) crystals were subsequently annealed at 800 K for 10 mins. To remove more persistent carbon impurities on Pt(111), the crystal was annealed to 1100 K for 10 min, then exposed to an oxygen atmosphere ($p = 10^{-7}$ mbar) at 800 K for 10 min, and subsequently flashed to 1000 K. The cleanliness and long-range order of all crystals was checked by XPS and Low Energy Electron Diffraction (LEED), respectively. After sample cleaning, well defined amounts of ILs were deposited by Physical Vapor Deposition (PVD) in UHV from modified Knudsen cells with boron nitride crucibles. [dema][TfO], $[C_8C_1Im][PF_6]$ and $[C_1C_1Im][Tf_2N]$ were deposited at cell temperatures of 70-80, 175 and 125°C, respectively. The details of the Knudsen cell were published in Ref.[73]

Coverage determination: The IL film thickness on surfaces were derived from the attenuation of the XPS signals of the support. The thickness of an ideal flat film in nanometer (d) can be calculated in normal emission ($\vartheta = 0°$) according to Lambert-Beer's Law:[74]

$$\frac{I_{d,\ substrate}}{I_{0,\ substrate}} = e^{-\frac{d}{\lambda \cdot cos\vartheta}}$$

with the mean free path (λ), the intensity of the IL-covered substrate ($I_{d,\ substrate}$), and the clean substrate ($I_{0,\ substrate}$) taking only inelastic scattering into account. The inelastic mean free path for the Au 3d, Ag 3d, Cu 2p and Pt 4f electrons in ILs is 3.0,[75-77] 2.5,[78] 1.5[P3] and 3.1[P4] nm, respectively.

In line with earlier publications by our group,[76] for the determination of the IL coverage the monolayer (ML) height (h) is approximated via the cubic root of the bulk molecular volume (V_m):

$$h = \sqrt[3]{V_m} = \sqrt[3]{\frac{M}{N_A \cdot \rho}}$$

using the molar mass (M), Avogadro constant (N_A) and mass density (ρ). Hereby, 1 ML is defined as a closed double layer of ions irrespective of their arrangement. In a simplified picture, a single wetting layer with all ions in direct contact with the substrate corresponds to 0.5 ML. Based on this approach, h was determined to 0.67 nm for [dema][TfO],[79] 0.77 nm for $[C_8C_1Im][PF_6]$[80-81] and 0.74 nm for $[C_1C_1Im][Tf_2N]$.[80]

It should be noted that for ideal layer-by-layer growth, the substrate signal should decrease in a section-wise linear fashion for each layer. Consequently, Lambert Beer's Law is mathematically only correct for each fully closed layer (*e.g.* 0.5, 1.0, 1.5… ML) but not for partly filled layers. Nevertheless, in 0° emission the discrepancy is marginal and thus this approach was applied for the coverage determination. However, in 80° emission the deviation is considerably more prominent and needs to be considered, see next paragraph.[43, 82]

Film morphology and growth mode: The growth mode of IL films on surfaces can be monitored via the support XPS signals in 0° (normal emission) and 80° (grazing emission). Based on the measured attenuation ratio $I_{d,\ substrate}/I_{0,\ substrate}$ in the bulk sensitive 0° geometry and the thereof derived film thickness d, the expected attenuation ratio in 80° for an ideally flat film can be calculated via Lambert Beer's Law. Note again for the sake of clarity, the expected ratio in 80° is only valid for fully closed layers of a layer-by-layer growing film while in-between, a section-wise linear decrease of the substrate signal occurs, see previous paragraph. The exponential decay for 0° (solid line) and the section-wise linear decay for 80° (dashed line) of the support signal is illustrated in Figure 6. Comparing the ideally expected behavior in 80° (dashed line) and the experimental values measured in 80°, information on the growth mode can be deduced. Agreement indicates two-dimensional (2D) growth while experimental ratios above the ideal dashed lines indicates a three-dimensional (3D) morphology of the film.[43, 82]

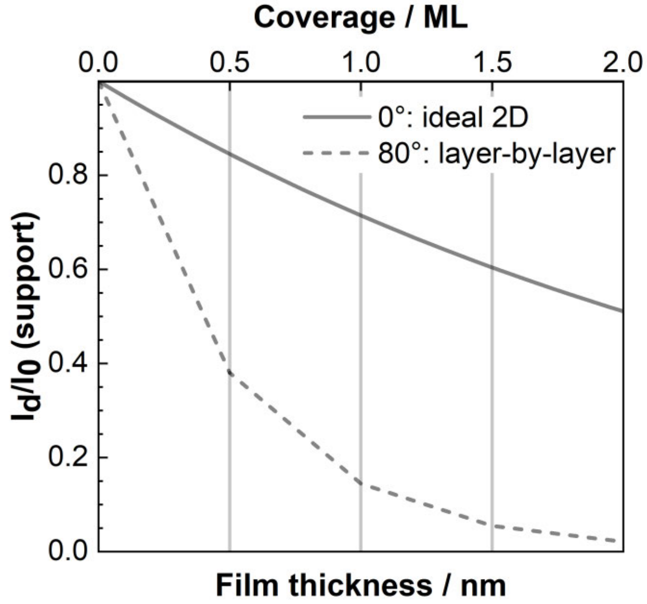

Figure 6: Dependence of the support signal ($I_{d,\ substrate}/I_{0,\ substrate}$) upon film thickness. The solid and dashed lines indicate ideal 2D growth in 0° and layer-by-layer growth in 80°, respectively.

Damping Factor determination: Additional to substrate related XP-signals, intrinsic Auger signals and extrinsic XP-signals of surface contaminations may occur even on freshly cleaned single crystals. For thin IL films, these additional signals need to be considered and subtracted for the quantitative analysis when they interfere with IL related signals. Upon film deposition, these signals are attenuated similarly to the damping of the substrate signal ($I_{d,\ substrate}/I_{0,\ substrate}$). The expected damping factor ($I_{d,\ Auger/\mathrm{cont.}}/I_{0,\ Auger/cont.}$) is calculated via the damping of the substrate considering the different mean free pathes $\lambda_{substrate}$ and $\lambda_{Auger/cont.}$ for substrate photoelectrons and Auger electrons/contamination photoelectrons, respectively:

$$\frac{I_{d,\,\mathrm{Auger/cont.}}}{I_{0,\,\mathrm{Auger/cont.}}} = \left(\frac{I_{d,\,substrate}}{I_{0,\,substrate}}\right)^{\frac{\lambda_{substrate}}{\lambda_{Auger/cont.}}}$$

3. Results and Discussion

The focus of this thesis was the investigation of the interactions of ILs with metallic supports. Understanding of such systems on the molecular scale is essential for thin film applications like SCILL. In particular, the cleanliness, film growth mode, wetting behaviour, arrangement of the ions at the IL/metal interface and thermal stability of ultra-thin IL films were studied in detail. The results of this dissertation were published in four individual journal articles and the major conclusions are summarized in the following four chapters (see also illustrative summaries shown in Figure 7). The author of this thesis contributed the entirety of the data for the publications [P1] & [P2] and the spectroscopic part for the publications [P3] & [P4]. Publications [P3] and [P4] exhibit complementary nc-AFM, STM and DFT results. For a more detailed description of the individual results, the reader is referred to the corresponding publications [P1-P4] in the Appendix.

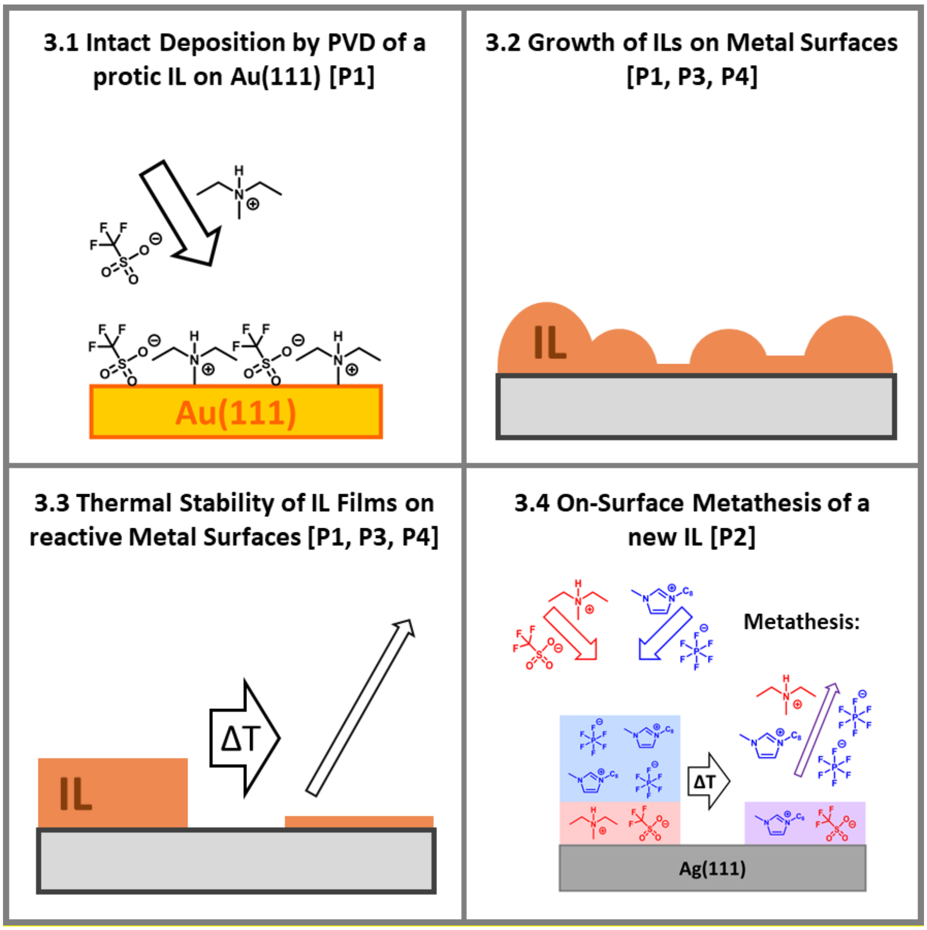

Figure 7: Illustration of chapter 3.1 Intact Deposition by PVD of a protic IL on Au(111) [P1], 3.2 Growth of ILs on Metal Surfaces [P1, P3, P4], 3.3 Thermal Stability of neat IL Films on reactive Metal Surfaces [P1, P3, P4] and 3.4 On-Surface Metathesis of a new IL [P2].

3.1 Intact Deposition by PVD of a protic IL on Au(111) [P1]

During the last 15 years, numerous studies of ultra-thin IL films deposited by PVD have been carried out. However, all studies were limited to aprotic ILs, and studies of protic ILs were missing until 2021 when the protic IL [dema][TfO] was successfully deposited by PVD for the first time *in vacuo* on Au(111) without decomposition. The results are published in paper [P1] and will be discussed in this chapter.

To proof that chemically intact ultra-thin protic IL films can be produced via PVD, [dema][TfO] was deposited on Au(111) at 200 K. The thickness was determined by Lambert Beer's Law (see Chapter 2.4, coverage determination) to 2.4 nm, which corresponds to 3.6 ML. All IL-related core level spectra along with their fits in 0° (black) and 80° (red) emission are shown in Figure 8. The corresponding binding energies (BEs) are summarized in Table 2. For the $[dema]^+$ cation, we observe two distinct signals in the C 1s and one in the N 1s region. The C_{alkyl} peak at 285.2 eV is assigned to the two alkyl carbon atoms at the end of the ethyl groups, and the C_{hetero} peak at 286.5 eV is assigned to the three carbon atoms in direct contact with the nitrogen (hetero) atom. The single N_{dema} peak at 402.3 eV is assigned to the ammonium nitrogen atom.[83-85] The $[TfO]^-$ anion displays one peak each in the C 1s, F 1s and O 1s region, and a doublet in the S 2p region. The C_{CF3} peak at 292.6 eV and the F_{CF3} peak at 688.5 eV are assigned to carbon and fluorine atoms of the trifluoromethyl groups. The spin orbit-split $2p_{3/2}/2p_{1/2}$ S_{SO3} doublet at 168.7/169.6 eV and the O_{SO3} peak at 532.3 eV are assigned to the sulphur and oxygen atoms of the sulfonate group.[83-85]

The corresponding quantitative analysis is summarized in Table 2. All signals are corrected for their cross sections by dividing the signal intensities by their corresponding ASF factors (see Chapter 2.4, data acquisition) before calculating the individual atom numbers. The experimental values in 0° (left value, **bold**) and nominal values (in brackets) show excellent agreement within the accuracy of our measurements (±10%). This is a strong proof that [dema][TfO] chemically stays intact during the PVD process and that intact protic IL films can be prepared *in vacuo* by PVD. By changing the emission angle to 80°, the measurement becomes about six times more surface sensitive, and information on enrichment effects can be gained. For the F 1s signal, the atom number is higher than the nominal value (3.5 *vs.* 3.0), whereas the O 1s signal is lower than the nominal value (2.7 *vs.* 3.0) in 80°. This observation is interpreted as an enrichment effect based on the preferential orientation of the $[TfO]^-$ anion at the outer surface with the CF_3 groups pointing towards the vacuum and the SO_3 groups away from the vacuum towards the bulk.

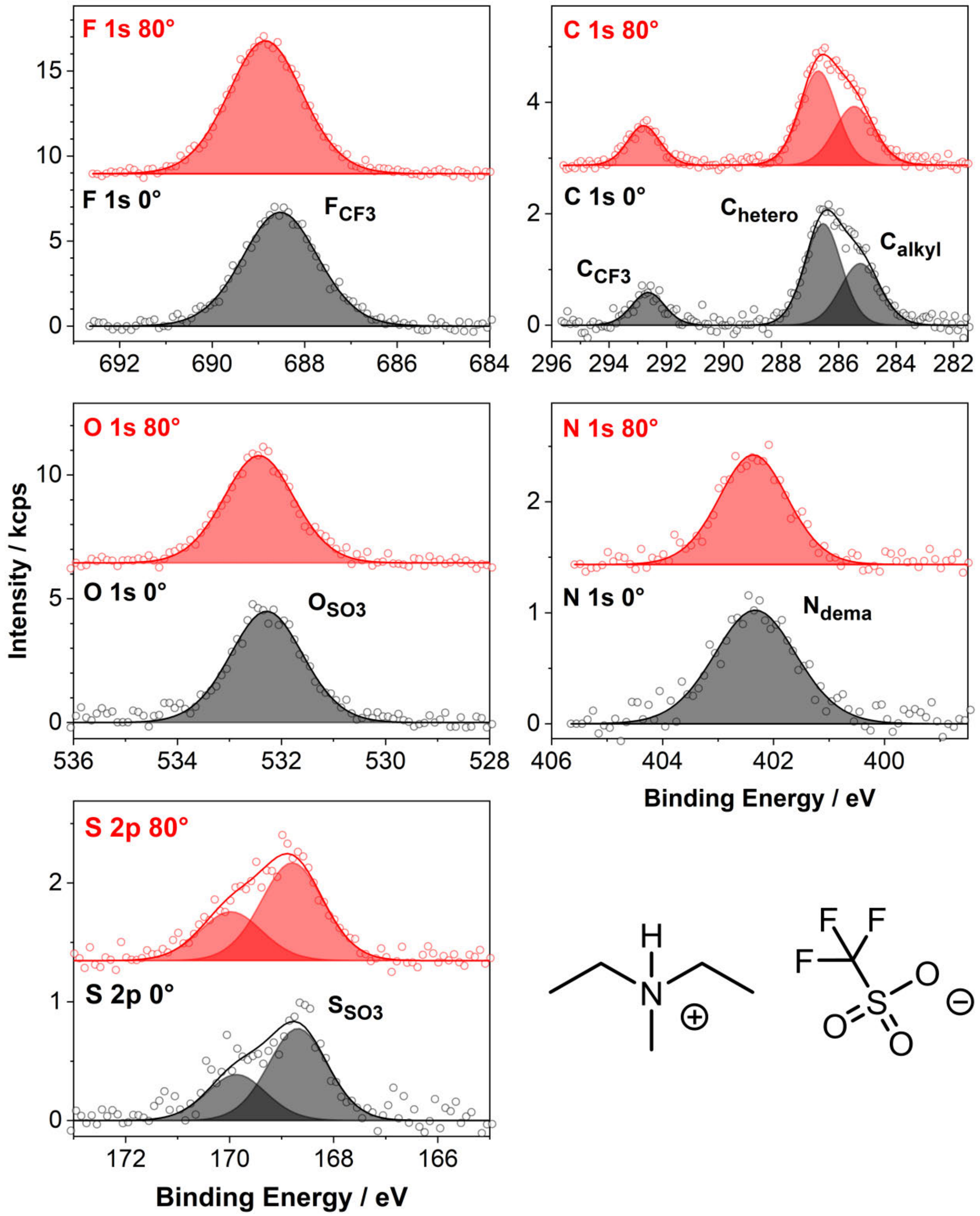

Figure 8: S 2p, C 1s, N 1s, O1s and F 1s XP spectra of a 2.4 nm thick [dema][TfO] film deposited onto Au(111) at 200 K, collected at 0° (black) and 80° (red) emission. At the right bottom, the molecular structure of diethylmethylammonium trifluoromethanesulfonate ([dema][TfO]) is shown. Taken from publication [P1].

For this investigation, a substrate temperature of 200 K was chosen, because the onset of the multilayer desorption, *i.e.* evaporation of the [dema][TfO] ions that are not in direct contact with the metal surface, already starts below RT. Please note, that on the slightly more reactive Ag(111) surface, [dema][TfO] already undergoes decomposition at the IL/silver interface below 200 K, see Chapter 3.3.

Table 2: Film composition as determined by XPS in normal emission (0°, top) and grazing emission (80°, bottom). The **bold** values (left) corresponds to the 2.4 nm thick film of [dema][TfO] on Au(111) in Figure 8; the nominal composition in atom numbers are given in (brackets). Also denoted are the corresponding binding energies. For S 2p doublet the binding energy (BE) of the S $2p_{3/2}$ peak is given; the S $2p_{1/2}$ peak is at 1.18 eV higher BE. Adapted from publication [P1].

0°	S_{SO3}	C_{CF3}	C_{hetero}	C_{alkyl}	N_{dema}	O_{SO3}	F_{CF3}
atom number	**0.9** (1)	**0.9** (1)	**3.1** (3)	**2.0** (2)	**1.2** (1)	**2.9** (3)	**3.0** (3)
BE / eV	**168.7**	**292.6**	**286.5**	**285.2**	**402.3**	**532.3**	**688.5**

80°	S_{SO3}	C_{CF3}	C_{hetero}	C_{alkyl}	N_{dema}	O_{SO3}	F_{CF3}
atom number	**1.0** (1)	**1.1** (1)	**2.9** (3)	**1.9** (2)	**0.9** (1)	**2.7** (3)	**3.5** (3)
BE / eV	**168.8**	**292.8**	**286.7**	**285.5**	**402.4**	**532.4**	**688.9**

3.2 Growth of ILs on Metal Surfaces [P1, P3, P4]

Wetting is an important requirement for SCILL catalysis in order to ensure that the whole surface of the catalyst particles is covered by ILs. In this context, the wetting and growth behaviour was investigated for [dema][TfO] on Au(111) and Ag(111), and [C_1C_1Im][Tf_2N] on Cu(111) and Pt(111). Increasing amounts of ILs were deposited onto the metallic supports at different temperatures by PVD, and the support intensities were monitored by ARXPS as a function of film thickness. The attenuation (I_d/I_0) characteristics of the substrate signals in 0° (closed symbols) and 80° (open symbols) as a function of film thickness are summarized in Figure 9a-d. Additionally, the exponential decay for ideal 2D growth in 0° (solid line) and the section-wise linear decrease for layer-by-layer growth in 80° (dashed line) are illustrated; for more details see Chapter 2.4 Experimental Aspects.

[dema][TfO] on Au(111) and Ag(111) [P1]: First, the very similar growth of [dema][TfO] on Au(111) and Ag(111) is discussed. In Figure 9a and b, the attenuation of the Au 4f and Ag 3d signals is shown for 90 K (only Ag 3d), 200 K and RT. For both surfaces, the 80° data points closely follow the prediction for layer-by-layer growth for all temperatures up to 0.5 ML. This behavior indicates the formation of a closed wetting layer where the cations and anions adsorb next to each other. This is attributed to strong attractive interactions of the ions with the metal. Interestingly at RT, the film thickness does not increase past wetting layer coverage despite further deposition. This can be explained by the onset of multilayer desorption that starts already at 292 K.[P1] At 90 and 200 K, the coverage continues to increase upon further IL deposition. For both temperatures, the 80° data points now slightly fall above the prediction for layer-by-layer growth. This behavior indicates “moderate” 3D island growth with comparable flat islands on top of the initial formed wetting layer.

[C_1C_1Im][Tf_2N] on Cu(111) [P3]: For low coverages up to 0.3 ML, where all ions are in direct contact with the surface, the 80° data points in Figure 9c follow the prediction for layer-by-layer growth for all temperatures. Again, this indicates that all ions are in direct contact with the surface. Between 0.3 and 0.5 ML, however, all measured data systematically fall slightly above, which indicates the onset of “moderate” 3D growth. This could be explained by the following. Strong interactions of the reactive Cu(111) surface and the IL could induce an adsorption geometry that is flatter than expected from the bulk molecular volume. As a consequence, the ions occupy a larger two-dimensional footprint at the IL/metal interface and hence only the amount of 0.3 ML is required to form a fully closed wetting layer. In this scenario, between 0.3 and 0.5 ML flat islands start to grow on top of the initially formed closed wetting layer with 0.3 ML coverage. By further increasing the coverage above 0.5 ML, the 80° data now falls well above the dashed line indicating more prominent 3D island growth.

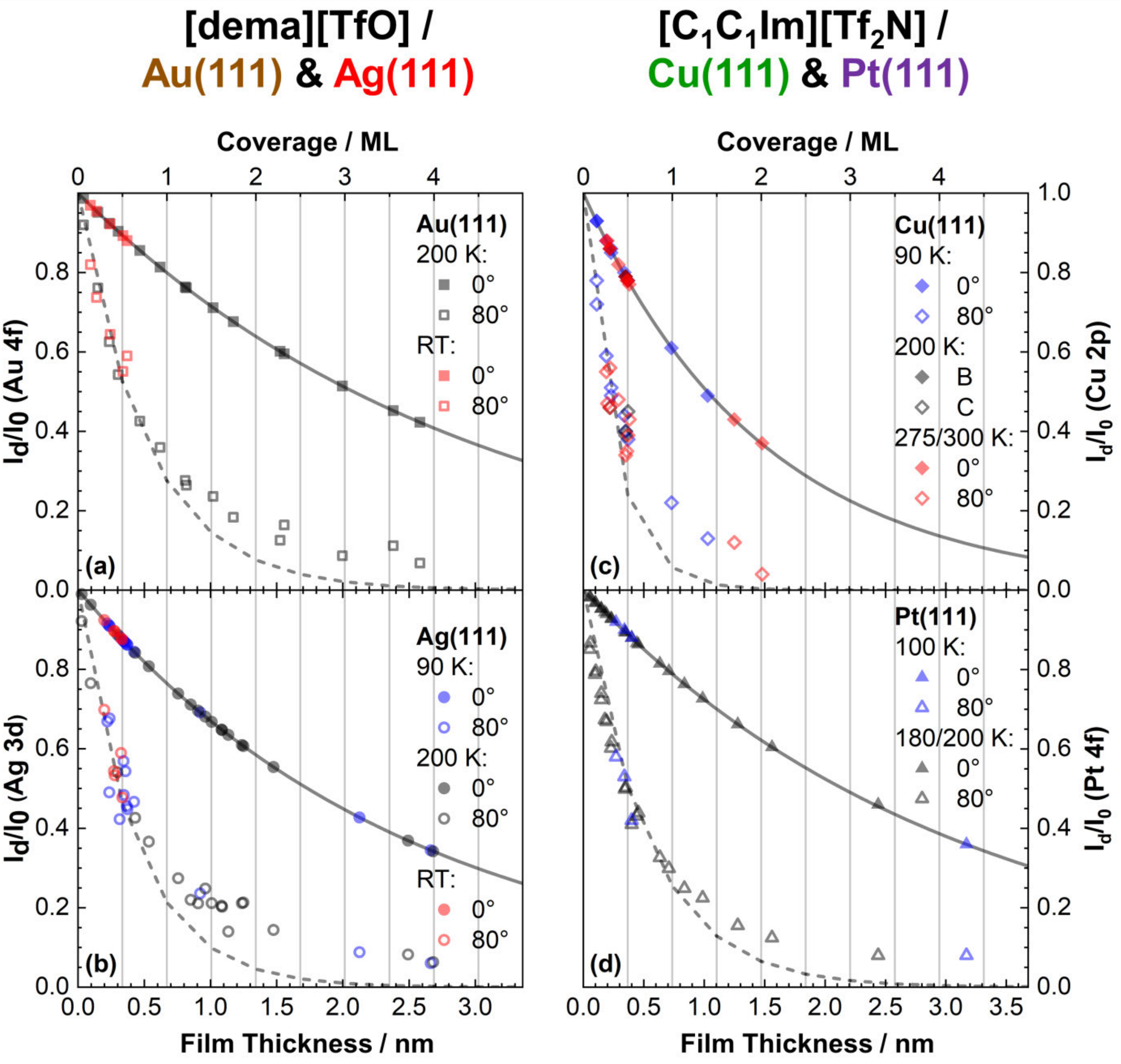

Figure 9: Dependence of the support signals (intensity I_d at film thickness d divided by the intensity of the uncovered surface I_0) upon IL deposition as a function of the mean film thickness derived from the 0° data: (a) [dema][TfO] on Au(111), (b) [dema][TfO] on Ag(111), (c) [C_1C_1Im][Tf_2N] on Cu(111), and (d) [C_1C_1Im][Tf_2N] on Pt(111). Data collected at 0° and 80° are shown as closed and open symbols, respectively. The solid lines indicate ideal 2D behavior in 0° and the dashed lines indicate layer-by-layer growth in 80°. Measurements were performed at 90/100 (blue), 180/200 (black) and 275/300 K (red). Adapted from publications [P1, P3, P4].

[C_1C_1Im][Tf_2N] on Pt(111) [P4]: On Pt(111), the growth of [C_1C_1Im][Tf_2N] is different to Cu(111). Up to 0.5 ML, the 80° data in Figure 9d follow the prediction for ideal layer-by-layer growth for all temperatures indicating the formation of a wetting layer with all ions in contact with the surface. In contrast to the other three systems, the 80° data continuous to follow the curve for 2D layer-by-layer growth up to ~1.0 ML. This indicates that on top of the initial formed wetting layer an additional flat 2D layer with 0.5 ML thickness is forming. By further increasing the coverage, the 80° data now progressively start to fall above the ideal line indicating "moderate" 3D island growth with comparable flat islands on top of the initial formed first 2D monolayer (1 ML).

Summary and comparison: In all investigated systems, upon IL deposition, a closed wetting layer is initially formed where the cations and anions adsorb next to each other. This behavior is common for ILs on metal surfaces and has been observed for most investigated systems.[43] However, the multilayer growth for these systems differ. Multilayers of [dema][TfO] on top of the wetting layer (with 0.5 ML coverage) only grow below RT with a "moderate" 3D behavior; at RT and above, no multilayers are formed in vacuum due to desorption. In comparison, [C_1C_1Im][Tf_2N] on Cu(111) shows a more prominent 3D behavior on top of the initial wetting layer (with 0.3 ML coverage), while on Pt(111) the 3D growth only starts on top of the first initial monolayer (1 ML).

3.3 Thermal Stability of neat IL Films on reactive Metal Surfaces [P1, P3, P4]

In general, ILs are known to exhibit a high thermal stability.[5-8] However, this behaviour can deviate when ILs are in direct contact with a reactive metal as it is the case for SCILL catalysis. Detailed information on decomposition processes at the interface between ILs and reactive metal surfaces is still scarce since studies in the past were often focused on unreactive surfaces.[43] In this chapter, the thermal behaviour of the following systems were investigated: (a) [dema][TfO] on the moderately reactive Ag(111), and [C_1C_1Im][Tf_2N] on the more reactive (b) Cu(111) and (c) Pt(111). For the three systems, films with 0.5 ML thickness were deposited on the respective metals; at this coverage (most of) the ions are expected to be in direct contact with the metal surface. The films were deposited at sample temperatures between 90 and 200 K where no decomposition of the IL is expected at the metal surface. Subsequently, detailed isothermal characterizations at these and higher temperatures were performed, and are discussed in Section 3.3.1. Furthermore, the thermal evolution of these films is discussed in Section 3.3.2. The ILs were monitored through F 1s and C 1s spectra in 0° emission. For both ILs, the F_{an} signal is assigned to the CF_3 groups of the anions (note that in case of Cu(111), a copper auger (LMM) signal occurs in the F 1s region, which is considered in the analysis). For [C_1C_1Im][Tf_2N], the C_{cat} signal is assigned to the five carbon atoms of the imidazolium cation. For [dema][TfO], the C_{cat} signal is composed of two signals assigned to the different carbon atoms of the cation (see Chapter 3.1). In the following discussions, the F_{an} signal will be treated as representative for the whole anion and the C_{cat} signal will be treated as representative for the whole cation. Further anion and cation signals (not shown) behave qualitatively the same and are presented in publication [P1], [P3] and [P4].

3.3.1 Isothermal Characterization

In contrast to the most inert Au(111) surface, [dema][TfO] and [C_1C_1Im][Tf_2N] showed thermal decomposition at the interface with the more reactive metal surfaces investigated here. In this section, the chemical nature of these processes is addressed. First, the behaviour of 0.5 ML thick films of the protic IL [dema][TfO] on the moderately reactive Ag(111) is presented in Figure 10a. Afterwards, 0.5 ML thick films of [C_1C_1Im][Tf_2N] on the more reactive Cu(111) and Pt(111) surfaces are discussed along with Figure 10b and c, respectively.

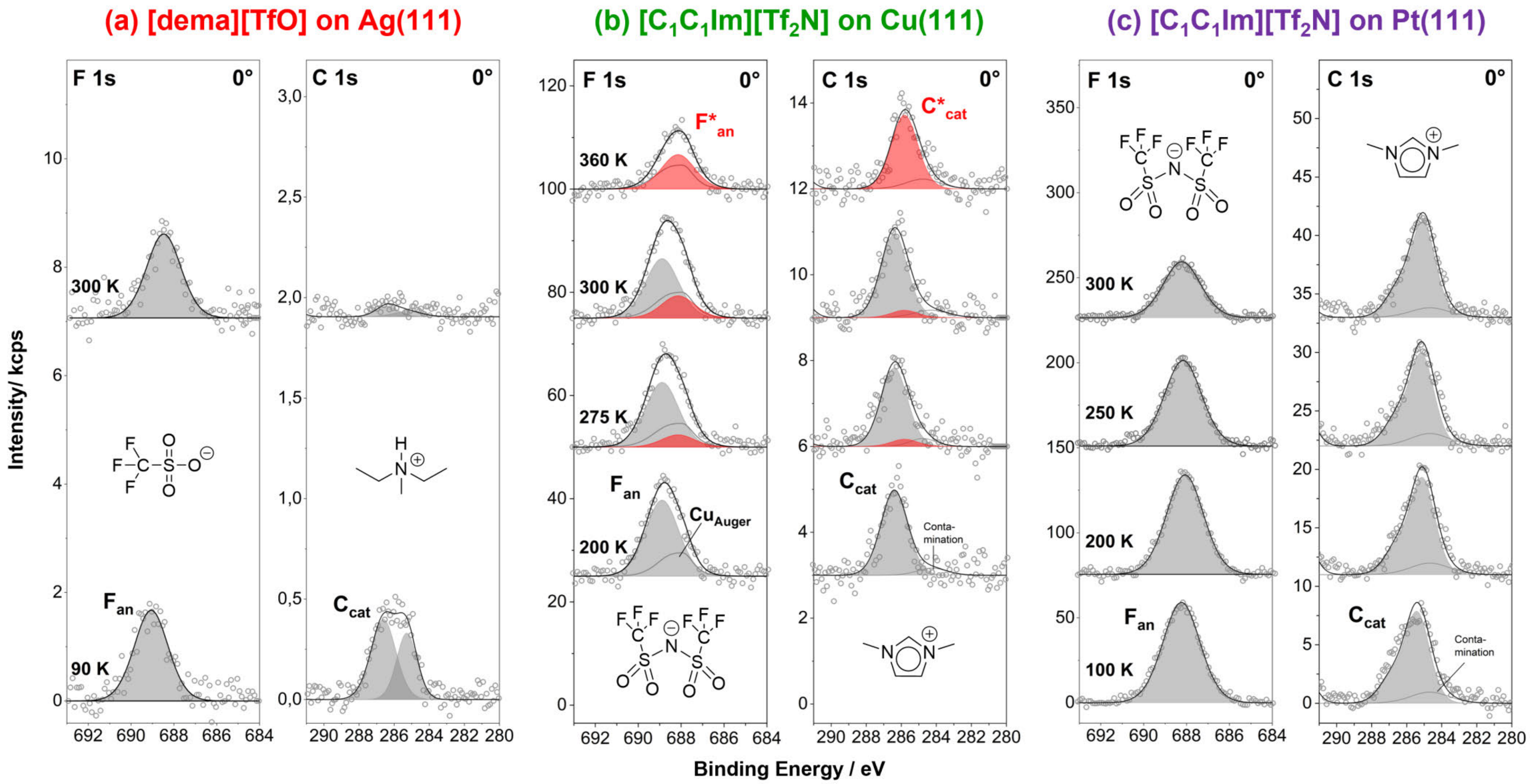

Figure 10: F 1s and C 1s spectra at selected temperatures of 0.5 ML IL films at 0° emission: (a) [dema][TfO] on Ag(111), (b) [C_1C_1Im][Tf_2N] on Cu(111), and (c) [C_1C_1Im][Tf_2N] on Pt(111). Additionally, the chemical structure of each IL is shown. Adapted from publications [P1, P3, P4].

(a) [dema][TfO] on Ag(111) [P1]: Thin films of [dema][TfO] were deposited on Ag(111) at 90 K. The corresponding F_{an} and C_{cat} signals shown in Figure 10a exhibit a ratio of 0.6 (= 3:5) which is in perfect agreement with the chemical structure and indicates that at 90 K [dema][TfO] is stable at the IL/Ag(111) interface. After heating to RT, the F_{an} binding energy shifts by -0.6 eV to lower binding energy. More importantly, the C_{cat} signal drastically decreases in intensity. Because desorption of isolated cations is not possible due to energetic reasons,[86] the substantial intensity loss clearly points towards decomposition of the $[dema]^+$ cations at the IL/Ag(111) interface upon heating to RT. In contrast to the non-reactive Au(111) surface,[P1] the Ag(111) surface could enable deprotonation of the ammonium based cation to form neutral diethylmethylamine ($[dema]^0$) and a proton (H^+). The neutral $[dema]^0$ is volatile and subsequently desorbs from the surface leaving H^+ and $[TfO]^+$ formally as trifluoromethanesulfonic acid (H[TfO]) behind. The shift of the anion signal to lower binding energy upon heating to RT thus might indeed be due to the exchange of the cation by a proton.

(b) [C_1C_1Im][Tf_2N] on Cu(111) [P3]: In Figure 10b, spectra of [C_1C_1Im][Tf_2N] films on Cu(111) are shown for selected temperatures. At 200 K, the F_{an} and the C_{cat} signals are composed of one peak each with the expected signal intensities. Besides, all remaining anion and cation signals in publication [P3] (not shown) exhibit the expected signal intensities corresponding to the nominal stoichiometry of the IL. This strongly indicates that the IL adsorbs and stays intact at 200 K.

After heating to and measuring at 275 and 300 K, new F^*_{an} and C^*_{cat} peaks start to grow (marked in red, with an additional asterisk) at the expense of the original peaks (marked in grey). The new peaks exhibit pronounced shifts towards lower binding energy, *i.e.* -0.7 eV for F^*_{an} and -0.6 eV for C^*_{cat}. However, the total signal intensity stays constant indicating that there is no desorption of IL-related species from the surface at these temperatures. At 300 K, this "signal conversion" is even more pronounced, especially in the F 1s region. Based on nc-AFM measurements in publication [P3] (not shown), we proposed that the unshifted signals correspond to intact ion pairs on the surface forming differently ordered islands that are denoted as stripy, hexagonal and honeycomb. The shifted (*) signals are related to decomposed IL fragments that agglomerate in many smaller disordered islands.

At 360 K, the original unshifted signals have disappeared and only F^*_{an} and C^*_{cat} signals remain. In particular, the remaining F^*_{an} anion signal at 360 K is about half in intensity compared to the total intensity between 200 and 300 K. The loss of ~50 % total anion signals between 300 and 360 K is a strong indication for the desorption of anion related decomposition fragments. Interestingly, the cation signals evolve independently from the anions. The C_{cat} cation signal is (almost) completely converted to the shifted C^*_{cat} species upon heating to 360 K. Again, we concluded along the nc-AFM results shown in publication [P3] that the small disordered islands completely covering the entire surface at 360 K (not shown) are solely composed of IL related decomposition products. At 500 K, the F^*_{an} signal has completely vanished and only decomposed sulphur, carbon and nitrogen residuals remain on the Cu(111) surface (not shown).

Next, the chemical nature of the decomposition products formed at 275/300 K is discussed. The anion most likely decomposes into small non-volatile fragments such as NH_x, SO_x, and CF_3 species and the cation eventually reacts to carbonaceous species. As mentioned above, at 275/300 K the degree of conversion to shifted (*) signals for the cation is smaller than for the anion. However, for charge neutrality reasons it is expected that the same amount of cations and anions should decompose. The smaller fraction of shifted C^*_{cat} signals could be explained by some “preliminary” decomposition products having binding energy values still close to the original peaks at 200 K. Only further decomposition leads to complete conversion to the “final” decomposition product with distinct lower binding energy at 360 K.

(c) [C_1C_1Im][Tf_2N] on Pt(111) [P4]: Finally, films of [C_1C_1Im][Tf_2N] were studied on a Pt(111) surface at selected temperatures. At 100 and 200 K, the F_{an} and the C_{cat} signals display one peak each and remain nearly unchanged in Figure 10c. Notably, the cation C 1s and N 1s signals are considerably shifted to lower binding energies as compared to Ag(111) and Cu(111) due to the strong interaction of imidazolium ring with the Pt surface. These signals and the remaining anion and cation signals in publication [P4] (not shown) all correspond to the stoichiometry of the intact IL. This indicates that the IL remains stable on Pt(111) until 200 K, which is confirmed by STM measurements (not shown) as discussed in [P4].

When the sample is heated to 250 and 300 K, the F_{an} intensity reduces by ~15 and ~50 %, respectively. The C_{cat} intensity remains more or less unchanged up to 300 K. Notably, the binding energies undergo only minor changes for both signals (±0.1 eV). In the following, an explanation is given for these observations. The IL likely decomposes to similar fragments as expected on Cu(111), *i.e.* NH_x, SO_x, and CF_3 species for the anion and carbonaceous species for the cation. However, the anion decomposition products are volatile and desorb from the surface at these temperatures leading to the observed intensity decreases. The remaining anion signal is solely assigned to intact anions. Along the anion decomposition, an equivalent number of cations also decompose due to charge neutrality reasons. These cation decomposition products, however, remain adsorbed at the metal surface; moreover, they exhibit similar binding energies as the intact cations, which explains the nearly unchanged C_{cat} peak. These cation-related decomposition products partly passivate the reactive Pt(111) surface and thus, enable that ~50 % of the IL stays intact on passivated surface areas when the sample is heated to 300 K. This process will be described in more detail in the next chapter.

3.3.2 Thermal evolution

In this section, the thermal evolution of thin IL films is addressed starting with the behaviour of [dema][TfO] on Ag(111) (Figure 11a), followed by [C_1C_1Im][Tf_2N] on Cu(111) and Pt(111) (Figure 11b and c). IL films with 0.5 ML coverage were deposited at ~100 K on the three different substrates and were subsequently heated to 600 K with a heating rate of 2 K/min while simultaneously performing temperature-programmed XPS measurements in 0°. For [C_1C_1Im][Tf_2N] on Cu(111) and Pt(111), at the end of the heating experiment the sample was additionally flashed to 800 K, and a last data set was recorded again at 600 K. The evolution of the F 1s (diamonds, in colour), C 1s (squares, grey) and support (Ag 3d, Cu 2p & Pt 4f: circles, light grey) signal intensities are shown in Figure 11. For better visualisation, the data points are superimposed by semi-transparent lines, and the (step-wise decreasing) evolution of the curves will (occasionally) be described by the inflection points (IPs). A decrease of the F_{an} and C_{cat} signals indicates desorption of IL-related species; the support signal is expected to increase accordingly due to a decrease of surface coverage.

(a) [dema][TfO] on Ag(111) [P1]: First, the thermal evolution of [dema][TfO] on Ag(111) is discussed. The F_{an} and C_{cat} signal intensities remain constant between 100 and ~180 K. This indicates that no IL-related species are desorbing from the surface and that the IL stays chemically intact on Ag(111) in this temperature range. Thereafter, the C_{cat} signal decreases to zero in two steps at ~185 K (IP) and ~305 K (IP). This can be explained by the deprotonation and desorption of the neutral diethylmethylamine ([dema]^0) that occurs in two steps. The formed protons remain next to the [TfO]$^-$ anions formally forming triflic acid (H[TfO]) adsorbed at the surface up to room temperature (note that the F_{an} intensity stays constant until a slight decrease by ~15 % at ~215 K (IP), which could indicate a temperature-induced reorientation of the [TfO]$^-$ anion). At higher temperatures, the F_{an} intensity first decreases to ~50 % at ~355 K (IP) and then to zero at ~570 K (IP). This behaviour can be explained as follows. The formed H[TfO] layer partly desorbs at ~355 K (IP) and partly decomposes to form a fluorine-containing decomposition product which is stable up to ~570 K (IP). Thereafter, no [dema][TfO]-related species remain on the surface.

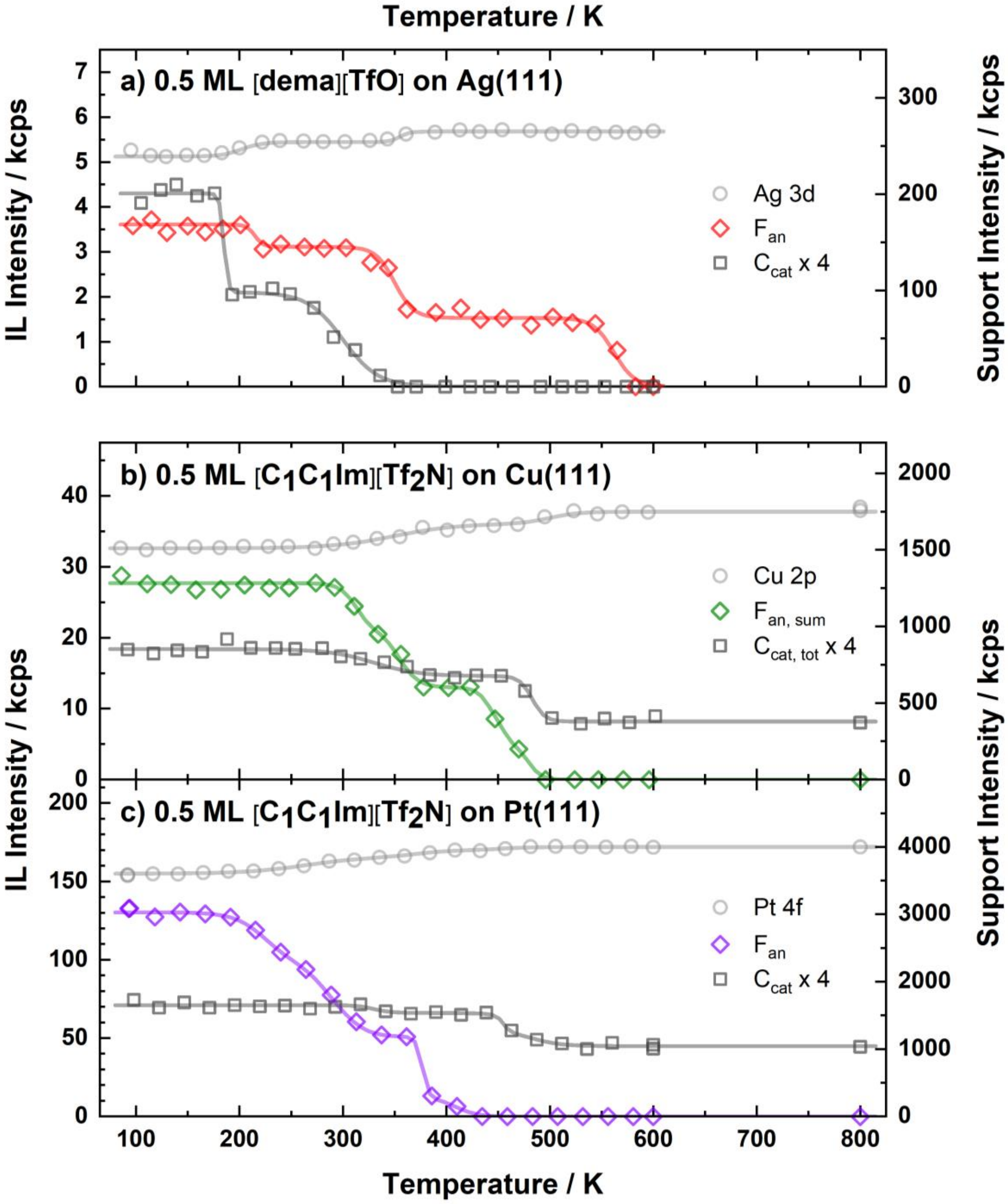

Figure 11: Thermal evolution of F_{an} (diamonds, in colour; for Cu(111), the sum of the shifted F* and non-shifted F-signals is shown), C_{cat} (squares, grey) and support (Ag 3d, Cu 2p & Pt 4f: circles, light grey) signal intensities at 0° emission upon heating 0.5 ML films of (a) [dema][TfO] on Ag(111), (b) $[C_1C_1Im][Tf_2N]$ on Cu(111) and (c) $[C_1C_1Im][Tf_2N]$ on Pt(111), all deposited at ~100 K. The intensities of the C 1s spectra were multiplied by a factor of four for better visualisation. Adapted from publications [P1, P3, P4].

(b) $[C_1C_1Im][Tf_2N]$ films on Cu(111) [P3]: For the TPXPS series of $[C_1C_1Im][Tf_2N]$ on Cu(111), the sum of the anion signals ($F_{an,\ sum} = F_{an} + F^*_{an}$) and the total $C_{cat,\ total}$ signal (including a residual signal above 400 K) will be discussed; one should remember that for all anion and cation core levels, starred (*) signals at lower binding energies appear at around

275 K, which are assigned to decomposition products initially adsorbed next to intact IL ions as it was thoroughly described in the previous chapter. The $F_{an, sum}$ intensity stays constant from 100 to ~300 K, indicating that no anion-related species is desorbing in this temperature range. Above 300 K, the total $F_{an, sum}$ signal decreases by ~50 % to reach a plateau at around 400 K (± 40 K) indicating the desorption of ~50% of anion-related decomposition products; note that at 360 K, only shifted species are observed in the isothermal measurements and thus, only anion and cation derived decomposition products are present at around 400 K. By further heating the sample, the remaining anion-related species desorb until 500 K, as indicated by the disappearance of the $F_{an, sum}$ signal. In contrast to the anion signals, the cation signals show much smaller changes in intensity. The $C_{cat, total}$ intensity initially stays constant until ~300 K indicating that also all cation-related species remain on the surface in this temperature range. Thereafter, the intensity slightly decreases by ~15 % to form a plateau with slightly reduced coverage between ~370 and ~450 K consisting of decomposition products. Finally, it drops to less than half of its original intensity at 485 K (IP) to form a broad remaining residual peak of fully decomposed carbon species that are stable even up to 800 K.

(c) $[C_1C_1Im][Tf_2N]$ films on Pt(111) [P4]: For thin films of $[C_1C_1Im][Tf_2N]$ on Pt(111), the F_{an} and C_{cat} signals are constant between 100 and ~200 K, which indicates that the IL film stays intact in this temperature window. Thereafter, the F_{an} signal starts to decrease by ~60 % until 300 K, indicating the desorption of anion-related decomposition products from the surface. As pointed out in the previous chapter, the C_{cat} intensity remains unchanged until 300 K. Since cations are also expected to decompose along with the decomposing anions, the cation-related decomposition products remain on the surface exhibiting binding energy values close to the remaining intact cations. By further heating the sample, the F_{an} anion signal forms a stable plateau between ~300 and ~375 K indicating that the remaining IL is stable in this temperature range. We assume that in the course of the ongoing IL decomposition starting from 200 K, the surface becomes more and more passivated by cation related decomposition products that remain on the surface. When a certain degree of passivation by these products is reached, further IL decomposition is suppressed, and the Pt surface is covered with intact IL co-adsorbed to the cation-related decomposition products up to ~375 K. Finally, at ~385 K (IP), the anion intensity drops rapidly to zero indicating further decomposition and/or desorption of the remaining IL. At around 400 K, the IL is expected to be fully decomposed since all anion signals are gone. In contrast to the F 1s intensity, the C_{cat} signal undergoes much less changes. The intensity decreases in two steps by 10 and further 30 % at ~330 K (IP) and above 450 K, respectively. The remaining cation signal is attributed to a residual carbon species that remains even up to 800 K.

Summary and Comparison: The thermal decomposition of the protic IL [dema][TfO] on the moderately reactive Ag(111) is governed and initiated by deprotonation of the cation. Already below 200 K, approximately half of the $[dema]^+$ cations deprotonate forming adsorbed triflic acid (H[TfO]), while the neutral diethylmethylamines ($[dema]^0$) desorb. Between 250 and 350 K, the remaining intact $[dema]^+$ cations deprotonate and desorb as neutral amine. The remaining H[TfO] layer partly desorbs and partly decomposes to form a fluorine-containing decomposition product that is stable up to much higher temperatures. The thermal behavior of the aprotic IL $[C_1C_1Im][Tf_2N]$ on Cu(111) and Pt(111) is quite different. On both surfaces, the IL remains chemically intact up to ~200 K. Starting at around 275 K for Cu(111) and already at 200 K for Pt(111), the anion likely decomposes to NH_x, SO_x, and CF_3 species that remain on the Cu(111) surface, but are volatile on Pt(111) and desorb from the surface. The concomitantly decomposing cations eventually react to carbonaceous species that are stable up to much higher temperatures. In contrast to Cu(111), the cation-related decomposition products partly passivate the Pt(111) surface and thus, enable some IL to remain intact at the IL/Pt interface even until ~375 K.

3.4 On-Surface Metathesis of a new IL [P2]

In this chapter, an alternative synthesis route for ILs is presented as compared to a classical wet-chemical approach. This novel “on-surface metathesis” could allow one to tackle challenges existing in the usual synthesis of ILs.[9, 87] To study this metathesis – along with enrichment, ion exchange and selective desorption processes – mixed thin films of [dema][TfO] and $[C_8C_1Im][PF_6]$ were sequentially deposited on Ag(111) and monitored by temperature-programmed XPS in 0° and 80°. In Figure 12, the preparation of the mixed film and the changes with temperature are summarized, and Figure 13 shows the corresponding F 1s and C 1s spectra in 0 and 80° at selected temperatures.

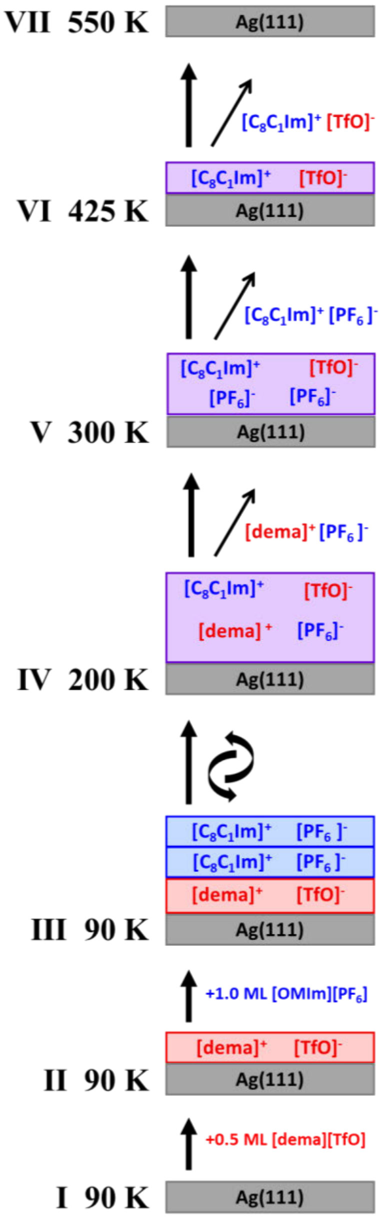

Figure 12: Scheme of the evolution of the film composition. Adapted from publication [P2].

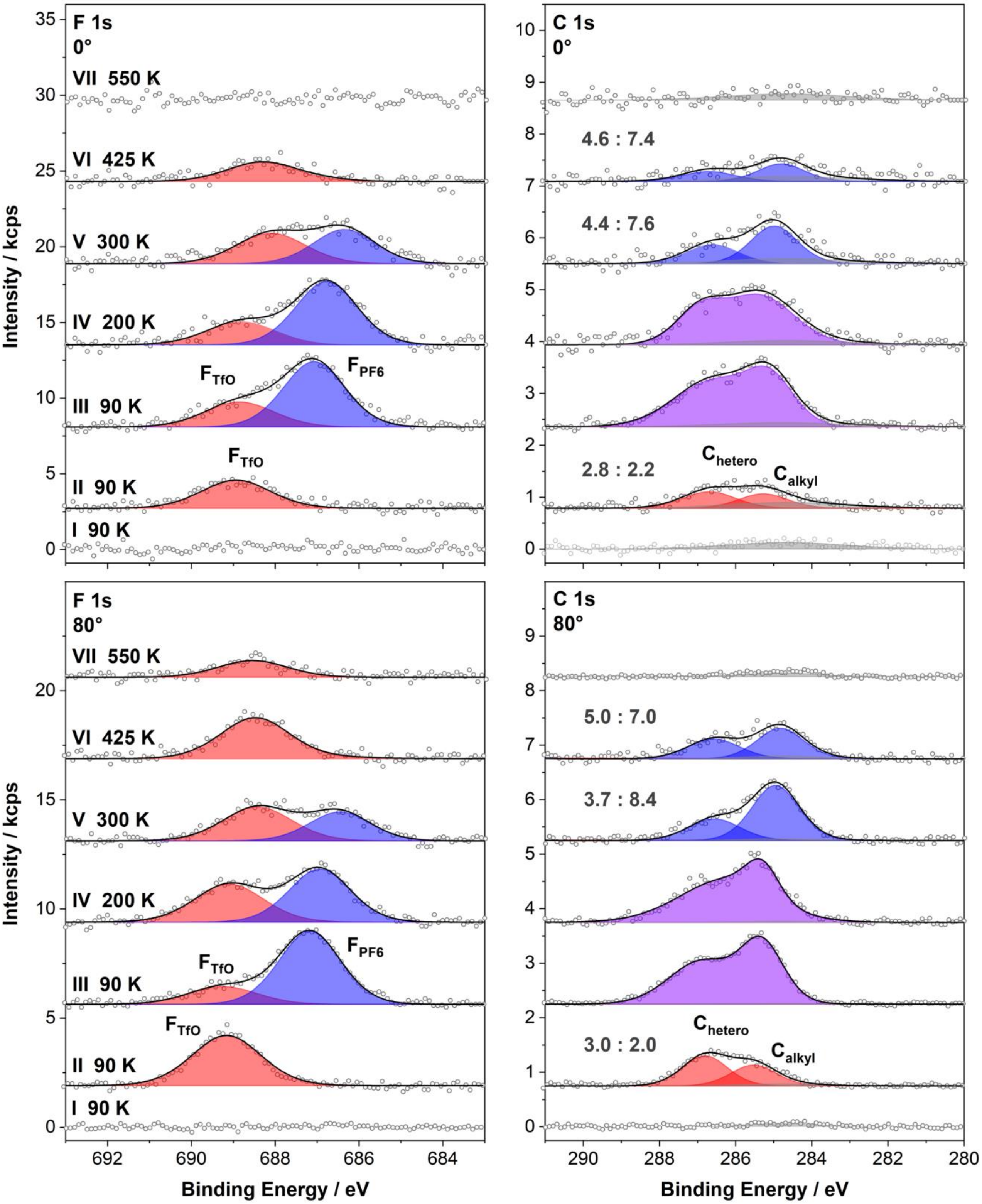

Figure 13: F 1s and C 1s spectra in 0° and 80° emission: **I** clean Ag(111) at ~90 K, **II** 0.5 ML [dema][TfO] at ~90 K, **III** 1 ML [C$_8$C$_1$Im][PF$_6$] on [dema][TfO] at ~90 K, **IV** ion exchange after heating to ~200 K, **V** desorption of [dema][PF$_6$] after heating to ~300 K, **VI** desorption of [C$_8$C$_1$Im][PF$_6$] after heating to ~425 K with [C$_8$C$_1$Im][TfO] remaining on Ag(111), **VII** complete desorption after heating to ~550K (roman numbers refer to Figure 12). Adapted from publication [P2].

In a first step, a wetting layer (*i.e.* 0.5 ML) of [dema][TfO] was deposited on Ag(111) at ~90 K. The corresponding XP spectra in Figure 13-II show the F_{TfO} signal representative of the $[TfO]^-$ anion and the C_{cat} signals (C_{hetero} and C_{alkyl}) representative of the $[dema]^+$ cation, all marked in red. The C_{hetero}:C_{alkyl} ratio is 2.8:2.2 in 0°, which is close to the nominal ratio of 3:2 and hence indicates that the IL adsorbs intact at low temperatures. Subsequently, 1 ML of $[C_8C_1Im][PF_6]$ was deposited on top of the [dema][TfO] wetting layer. The F 1s spectrum in Figure 13-III now displays an additional F_{PF6} contribution at 687.1 eV (marked in blue) representative of the $[PF_6]^-$ anion. In 80° emission, the F_{CF3} signal becomes strongly attenuated and indicates that the post-deposited $[C_8C_1Im][PF_6]$ layer covers the initial [dema][TfO] wetting layer resulting in a frozen, layered system at ~90 K. The C_{hetero} and C_{alkyl} peaks of the $[C_8C_1Im]^+$ cation have only slightly different binding energies than the peaks of the $[dema]^+$ cation. As a consequence, the C 1s peaks of the two cations cannot be deconvoluted and hence, the sum of all signals is shown in purple in Figure 13-III.

As a next step, this layered system was heated from 90 to 550 K and simultaneously TP-XP spectra in the Ag 3d, F 1s and C 1s regions were recorded. The corresponding quantitative analysis of the Ag 3d substrate signal, the F_{TfO} and F_{PF6} signals of the two anions, and the combined C_{Cat} signal (related to all carbon atoms of the two cations) is depicted in Figure 14a and b for 0° and 80° emission, respectively. For better visualisation the data points are superimposed by semi-transparent lines and the (step-wise) evolution of the curves will be described by the inflection points (IPs). A decrease of the F_{TfO}, F_{PF6} and C_{cat} signals indicates desorption of IL-related species; the support signal is expected to increase accordingly due to a decrease of surface coverage.

In 0°, the Ag 3d (grey circles), F_{TfO} (red diamonds), F_{PF6} (blue diamonds) and C_{Cat} (black triangles) intensities stay constant up to ~200 K, indicating that the total coverage of all ions stays constant and that no ions are desorbing. In 80°, however, the F_{PF6} signal decreases and simultaneously, the F_{TfO} signal increases starting from ~135 K; both signals reach a plateau around 200 K (see Figure 13-IV). This indicates that the frozen IL film is melting and the ions are mixing in this temperature range. Moreover, the $[TfO]^-$ anions at the IL/Ag(111) interface are exchanged by $[PF_6]^-$ anions and are enriched at the IL/vacuum interface, leading to the increase and decrease of the F_{TfO} and F_{PF6} signals, respectively, in the 80° spectra. Based on a more detailed analysis in publication [P2], we further concluded that the $[TfO]^-$ anions are enriched together with the $[C_8C_1Im]^+$ cations at the IL/vacuum interface. The driving force for this ion exchange and surface enrichment is likely the lowering in surface tension of the resulting film.

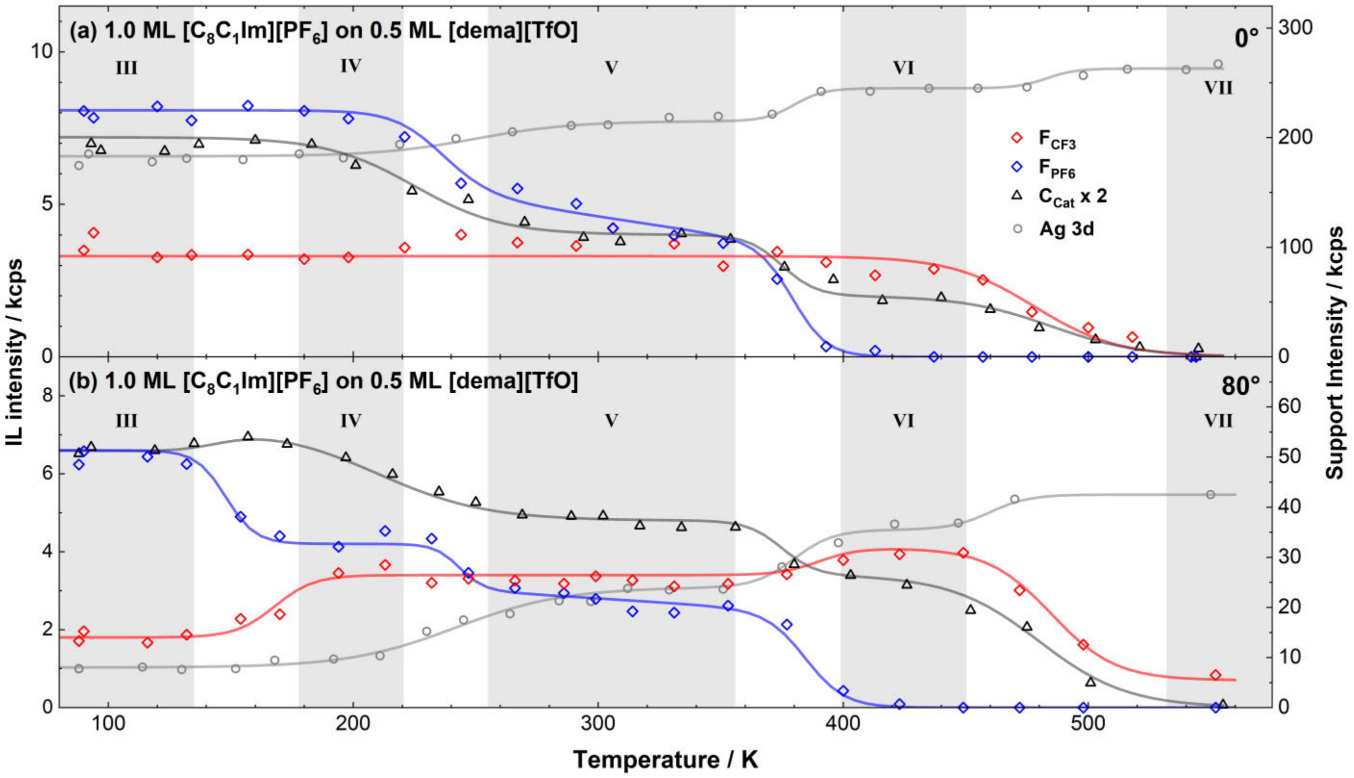

Figure 14: TPXPS of $[C_8C_1Im][PF_6]$/[dema][TfO] on Ag(111) in (a) 0° and (b) 80°; shown are the peak intensities related to the $[TfO]^-$ and $[PF_6]^-$ anions (F 1s, red and blue diamonds, respectively), the cations (C 1s, black triangles), and the supporting Ag crystal (Ag 3d, grey circles). C 1s intensities are multiplied by a factor of two. Adapted from publication [P2].

In the following, the selective desorption steps for three different ion pairs from the surface upon heating the surface to 550 K are discussed based on the quantitative 0° data; the 80° data evolves qualitatively similar. The Ag 3d signal in 0° shows a small increase at ~235 K (IP) indicating a coverage decrease. At the same time, the F_{PF6} and the C_{cat} signals decrease, whereas the F_{CF3} signal remains constant until much higher temperatures. This behavior indicates the selective desorption of $[PF_6]^-$ anions together with $[dema]^+$ cations from the surface. Please note, that $[C_8C_1Im][PF_6]$ would desorb at much higher temperatures.[75, 88] Thereafter, only $[C_8C_1Im]^+$ cations remain on the surface between ~260 and ~360 K, and consequently, the C_{hetero} and C_{alkyl} signals can be analysed quantitatively. Indeed, a C_{hetero}:C_{alkyl} ratio of 4.4:7.6 in Figure 13-V is close to the nominal value of 5:7 for $[C_8C_1Im][PF_6]$, and further indicates that the $[dema]^+$ cations have completely left the surface together with $[PF_6]^-$ anions. Upon subsequent heating, the Ag 3d signal increases step-like at ~380 K (IP) indicating a further coverage decrease. The F_{PF6} and C_{Cat} signals decrease accordingly, indicating the desorption of [C_8C_1Im][PF_6] while the F_{TfO} signal still stays constant. After the selective desorption of [dema][PF_6] at ~235 K (IP) and [C_8C_1Im][PF_6] at ~380 K (IP), a new anion/cation combination of [C_8C_1Im][TfO] is formed as wetting layer by this on-surface metathesis at the IL/metal interface: The quantitative analysis of the C 1s spectra in Figure 13-VI at 425 K yields a C_{alkyl}:C_{hetero} ratio of 7.4:4.6 very close to the nominal value of 7:5. The F 1s region in Figure 13-VI only shows the F_{TfO} signal of the remaining $[TfO]^+$ anion. Finally, a stepwise increase of the Ag 3d signal at ~480 K (IP) indicates the desorption of the remaining [C_8C_1Im][TfO] wetting layer. The F_{TfO}, C_{hetero} and C_{alkyl} signals have completely vanished until 550 K in Figure 13-VII and indicate complete desorption; only in the surface sensitive 80° F 1s spectrum, a small residual is apparent.

It is important to emphasize that neat films of [dema][TfO] on Ag(111) undergo significant deprotonation and decomposition already below 200 K (see Chapter 3.3). However, by applying a second aprotic IL, namely [C_8C_1Im][PF_6], to a [dema][TfO] coating layer, decomposition can be prevented at the interface until much higher temperatures by evaporating the labile IL species. Thus, the resulting new IL system might become more suitable for a SCILL process.

4. Summary

In the following, the results and conclusions of four publications [P1-P4] contributing to this this cumulative thesis are summarized. Thin films of ionic liquids (ILs) on high surface area solid supports are a key technology in a novel catalytic concept, the so-called SCILL (Solid Catalyst with Ionic Liquid Layer) approach.[29-32] Hereby, the performance of the catalyst system is strongly determined by the properties of the interface formed by the ionic liquid and the solid catalyst. In this thesis, the properties of this interface were studied on the molecular level in ultra-high vacuum (UHV) for several model systems based on ultra-thin IL films on model metal surfaces. In particular, the cleanliness, film growth mode, wetting behaviour, arrangement of the ions at the interface and thermal stability of thin IL films on defined metal surfaces were studied by angle-resolved and temperature-programmed X-ray Photoelectron Spectroscopy (XPS).

Intact Deposition by PVD of a protic IL on Au(111) [P1]: For the first time, a protic IL was deposited by PVD *in vacuo* on a (metal) substrate: a multilayer (2.4 nm) thick film of [dema][TfO] was deposited on Au(111) at 200 K and subsequently analysed quantitatively by angle-resolved XPS. The stoichiometry as derived from all IL core level signals in 0° corresponds to the expected nominal values. This observation indicates that [dema][TfO] stays chemically intact during the PVD process and that intact IL films can be prepared in vacuum. The about six times more surface-sensitive 80° measurements indicate preferential orientation of the $[TfO]^-$ anions at the outer surface with the CF_3 groups pointing towards the vacuum and the SO_3 groups away from the vacuum towards the bulk.

Growth of ILs on Metal Surfaces [P1, P3, P4]: Wetting of ILs on solid catalysts is an important parameter for thin film applications like SCILL catalysis. In this context, the growth behavior of [dema][TfO] on Au(111) and Ag(111), and of $[C_1C_1Im][Tf_2N]$ on Cu(111) and Pt(111) was investigated at different temperatures. All investigated systems show a similar behaviour for low coverages. In the wetting layer regime, the cations and anions initially adsorb next to each other in direct contact with the metal surface. The behavior changes for higher coverages to a more or less pronounced 3D island growth for all systems. Notably for [dema][TfO], the coverage does not increase beyond one wetting layer upon IL deposition at RT due to the onset of multilayer desorption that starts already below RT.

Thermal Stability of neat IL Films on reactive Metal Surfaces [P1, P3, P4]: Fundamental knowledge on the thermal stability of ILs in direct contact with metal catalysts is important to thoroughly understand SCILL catalysis on the molecular scale. In order to determine possible decomposition processes at the IL/metal interface, thin films of [dema][TfO] on the moderately reactive Ag(111) surface, and [C_1C_1Im][Tf_2N] on the more reactive Cu(111) and Pt(111) surfaces were investigated. The cation of [dema][TfO] on Ag(111) deprotonates starting already below 200 K. The formed proton is then transferred to the [TfO]$^-$ anion to form neutral triflic acid (H[TfO]) that partly desorbs and partly decomposes to form a fluorine-containing decomposition product that is stable up to much higher temperatures. For [C_1C_1Im][Tf_2N] on both more reactive surfaces, the anion decomposes to NH_x, SO_x, and CF_3 species starting above 200 K. On Cu(111), the decomposition products remain on the surface until higher temperatures, while they are volatile on Pt(111) and desorb from the surface. In the same temperature range, the cation likely decomposes to non-volatile and mainly carbon containing species on both surfaces.

On-Surface Metathesis of a new IL [P2]: A novel synthesis approach of ILs on surfaces is presented. Mixed thin films of the protic [dema][TfO] and the aprotic [C_8C_1Im][PF_6] were sequentially deposited on Ag(111) at 90 K, and monitored by temperature-programmed XPS. Upon heating, thermally induced phenomena of ion exchange and preferential enrichment at the interfaces are observed. Furthermore, selective desorption of specific ion pairs leads to the formation of the new IL [C_8C_1Im][TfO] by on-surface metathesis at the IL/metal interface.

5. Kurzfassung der Arbeit

Im Folgenden werden die Ergebnisse von vier Publikationen [P1-P4] zusammengefasst, die zu dieser kumulativen Arbeit beitragen. Dünne Filme ionischer Flüssigkeiten (engl. ionic liquids, ILs) auf festen Trägermaterialien mit großer Oberfläche spielen eine Schlüsselrolle in dem neuartigen katalytischen Konzept SCILL (engl. Solid Catalyst with Ionic Liquid Layer).[29-32] In SCILL wird die Leistung des Katalysatorsystems stark von der Grenzfläche zwischen der ionischen Flüssigkeit und dem Katalysator (meist metallische Partikel auf Oxidträgern) bestimmt. In dieser Arbeit wurden die Eigenschaften dieser Grenzfläche auf molekularer Ebene im Ultrahochvakuum (UHV) für mehrere Modellsysteme mittels ultradünner IL-Filme auf Einkristalloberflächen untersucht. Insbesondere wurden die Reinheit, die Art des Filmwachstums, das Benetzungsverhalten, die Anordnung der Ionen an der Grenzfläche und die thermische Stabilität dünner IL-Filme auf definierten Metalloberflächen mittels winkelaufgelöster und temperaturprogrammierter Röntgen-Photoelektronen Spektroskopie (engl. XPS) untersucht.

Intaktes Aufdampfen einer protischen IL auf Au(111) durch PVD [P1]: Zum ersten Mal wurde eine protische IL durch physikalische Gasphasenabscheidung (engl. physical vapour deposition, PVD) im Vakuum auf einem (Metall-)Substrat deponiert. Ein Multilagenfilm von 2.4 nm Dicke der IL [dema][TfO] wurde auf Au(111) bei 200 K deponiert und anschließend quantitativ mittels winkelaufgelöster XPS analysiert. Die Stöchiometrie aller IL-Rumpfniveausignale in 0° entspricht den erwarteten Nominalwerten. Dies deutet darauf hin, dass [dema][TfO] während des Prozesses der PVD chemisch intakt bleibt und dass intakte IL Filme im Vakuum hergestellt werden können. Die etwa sechsmal oberflächenempfindlicheren 80° Messungen deuten auf eine bevorzugte Ausrichtung des $[TfO]^-$ Anions an der äußeren Oberfläche hin, wobei die CF_3 Gruppen zum Vakuum hin und die SO_3 Gruppen vom Vakuum weg in das Innere des IL-Films zeigen.

IL-Wachstumsverhalten auf Metalloberflächen [P1, P3, P4]: Das Benetzungsverhalten von ILs auf Katalysatoren ist ein wichtiger Parameter für Dünnschichtanwendungen wie der SCILL-Katalyse. In diesem Zusammenhang wurde das Wachstumsverhalten von [dema][TfO] auf Au(111) und Ag(111) sowie von $[C_1C_1Im][Tf_2N]$ auf Cu(111) und Pt(111) bei verschiedenen Temperaturen untersucht. Alle untersuchten Systeme zeigen für geringe Bedeckungen ein ähnliches Verhalten. Für Filmdicken bis zu einer ersten Benetzungslage adsorbieren die Kationen und Anionen zunächst nebeneinander in direktem Kontakt mit der Metalloberfläche. Bei höherer Bedeckung tritt bei allen Systemen ein mehr oder weniger ausgeprägtes 3D-Inselwachstum auf. Bemerkenswert ist, dass für [dema][TfO] bei Raumtemperatur keine Filme hergestellt werden können, welche dicker als eine erste Benetzungslage sind. Dies liegt an dem Einsetzen der Desorption der Multilagen bereits unterhalb von Raumtemperatur.

Thermische Stabilität von reinen IL-Filmen auf reaktiven Metalloberflächen [P1, P3, P4]: Grundlegende Kenntnisse über die thermische Stabilität von ILs in direktem Kontakt mit Metallkatalysatoren sind wichtig, um die SCILL-Katalyse auf molekularer Ebene zu verstehen. Um mögliche Zersetzungsprozesse an der IL/Metall-Grenzfläche zu identifizieren, wurden dünne Filme von [dema][TfO] auf der weniger reaktiven Ag(111)- sowie [C_1C_1Im][Tf_2N] auf den reaktiveren Cu(111)- und Pt(111)-Oberflächen untersucht. Das Kation von [dema][TfO] auf Ag(111) deprotoniert bereits unterhalb von 200 K. Das gebildete Proton wird letztlich auf das [TfO]$^-$ Anion übertragen. Hierbei wird neutrale Trifluorsulfonsäure (H[TfO]) gebildet, welche zum Teil desorbiert, zum Teil jedoch zersetzt wird und bis zu höheren Temperaturen auf der Oberfläche verbleibt. Im Vergleich dazu zersetzt sich das Anion von [C_1C_1Im][Tf_2N] auf den beiden reaktiveren Oberflächen ab 200 K zu NH_x, SO_x und CF_3 Fragmenten. Auf Cu(111) bleiben die Zersetzungsprodukte bis zu höheren Temperaturen auf der Oberfläche, während sie auf Pt(111) unmittelbar von der Oberfläche desorbieren. Parallel zu den Anionen zersetzen sich im gleichen Temperaturbereich ein Anteil der Kationen auf beiden Oberflächen zu nicht flüchtigen und vor allem kohlenstoffhaltigen Produkten, die auf der Oberfläche verbleiben.

Oberflächen-Metathese einer neuen IL [P2]: Hier wird eine neue Methode zur IL-Synthese auf Oberflächen vorgestellt. Dünne Filme aus der protischen IL [dema][TfO] und der aprotischen IL [C_8C_1Im][PF_6] wurden nacheinander bei 90 K auf Ag(111) deponiert und anschließend mittels temperaturprogrammierter XPS untersucht. Während des Erhitzens der Probe lassen sich so thermisch induzierte Phänomene wie Ionenaustausch und bevorzugte An- und Abreicherungseffekte von Ionen verfolgen. Darüber hinaus desorbieren unterschiedliche Ionenpaare selektiv, was letztlich zur Bildung der neuen IL [C_8C_1Im][TfO] durch Metathese an der IL/Metall-Grenzfläche führt.

6. References

1. Freemantle, M., *An Introduction to Ionic Liquids*. 10 ed.; Royal Society of Chemistry: 2009.
2. Trohalaki, S.; Pachter, R., Prediction of Melting Points for Ionic Liquids. *QSAR & Combinatorial Science* **2005,** *24* (4), 485-490.
3. Lovelock, K. R. J., Quantifying intermolecular interactions of ionic liquids using cohesive energy densities. *Royal Society Open Science* **2017,** *4* (12), 171223.
4. Esperança, M. S. S. J.; Canongia Lopes, J. N.; Tariq, M.; Santos, L. M. N. B. F.; Magee, J. W.; Rebelo, L. P. N., Volatility of Aprotic Ionic Liquids — A Review. *Journal of Chemical & Engineering Data* **2010,** *55* (1), 3-12.
5. Cao, Y.; Mu, T., Comprehensive Investigation on the Thermal Stability of 66 Ionic Liquids by Thermogravimetric Analysis. *Industrial & Engineering Chemistry Research* **2014,** *53* (20), 8651-8664.
6. Maton, C.; De Vos, N.; Stevens, C. V., Ionic liquid thermal stabilities: decomposition mechanisms and analysis tools. *Chemical Society Reviews* **2013,** *42* (13), 5963-5977.
7. Huang, Y.; Chen, Z.; Crosthwaite, J. M.; N.V.K. Aki, S.; Brennecke, J. F., Thermal stability of ionic liquids in nitrogen and air environments. *The Journal of Chemical Thermodynamics* **2021,** *161*, 106560.
8. Cassity, C.; Mirjafari, A.; Mobarrez, N.; Strickland, K.; O'Brien, R.; Davis, J., Ionic liquids of superior thermal stability. *Chemical communications* **2013,** *49*, 7590-7592.
9. Wasserscheid, P.; Welton, T., *Ionic Liquids in Synthesis, Second Edition*. Wiley-VCH Verlag GmbH & Co. KGaA 2007.
10. Smiglak, M.; Reichert, W. M.; Holbrey, J. D.; Wilkes, J. S.; Sun, L.; Thrasher, J. S.; Kirichenko, K.; Singh, S.; Katritzky, A. R.; Rogers, R. D., Combustible ionic liquids by design: is laboratory safety another ionic liquid myth? *Chemical Communications* **2006,** (24), 2554-2556.
11. Jacquemin, J.; Husson, P.; Padua, A. A. H.; Majer, V., Density and viscosity of several pure and water-saturated ionic liquids. *Green Chemistry* **2006,** *8* (2), 172-180.
12. Hayyan, M.; Mjalli, F. S.; Hashim, M. A.; AlNashef, I. M.; Mei, T. X., Investigating the electrochemical windows of ionic liquids. *Journal of Industrial and Engineering Chemistry* **2013,** *19* (1), 106-112.
13. Crowhurst, L.; Lancaster, N. L.; Pérez Arlandis, J. M.; Welton, T., Manipulating Solute Nucleophilicity with Room Temperature Ionic Liquids. *Journal of the American Chemical Society* **2004,** *126* (37), 11549-11555.
14. Earle, M. J.; Seddon, K. R., Ionic liquids. Green solvents for the future. *Pure and Applied Chemistry* **2000,** *72* (7), 1391-1398.
15. Welton, T., Ionic liquids in Green Chemistry. *Green Chemistry* **2011,** *13* (2), 225-225.
16. Zhou, F.; Liang, Y.; Liu, W., Ionic liquid lubricants: designed chemistry for engineering applications. *Chemical Society Reviews* **2009,** *38* (9), 2590-2599.
17. Minami, I., Ionic Liquids in Tribology. *Molecules* **2009,** *14* (6), 2286-2305.
18. Silvester, D. S.; Compton, R. G., Electrochemistry in Room Temperature Ionic Liquids: A Review and Some Possible Applications. *Zeitschrift für Physikalische Chemie* **2006,** *220* (10), 1247-1274.
19. MacFarlane, D. R.; Forsyth, M.; Howlett, P. C.; Pringle, J. M.; Sun, J.; Annat, G.; Neil, W.; Izgorodina, E. I., Ionic Liquids in Electrochemical Devices and Processes: Managing Interfacial Electrochemistry. *Accounts of Chemical Research* **2007,** *40* (11), 1165-1173.
20. Buzzeo, M. C.; Evans, R. G.; Compton, R. G., Non-Haloaluminate Room-Temperature Ionic Liquids in Electrochemistry—A Review. *ChemPhysChem* **2004,** *5* (8), 1106-1120.

21. Wasserscheid, P.; Keim, W., Ionic Liquids—New “Solutions” for Transition Metal Catalysis. *Angewandte Chemie International Edition* **2000,** *39* (21), 3772-3789.
22. Breitenlechner, S.; Fleck, M.; Müller, T. E.; Suppan, A., Solid catalysts on the basis of supported ionic liquids and their use in hydroamination reactions. *Journal of Molecular Catalysis A: Chemical* **2004,** *214* (1), 175-179.
23. Riisager, A.; Fehrmann, R.; Flicker, S.; van Hal, R.; Haumann, M.; Wasserscheid, P., Very Stable and Highly Regioselective Supported Ionic-Liquid-Phase (SILP) Catalysis: Continuous-Flow Fixed-Bed Hydroformylation of Propene. *Angewandte Chemie International Edition* **2005,** *44* (5), 815-819.
24. Virtanen, P.; Salmi, T.; Mikkola, J.-P., Kinetics of Cinnamaldehyde Hydrogenation by Supported Ionic Liquid Catalysts (SILCA). *Industrial & Engineering Chemistry Research* **2009,** *48* (23), 10335-10342.
25. Haumann, M.; Schönweiz, A.; Breitzke, H.; Buntkowsky, G.; Werner, S.; Szesni, N., Solid-State NMR Investigations of Supported Ionic Liquid Phase Water-Gas Shift Catalysts: Ionic Liquid Film Distribution vs. Catalyst Performance. *Chemical Engineering & Technology* **2012,** *35* (8), 1421-1426.
26. Seddon, K. R., A taste of the future. *Nature Materials* **2003,** *2* (6), 363-365.
27. Plechkova, N. V.; Seddon, K. R., Applications of ionic liquids in the chemical industry. *Chemical Society Reviews* **2008,** *37* (1), 123-150.
28. Meindersma, G. W.; Maase, M.; De Haan, A. B., Ionic Liquids. In *Ullmann's Encyclopedia of Industrial Chemistry*.
29. Kernchen, U.; Etzold, B.; Korth, W.; Jess, A., Solid Catalyst with Ionic Liquid Layer (SCILL) – A New Concept to Improve Selectivity Illustrated by Hydrogenation of Cyclooctadiene. *Chemical Engineering & Technology* **2007,** *30* (8), 985-994.
30. Steinrück, H.-P.; Libuda, J.; Wasserscheid, P.; Cremer, T.; Kolbeck, C.; Laurin, M.; Maier, F.; Sobota, M.; Schulz, P. S.; Stark, M., Surface Science and Model Catalysis with Ionic Liquid-Modified Materials. *Advanced Materials* **2011,** *23* (22-23), 2571-2587.
31. Bartlewicz, O.; Dąbek, I.; Szymańska, A.; Maciejewski, H., Heterogeneous Catalysis with the Participation of Ionic Liquids. *Catalysts* **2020,** *10* (11), 1227.
32. Korth, W.; Jess, A., Solid Catalysts with Ionic Liquid Layer (SCILL). In *Supported Ionic Liquids*, Rasmus, F.; Riisager, A.; Haumann, M., Eds. Wiley-VCH Verlag GmbH & Co. KGaA: 2014; pp 279-306.
33. Sobota, M.; Happel, M.; Amende, M.; Paape, N.; Wasserscheid, P.; Laurin, M.; Libuda, J., Ligand Effects in SCILL Model Systems: Site-Specific Interactions with Pt and Pd Nanoparticles. *Advanced Materials* **2011,** *23* (22-23), 2617-2621.
34. Arras, J.; Paki, E.; Roth, C.; Radnik, J.; Lucas, M.; Claus, P., How a Supported Metal Is Influenced by an Ionic Liquid: In-Depth Characterization of SCILL-Type Palladium Catalysts and Their Hydrogen Adsorption. *The Journal of Physical Chemistry C* **2010,** *114* (23), 10520-10526.
35. Bauer, T.; Mehl, S.; Brummel, O.; Pohako-Esko, K.; Wasserscheid, P.; Libuda, J., Ligand Effects at Ionic Liquid-Modified Interfaces: Coadsorption of [C_2C_1Im][OTf] and CO on Pd(111). *The Journal of Physical Chemistry C* **2016,** *120* (8), 4453-4465.
36. Szesni, N.; Fischer, R.; Hagemeyer, A.; Großmann, F.; Boyer, J.; Hou, H. C.; Lowe, D. M.; Lugmair, C.; Sun, M.; Urbancic, M., Catalyst composition for selective hydrogenation with improved characteristics. *European Patent Application* **2013**, EP2583751B1.
37. Clariant OleMax® 260: New acetylene selective hydrogenation catalyst starts strong at Dow. https://www.clariant.com/en/Corporate/News/2018/05/Clariant-Olemax-260-new-acetylene-selective-hydrogenation-catalyst-starts-strong-at-DOW (accessed 09.05.2023).

38. Steinrück, H.-P., Recent developments in the study of ionic liquid interfaces using X-ray photoelectron spectroscopy and potential future directions. *Physical Chemistry Chemical Physics* **2012,** *14* (15), 5010-5029.
39. Armor, J. N., A history of industrial catalysis. *Catalysis Today* **2011,** *163* (1), 3-9.
40. Smith, J. K., History of Catalysis. In *Encyclopedia of Catalysis*, Horáth, I., Ed. John Wiley & Sons, Inc. : 2002.
41. Austen Angell, C.; Ansari, Y.; Zhao, Z., Ionic Liquids: Past, present and future. *Faraday Discussions* **2012,** *154*, 9-27.
42. Lei, Z.; Chen, B.; Yoon-Mo, K.; MacFarlane, D. R., Introduction: Ionic Liquids. *Chemical Reviews* **2017,** *117* (10), 6633-6635.
43. Lexow, M.; Maier, F.; Steinrück, H.-P., Ultrathin ionic liquid films on metal surfaces: adsorption, growth, stability and exchange phenomena. *Advances in Physics: X* **2020,** *5* (1), 1761266.
44. Freund, H. J.; Kuhlenbeck, H.; Libuda, J.; Rupprechter, G.; Bäumer, M.; Hamann, H., Bridging the pressure and materials gaps between catalysis and surface science: clean and modified oxide surfaces. *Topics in Catalysis* **2001,** *15* (2), 201-209.
45. Santos, C. S.; Baldelli, S., Gas–liquid interface of room-temperature ionic liquids. *Chemical Society Reviews* **2010,** *39* (6), 2136-2145.
46. Jeon, Y.; Sung, J.; Bu, W.; Vaknin, D.; Ouchi, Y.; Kim, D., Interfacial Restructuring of Ionic Liquids Determined by Sum-Frequency Generation Spectroscopy and X-Ray Reflectivity. *The Journal of Physical Chemistry C* **2008,** *112* (49), 19649-19654.
47. Bowers, J.; Vergara-Gutierrez, M. C.; Webster, J. R. P., Surface Ordering of Amphiphilic Ionic Liquids. *Langmuir* **2004,** *20* (2), 309-312.
48. Sloutskin, E.; Ocko, B. M.; Tamam, L.; Kuzmenko, I.; Gog, T.; Deutsch, M., Surface Layering in Ionic Liquids: An X-ray Reflectivity Study. *Journal of the American Chemical Society* **2005,** *127* (21), 7796-7804.
49. Yano, Y. F.; Yamada, H., Surface Structure of a Neat Ionic Liquid Investigated by Grazing-incidence X-ray Diffraction. *Analytical Sciences* **2008,** *24* (10), 1269-1271.
50. Steinrück, H.-P.; Wasserscheid, P., Ionic Liquids in Catalysis. *Catalysis Letters* **2015,** *145* (1), 380-397.
51. Cremer, T.; Killian, M.; Gottfried, J. M.; Paape, N.; Wasserscheid, P.; Maier, F.; Steinrück, H.-P., Physical Vapor Deposition of [EMIm][Tf_2N]: A New Approach to the Modification of Surface Properties with Ultrathin Ionic Liquid Films. *ChemPhysChem* **2008,** *9* (15), 2185-2190.
52. Lee, S.-Y.; Ogawa, A.; Kanno, M.; Nakamoto, H.; Yasuda, T.; Watanabe, M., Nonhumidified Intermediate Temperature Fuel Cells Using Protic Ionic Liquids. *Journal of the American Chemical Society* **2010,** *132* (28), 9764-9773.
53. Nakamoto, H.; Watanabe, M., Brønsted acid–base ionic liquids for fuel cell electrolytes. *Chemical Communications* **2007,** (24), 2539-2541.
54. Yoshizawa, M.; Xu, W.; Angell, C. A., Ionic Liquids by Proton Transfer: Vapor Pressure, Conductivity, and the Relevance of ΔpKa from Aqueous Solutions. *Journal of the American Chemical Society* **2003,** *125* (50), 15411-15419.
55. Miran, M. S.; Kinoshita, H.; Yasuda, T.; Susan, M. A. B. H.; Watanabe, M., Physicochemical properties determined by ΔpKa for protic ionic liquids based on an organic super-strong base with various Brønsted acids. *Physical Chemistry Chemical Physics* **2012,** *14* (15), 5178-5186.
56. Hertz, H., Ueber einen Einfluss des ultravioletten Lichtes auf die electrische Entladung. *Annalen der Physik* **1887,** *267* (8), 983-1000.
57. Hallwachs, W., Ueber den Einfluss des Lichtes auf electrostatisch geladene Körper. *Annalen der Physik* **1888,** *269* (2), 301-312.

58. Einstein, A., Über einen die Erzeugung und Verwandlung des Lichtes betreffenden heuristischen Gesichtspunkt. *Annalen der Physik* **1905,** *322* (6), 132-148.
59. Seah, M. P.; Dench, W. A., Quantitative electron spectroscopy of surfaces: A standard data base for electron inelastic mean free paths in solids. *Surface and Interface Analysis* **1979,** *1* (1), 2-11.
60. van der Heide, P., *X-ray Photoelectron Spectroscopy: An Introduction to Principles and Practices*. John Wiley & Sons, Inc.: Hoboken, NJ, 2012.
61. Hüfner, S., *Photoelectron Spectroscopy: Principles and Applications*. Springer-Verlag: Berlin, 2003; Vol. Third Edition.
62. Briggs, D.; Seah, M. P., *Practical Surface Analysis: Volume 1 – Auger and X-ray Photoelectron Spectroscopy*. John Wiley & Sons Ltd: Chichester, 1990; Vol. 2nd Edition.
63. Sasaki, T.; Inoue, S.; Kuwabata, S., Room-Temperature Fabrication of Electrocatalyst for Oxygen Reduction Using Pt Nanoparticle-dispersed Protic Ionic Liquid with Poly(3,4-ethylenedioxythiophene). *Electrochemistry* **2021,** *89* (2), 83-86.
64. Huddleston, J. G.; Visser, A. E.; Reichert, W. M.; Willauer, H. D.; Broker, G. A.; Rogers, R. D., Characterization and comparison of hydrophilic and hydrophobic room temperature ionic liquids incorporating the imidazolium cation. *Green Chemistry* **2001,** *3* (4), 156-164.
65. Sippel, P.; Lunkenheimer, P.; Krohns, S.; Thoms, E.; Loidl, A., Importance of glassy fragility for energy applications of ionic liquids. *Scientific Reports* **2015,** *5* (1), 13922.
66. Dzyuba, S.; Bartsch, R., Influence of Structural Variations in 1-Alkyl(aralkyl)-3-Methylimidazolium Hexafluorophosphates and Bis(trifluoromethylsulfonyl)imides on Physical Properties of the Ionic Liquids. *ChemPhysChem* **2002,** *3* (2), 161-166.
67. Law, G.; Watson, P. R., Surface Tension Measurements of N-Alkylimidazolium Ionic Liquids. *Langmuir* **2001,** *17* (20), 6138-6141.
68. Tokuda, H.; Hayamizu, K.; Ishii, K.; Susan, M. A. B. H.; Watanabe, M., Physicochemical Properties and Structures of Room Temperature Ionic Liquids. 2. Variation of Alkyl Chain Length in Imidazolium Cation. *The Journal of Physical Chemistry B* **2005,** *109* (13), 6103-6110.
69. Cremer, T. Ionic Liquid Bulk and Interface Properties: Electronic Interaction, Molecular Orientation and Growth Characteristics. Dissertation, Friedrich-Alexander-Universität Erlangen-Nürnberg, 2012.
70. Rietzler, F. Interfaces of Ionic Liquids and of Liquid Metals Studied by X-Ray Photoelectron Spectroscopy. Dissertation, Friedrich-Alexander-Universität Erlangen-Nürnberg, 2016.
71. Shirley, D. A., High-Resolution X-Ray Photoemission Spectrum of the Valence Bands of Gold. *Physical Review B* **1972,** *5* (12), 4709-4714.
72. Lexow, M. Ultrathin Ionic Liquid Films on Metal Surfaces: Growth, Stability and Exchange Phenomena. Dissertation, Friedrich-Alexander-Universität Erlangen-Nürnberg, 2020.
73. Lexow, M.; Heller, B. S. J.; Maier, F.; Steinrück, H.-P., Anion Exchange at the Liquid/Solid Interface of Ultrathin Ionic Liquid Films on Ag(111). *ChemPhysChem* **2018,** *19* (22), 2978-2984.
74. Swinehart, D. F., The Beer-Lambert Law. *Journal of Chemical Education* **1962,** *39* (7), 333.
75. Lexow, M.; Massicot, S.; Maier, F.; Steinrück, H.-P., Stability and Exchange Processes in Ionic Liquid/Porphyrin Composite Films on Metal Surfaces. *The Journal of Physical Chemistry C* **2019,** *123* (49), 29708-29721.
76. Cremer, T.; Stark, M.; Deyko, A.; Steinrück, H.-P.; Maier, F., Liquid/Solid Interface of Ultrathin Ionic Liquid Films: $[C_1C_1Im][Tf_2N]$ and $[C_8C_1Im][Tf_2N]$ on Au(111). *Langmuir* **2011,** *27* (7), 3662-3671.

77. Rietzler, F.; May, B.; Steinrück, H.-P.; Maier, F., Switching adsorption and growth behavior of ultrathin [C_2C_1Im][OTf] films on Au(111) by Pd deposition. *Physical Chemistry Chemical Physics* **2016,** *18* (36), 25143-25150.
78. Lexow, M.; Talwar, T.; Heller, B. S. J.; May, B.; Bhuin, R. G.; Maier, F.; Steinrück, H.-P., Time-dependent changes in the growth of ultrathin ionic liquid films on Ag(111). *Physical Chemistry Chemical Physics* **2018,** *20* (18), 12929-12938.
79. Atilhan, M.; Anaya, B.; Ullah, R.; Costa, L. T.; Aparicio, S., Double Salt Ionic Liquids Based on Ammonium Cations and Their Application for CO_2 Capture. *The Journal of Physical Chemistry C* **2016,** *120* (31), 17829-17844.
80. Kolbeck, C.; Lehmann, J.; Lovelock, K. R. J.; Cremer, T.; Paape, N.; Wasserscheid, P.; Fröba, A. P.; Maier, F.; Steinrück, H.-P., Density and Surface Tension of Ionic Liquids. *The Journal of Physical Chemistry B* **2010,** *114* (51), 17025-17036.
81. Gu, Z.; Brennecke, J. F., Volume Expansivities and Isothermal Compressibilities of Imidazolium and Pyridinium-Based Ionic Liquids. *Journal of Chemical & Engineering Data* **2002,** *47* (2), 339-345.
82. Argile, C.; Rhead, G. E., Adsorbed layer and thin film growth modes monitored by Auger electron spectroscopy. *Surface Science Reports* **1989,** *10* (6), 277-356.
83. Fogarty, R. M.; Matthews, R. P.; Ashworth, C. R.; Brandt-Talbot, A.; Palgrave, R. G.; Bourne, R. A.; Hoogerstraete, T. V.; Hunt, P. A.; Lovelock, K. R. J., Experimental validation of calculated atomic charges in ionic liquids. *The Journal of Chemical Physics* **2018,** *148* (19), 193817.
84. Fogarty, R. M.; Palgrave, R. G.; Bourne, R. A.; Handrup, K.; Villar-Garcia, I. J.; Payne, D. J.; Hunt, P. A.; Lovelock, K. R. J., Electron spectroscopy of ionic liquids: experimental identification of atomic orbital contributions to valence electronic structure. *Physical Chemistry Chemical Physics* **2019,** *21* (35), 18893-18910.
85. Fogarty, Richard M.; Rowe, R.; Matthews, R. P.; Clough, M. T.; Ashworth, C. R.; Brandt, A.; Corbett, P. J.; Palgrave, R. G.; Smith, E. F.; Bourne, R. A.; Chamberlain, T. W.; Thompson, P. B. J.; Hunt, P. A.; Lovelock, K. R. J., Atomic charges of sulfur in ionic liquids: experiments and calculations. *Faraday Discussions* **2018,** *206*, 183-201.
86. Zaitsau, D. H.; Emel'yanenko, V. N.; Stange, P.; Verevkin, S. P.; Ludwig, R., Dissecting the Vaporization Enthalpies of Ionic Liquids by Exclusively Experimental Methods: Coulomb Interaction, Hydrogen Bonding, and Dispersion Forces. *Angewandte Chemie International Edition* **2019,** *58* (25), 8589-8592.
87. Srour, H.; Rouault, H.; Santini, C. C.; Chauvin, Y., A silver and water free metathesis reaction: a route to ionic liquids. *Green Chemistry* **2013,** *15* (5), 1341-1347.
88. Lexow, M.; Heller, B. S. J.; Partl, G.; Bhuin, R. G.; Maier, F.; Steinrück, H.-P., Cation Exchange at the Interfaces of Ultrathin Films of Fluorous Ionic Liquids on Ag(111). *Langmuir* **2019,** *35* (2), 398-405.

7. Acknowledgement

This thesis would certainly not have been possible without the support of many people. For this reason, I would like to express my gratitude to:

Professor Hans-Peter Steinrück for giving me the opportunity to do my PhD at the chair of Physical Chemistry II, and for his considerable and valuable scientific guidance and mentorship.

PD Dr. Hubertus Marbach for supervising my master thesis and for allowing me to contribute as a student assistant in his group from 2015 to 2019.

Dr. Florian Maier for his supervision as head of the IL group, his comprehensive support and numerous fruitful discussions.

All my former and current colleagues, Afra Gezmis, Dr. Andreas Bayer, Dr. Benjamin May, Dr. Bettina Heller, Dr. Cynthia C. Fernández, Daniel Hemmeter, Dr. Francesco Greco, Leonhard Winter, Jade Baretto, Dr. Jan Brox, Dr. Manuel Meusel, Majid Shaker, Dr. Michael Lepper, Dr. Radha Bhuin, Rajan Adhikari, Dr. Simon Jaekel, Dr. Sunghwan Shin and Dr. Ulrike Paap for the great working atmosphere; and especially Dr. Matthias Lexow and Timo Talwar for the productive and uncomplicated cooperation in the ESCA laboratory.

Hans-Peter Bäumler, Bernd Kreß, Friedhold Wölfel and all members of the mechanical workshop for their dedicated technical support.

My collaboration partners Prof. Andreas Görling and Dr. Lukas Fromm (Chair of Theoretical Chemistry), and Prof. Susumu Kuwabata and Dr. Tomoya Sasaki (Osaka University).

Andrea Meixner-Wolf and Susana Kreß for their valuable help in all administrative matters, and Norman-Anja Schmidt for IT support.

All chair members of Physical Chemistry II for the great time.

Besides my colleagues, I would like to thank my friends and family for their invaluable support.

8. Appendix

In this chapter, the publications [P1-P4] are reproduced under the licenses CC BY-NC-ND 4.0 ([P1, P2]), CC BY 4.0 ([P3]) and CC BY-NC ([P4]).

[P1] S. Massicot, T. Sasaki, M. Lexow, S. Shin, F. Maier, S. Kuwabata, H.-P. Steinrück:

Adsorption, Wetting, Growth and Thermal Stability of the Protic Ionic Liquid Diethylmethylammonium Trifluoromethanesulfonate on Ag(111) and Au(111).

Langmuir **2021**, *37*, 11552-11560

DOI: 10.1021/acs.langmuir.1c01823

[P2] S. Massicot, T. Sasaki, M. Lexow, F. Maier, S. Kuwabata, H.-P. Steinrück:

On-Surface Metathesis of an Ionic Liquid on Ag(111).

Chem. Eur. J. **2022**, e202200167

DOI: 10.1002/chem.202200167

[P3] R. Adhikari*, S. Massicot*, L. Fromm, A. Gezmis, M. Meusel, A. Bayer, S. Jaekel, F. Maier, A. Görling, H.-P. Steinrück:

Structure and Reactivity of the Ionic Liquid [C_1C_1Im][Tf_2N] on Cu(111).

Top Catal **2023**, 66, 1178-1195

DOI: 10.1007/s11244-023-01801-y

[P4] S. Massicot, A. Gezmis, T. Talwar, M. Meusel, S. Jaekel, R. Adhikari, L. Winter, C. C. Fernández, A. Bayer, F. Maier, H.-P. Steinrück:

Adsorption and Thermal Evolution of [C_1C_1Im][Tf_2N] on Pt(111).

Phys. Chem. Chem. Phys. **2023**, 25, 27953-27966

DOI: 10.1039/d3cp02743k

*shared first-authorship.

[P1]

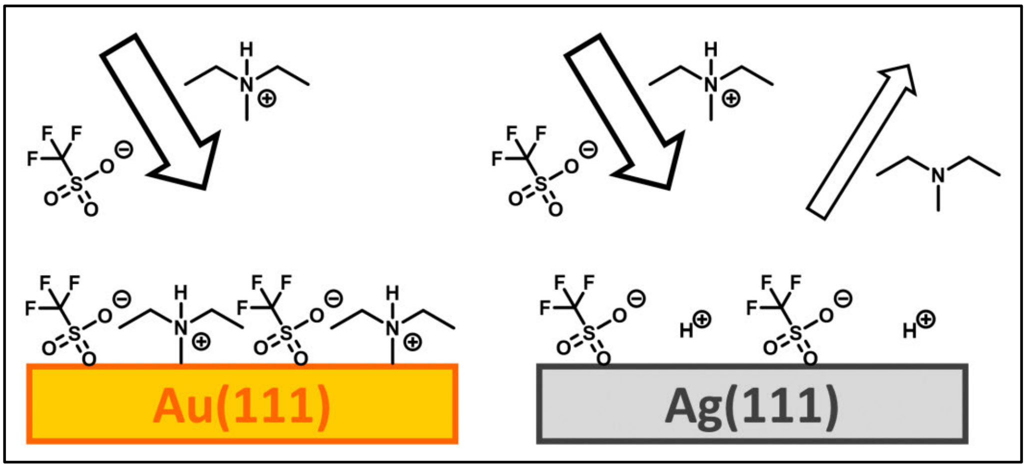

Adsorption, Wetting, Growth and Thermal Stability of the Protic Ionic Liquid Diethylmethylammonium Trifluoromethanesulfonate on Ag(111) and Au(111).

S. Massicot, T. Sasaki, M. Lexow, S. Shin., F. Maier, S. Kuwabata, H.-P. Steinrück.

Langmuir **2021**, 37, 11552-11560

DOI: 10.1021/acs.langmuir.1c01823

LANGMUIR

pubs.acs.org/Langmuir

Article

Adsorption, Wetting, Growth, and Thermal Stability of the Protic Ionic Liquid Diethylmethylammonium Trifluoromethanesulfonate on Ag(111) and Au(111)

Stephen Massicot, Tomoya Sasaki, Matthias Lexow, Sunghwan Shin, Florian Maier, Susumu Kuwabata, and Hans-Peter Steinrück*

Cite This: *Langmuir* 2021, 37, 11552−11560

Read Online

ACCESS | Metrics & More | Article Recommendations | Supporting Information

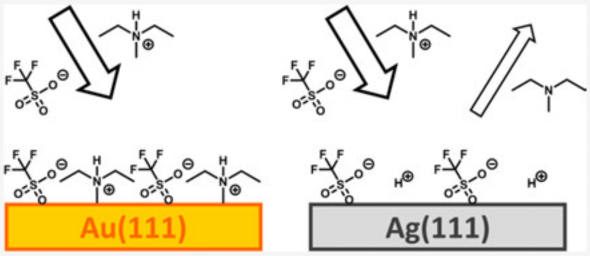

ABSTRACT: We have studied the adsorption, wetting, growth, and thermal evolution of the protic IL diethylmethylammonium trifluoromethanesulfonate ([dema][TfO]) on Au(111) and Ag(111). Ultrathin films were deposited at room temperature (RT) and at 90 K, and were characterized *in situ* by angle-resolved X-ray photoelectron spectroscopy. For both surfaces, we observe that independent of temperature, initially, a closed 2D wetting layer forms. While the film thickness does not increase past this wetting layer at RT, at 200 K and below, "moderate" 3D island growth occurs on top of the wetting layer. Upon heating, on Au(111), the [dema][TfO] multilayers desorb at 292 K, leaving an intact [dema][TfO] wetting layer, which desorbs intact at 348 K. The behavior on Ag(111) is much more complex. Upon heating [dema][TfO] deposited at 90 K, the $[dema]^+$ cations deprotonate in two steps at 185 and 305 K, yielding H[TfO] and volatile $[dema]^0$. At 355 K, the formed H[TfO] wetting layer partly desorbs (∼50%) and partly decomposes to form an F-containing surface species, which is stable up to 570 K.

■ INTRODUCTION

Ionic liquids (ILs) are salts that are composed of poorly coordinating ions and thus exhibit melting points typically well below 100 °C. An interesting, but hitherto not much studied subset of ILs are protic ionic liquids (PILs), which are prepared through the stoichiometric neutralization of a strong Brønsted acid with a strong Brønsted base.[1] This simple synthetic pathway makes them much cheaper than aprotic ionic liquids (AIL) and hence suitable for large-scale commercial applications.[2,3] One further key feature, in contrast to AILs, is the proton availability for transfer reactions due to the presence of proton donor/proton acceptor sites. This property also allows for the formation of extensive hydrogen bond networks[4] and makes PILs promising candidates as electrolytes in fuel cells and in catalysis.[1,4−10] The PIL addressed in the present investigation, diethylmethylammonium trifluoromethanesulfonate, [dema][TfO] (Figure 1), e.g., enables reliable O_2 reduction conditions due to its high and stable open-circuit potential combined with a wide liquid temperature range and high thermal stability.[10]

As fuel cells and catalysts usually are operated at elevated temperature, high thermal stability of the PIL at the interface of the electrode and catalyst material is of upmost interest.[5−7,9,10] In the present work, we characterize in detail the interface formed by [dema][TfO] with Au(111) and Ag(111) as model metal substrates. We investigated the temperature dependent stability of the PIL on both substrates. On gold, the PIL remains intact; however, on silver, it deprotonates and partially decomposes. For future applications, these differences show the importance of choosing suitable PIL and electrode/catalyst material combinations.

Information on the adsorption, wetting, and growth of PILs on solid substrates also is highly relevant for applications like nanofabrication. On the basis of the very low vapor pressure of ILs in general,[11,12] stable nanodroplets of PILs on solid supports have recently been used for templating nanostructures.[13,14] This is not possible with conventional molecular liquids due to their typically finite vapor pressure.[14] Fundamental knowledge on the PIL/solid interaction and wetting characteristics is essential for understanding and tailoring the formation of such nanodroplets, and for rationalizing the sometimes unexpected interfacial properties of PILs.[5] Other interesting applications are heterogeneous metal catalysis using PILs,[15,16] batteries with PIL electrolyte,[17,18] biomass processing with PILs,[19,20] hydrogen storage

Received: July 8, 2021
Published: September 27, 2021

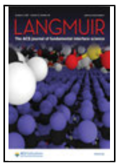

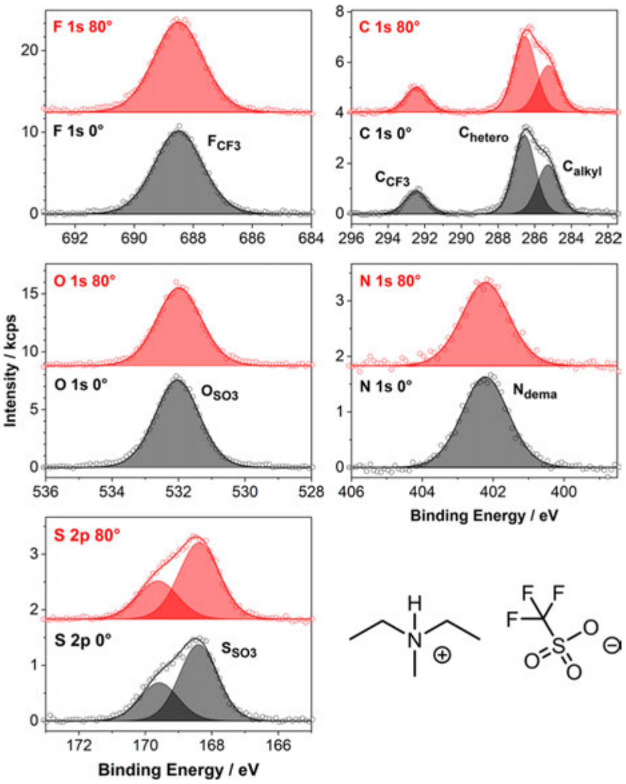

Figure 1. F 1s, C 1s, O 1s, N 1s, and S 2p XP spectra of a macroscopic film of [dema][TfO] on a Ag foil at RT, collected at 0° (black) and 80° (red) emission. At the right bottom, the molecular structure of diethylmethylammonium trifluoromethanesulfonate, [dema][TfO], is shown.

in palladium in PIL electrolyte,[21] and metal nanoparticle synthesis in PILs.[22−27]

The goal of this study thus is the detailed characterization of the PIL/support interface. Such information is presently not available. In the past, we already acquired extensive knowledge on interfacial characteristics of ultrathin AIL films on single crystal surfaces under well-defined ultrahigh vacuum (UHV) conditions (see, e.g., recent comprehensive review by Lexow et al.[28]). This paper is to the best of our knowledge the first work addressing ultrathin PIL films under similar conditions.

We have chosen the above-mentioned PIL [dema][TfO] due to its melting point below RT (260−267 K),[5,10] its high thermal stability (decomposition at ∼630 K),[5,10] and its equilibrium very far on the ionic side (ΔpK_a well above 17[5,7,29]). Moreover, the electronic structure of macroscopic samples of [dema][TfO] has already been studied by X-ray photoelectron spectroscopy (XPS),[30−32] proving the stability of this PIL under UHV and serving as references for our analysis.

We investigate ultrathin films of [dema][TfO] from submonolayer coverage up to several nanometer thickness, which are deposited by physical vapor deposition (PVD) on Ag(111) and Au(111) at temperatures between 90 and 300 K; PVD allows for the preparation of ultraclean IL films of variable thickness under ultrahigh vacuum conditions.[28,33] The experiments are performed by angle-resolved X-ray photoelectron spectroscopy (ARXPS). By measuring different electron emission angles of 0° and 80° with respect to the surface normal, we can tune our measurements from bulk-sensitive to surface-sensitive, respectively. Using Al $K\alpha$ radiation, the information depth (ID) at 0° is 7−9 nm, depending on the kinetic energy. At 80°, the ID is 1−1.5 nm, which means that only the outermost surface layers are probed. For bulk ILs, ARXPS thus allows for extracting information on molecular orientation and enrichment effects at the IL/vacuum interface, and for ultrathin IL films, it provides access to the initial adsorption steps, molecular orientation, film growth, and decomposition effects.[34] The two noble metal substrates Ag(111) and Au(111) were selected due to their overall low reactivity in general and with ultrathin AIL films in particular. For both, no reactions with metal atoms or reconstruction effects upon AIL deposition were found in previous studies.[28,35] Nevertheless, Ag is known to be more reactive than Au, e.g., it acts as heterogeneous catalyst for activating molecular oxygen in coupling reactions.[36,37] By covering temperatures up to 600 K, we also address the desorption of [dema][TfO] multilayers and wetting layers with a focus on adsorption strength, film stability, and thermal decomposition. ARXPS data collected from macroscopic [dema][TfO] samples are used as reference for our thin film studies. This work provides the beginning for PIL/metal interface investigations on the molecular level and will serve as a basis for studies on more reactive PIL/support combinations.

■ RESULTS AND DISCUSSION

Macroscopic [dema][TfO] Film. We start with addressing a macroscopic [dema][TfO] film with around 0.1 mm thickness that was prepared *ex situ* by spreading the PIL on a polycrystalline Ag foil. At this film thickness, no influence of the substrate is expected. The corresponding ARXP spectra, taken at room temperature (RT), allow for verifying the purity of the PIL and serve as a reference system for comparison with the ultrathin films studied below.

Figure 1 shows F 1s, C 1s, O 1s, N 1s, and S 2p spectra for emission angles of 0° (normal emission, black) and 80° (grazing emission, red) along with their fits (for details, see the Experimental Section). The [dema]$^+$ cation displays two

Table 1. Film Composition as Determined from by XPS in Normal Emission (0°, top) and Grazing Emission (80°, bottom)[a]

0°	C_{CF3}	C_{hetero}	C_{alkyl}	N_{dema}	F_{CF3}	O_{SO3}	S_{SO3}
atom number	**0.9** /*0.9* (1)	**3.1** /*3.1* (3)	**2.1** /*2.0* (2)	**0.9** /*1.1* (1)	**3.2** /*3.0* (3)	**3.0** /*3.0* (3)	**0.9** /*1.0* (1)
BE/eV	**293.0**/*292.5*	**286.9**/*286.6*	**285.6**/ *285.3*	**402.5**/*402.2*	**689.1**/ *688.5*	**532.6**/ *532.0*	**168.9**/*168.4*
80°	C_{CF3}	C_{hetero}	C_{alkyl}	N_{dema}	F_{CF3}	O_{SO3}	S_{SO3}
atom number	**1.0** /*1.0* (1)	**3.2** /*3.1* (3)	**2.1** /*1.9* (2)	**0.9** /*1.0* (1)	**3.2** /*3.3* (3)	**2.6** /*2.7* (3)	**1.0** /*1.1* (1)
BE/eV	**293.1**/*292.5*	**287.0**/*286.5*	**285.8**/*285.2*	**402.6**/ *402.2*	**689.2**/ *688.5*	**532.8**/ *532.0*	**169.1** / *168.4*

[a] Also denoted are the corresponding binding energies. The **bold** values (left) corresponds to a 2.6 nm thick film of [dema][TfO] on Ag(111) at 90 K prepared by PVD, the *italic* values (right) to a macroscopic droplet of ∼0.1 mm thickness at RT; the nominal composition in atom numbers are given in (brackets). For S 2p, the binding energy (BE) of the S 2p$_{3/2}$ peak is given; the S 2p$_{1/2}$ peak is at 1.18 eV higher BE.

distinct signals in the C 1s and one in the N 1s region. The C_{hetero} peak at 286.6 eV binding energy (BE) is assigned to the three carbon atoms in direct contact with the nitrogen (hetero) atom and the C_{alkyl} peak at 285.3 eV is assigned to the two alkyl carbon atoms at the end of the ethyl groups. The C_{alkyl}:C_{hetero} ratio of 3.1:2.0 at 0° emission is in excellent agreement with the nominal ratio of 3:2. The single N_{dema} peak at 402.2 eV corresponds to the ammonium nitrogen atom.[30−32] For the $[TfO]^-$ anion, we observe one peak each in the C 1s, F 1s, and O 1s region. The C_{CF3} peak at 292.5 eV and the F_{CF3} peak at 688.5 eV are assigned to carbon and fluorine atoms of the trifluoromethyl group, and the O_{SO3} peak at 532.0 eV and the spin orbit-split $2p_{3/2}/2p_{1/2}$ S_{SO3} doublet at 168.4/169.6 eV are assigned to the oxygen and sulfur atoms of the sulfonate group.[30−32]

The quantitative analysis of the XP spectra of the macroscopic [dema][TfO] film is summarized in Table 1. For the bulk-sensitive spectra at 0°, the measured atom numbers obtained from the intensities of the different peaks (right value, italics) show excellent agreement with the nominal values (in brackets), within the accuracy of our measurements (±5%). For the ∼6× more surface-sensitive spectra at 80°, the F 1s signal is higher than the nominal value (3.3 vs. 3.0), whereas the O 1s signal is lower than the nominal value (2.7 vs 3.0). We interpret this observation as an enrichment effect based on preferential orientation of the $[TfO]^-$ anion at the outer surface with the CF_3 groups pointing toward the vacuum and the SO_3 groups toward the bulk.[13] A similar preferential enrichment at the IL/vacuum interface was reported also for AILs with CF_3-containing anions such as bis[(trifluoromethyl)sulfonyl]imide[13,38] and cations like 3-methyl-1-(3,3,4,4,4-pentafluorobutyl)-imidazolium.[13,39,40]

As will be demonstrated in the following sections, multilayer desorption, that is, evaporation of the [dema][TfO] film already starts around 290 K, which indicates that macroscopic films are not fully stable at RT under UHV conditions. Notably, the evaporation temperature of this protic IL is lower than those of aprotic ILs (e.g., 345 K for $[C_1C_1Im][Tf_2N]$ on Ag(111) − for an overview see Lexow et al.[28]), which we have studied in the past. Since the desorption rate of [dema][TfO] at RT is still very low, macroscopically thick films effectively provide a seemingly infinite reservoir on the time scale of film preparation and measurement. For ultrathin films of few multilayers thickness, however, the situation is quite different, as will be discussed below.

Growth of Ultrathin [dema][TfO] Films on Ag(111) and Au(111). To study the adsorption and growth of [dema][TfO], increasing amounts of the PIL were deposited onto clean Ag(111) and Au(111) surfaces by PVD, with sample temperatures of 90 K, 200 K and RT. After each experiment, the crystal surfaces were cleaned by heating above 500 K (leading to thermal desorption), Ar^+ sputtering, and annealing.

In Table 1, we summarize the quantitative analysis of a 2.6 nm thick film of [dema][TfO] deposited and measured on Ag(111) at 90 K; the corresponding spectra are shown in the SI, Figure S1. The composition values for this film as derived from the 0° and 80° ARXP spectra (left values in bold) show within the accuracy of our measurements (±10% for the ultrathin films, due to the low intensity of the IL signals and uncertainties in background subtraction) the same composition as that described above for the macroscopic film (italic numbers). This clearly indicates that [dema][TfO] films can be prepared on Ag(111) by PVD in UHV without decomposition during evaporation and remain intact on the surface at low temperatures. The same holds true for [dema][TfO] films on Au(111) (see Figure S2 in the SI for a 2.4 nm film deposited at 200 K).

The film growth behavior can be deduced from the attenuation of the substrate signal as a function of the amount of deposited IL, using our previously established approach (for details see refs.[28,33,35]). For perfect 2D growth, the Ag or Au signals decrease exponentially from the value I_0 for the clean surface to the value I_d for a 2D layer with thickness d, according to $I_d/I_0 = \exp(-d/(\lambda\cdot\cos\vartheta))$, with ϑ being the electron emission angle relative to surface normal. For the inelastic mean free path λ of Ag 3d electrons (kinetic energy: ∼1100 eV), we employ 2.5 nm,[35,41] for Au 4f electrons (kinetic energy: ∼1400 eV), we use 3.0 nm.[42−45]

In our analysis, we first determine the mean film thickness d from the I_d/I_0 ratio at 0° by assuming perfect 2D growth. In the next step, the I_d/I_0 ratio for this thickness at 80° is calculated, and the experimentally measured ratio is then compared to this calculated value. Agreement between the two values indicates 2D growth, and an experimental 80° value larger than the calculated one indicates a 3D morphology of the IL film.[28] The height h of a monolayer (1 ML) of [dema][TfO] is estimated in agreement with previous publications:[28,33] a closed film of 1 ML coverage corresponds to a bilayer of cations and anions irrespective of their relative arrangement. On the basis of the molar volume of bulk [dema][TfO] ($183.6\ cm^3/mol$),[46] a closed 1 ML film has a height $h = 0.67$ nm. On the other hand, a closed single layer of ions adsorbed next to each other, with 0.5 ML coverage, has half of this height, that is, 0.34 nm. Such a film is denoted as "wetting layer" (WL) in the following.

In Figure 2a, we plot the attenuation of the Ag 3d signal at 0° and 80° emission as a function of the [dema][TfO] film thickness at 90 K (blue), 200 K (red), and RT (black). The solid and dashed lines indicate the behavior for perfect 2D growth at 0° and 80°, respectively. Up to about 0.34 nm (or 0.5 ML coverage), the 80° data closely follows the prediction for 2D growth for all temperatures. This behavior indicates the formation of a closed wetting layer where the anions and cations adsorb next to each other alternatingly, that is, in a checkerboard-like structure with a saturation coverage of 0.5 ML. This adsorption behavior with both ions in direct contact with the metal surface was also observed for most AILs on metal surfaces so far.[28]

Interestingly, at RT, the film thickness does not increase past wetting layer coverage. This behavior is attributed to the onset of multilayer desorption already below RT as will be explained in the following section in more detail. At 200 K and below, the coverage continues to increase beyond the wetting layer coverage, but while it is still decreasing, the 80° data points fall above the prediction for 2D growth. Such a behavior has been classified as "moderate" 3D island growth (that is, comparably flat 3D islands) on top of the initially formed wetting layer and is again quite commonly observed for ILs on various metal surfaces.[28]

For the Au(111) surface, the film growth of [dema][TfO] is very similar to that on Ag(111) as is evident from the attenuation of the Au 4f signal as a function of the film thickness in Figure 2b. Again, we do not observe multilayer growth at RT (black). At 200 K (red), first a closed wetting

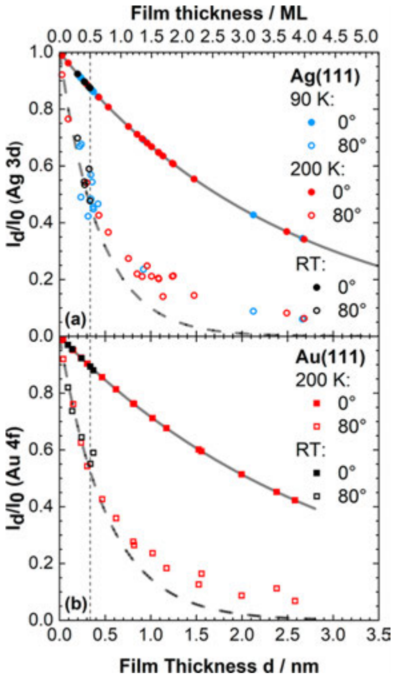

Figure 2. Dependence of the Ag 3d (circles) and Au 4f (squares) substrate signals (intensity I_d at film thickness d divided by the intensity of the uncovered surface I_0) upon deposition of [dema][TfO] on (a) Ag(111) and (b) Au(111), as a function of the film thickness (axis at bottom of the figure) and in units of monolayers (ML; axis at top of the figure). Data collected at 0° are shown as closed symbols and data at 80° as open symbols. The solid and dashed lines indicate the behavior for perfect 2D growth at 0° and 80°, respectively. Measurements were performed at 90 K (blue), 200 K (red), and RT (black).

layer forms, followed by similarly moderate 3D growth as on Ag(111).

[dema][TfO] Wetting Layers on Ag(111) and Au(111). Next, we address the nature of the saturated wetting layers of [dema][TfO] on the two surfaces in detail. We start with discussing the results for Au(111), since the situation is more complex for Ag(111). In Figure 3a, C 1s, O 1s, and F 1s spectra at 0° emission of 0.5 ML on Au(111) deposited at RT are shown (note that all core level signals of the wetting layer are shifted by about 0.4–0.7 eV toward lower binding energy with respect to the ones of the macroscopic films, which is attributed to improved final state screening by the metal in the photoemission process).[43] The S 2p and N 1s regions were not measured due to the low signal intensities for wetting layer coverages. The quantification of the signal intensities provides overall the nominal stoichiometry, albeit with slightly larger CF_3-related F 1s and C 1s signals and slightly lower cationic C 1s and anionic O 1s signals (see Table 2). Quantification of the XP spectra of the [dema][TfO] wetting layer at 80° emission (not shown) reveals an even stronger attenuation of the cation-related contributions and the anion-related oxygen signal whereas anionic carbon and fluorine signals are relatively higher in intensity. This behavior indicates that the $[TfO]^-$ anion adsorbs vertically on Au(111), with the SO_3 group pointing toward and the CF_3 group away from the metal surface. Similar preferential orientation of $[TfO]^-$ anion at AIL/metal interfaces was reported previously from *in situ* IR spectroscopy studies of 1-ethyl-3-methylimidazolium trifluoromethanesulfonate ($[C_2C_1Im][TfO]$), on Pd(111)[47−49] and on Co-covered Pd(111).[50] For the $[dema]^+$ cation, our ARXPS results show no signs of preferential orientation.

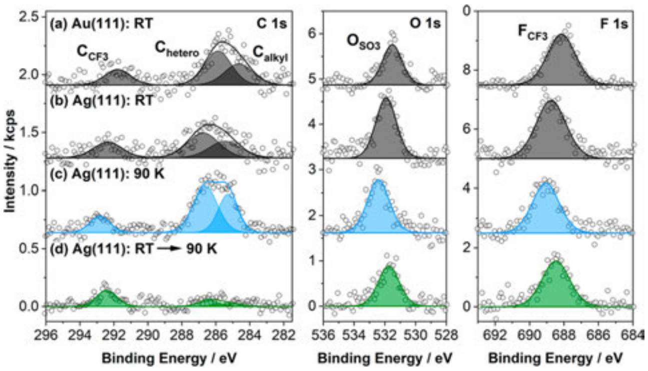

Figure 3. C 1s, O 1s, and F 1s spectra at 0° emission. (a) saturated wetting layer (= 0.5 ML) of [dema][TfO] on Au(111) deposited at RT (black); (b) saturated wetting layer of [dema][TfO] on Ag(111) deposited at RT (black); (c) 0.5 ML of [dema][TfO] on Ag(111) deposited at 90 K (blue); (d) after heating this film from 90 K to RT (green).

Table 2. Composition of Layers as Obtained from Quantitative Analysis of Spectra Shown in Figure 3[a]

	C_{CF3}	C_{hetero}	C_{alkyl}	O_{SO3}	F_{CF3}
nominal	**1**	**3**	**2**	**3**	**3**
(a) Au(111): RT	1.2	2.8	1.8	2.7	3.5
(b) Ag(111): RT	1.4	2.0	1.3	3.6	4.1
(c) Ag(111): 90 K	0.9	3.0	2.0	3.1	3.0
(d) Ag(111): 90 K → RT	1.7	0.7	0.4	4.2	5.1

[a] (a) Saturated wetting layer of [dema][TfO] on Au(111) deposited at RT (black); (b) saturated wetting layer layer of [dema][TfO] on Ag(111) deposited at RT (black); (c) 0.5 ML of [dema][TfO] on Ag(111) deposited at 90 K (blue); (d) after heating this film from 90 K to RT (green).

The situation is different for the saturated layer of [dema][TfO] adsorbed on Ag(111) at RT as is evident from the corresponding C 1s, F 1s, and O 1s spectra in Figure 3b. Notably, we observe a strong deviation from the expected stoichiometry: while the C_{CF3}, F_{CF3} and O_{SO3} signals of the anion are increased by about 30% compared to the nominal values, the cation-related C_{hetero} and C_{alkyl} signals are concomitantly decreased, which points to a considerable excess of $[TfO]^-$ in the wetting layer on Ag(111) at RT. Moreover, all absolute intensities of the anion signals are significantly higher (35 ± 8%) as compared to the saturated wetting layer on Au(111), which implies a larger amount of adsorbed anions on Ag(111): taking F 1s as the most intense anion signal for the saturated wetting layers at RT, we measure an absolute count rate of 3.4 ± 0.4 kcps for Au(111) versus 4.5 ± 0.5 kcps for Ag(111). In addition to the observed intensity changes, we also find shifts of all peaks to higher binding energy, as compared to Au(111).

To understand the observed differences, we also measured C 1s, F 1s, and O 1s spectra at 0° after depositing 0.5 ML of [dema][TfO] on Ag(111) at 90 K (Figure 3c) and after subsequent heating to RT (Figure 3d). The 0° spectra at 90 K match exactly the nominal composition indicating adsorption of intact [dema][TfO]. In particular, the observed F:O = 2.9:3.1 ratio rules out pronounced anion orientation effects at this low temperature, where a hit-and-stick adsorption behavior has been observed for AILs.[39,41] After heating to RT, the anion-related C 1s, F 1s, and O 1s peaks shift by about −0.5 eV to lower binding energy. More importantly, the cationic C 1s signals drastically decrease in intensity.

Since desorption of isolated cations is not possible due to energetic reasons (note that thermal evaporation of ILs only takes place in form of neutral ion pairs[51]), the substantial loss in cation XPS signals clearly points toward decomposition of the $[dema]^+$ cations in the wetting layer on Ag(111). As the changes in XP spectra occur during heating to RT (see also next section), we propose that the Ag(111) surface, in contrast to Au(111), enables deprotonation of the ammonium cation to form neutral diethylmethylamine ($[dema]^0$), with the latter desorbing from the surface, which leaves H^+ and $[TfO]^-$ as adsorbed trifluoromethanesulfonic acid, H[TfO], behind. The observed shifts of the anion signals to lower binding energy upon heating thus might indeed be related to this cation exchange process. The remaining $[TfO]^-$ anions are well-oriented at RT with the oxygen atoms pointing toward the Ag surface and the CF_3 groups toward vacuum as shown by the F:O = 5.1:4.2 = 1.2 ratio (this ratio is similar to that of the [dema][TfO] wetting layer on Au(111) at RT; see Table 2).

With this reaction in mind, our findings for the saturated wetting layer deposited on Ag(111) at RT in Figure 3b can be explained. In course of the deposition of [dema][TfO] at RT, part of the $[dema]^+$ cations deprotonate and leave the surface as neutral diethylmethylamine. The liberated space allows for further [dema][TfO] adsorption next to H[TfO] sites, which explains the overall higher amount of $[TfO]^-$ anions mentioned above. Since we still observe notable C 1s contributions related to intact $[dema]^+$ cations in Figure 3b, the deprotonation process described above apparently leads not to a full layer of H[TfO] but rather to a wetting layer consisting of [dema][TfO] and H[TfO] adsorbed next to each other. This also explains why the binding energies of the F 1s and O 1s peaks of the RT-deposited film in Figure 3b lie between the values for the 0.5 ML film at 90 K (Figure 3c) and the values obtained after subsequently heating this film to RT (Figure 3d).

Thermal Evolution of [dema][TfO] on Au(111) and Ag(111). To investigate the desorption of [dema][TfO] from Au(111), we heated a 1.5 ML film from 196 to 401 K at a heating rate of 2 K/min and simultaneously recorded Au 4f spectra of the substrate and F 1s spectra representative of the $[TfO]^-$ anion all at 0° emission (see Figure S3 in the SI). The quantitative analysis of the data is shown in Figure 4a. The intensity of anion-related F 1s signal (red) decreases in two well-separated steps while the Au 4f intensity (gray) of the Au(111) crystal increases accordingly. With reference to previous desorption studies of ILs on Ag(111) and Au(111),[28,35,39,41] we interpret the first step with an inflection point of 292 ± 2 K as multilayer desorption of [dema][TfO]. From a simple leading edge-type analysis,[28,52] we obtain an activation energy of multilayer desorption of $E_a = 101 \pm 10$ kJ/mol. This value agrees within the margins of error with the value of 91 ± 15 kJ/mol reported by Hessey et al.[53] with an preexponential factor of 10^{16} s^{-1}, and also with an earlier report of the enthalpy of vaporization of a structurally very similar IL, [triethylammonium][TfO], of 104.9 ± 1.3 kJ/mol.[51] The onset of multilayer desorption below RT provides the explanation for the absence of multilayer growth at RT described above. The remaining intensity of 3.4 ± 0.4 kcps between 300 and 340 K is ascribed to the wetting layer in direct contact with the Au(111) substrate and indicates its higher stability compared to the multilayers. The second desorption step at 348 ± 2 K is attributed to the desorption of the [dema][TfO] wetting layer from the Au(111) surface. XPS after heating above 400 K shows no IL residuals in the F 1s, C 1s and O 1s region on Au(111). Hence we conclude that [dema][TfO] desorbs intact from Au(111).

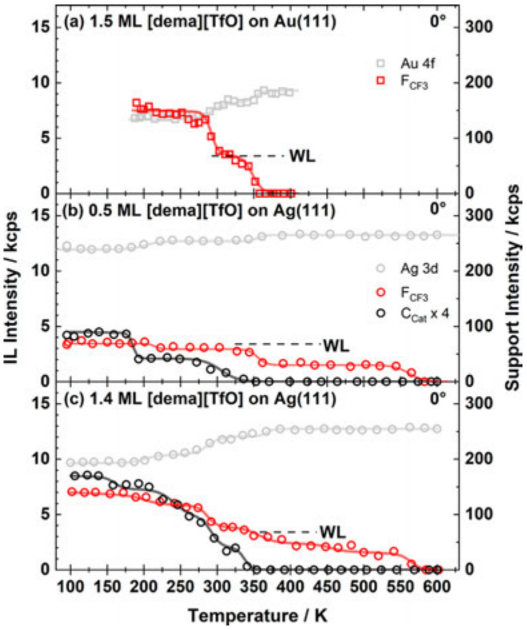

Figure 4. Thermal evolution of F 1s (red), C 1s (black), Au 4f (gray), and Ag 3d (gray) signal intensities at 0° emission upon heating films of [dema][TfO] deposited at low temperature. (a) 1.5 ML on Au(111), (b) 0.5 ML on Ag(111), and (c) 1.4 ML on Ag(111). Heating rate: 2 K/min. The dashed lines indicate the nominal intensity of a saturated wetting layer (WL) of [dema][TfO] as determined from XPS after direct deposition on Au(111) at RT and on Ag(111) at 90 K. The solid lines serve as guide to the eye.

After discussing the behavior on Au(111), we address the significantly more complex thermal evolution of [dema][TfO] from Ag(111) for two different initial coverages, 0.5 and 1.4 ML. The behavior of the F 1s and C 1s signals for 0.5 ML is shown in Figure 4b. This coverage corresponds to a wetting layer completely covering the surface. The anion-related F 1s intensity (red symbols) is initially constant and shows a slight decrease from ∼3.4 to ∼2.9 kcps at ∼215 K. Thereafter, it stays constant up to ∼355 K where it decreases by ∼50% to ∼1.5 kcps, stays constant, and finally vanishes at ∼570 K; these intensity changes are also reflected by changes of the F 1s binding energy from 688.9 ± 0.1 eV (<200 K) to 688.5 ± 0.3 eV and finally to 687.9 ± 0.2 eV (>350 K); see Figure S4 in the SI. The cation-related C 1s signal (black) shows a quite different behavior, that is, it decreases to zero in two steps with inflection points at 185 ± 2 K and 305 ± 2 K. This behavior is interpreted as follows. At 185 K, roughly half of the $[dema]^+$ cations deprotonate yielding H[TfO], with the neutral diethylmethylamine desorbing, which leads to the decrease of the C 1s signal. The minor step in the F 1s signals at 215 K could be a temperature-induced reorientation of the $[TfO]^-$ anion. At 305 K, the remaining $[dema]^+$ cations deprotonate yielding H[TfO] and diethylmethylamine desorption. At 355 K, the formed H[TfO] wetting layer partly desorbs (∼50%), which leads to the decrease of the F 1s signals, and partly decomposes to form a F-containing decomposition product, which is stable up to 570 K. Alternatively, 50% of H[TfO] could be stable up 570 K, which however appears unlikely to us. Each desorption step is accompanied by a slight increase in the Ag 3d substrate signal, due to less damping by the adsorbed species. Notably, the H[TfO] desorption temperature of 355 K on Ag(111) is very similar to that of the [dema][TfO] wetting layer on Au(111).

The corresponding behavior of the 1.4 ML film is shown in Figure 4c and in Figure S5 in the SI. This coverage corresponds to a full wetting layer plus multilayers (equivalent of ~2 wetting layers) on top of it. The anion-related F 1s signal is constant at 6.8 ± 0.4 kcps up to 190 K, and thereafter slightly decreasing to 5.8 ± 0.4 kcps, which is accompanied by a slight increase of the Ag 3d signal. This behavior could be again due to reorganization orientation of the anions. At ~ 287 K and ~350 K (inflection points), the F 1s signals show small step-like decreases, which are followed by continuous decease, until the signal disappears at 570 K. The cation-related C 1s signal again evolves independently from the anion signals. It stay more or less constant up to 215 K, apart from a slight decrease at ~150 K, which could be due to reorientation effects. Above 215 K, the C 1s signal decreases continuously to zero until 350 K. The behavior observed for 1.4 ML can be understood along the lines discussed for the 0.5 ML film. Starting at ~215 K, a fraction of the $[\mathrm{dema}]^+$ cations deprotonate yielding H[TfO] and a decrease of the C 1s signal due to diethylmethylamine desorption. This process continues up to 350 K, where the C 1s signal disappears. The step-like decrease of the F 1s signal and the simultaneous decrease of the C 1c signals at 287 K is attributed to a desorption of remaining [dema][TfO] multilayers, from the similarity of this temperature to the multilayer desorption temperature on Au(111). The small step-like decrease of the F 1s signals at ~350 K, where for 0.5 ML a pronounced step was seen, is attributed to the onset of the decomposition of H[TfO] to a F-containing surface species, which is stable up to 570 K.

■ CONCLUSIONS

The goal of this study is the detailed characterization of the adsorption, wetting, growth, and thermal evolution of protic IL [dema][TfO] films deposited onto the noble metal Au(111) and Ag(111) surfaces under well-defined UHV conditions. The quantitative analysis of several nm thick films showed the same behavior as that observed for a macroscopically thick film, which was studied as reference, confirming that [dema][TfO] remains intact upon evaporation. From angle-resolved XPS measurements, we deduce a preferential orientation of the $[\mathrm{TfO}]^-$ anions at the IL/vacuum interface with the CF_3 group preferentially pointing toward the vacuum side and the SO_3 groups pointing toward the bulk, in line with previous observations for aprotic ILs.

The ultrathin films of [dema][TfO] were deposited on Ag(111) and Au(111) at 90, 200, and 300 K and characterized *in situ* by ARXPS. We studied the growth behavior via the attenuation of the Ag 3d and Au 4f signals at electron emission angles of 0° and 80°. Overall, we observe a similar behavior for both surfaces. For all studied temperatures, we observe the initial growth of a closed 2D wetting layer. At RT, the film thickness does not increase past this wetting layer coverage due to multilayer desorption starting at around 290 K. Below 200 K, the coverage continues to increase, with "moderate" 3D island growth on top of the initially formed wetting layer.

On Au(111), [dema][TfO] is stable at RT. In contrast, on the more reactive Ag(111) surface, the $[\mathrm{dema}]^+$ cations partly deprotonate well below RT yielding H[TfO] and neutral diethylmethylamine $[\mathrm{dema}]^0$. The formed amine is volatile and desorbs instantaneously leaving a mixture of H[TfO] and [dema][TfO] on the surface. Consequently, a higher coverage of $[\mathrm{TfO}]^-$ is achieved than on Au(111) due to the smaller size of H^+ as compared to $[\mathrm{dema}]^+$. When adsorbing a WL of [dema][TfO] on Ag(111) at 90 K and subsequently heating to RT, nearly all [dema][TfO] is deprotonated to H[TfO]. The larger amount of intact [dema][TfO] observed for adsorption at RT in comparison to the amount obtained after adsorption at 90 K plus heating to RT is attributed to further adsorption of intact [dema][TfO] at free adsorption sites after desorption of $[\mathrm{dema}]^0$.

Further insight was obtained by following the thermal evolution *in situ* during heating, after deposition at low temperature. On Au(111), we deposited 1.5 ML [dema][TfO] at 200 K and subsequently heated it to 400 K. We observe the desorption of the [dema][TfO] multilayer at 292 K, leaving an intact [dema][TfO] wetting layer on Au(111). The onset of multilayer desorption below RT is the reason for the absence of multilayer growth at RT. The wetting layer desorbs intact at 348 K leaving a clean Au(111) surface above 400 K.

The behavior on Ag(111) is much more complex. Upon heating a [dema][TfO] wetting layer (0.5 ML) deposited at 90 K, we observe that the $[\mathrm{dema}]^+$ cations deprotonate in two steps at 185 and 305 K, yielding H[TfO] and volatile $[\mathrm{dema}]^0$. At 355 K, the formed H[TfO] wetting layer partly desorbs (~50%) and partly decomposes forming a F-containing surface species, which is stable up to 570 K. The behavior observed for a 1.4 ML [dema][TfO] film deposited at 90 K and heated up to 600 K can be understood along the deprotonation effects at the Ag-PIL interface as found in the wetting layer film superimposed by the multilayer signals.

All in all, our results demonstrate a rather complex behavior of this protic IL in contact with the moderately reactive Ag(111) surface even well below room temperature. The discussed deprotonation effects should thus be taken into consideration in all situations where PIL/solid interfaces are present such as in electrochemistry, nanoparticle formation, and many more, particularly, when more reactive metals than silver are involved.

■ EXPERIMENTAL SECTION

The synthesis and characterization of [dema][TfO] was described in ref 54. After careful degassing in UHV, it was deposited onto Au(111) and Ag(111) via physical vapor deposition (PVD) in UHV from a modified Knudsen cell with a boron nitride crucible at a temperature between 343 and 353 K, which provides a very stable IL flux; the details of the Knudsen cell have been published in ref 41. The PIL flux was monitored with a quartz crystal microbalance before and after deposition to ensure a constant evaporation rate. We found no signs of decomposition of [dema][TfO] in our quantitative XPS analysis of multilayer films from PVD on Ag(111) at 90 K and Au(111) at 200 K. This behavior is in line with literature reports, where decomposition of bulk [dema][TfO] is only found at temperatures above 633 K.[10] Furthermore, it agrees also with more recent observations for a similar PIL, [triethylammonium][TfO], which has been shown to evaporate as ion pairs.[51,55]

The Ag(111) and Au(111) single crystals with circular shapes were purchased from MaTeck (15 mm in diameter, purity 99.999%, polished with an alignment better than 0.1° to the (111) plane). They were cleaned in UHV by short heating to >500 K and subsequent Ar$^+$ sputtering (600 V, 8 μA) for 30 min at RT, followed by an annealing step at 800 K for 10 min. The surface temperature was measured using type-K thermocouple wires inserted into a 0.5 mm pinhole of the crystal with an absolute accuracy of ±20 K (at 500 K) and a reproducibility of ±2 K.

The UHV system for angle-resolved X-ray photoelectron spectroscopy (ARXPS) contains a nonmonochromated Al Kα X-ray source (SPECS XR 50, 1486.6 eV, 240 W) and a hemispherical electron analyzer (VG SCIENTA R3000) (described in more detail in ref 35). A pass energy of 100 eV was applied for all spectra leading to an overall energy resolution of about 0.9 eV.[35] The spectra were quantitatively evaluated in CasaXPS V2.3.16Dev6. Shirley backgrounds[56] were subtracted for Ag 3d and Au 4f core levels. For the F 1s, C 1s, O 1s, S 2p, and N 1s regions, linear backgrounds were subtracted and then peaks were fitted with Voigt profiles (30% Lorentzian contribution). The binding energy scale for XPS of the macroscopic films of [dema][TfO] was calibrated such that the F$_{CF3}$ peak is located at 688.5 eV.[30−32] The spectra of thin films of the ILs of Ag(111) and Au(111) were referenced to the Fermi edge yielding 368.20 eV for the Ag 3d$_{5/2}$ level and 83.85 eV for the Au 4f$_{7/2}$ level. In agreement with literature,[31,32] we fitted the C 1s components related to the [dema]$^+$ cation with two contributions: C$_{hetero}$ for the three carbon atoms directly bonded to the nitrogen atom and C$_{alkyl}$ for the two alkyl carbon atoms further away from the central nitrogen atom. For the measurements of the wetting layer in 0° emission, we applied a constraint to the peak areas of C$_{hetero}$/C$_{alkyl}$ = 3:2. Additionally, we subtracted a residual carbon contamination signal that could not be removed even after repeated cleaning cycles from both surfaces. In case of Ag(111), we also subtracted the K$_\beta$ satellite of the Ag 3d signal above 296 eV. Temperature-programmed XPS was measured at a heating rate of 2 K/min.

■ ASSOCIATED CONTENT

Supporting Information

The Supporting Information is available free of charge at https://pubs.acs.org/doi/10.1021/acs.langmuir.1c01823.

Additional XPS spectra addressing the chemical composition and thermal evolution of ultrathin [dema]-[TfO] films (PDF)

■ AUTHOR INFORMATION

Corresponding Author

Hans-Peter Steinrück − *Lehrstuhl für Physikalische Chemie 2, Friedrich-Alexander-Universität Erlangen-Nürnberg, 91058 Erlangen, Germany;* orcid.org/0000-0003-1347-8962; Email: hans-peter.steinrueck@fau.de

Authors

Stephen Massicot − *Lehrstuhl für Physikalische Chemie 2, Friedrich-Alexander-Universität Erlangen-Nürnberg, 91058 Erlangen, Germany;* orcid.org/0000-0002-2530-8015

Tomoya Sasaki − *Department of Applied Chemistry, Graduate School of Engineering, Osaka University, Suita, Osaka 565-0871, Japan;* orcid.org/0000-0001-5503-5823

Matthias Lexow − *Lehrstuhl für Physikalische Chemie 2, Friedrich-Alexander-Universität Erlangen-Nürnberg, 91058 Erlangen, Germany;* orcid.org/0000-0002-1441-2909

Sunghwan Shin − *Lehrstuhl für Physikalische Chemie 2, Friedrich-Alexander-Universität Erlangen-Nürnberg, 91058 Erlangen, Germany*

Florian Maier − *Lehrstuhl für Physikalische Chemie 2, Friedrich-Alexander-Universität Erlangen-Nürnberg, 91058 Erlangen, Germany;* orcid.org/0000-0001-9725-8961

Susumu Kuwabata − *Department of Applied Chemistry, Graduate School of Engineering, Osaka University, Suita, Osaka 565-0871, Japan;* orcid.org/0000-0002-4606-964X

Complete contact information is available at:
https://pubs.acs.org/10.1021/acs.langmuir.1c01823

Notes

The authors declare no competing financial interest.

■ ACKNOWLEDGMENTS

H.-P.S. and M.L. thank the European Research Council (ERC) for support through the Advanced Investigator Grant “ILID” to H.-P.S. (grant agreement no. 693398-ILID) under the European Union’s Horizon 2020 research and innovation programme. S. S. thanks the Alexander von Humboldt Foundation for a research fellowship. S.M. was funded by the Deutsche Forschungsgemeinschaft (DFG, German Research Foundation) − Project-ID 431791331 − SFB 1452.

■ REFERENCES

(1) Greaves, T. L.; Drummond, C. J. Protic Ionic Liquids: Properties and Applications. *Chem. Rev.* **2008**, *108*, 206−237.

(2) Brzeczek-Szafran, A.; Wiecławik, J.; Barteczko, N.; Szelwicka, A.; Byrne, E.; Kolanowska, A.; Swadźba Kwaśny, M.; Chrobok, A. Protic Ionic Liquids from Di- or Triamines: Even Cheaper Brønsted Acidic Catalysts. *Green Chem.* **2021**, *23*, 4421−4429.

(3) Chen, L.; Sharifzadeh, M.; Mac Dowell, N.; Welton, T.; Shah, N.; Hallett, J. P. Inexpensive Ionic Liquids: [HSO$_4$]−Based Solvent Production at Bulk Scale. *Green Chem.* **2014**, *16*, 3098−3106.

(4) Greaves, T. L.; Drummond, C. J. Protic Ionic Liquids: Evolving Structure-Property Relationships and Expanding Applications. *Chem. Rev.* **2015**, *115*, 11379−11448.

(5) Lee, S.-Y.; Ogawa, A.; Kanno, M.; Nakamoto, H.; Yasuda, T.; Watanabe, M. Nonhumidified Intermediate Temperature Fuel Cells Using Protic Ionic Liquids. *J. Am. Chem. Soc.* **2010**, *132*, 9764−9773.

(6) Pourcelly, G. Membranes for Low and Medium Temperature Fuel Cells. State-of-the-Art and New Trends. *Pet. Chem.* **2011**, *51*, 480−491.

(7) Yoshizawa, M.; Xu, W.; Angell, C. A. Ionic Liquids by Proton Transfer: Vapor Pressure, Conductivity, and the Relevance of Δpka from Aqueous Solutions. *J. Am. Chem. Soc.* **2003**, *125*, 15411−15419.

(8) Hallett, J. P.; Welton, T. Room-Temperature Ionic Liquids: Solvents for Synthesis and Catalysis. 2. *Chem. Rev.* **2011**, *111*, 3508−3576.

(9) Yasuda, T.; Watanabe, M. Protic Ionic Liquids: Fuel Cell Applications. *MRS Bull.* **2013**, *38*, 560−566.

(10) Nakamoto, H.; Watanabe, M. Brønsted Acid-Base Ionic Liquids for Fuel Cell Electrolytes. *Chem. Commun.* **2007**, 2539−2541.

(11) Lovelock, K. R. J. Quantifying Intermolecular Interactions of Ionic Liquids Using Cohesive Energy Densities. *R. Soc. Open Sci.* **2017**, *4*, 171223.

(12) Esperanca, J. M. S. S.; Canongia Lopes, J. N.; Tariq, M.; Santos, L. M. N. B. F.; Magee, J. W.; Rebelo, L. P. N. Volatility of Aprotic Ionic Liquids — a Review. *J. Chem. Eng. Data* **2010**, *55*, 3−12.

(13) Lovelock, K. R. J. Influence of the Ionic Liquid/Gas Surface on Ionic Liquid Chemistry. *Phys. Chem. Chem. Phys.* **2012**, *14*, 5071−5089.

(14) Yu, H.; Dyett, B. P.; Pathirannahalage, S. K.; Li, M.; Drummond, C. J.; Greaves, T. L. Formation of Surface Protic Ionic Liquid Nanodroplets for Nanofabrication. *Adv. Mater. Interfaces* **2020**, *7*, 1901647.

(15) Johnson, L.; Ejigu, A.; Licence, P.; Walsh, D. A. Hydrogen Oxidation and Oxygen Reduction at Platinum in Protic Ionic Liquids. *J. Phys. Chem. C* **2012**, *116*, 18048−18056.

(16) Ejigu, A.; Johnson, L.; Licence, P.; Walsh, D. A. Electrocatalytic Oxidation of Methanol and Carbon Monoxide at Platinum in Protic Ionic Liquids. *Electrochem. Commun.* **2012**, *23*, 122−124.

(17) Ingale, P.; Sakthivel, M.; Drillet, J. F. Test of Diethylmethylammonium Trifluoromethanesulfonate Ionic Liquid as Electrolyte in Electrically Rechargeable Zn/Air Battery. *J. Electrochem. Soc.* **2017**, *164*, H5224−H5229.

(18) Meng, T.; Young, K.-H.; Wong, D. F.; Nei, J. Ionic Liquid-Based Non-Aqueous Electrolytes for Nickel/Metal Hydride Batteries. *Batteries* **2017**, *3*, 4.

(19) George, A.; et al. Design of Low-Cost Ionic Liquids for Lignocellulosic Biomass Pretreatment. *Green Chem.* **2015**, *17*, 1728−1734.

(20) Verdía, P.; Brandt, A.; Hallett, J. P.; Ray, M. J.; Welton, T. Fractionation of Lignocellulosic Biomass with the Ionic Liquid 1-Butylimidazolium Hydrogen Sulfate. *Green Chem.* **2014**, *16*, 1617−1627.

(21) Pająk, M.; Hubkowska, K.; Czerwiński, A. The Study of Hydrogen Sorption in Palladium Limited Volume Electrode from Dema-Tfo Ionic Liquid. *J. Electroanal. Chem.* **2018**, *825*, 73−76.

(22) Hamm, S. C.; et al. Sputter-Deposition of Silver Nanoparticles into Ionic Liquid as a Sacrificial Reservoir in Antimicrobial Organosilicate Nanocomposite Coatings. *ACS Appl. Mater. Interfaces* **2012**, *4*, 178−184.

(23) Bhujbal, A. V.; Raut, A. B.; Bhanage, B. M. Water-Assisted Electrochemical Fabrication of Cu/Cu_2O Nanoparticles in Protic Ionic Liquid and Their Catalytic Activity in the Synthesis of Quinazolinones. *React. Kinet., Mech. Catal.* **2020**, *131*, 905.

(24) Izumi, R.; Yao, Y.; Tsuda, T.; Torimoto, T.; Kuwabata, S. Pt-Nanoparticle-Supported Carbon Electrocatalysts Functionalized with a Protic Ionic Liquid and Organic Salt. *Adv. Mater. Interfaces* **2018**, *5*, 1701123.

(25) Sasaki, T.; Uematsu, T.; Tsuda, T.; Kuwabata, S. Operando Observation of Vacuum and Liquid Interface While Conducting Gold Sputtering onto Ionic Liquid for Preparation of Au Nanoparticles. *Electrochemistry* **2018**, *86*, 223−225.

(26) Tsuda, T.; Kurihara, T.; Hoshino, Y.; Kiyama, T.; Okazaki, K.-i.; Torimoto, T.; Kuwabata, S. Electrocatalytic Activity of Platinum Nanoparticles Synthesized by Room-Temperature Ionic Liquid-Sputtering Method. *Electrochemistry* **2009**, *77*, 693−695.

(27) Yoshii, K.; Tsuda, T.; Arimura, T.; Imanishi, A.; Torimoto, T.; Kuwabata, S. Platinum Nanoparticle Immobilization onto Carbon Nanotubes Using Pt-Sputtered Room-Temperature Ionic Liquid. *RSC Adv.* **2012**, *2*, 8262−8264.

(28) Lexow, M.; Maier, F.; Steinrück, H.-P. Ultrathin Ionic Liquid Films on Metal Surfaces: Adsorption, Growth, Stability and Exchange Phenomena. *Advances in Physics: X* **2020**, *5*, 1761266.

(29) Miran, M. S.; Kinoshita, H.; Yasuda, T.; Susan, M. A. B. H.; Watanabe, M. Physicochemical Properties Determined by Δpka for Protic Ionic Liquids Based on an Organic Super-Strong Base with Various Brønsted Acids. *Phys. Chem. Chem. Phys.* **2012**, *14*, 5178−5186.

(30) Fogarty, R. M.; Matthews, R. P.; Ashworth, C. R.; Brandt-Talbot, A.; Palgrave, R. G.; Bourne, R. A.; Hoogerstraete, T. V.; Hunt, P. A.; Lovelock, K. R. J. Experimental Validation of Calculated Atomic Charges in Ionic Liquids. *J. Chem. Phys.* **2018**, *148*, 193817.

(31) Fogarty, R. M.; Palgrave, R. G.; Bourne, R. A.; Handrup, K.; Villar-Garcia, I. J.; Payne, D. J.; Hunt, P. A.; Lovelock, K. R. J. Electron Spectroscopy of Ionic Liquids: Experimental Identification of Atomic Orbital Contributions to Valence Electronic Structure. *Phys. Chem. Chem. Phys.* **2019**, *21*, 18893−18910.

(32) Fogarty, R. M.; Rowe, R.; Matthews, R. P.; Clough, M. T.; Ashworth, C. R.; Brandt, A.; Corbett, P. J.; Palgrave, R. G.; Smith, E. F.; Bourne, R. A.; Chamberlain, T. W.; Thompson, P. B. J.; Hunt, P. A.; Lovelock, K. R. J.; et al. Atomic Charges of Sulfur in Ionic Liquids: Experiments and Calculations. *Faraday Discuss.* **2018**, *206*, 183−201.

(33) Cremer, T.; Killian, M.; Gottfried, J. M.; Paape, N.; Wasserscheid, P.; Maier, F.; Steinrück, H.-P. Physical Vapor Deposition of [Emim][Tf2n]: A New Approach to the Modification of Surface Properties with Ultrathin Ionic Liquid Films. *ChemPhysChem* **2008**, *9*, 2185−2190.

(34) Steinrück, H.-P. Recent Developments in the Study of Ionic Liquid Interfaces Using X-Ray Photoelectron Spectroscopy and Potential Future Directions. *Phys. Chem. Chem. Phys.* **2012**, *14*, 5010−5029.

(35) Lexow, M.; Talwar, T.; Heller, B. S. J.; May, B.; Bhuin, R. G.; Maier, F.; Steinrück, H.-P. Time-Dependent Changes in the Growth of Ultrathin Ionic Liquid Films on Ag(111). *Phys. Chem. Chem. Phys.* **2018**, *20*, 12929−12938.

(36) Wittstock, A.; et al. Nanoporous Au: An Unsupported Pure Gold Catalyst? *J. Phys. Chem. C* **2009**, *113*, 5593−5600.

(37) Xu, B.; Siler, C.; Madix, R.; Friend, C., Ag/Au Mixed Sites Promote Oxidative Coupling of Methanol on the Alloy Surface. *Chem. - Eur. J.* **2014**, *20*.4646

(38) Maier, F.; Cremer, T.; Kolbeck, C.; Lovelock, K. R. J.; Paape, N.; Schulz, P. S.; Wasserscheid, P.; Steinrück, H. P. Insights into the Surface Composition and Enrichment Effects of Ionic Liquids and Ionic Liquid Mixtures. *Phys. Chem. Chem. Phys.* **2010**, *12*, 1905−1915.

(39) Lexow, M.; Heller, B. S. J.; Partl, G.; Bhuin, R. G.; Maier, F.; Steinrück, H.-P. Cation Exchange at the Interfaces of Ultrathin Films of Fluorous Ionic Liquids on Ag(111). *Langmuir* **2019**, *35*, 398−405.

(40) Heller, B.; Lexow, M.; Greco, F.; Shin, S.; Partl, G. J.; Maier, F.; Steinrück, H.-P., Temperature-Dependent Surface Enrichment Effects in Binary Mixtures of Fluorinated and Non-Fluorinated Ionic Liquids. *Chem. - Eur. J.* **2020**, *26*.1117

(41) Lexow, M.; Heller, B. S. J.; Maier, F.; Steinrück, H.-P. Anion Exchange at the Liquid/Solid Interface of Ultrathin Ionic Liquid Films on Ag(111). *ChemPhysChem* **2018**, *19*, 2978−2984.

(42) Rietzler, F.; May, B.; Steinrück, H. P.; Maier, F. Switching Adsorption and Growth Behavior of Ultrathin [C2C1Im][Otf] Films on Au(111) by Pd Deposition. *Phys. Chem. Chem. Phys.* **2016**, *18*, 25143−25150.

(43) Cremer, T.; Stark, M.; Deyko, A.; Steinrück, H. P.; Maier, F. Liquid/Solid Interface of Ultrathin Ionic Liquid Films: [C1C1Im]-[Tf2N] and [C8C1Im][Tf2N] on Au(111). *Langmuir* **2011**, *27*, 3662−3671.

(44) Deyko, A.; Bajus, S.; Rietzler, F.; Bösmann, A.; Wasserscheid, P.; Steinrück, H.-P.; Maier, F. Interface Properties and Physicochemical Characterization of the Low-Temperature Molten Salt Li/K/Cs Acetate. *J. Phys. Chem. C* **2013**, *117*, 22939−22946.

(45) Rietzler, F.; Piermaier, M.; Deyko, A.; Steinrück, H.-P.; Maier, F. Electrospray Ionization Deposition of Ultrathin Ionic Liquid Films: [C8C1Im]Cl and [C8C1Im][Tf2N] on Au(111). *Langmuir* **2014**, *30*, 1063−1071.

(46) Atilhan, M.; Anaya, B.; Ullah, R.; Costa, L. T.; Aparicio, S. Double Salt Ionic Liquids Based on Ammonium Cations and Their Application for Co2 Capture. *J. Phys. Chem. C* **2016**, *120*, 17829−17844.

(47) Bauer, T.; Mehl, S.; Brummel, O.; Pohako-Esko, K.; Wasserscheid, P.; Libuda, J. Ligand Effects at Ionic Liquid-Modified Interfaces: Coadsorption of [C2C1Im][Otf] and Co on Pd(111). *J. Phys. Chem. C* **2016**, *120*, 4453−4465.

(48) Schernich, S.; Kostyshyn, D.; Wagner, V.; Taccardi, N.; Laurin, M.; Wasserscheid, P.; Libuda, J. Interactions between the Room-Temperature Ionic Liquid [C2C1Im][Otf] and Pd(111), Well-Ordered Al2o3, and Supported Pd Model Catalysts from Ir Spectroscopy. *J. Phys. Chem. C* **2014**, *118*, 3188−3193.

(49) Schernich, S.; Wagner, V.; Taccardi, N.; Wasserscheid, P.; Laurin, M.; Libuda, J. Interface Controls Spontaneous Crystallization in Thin Films of the Ionic Liquid [C2C1Im][Otf] on Atomically Clean Pd(111). *Langmuir* **2014**, *30*, 6846−6851.

(50) Mehl, S.; Bauer, T.; Brummel, O.; Pohako-Esko, K.; Schulz, P.; Wasserscheid, P.; Libuda, J. Ionic-Liquid-Modified Hybrid Materials Prepared by Physical Vapor Codeposition: Cobalt and Cobalt Oxide Nanoparticles in [C1C2Im][Otf] Monitored by in Situ Ir Spectroscopy. *Langmuir* **2016**, *32*, 8613−8622.

(51) Zaitsau, D. H.; Emel'yanenko, V. N.; Stange, P.; Verevkin, S. P.; Ludwig, R. Dissecting the Vaporization Enthalpies of Ionic Liquids by

Exclusively Experimental Methods: Coulomb Interaction, Hydrogen Bonding, and Dispersion Forces. *Angew. Chem., Int. Ed.* **2019**, *58*, 8589−8592.

(52) Lexow, M.; Massicot, S.; Maier, F.; Steinrück, H.-P. Stability and Exchange Processes in Ionic Liquid/Porphyrin Composite Films on Metal Surfaces. *J. Phys. Chem. C* **2019**, *123*, 29708−29721.

(53) Hessey, S.; Jones, R. On the Evaporation, Bonding, and Adsorbate Capture of an Ionic Liquid on Au(111). *Chem. Sci.* **2013**, *4*, 2519−2529.

(54) Sasaki, T.; Inoue, S.; Kuwabata, S. Room-Temperature Fabrication of Electrocatalyst for Oxygen Reduction Using Pt Nanoparticle-Dispersed Protic Ionic Liquid with Poly(3,4-Ethylenedioxythiophene). *Electrochemistry* **2021**, *89*, 83−86.

(55) Horikawa, M.; Akai, N.; Kawai, A.; Shibuya, K. Vaporization of Protic Ionic Liquids Studied by Matrix-Isolation Fourier Transform Infrared Spectroscopy. *J. Phys. Chem. A* **2014**, *118*, 3280−3287.

(56) Shirley, D. A. High-Resolution X-Ray Photoemission Spectrum of the Valence Bands of Gold. *Phys. Rev. B* **1972**, *5*, 4709−4714.

Supporting Information

Adsorption, Wetting, Growth and Thermal Stability of the Protic Ionic Liquid Diethylmethylammonium Trifluoromethanesulfonate on Ag(111) and Au(111)

Stephen Massicot[1,*ORCID*: 0000-0002-2530-8015], Tomoya Sasaki[2,*ORCID*: 0000-0001-5503-5823],
Matthias Lexow[1,*ORCID*: 0000-0002-1441-2909], Sunghwan Shin[1,*ORCID*: 0000-0002-2773-7649],
Florian Maier[1,*ORCID*: 0000-0001-9725-8961], Susumu Kuwabata[2,*ORCID*: 0000-0002-4606-964X],
Hans-Peter Steinrück[1,* *ORCID*: 0000-0003-1347-8962]

[1] Lehrstuhl für Physikalische Chemie 2, Friedrich-Alexander-Universität Erlangen-Nürnberg,
Egerlandstr. 3, 91058 Erlangen, Germany

[2] Department of Applied Chemistry, Graduate School of Engineering, Osaka University,
Yamada-oka 2-1, Suita, Osaka 565-0871, Japan

2.6 nm [dema][TfO] on Ag(111) at 90 K

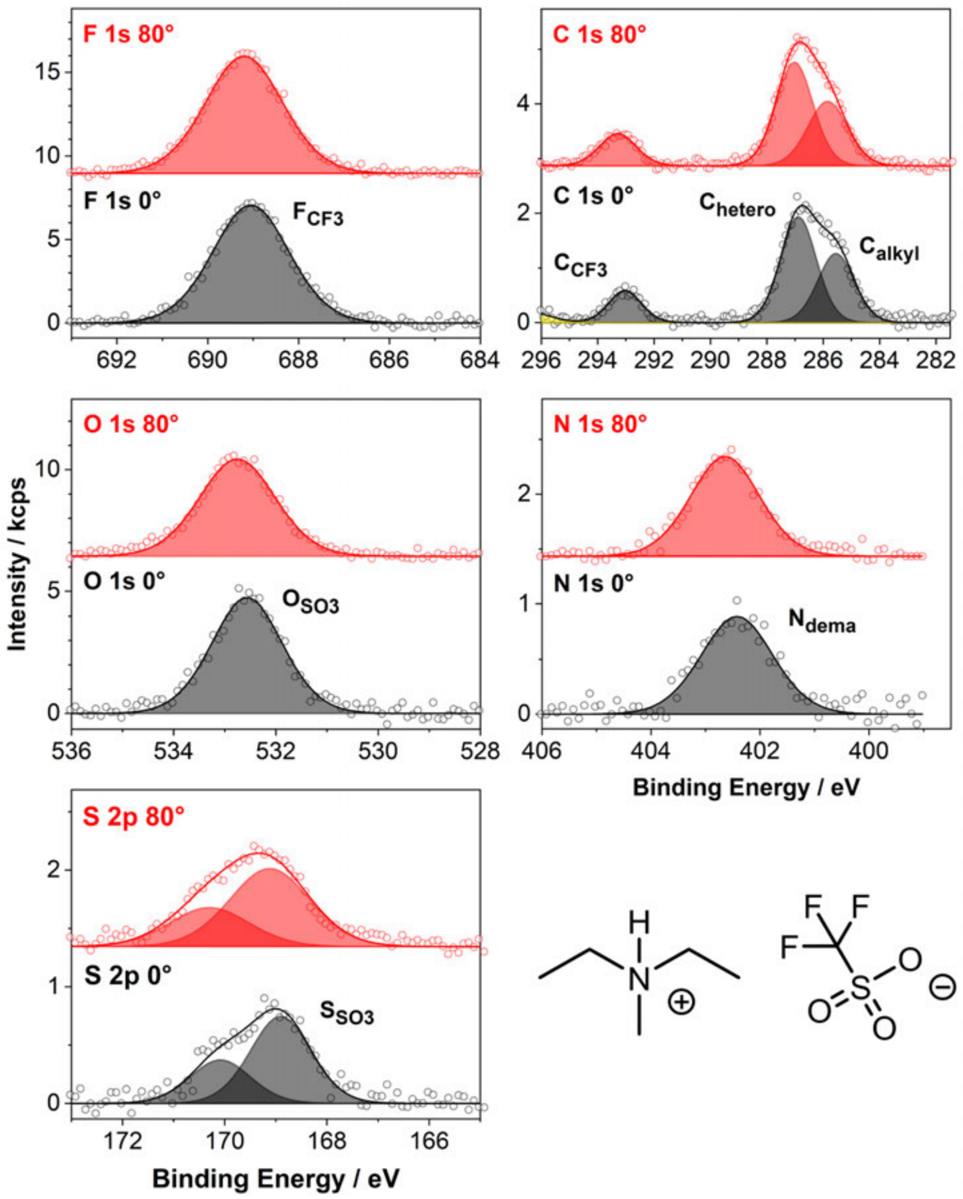

	C_{CF3}	C_{hetero}	C_{alkyl}	F_{CF3}	O_{SO3}	N_{dema}	S_{SO3}
nominal	**1**	**3**	**2**	**3**	**3**	**1**	**1**
0°	0.9	3.1	2.1	3.2	3.0	0.9	0.9
80°	1.0	3.2	2.1	3.2	2.6	0.9	1.0

Figure S1: F 1s, O1s, N 1s, C 1s and S 2p XP spectra of a 2.6 nm thick [dema][TfO] deposited onto Ag(111) at 90 K, collected at in 0° (black) and 80° (red) emission. At the right bottom, the molecular structure of [dema][TfO], is shown. The table below the figure shows the quantitative analysis of the spectra.

2.4 nm [dema][TfO] on Au(111) at 200 K

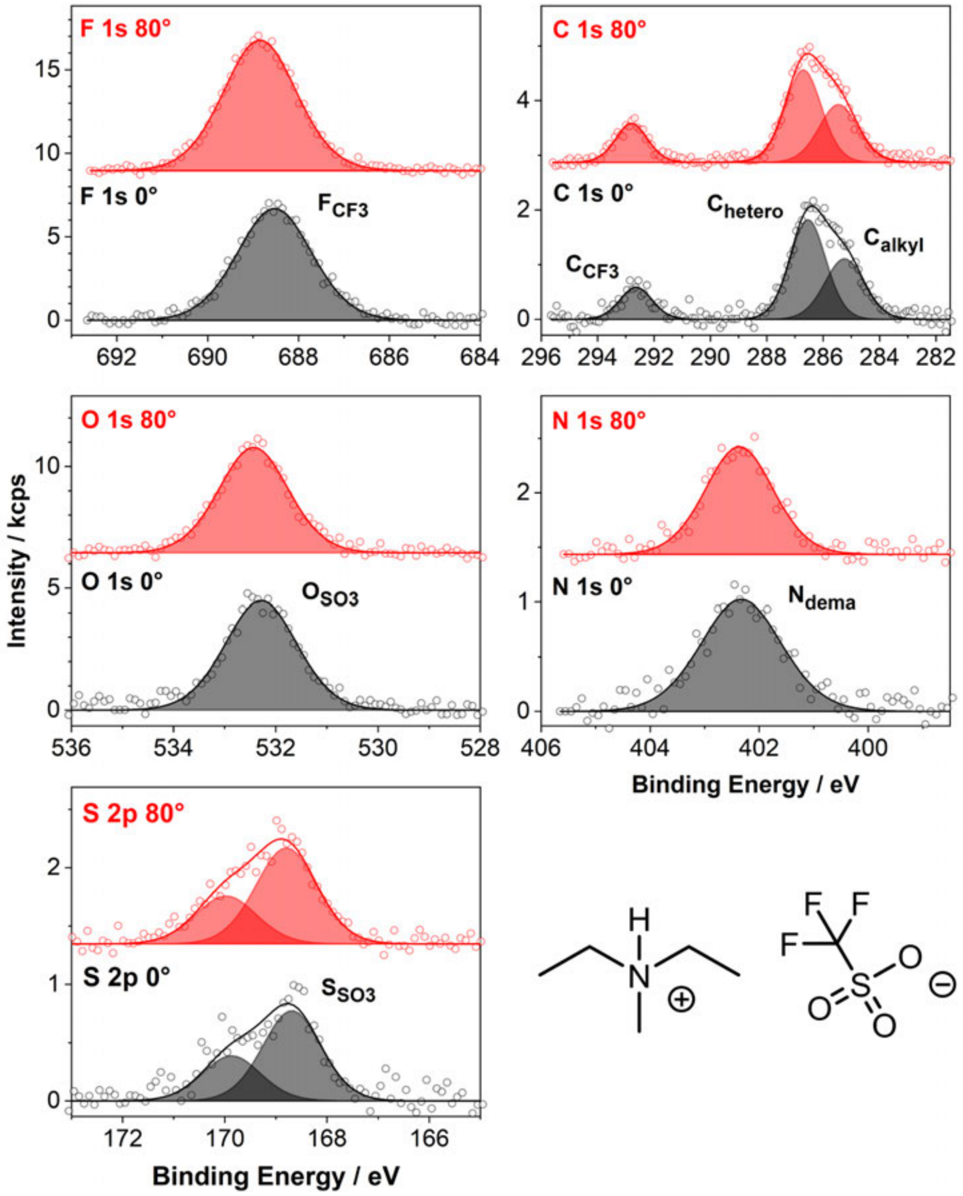

	C_{CF3}	C_{hetero}	C_{alkyl}	F_{CF3}	O_{SO3}	N_{dema}	S_{SO3}
nominal	1	3	2	3	3	1	1
0°	0.9	3.1	2.0	3.0	2.9	1.2	0.9
80°	1.1	2.9	1.9	3.5	2.7	0.9	1.0

Figure S2: F 1s, O1s, N 1s, C 1s and S 2p XP spectra of a 2.4 nm thick [dema][TfO] deposited onto Au(111) at 200 K, collected at in 0° (black) and 80° (red) emission. At the right bottom, the molecular structure of [dema][TfO], is shown. The table below the figure shows the quantitative analysis of the spectra.

TPXPS of 1.5 ML on Au(111)

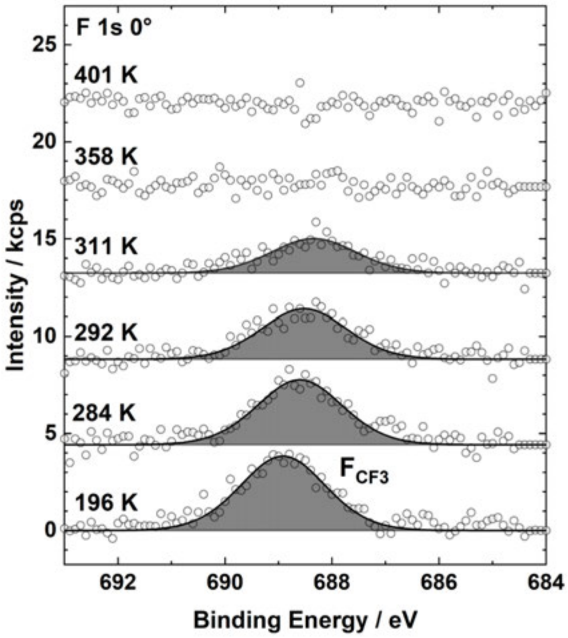

Figure S3: Waterfall plot of selected F 1s of 1.5 ML [dema][TfO] deposited onto Au(111) at 198 K, and collected during heating to 401 K. The spectra are measured at an emission angle of 0°.

TPXPS of 0.5 ML on Ag(111)

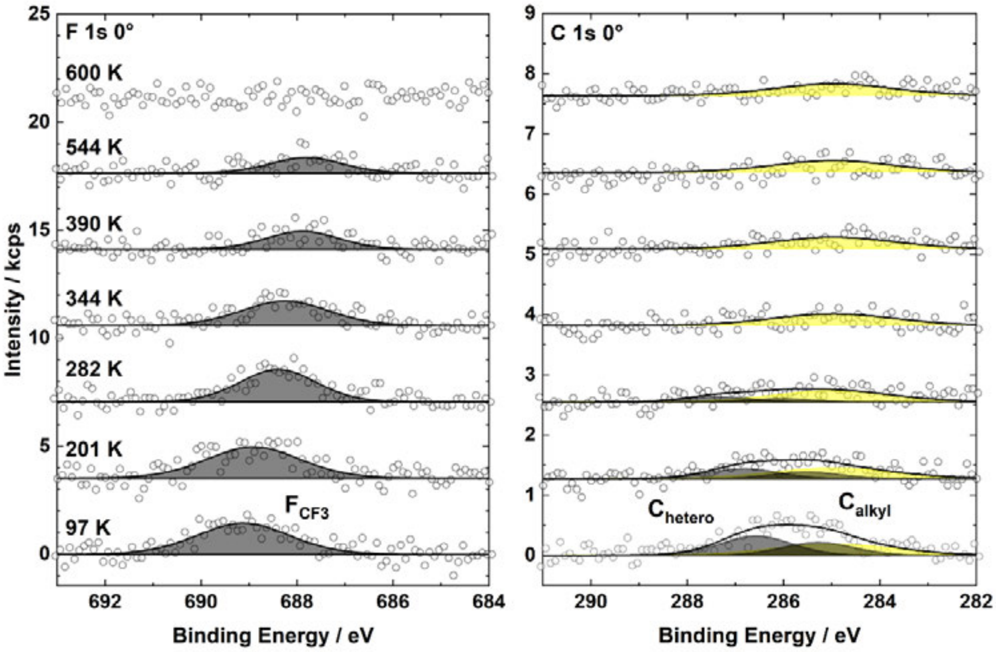

Figure S4: Waterfall plots of selected F 1s (left) and C 1s spectra (right) of a 0.5 ML [dema][TfO] film (wetting layer) deposited onto Ag(111) at 96 K, and collected during heating to 600 K. The spectra are measured at an emission angle of 0°. For the quantitative analysis of the C 1s spectra, the broad signal of a carbon contamination (shaded in yellow) was subtracted.

TPXPS of 1.4 ML on Ag(111)

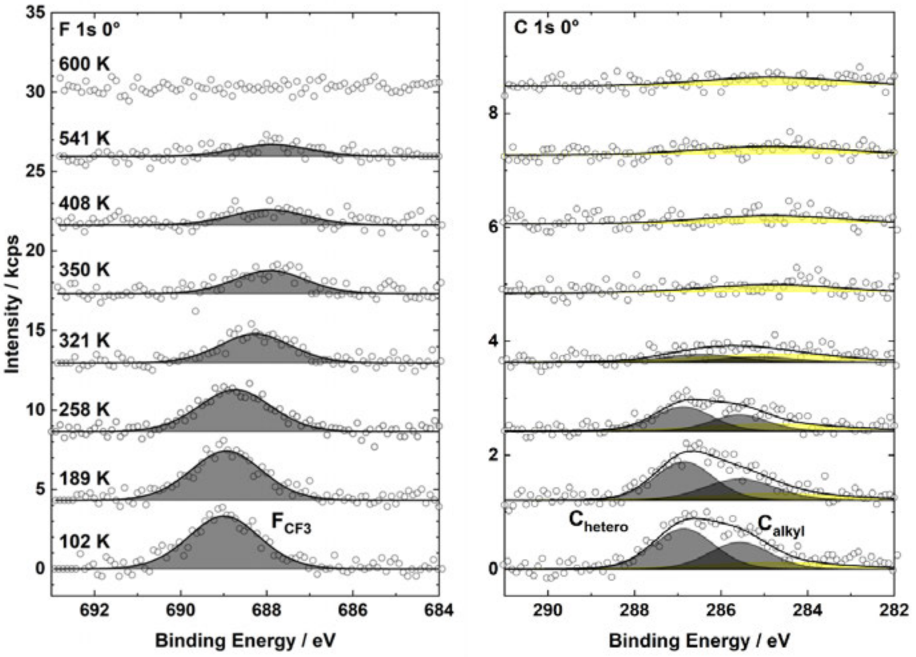

Figure S5: Waterfall plots of selected F 1s (left) and C 1s spectra (right) of 1.4 ML [dema][TfO] deposited onto Ag(111) at 101 K, and collected during heating to 600 K. The spectra are measured at an emission angle of 0°. For the quantitative analysis of the C 1s spectra, the broad signal of a carbon contamination (shaded in yellow) was subtracted.

[P2]

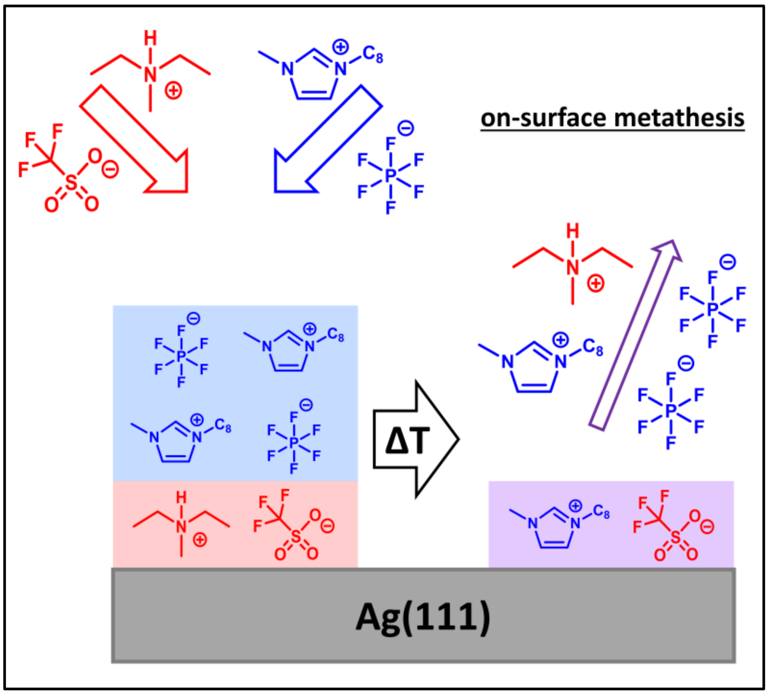

On-Surface Metathesis of an Ionic Liquid on Ag(111).

S. Massicot, T. Sasaki, M. Lexow, F. Maier, S. Kuwabata, H.-P. Steinrück.

Chem. Eur. J. **2022**, *e202200167*

DOI: 10.1002/chem.202200167

Chemistry–A European Journal
Research Article
doi.org/10.1002/chem.202200167
Chemistry Europe
European Chemical Societies Publishing
www.chemeurj.org

On-Surface Metathesis of an Ionic Liquid on Ag(111)

Stephen Massicot,[a] Tomoya Sasaki,[b] Matthias Lexow,[a] Florian Maier,[a]
Susumu Kuwabata,[b] and Hans-Peter Steinrück*[a]

Abstract: We investigated the adsorption, surface enrichment, ion exchange, and on-surface metathesis of ultrathin mixed IL films on Ag(111). We stepwise deposited 0.5 ML of the protic IL diethylmethylammonium trifluoromethanesulfonate ([dema][TfO]) and 1.0 ML of the aprotic IL 1-methyl-3-octylimidazolium hexafluorophosphate ([C_8C_1Im][PF_6]) at around 90 K. Thereafter, the resulting layered frozen film was heated to 550 K, and the thermally induced phenomena were monitored in situ by angle-resolved X-ray photoelectron spectroscopy. Between 135 and 200 K, [TfO]$^-$ anions at the Ag(111) surface are exchanged by [PF_6]$^-$ anions and enriched together with [C_8C_1Im]$^+$ cations at the IL/vacuum interface. Upon further heating, [dema][PF_6] and [OMIm][PF_6] desorb selectively at ~235 and ~380 K, respectively. Hereby, a wetting layer of pure [C_8C_1Im][TfO] is formed by on-surface metathesis at the IL/metal interface, which completely desorbs at ~480 K. For comparison, ion enrichment at the vacuum/IL interface was also studied in macroscopic IL mixtures, where no influence of the solid support is expected.

Introduction

Ionic liquids (ILs) are salts with melting points typically well below 100 °C and with an extremely low vapor pressure. They are composed of poorly coordinating organic cations and organic or inorganic anions, and hence exhibit a wide structural variability with the possibility to tune their physico-chemical properties for desired applications.[1] Besides batteries,[2] fuel cells,[3] organic[4] and nanoparticle[5] synthesis, to name just a few examples, ILs are also very well suited for applications in catalysis.[6] This is due to their low vapor pressure[7] and high thermal stability.[8] The first commercial and still maybe most important application of ILs in catalysis is the BASIL™ (Biphasic Acid Scavenging using Ionic Liquids) process for the production of alkoxyphenylphosphines.[9] Furthermore, different novel catalytic concepts were developed in the past decades, like the SCILL (Solid Catalyst with Ionic Liquid Layer) approach.[1f,6d,10] Thereby, a thin IL film modifies the solid catalytic support material by making the reactive sites of the heterogeneous catalyst less vulnerable towards poisoning while simultaneously modifying or improving selectivity and reactivity.[6d,11] In order to obtain the desired behaviour, it is crucial to choose the right IL/support combination. While solid catalysts are well known and were intensively studied for several decades, if not centuries,[12] ILs are a comparably novel class of materials and have only been studied in-depth for a few decades.[13] In particular, the adsorption and thermal stability of IL films on metal surfaces have been addressed only for a few systems.[14] This is especially true for exchange phenomena in mixed IL films, which have been only addressed for a few aprotic ILs and no study involving protic ILs exists.[14c,d] Such studies could also open new routes for the IL synthesis, in order to tackle challenges existing in the synthesis of new ILs.[1c,15] In this study, we evaluate a novel type of IL synthesis, i.e. an on-surface metathesis at a metal support in UHV, which could allow for surface coating with an IL, which cannot be deposited by evaporation, for example due to its thermal instability.

In order to investigate these questions, we sequentially deposited ultrathin films of the protic IL diethylmethylammonium trifluoromethanesulfonate ([dema][TfO]) and the aprotic IL 1-methyl-3-octylimidazolium hexafluorophosphate ([C_8C_1Im][PF_6]) on a Ag(111) substrate by in situ physical vapor deposition (PVD) at 90 K. The molecular structure of both ILs is shown in Figure 1. We have chosen these particular two ILs because (i) we wanted to study the behaviour of ultrathin mixed films of a protic and an aprotic IL, (ii) the spectroscopic signature (in particular of the F atoms) allowed us to differentiate between the different ions, and (iii) both ILs have already been characterized on the required level of detail by us in the past as neat ILs.[14c,f,16] After deposition, we heated the layered IL film to 550 K and simultaneously monitored thermally induced phenomena by angle-resolved X-ray photoelectron spectroscopy (ARXPS). In particular, we measured the Ag 3d and the IL XPS signals at emission angles of $\vartheta = 0°$ and 80° relative to the surface normal. For Al Kα radiation, the information depth (ID) at normal emission ($\vartheta = 0°$) is 7–9 nm (depending on the kinetic energy), while at $\vartheta = 80°$ ID it is only

---

[a] S. Massicot, Dr. M. Lexow, Dr. F. Maier, Prof. Dr. H.-P. Steinrück
Lehrstuhl für Physikalische Chemie II
Friedrich-Alexander-Universität Erlangen-Nürnberg
Egerlandstr. 3, 91058 Erlangen (Germany)
E-mail: hans-peter.steinrueck@fau.de

[b] T. Sasaki, Prof. Dr. S. Kuwabata
Department of Applied Chemistry, Graduate School of Engineering
Osaka University
Yamada-oka 2–1, Suita, Osaka 565-0871 (Japan)

Supporting information for this article is available on the WWW under https://doi.org/10.1002/chem.202200167

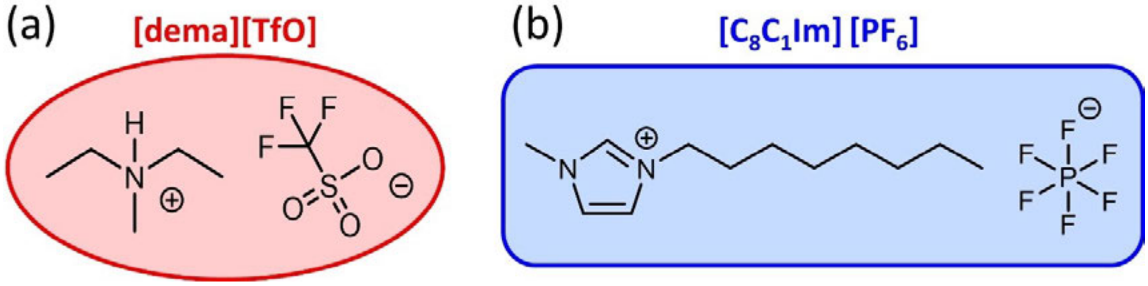

Figure 1. Molecular structures of (a) diethylmethylammonium trifluoromethanesulfonate, [dema][TfO], and (b) 1-methyl-3-octylimidazolium hexafluorophosphate, $[C_8C_1Im][PF_6]$.

1–1.5 nm. Thus, measurements at 0° provide information on the IL bulk (10–15 layers), and measurements at 80° only probe the outer surface (topmost 1–2 layers). From our measurements, we can deduce ion exchange and preferential enrichment processes at both the metal/IL and the IL/vacuum interfaces. Most interestingly, we find that selective ion desorption leads to the on-surface formation of a new IL by metathesis at the IL/metal interface.

Results and Discussion

Macroscopic mixtures of [dema][TfO] and $[C_8C_1Im][PF_6]$

We investigated the surface composition at the IL/vacuum interface and possible enrichment effects at the outmost surface for macroscopic films of [dema][TfO] and $[C_8C_1Im][PF_6]$ mixtures with [dema][TfO] contents of $x_i = 1.00$, 0.85, 0.50, 0.20, 0.09 and 0.00. The films had thicknesses in the order of 0.1 mm, and thus no influence of the IL/metal interface[14c] is expected; they will serve as a reference for the following examination of ultrathin films. The quantitative analysis of the ARXPS spectra of the various mixtures is summarized in Table S1 (the data for neat [dema][TfO] and $[C_8C_1Im][PF_6]$ are taken from Ref. [14f] and Ref. [14c], respectively). For the bulk-sensitive data at 0° (see Experimental Section), the measured atom numbers are in good agreement with the nominal values. For the surface-sensitive data at 80°, the atom numbers deviate considerably from the nominal values, especially for the F 1s and C 1s spectra. Therefore, the F 1s and C 1s spectra in both geometries will be discussed in more detail.

In Figure 2 (left), the F 1s spectra of the four mixtures and also of the pure compounds are shown. The F_{CF3} peak at 688.5 eV is assigned to the $[TfO]^-$ anion,[14f,17] and the F_{PF6} peak at 686.8 eV to the $[PF_6]^-$ anion.[14a,d,18] For neat [dema][TfO] ($x_i = 1.00$; top spectrum), the F_{CF3} peak slightly increases when changing the emission angle from 0° (black) to 80° (green). This indicates that at the outer surface the $[TfO]^-$ anion is oriented with the CF_3 groups pointing towards the vacuum side.[14f] For neat $[C_8C_1Im][PF_6]$ ($x_i = 0.0$; bottom spectrum), the F_{PF6} signal at 80° is significantly smaller than at 0°, which is attributed to a damping effect due to the well-known surface enrichment of the octyl chain of the $[C_8C_1Im]^+$ cation (see below).[1d,14c,18–19] For all mixtures, the F_{CF3} peak still slightly increases when changing the emission angle from 0° (black) to 80° (green), while at the same time for the F_{PF6} peak an even more pronounced relative decrease of the signals at 80° as compared to that for neat $[C_8C_1Im][PF_6]$ is observed. This behaviour indicates a pronounced enrichment of the $[TfO]^-$ anions at and a depletion of the $[PF_6]^-$ anions from the IL/vacuum interface for the mixtures of [dema][TfO] and $[C_8C_1Im][PF_6]$.

For further quantification of this enrichment and depletion of the different anions in the four mixtures, we plotted the ratio of the normalized F_{CF3} and F_{PF6} signals vs. the IL mole fractions x_i of [dema][TfO] in Figure 3 for 0° (black) and 80° (green) emission. For $x_i = 0.85$, i.e., [dema][TfO]: $[C_8C_1Im][PF_6] = 5.7:1$, the ratio of 1.2 at 0° emission is close to the nominal value of 1.0, which is indicated by a dashed horizontal line. For 80° emission, the ratio increases to 1.7 indicating a pronounced enrichment of the $[TfO]^-$ anion. For $x_i = 0.50$ (1:1), $x_i = 0.20$ (1:4) and $x_i = 0.09$ (1:10), the ratio at 0° increases to 1.2, 1.6 and 2.2, respectively, and at 80° to 2.1, 3.6 and 4.6, respectively. Again, this reflects the enrichment of the $[TfO]^-$ relative to the $[PF_6]$ anions, which is most prominent for mixtures with low [dema][TfO] content. This high degree of enrichment is responsible for the fact that even at 0°, i.e., in the so-called bulk-sensitive geometry, the contribution of the topmost layer is so strong that it is reflected in a ratio that is larger than the nominal value of one. A similar effect has been observed before in studies of IL mixtures with pronounced surface enrichment of one species.[14d,f,20]

One driving force for the enrichment of $[TfO]^-$ over $[PF_6]^-$ could be a lower surface tension of a mixture with a $[TfO]^-$-terminated surface. Indeed, Freie et al. reported that ILs with $[TfO]^-$ anions have lower surface tension than ILs with $[PF_6]^-$ anions.[21] Also, Martino et al. showed that $[C_2C_1Im][TfO]$ has a lower surface tension than $[C_2C_1Im][BF_4]$; this observation can be tentatively used for a comparison, since $[BF_4]^-$ ILs often have similar surface tension as the corresponding $[PF_6]^-$ ILs.[22]

Next, we discuss the C 1s spectra of the mixtures, which are depicted in Figure 2 (right) along with the spectra of the neat ILs, at 0° (black) and 80° (green) emission. For both ILs, the C_{hetero} peak at ≈286.8 eV binding energy is assigned to the carbon atoms in direct contact with nitrogen (hetero) atoms and the C_{alkyl} peak at ≈285.0 eV to carbon atoms not in contact with nitrogen atoms of the ethyl ([dema][TfO]) or octyl

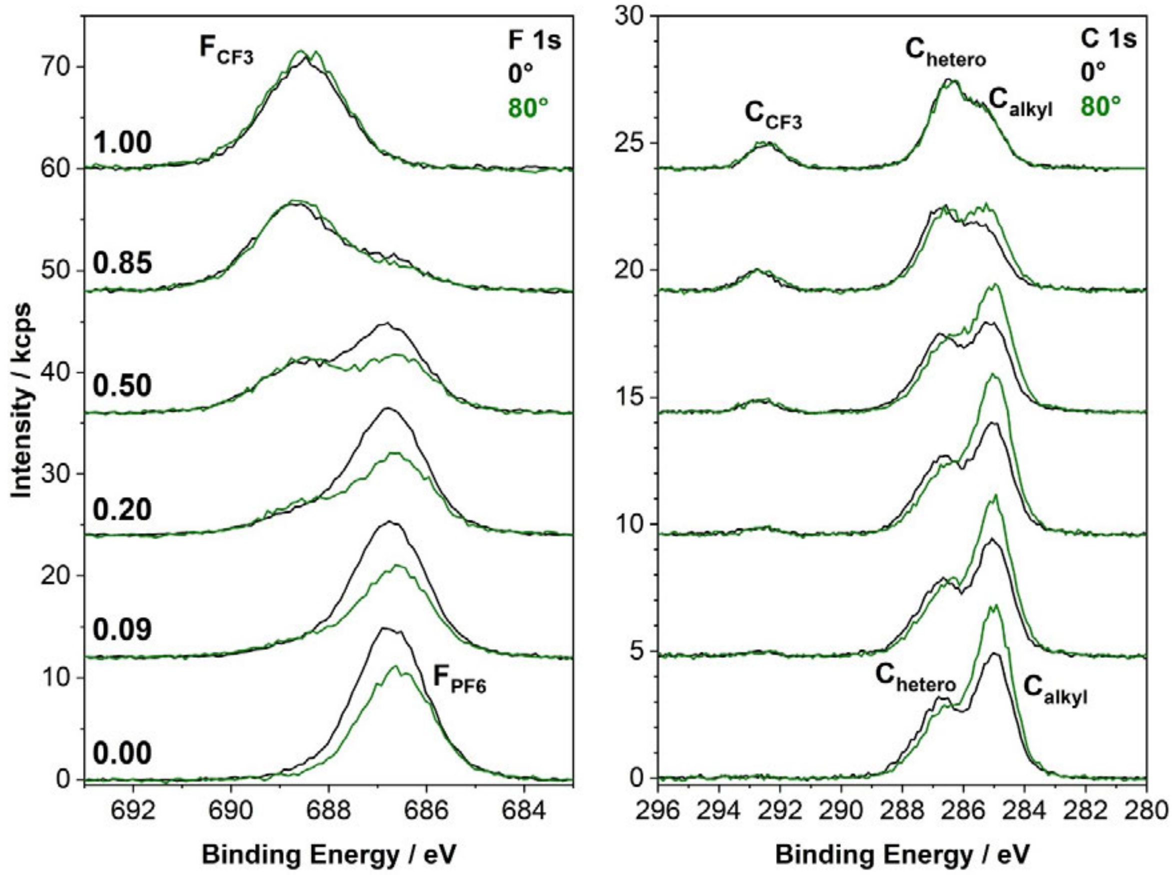

Figure 2. F 1s and C 1s spectra in 0° and 80° emission of macroscopic mixtures of [dema][TfO] and $[C_8C_1Im][PF_6]$ at RT; for [dema][TfO] contents of $x_i = 1.00$ (neat [dema][TfO], top), $x_i = 0.85$ (ratio = 5.7 : 1), $x_i = 0.50$ (1 : 1), $x_i = 0.20$ (1 : 4), $x_i = 0.09$ (1 : 10), and $x_i = 0.00$ (neat $[C_8C_1Im][PF_6]$, bottom).

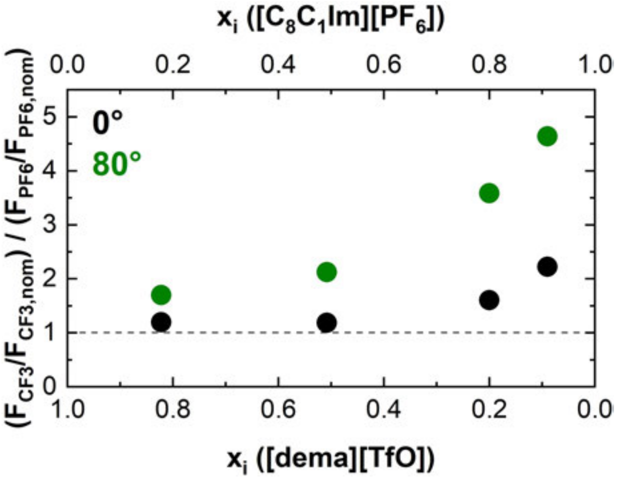

Figure 3. Ratio of XPS peak intensities of the two anionic F 1s signals (normalized to their nominal values), in 0° and 80° emission, as a function of the content of [dema][TfO] in macroscopic mixtures with $[C_8C_1Im][PF_6]$. The dashed line indicates the nominal ratio of 1.

($[C_8C_1Im][PF_6]$) chains. For neat [dema][TfO], the 0° and 80° signals in Figure 2 (top) are nearly identical. In contrast, the C_{alkyl} contribution for neat $[C_8C_1Im][PF_6]$ in Figure 2 (bottom) is more prominent at 80° than at 0°, which indicates the surface enrichment of the octyl chain, as reported previously.[1d,14c,18–19] Unfortunately, for the mixtures the C_{hetero} and the C_{alkyl} peaks of the two cations are too close together for an unequivocal separation of the different cation contributions. The same holds true for the N 1s spectra, with binding energies of 402.1 eV for $[C_8C_1Im]^+$ and 402.5 eV for $[dema]^+$. For the 0° C 1s spectra, constraining the respective C_{hetero} and C_{alkyl} contributions to the exact amount of each IL from the preparation of the mixtures matches very well the shape of the superimposed signals, and the areas of the cation signals correspond exactly to the expected stoichiometry of the mixture. Due to the above mentioned selective enrichment effects, it is not possible to use this approach for the spectra at grazing emission. Therefore at 80°, the C 1s spectra will be discussed only qualitatively. For all mixtures, the C_{alkyl} signals, which originate predominantly from the $[C_8C_1Im]^+$ cation, increase in the 80° spectra compared to the 0° spectra. Furthermore, the combined cation C 1s intensities at 80° yield higher atom numbers than the respective nominal values, see Table S1. These observations indicate that the $[C_8C_1Im]^+$ cation, and specifically the octyl chain is always preferentially enriched at the IL/vacuum interface for all mixtures, as was observed for neat $[C_8C_1Im][PF_6]$.[1d,14c,18–19] Consequently, the $[dema]^+$ cation is surface-depleted in the

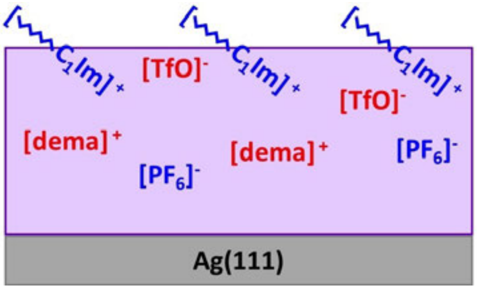

Figure 4. Scheme of proposed surface enrichment of $[C_8C_1Im]^+$ and $[TfO]^-$ and surface depletion of $[PF_6]^-$ for a 1:1 mixture of [dema][TfO] and $[C_8C_1Im][PF_6]$.

mixtures with $[C_8C_1Im]^+$. Figure 4 provides a schematic summary of the enrichment and depletion effects.

On-surface metathesis of $[C_8C_1Im][TfO]$ on Ag(111)

To study possible ion exchange processes along with preferential enrichment and selective desorption as a function of temperature, we sequentially deposited thin films of [dema][TfO] and $[C_8C_1Im][PF_6]$ on Ag(111), and monitored the bulk and surface composition with temperature-programmed XPS. To avoid switching between the 0° and 80° emission angles (by tilting the sample) at each temperature, we performed separate heating experiments at 0° and 80°. The comparison of Ag 3d, F 1s and C 1s spectra directly after deposition evidenced the reproducible preparation of the starting films for the two experiments (note that due to the overall low IL signals in these ultrathin films, particularly for the N 1s and S 2p regions with their small XPS cross sections, we restricted our temperature-dependent ARXPS measurements to the representative F 1s and C 1s regions to characterize the behaviour for the anions and cations). Figure 5 shows C 1s and F 1s spectra at selected temperatures. In Figure 6c and 6d, the quantitative analysis of the thermal evolution of the signals related to the anions (F_{CF3} and F_{PF6}) and cations (C_{cat}) of the two ILs, and of the Ag(111) substrate (Ag 3d) are shown at emission angles of 0° and 80°, respectively. Figure 7 provides a schematic sketch of the film composition at selected temperatures according to Figure 5.

In a first step, we deposited a wetting layer (i.e., 0.5 ML) of [dema][TfO] on clean Ag(111) at a temperature around 90 K. The XP spectra in Figure 5–II show the F_{CF3} and C_{CF3} peaks of the $[TfO]^-$ anion and the C_{hetero} and C_{alkyl} signals of the $[dema]^+$ cation.[14f,17] The C_{anion}:C_{hetero}:C_{alkyl} ratio is 1.0:2.8:2.2 in 0° and 0.9:3.0:2.1 in 80°, which is close to the nominal ratio of 1:3:2 and indicates an intact WL of [dema][TfO] on Ag(111) at low temperature.

After subsequent deposition of 1 ML of $[C_8C_1Im][PF_6]$ on top of the [dema][TfO] WL at around 90 K, the F 1s spectra in Figure 5–III show an additional contribution F_{PF6} at 687.1 eV related to the $[PF_6]^-$ anion.[14a,d,18] The expected nominal F_{CF3}/F_{PF6} peak ratio in 0° is 0.33. In an simple picture one would expect a ratio of 0.25 (=1:4) because $[C_8C_1Im][PF_6]$ has twice the amount of fluorine atoms per IL pair and a twice as thick film was deposited (1.0 vs. 0.5 ML). However, the molecular volume of $[C_8C_1Im][PF_6]$ (0.458 nm^3)[23] is higher than for [dema][TfO] (0.305 nm^3).[24] Hence, [dema][TfO] has a 1.32 times smaller 2-dimensional footprint ($=V^{2/3}$) leading to an expected ratio of 0.33 ($=0.25\times1.32$). This is in excellent agreement with the measured peak ratio F_{CF3}/F_{PF6} in 0° of 0.33. This ratio changes to 0.27 at 80°, which reflects a substantial decrease of the F_{CF3} signal. The C_{CF3} peak at 80° in Figure 5-III shows a similar substantial attenuation. Both observations indicate that the post-deposited $[C_8C_1Im][PF_6]$ film covers the [dema][TfO] wetting layer, as is expected for the low deposition temperature of ~90 K. The C_{hetero} and C_{alkyl} peaks of $[C_8C_1Im][PF_6]$ have only slightly different binding energies than the peaks of the $[dema]^+$ cation. Thus, as for the macroscopic films this means the C 1s peaks of the two cations cannot be deconvoluted. Nevertheless, the qualitative comparison of the C 1s spectra in Figure 5-III reveals a relative increase of the C_{alkyl} peak as compared to the C_{hetero} peak, when increasing the emission angle from 0° to 80°. This observation further supports our interpretation that the post-deposited film of $[C_8C_1Im][PF_6]$ (which contains the octyl chains) covers the [dema][TfO] wetting layer.

As a next step, we heated this layered system from 90 to 550 K with a heating rate of 2 K/min and simultaneously recorded TP-XP spectra in the Ag 3d, F 1s and C 1s regions. The corresponding quantitative analysis of the Ag 3d substrate signal, the F_{CF3} and F_{PF6} signals of the two anions, and the combined C_{Cat} intensity (related to all carbon atoms of the two cations) is depicted in Figure 6c and 6d for 0° and 80° emission, respectively. For comparison, the thermal evolution of pure [dema][TfO] (for a similar experiment, see also Ref. [14f]) and $[C_8C_1Im][PF_6]$[14a,c,18] on Ag(111) are shown in Figure 6a and 6b.

Desorption effects – XPS measurements at 0°

We start with the discussion of the data for 0° emission in Figure 5 (top) and Figure 6c, which provide information on the amount of the individual ions in the mixed film, since self-damping plays only a minor role in this bulk-sensitive geometry. Notably, all transition or desorption temperatures are determined from the inflection points of the corresponding intensities.

Starting from ~200 K, the Ag 3d signal (grey circles) shows a small increase (inflection point at ~235 K), and the F_{PF6} signal (blue diamonds) and the combined cationic C 1s signals (black triangles) decrease. This behaviour indicates the desorption of the $[PF_6]^-$ anion and one of the cations. The F_{CF3} signal (red diamonds) remains constant until much higher temperatures. Since for pure $[C_8C_1Im][PF_6]$ films multilayer desorption occurs only at 405 K,[14a,d,18] we assume that it is $[dema][PF_6]$ which desorbs at this low temperature. The quantitative analysis of the C 1s spectra in Figure 5-V yields a C_{alk}/C_{het} ratio of $7.6:4.4=1.7$, which is very close to the nominal ratio of $7:5=1.4$ for $[C_8C_1Im]^+$ (note that for $[dema]^+$ the nominal ratio would be very different, namely $2:3=0.67$). The observed behaviour

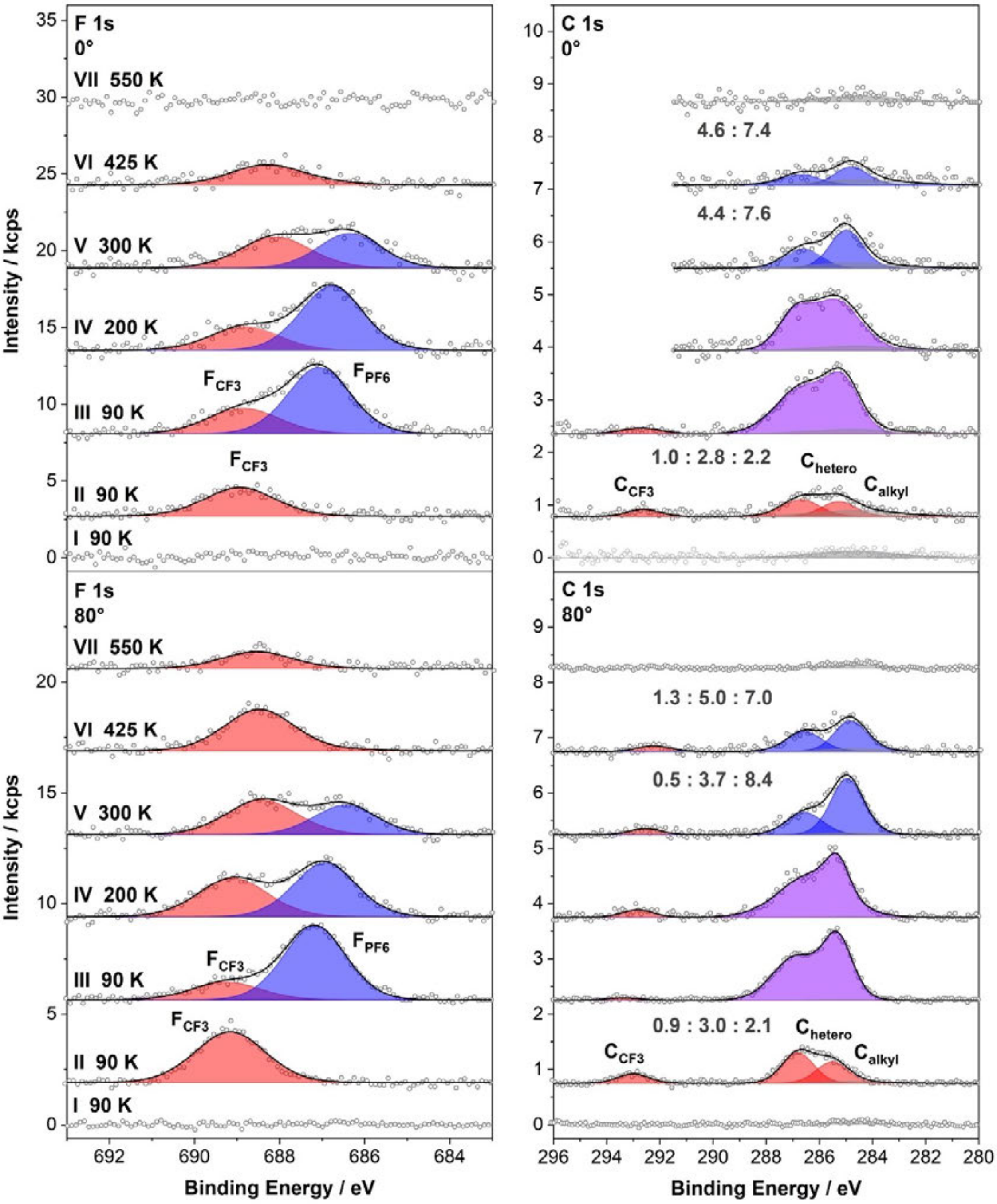

Figure 5. F 1s and C 1s spectra in 0° and 80° emission: **I** clean Ag(111) at ~90 K, **II** 0.5 ML [dema][TfO] at ~90 K, **III** 1 ML [C_8C_1Im][PF_6] on [dema][TfO] at ~90 K, **IV** ion exchange after heating to ~200 K, **V** desorption of [dema][PF_6] after heating to ~300 K, **VI** desorption of [C_8C_1Im][PF_6] after heating to ~425 K with [C_8C_1Im][TfO] remaining on Ag(111), **VII** complete desorption after heating to ~550 K.

indicates complete desorption of [dema]$^+$ cations, with only [C_8C_1Im]$^+$ remaining in the film. The slightly higher ratio than expected is within the uncertainty of the experiment, due to the low signal to noise ratio.

Upon further heating, the F_{PF6} signal starts to further decrease at ~360 K and reaches zero at ~400 K, which indicates desorption of the remaining [PF_6]$^-$ as [C_8C_1Im][PF_6]. The decrease of the total surface coverage is also indicated by the step-like increase of the Ag 3d signal at ~380 K. The multilayer desorption temperature for pure [C_8C_1Im][PF_6] of ~405 K[14a,d,18] is 25 K higher as is evident from comparison to Figure 6b. This lower temperature could indicate that the interaction of [C_8C_1Im][PF_6] with the remaining wetting layer of [C_8C_1Im][TfO] at the IL/Ag(111) interface is less favorable than in films of pure [C_8C_1Im][PF_6], yielding a lower desorption temperature in case of the mixed thin film. Above 410 K, desorption of [C_8C_1Im][PF_6]

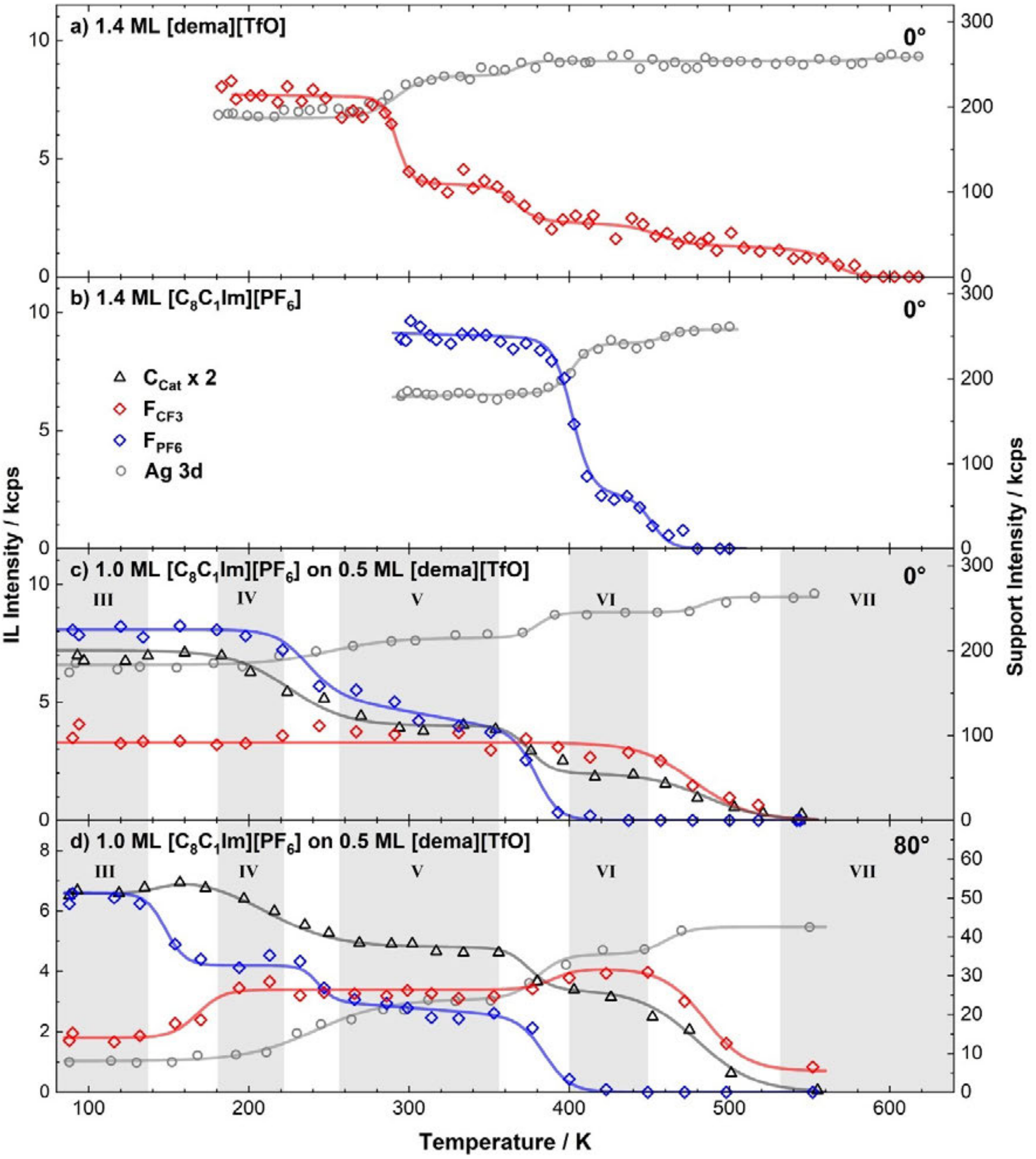

Figure 6. TPXPS on pure and mixed IL thin films on Ag(111): peak intensities related to the $[TfO]^-$ and $[PF_6]^-$ anions (F 1s), the cations (C 1s) and the supporting Ag crystal (Ag 3d). C 1s intensities are multiplied by a factor of two. (a)–(c) 0° and (d) 80° emission, (a) [dema][TfO],[14f] (b) $[C_8C_1Im][PF_6]$,[14a,d,18] (c) and (d) $[C_8C_1Im][PF_6]$ on [dema][TfO]. The films were heated with a heating rate of 2 K/min.

is completed and no $[PF_6]^-$ anions remain on the surface. Based on the previous desorption steps, we expect that above 410 K a new anion-cation combination, i.e. pure $[C_8C_1Im][TfO]$, remains as wetting layer, which is formed by on-surface metathesis at the IL/metal interface. Indeed, the C 1s spectrum of the remaining wetting layer at ~425 K in Figure 5-VI (C_{alk}/C_{het} ratio of 7.4:4.6 = 1.6) is very similar to that of the pure macroscopic film of $[C_8C_1Im][TfO]$ in Figure S1 (C_{alk}/C_{het} ratio of 7.1:4.9 = 1.4); both values are very close to nominal value of 7:5 = 1.4. Again, the slightly higher ratio for the thin film is within the uncertainty of the experiment.

The F_{CF3} signal in 0° emission remains more or less constant from 90 to 440 K, until its subsequent decrease until 550 K indicates the final desorption of the remaining $[C_8C_1Im][TfO]$. This decrease in surface coverage is again also reflected in the step-like increase of the Ag 3d signal at ~480 K. The higher desorption temperature of ~480 K for the remaining $[C_8C_1Im][TfO]$ wetting layer indicates that the adsorption energy of $[C_8C_1Im][TfO]$ on Ag(111) is larger than that of a $[C_8C_1Im][PF_6]$

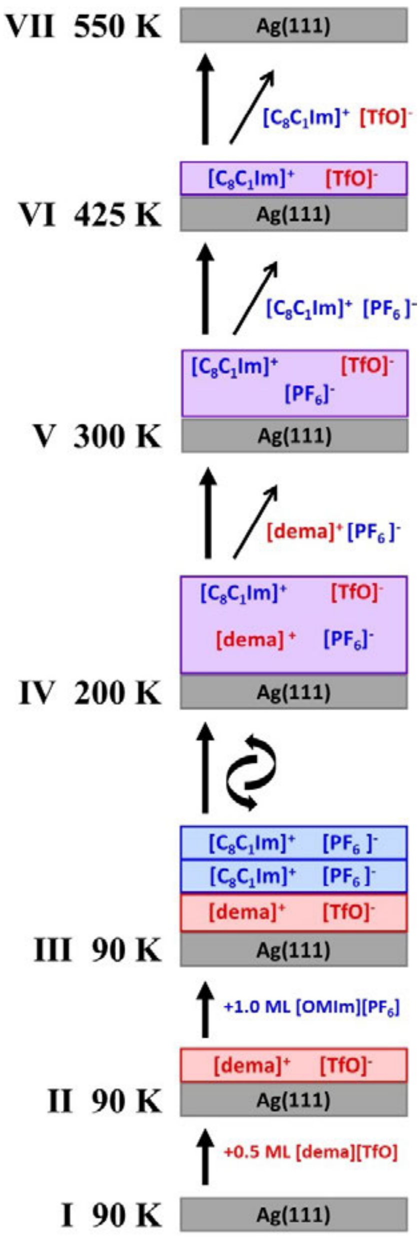

Figure 7. Scheme of the proposed changes in film composition when heating 1 ML [C_8C_1Im][PF_6] on 0.5 ML [dema][TfO] on Ag(111) from 90 to 550 K.

wetting layer on Ag(111), where a desorption temperature of ~445 K is observed (see Figure 6b).[14a,d,18]

At 550 K, the remaining F_{FC3} and C_{Cat} signals have disappeared in 0°, indicating complete desorption of the formed [C_8C_1Im][TfO] from Ag(111) (note that in the very surface-sensitive 80° geometry, remaining traces of decomposition products are detected at the silver surface, see next section). It is interesting to note that neat [dema][TfO] on Ag(111) undergoes significant deprotonation and decomposition at ~215 K and ~350 K, respectively.[14f] However, during the thermal evolution of our mixed thin films, we did not observe a similar [dema][TfO] decomposition at all.

Ion exchange and surface enrichment effects – measurements at 80°

Next, we analyze the thermal evolution of the 80° XPS signals in Figure 6d which provide information on the composition of the topmost layer of the mixed film as a function of temperature. Starting at ~135 K, the F_{PF6} signal (blue diamonds) starts to decrease and simultaneously the F_{CF3} signal (red diamonds) starts to increase, both reaching a plateau at ~200 K. Notably, the corresponding signals did not change in the 0° spectra in Figure 6c, which indicates that none of the respective species is desorbing. We thus propose that between 135 and 200 K, $[TfO]^-$ anions at the IL/Ag(111) interface are exchanged by $[PF_6]^-$ anions and likely are even enriched at the IL/vacuum interface. This conclusion is supported by the analysis of macroscopic mixtures of [dema][TfO] and [C_8C_1Im][PF_6] which indeed show a pronounced preferential enrichment of the $[TfO]^-$ anion over the $[PF_6]^-$ anion (see above). With reference to earlier work on other (purely aprotic) IL mixtures,[14c,d,18] we propose that the driving force for this exchange is a lower surface tension of the resulting film. Furthermore, it is likely that the octyl chain of the $[C_8C_1Im]^+$ cation is also enriched at the IL/vacuum interface as found in our macroscopic mixtures discussed above and as it was reported previously for other systems.[1d,14c,18–19] To further investigate this assumption, the C 1s spectra in 80° at 90 K (black) and 200 K (orange) are compared in Figure S2. In the absence of enrichment effects one might simply expect the C_{alkyl} contribution to decrease going from 90 to 200 K, since at 90 K the mixed film is frozen with the $[C_8C_1Im]^+$ cations fixed at the IL/vacuum interface, but upon melting intermixing of the two ILs occurs. Thus, the outermost surface (as the rest of the film) would then be composed of a homogeneous mixture of both ILs with a reduced C_{alkyl} content compared to the starting point. However, by comparing both spectra in Figure S2, the C_{alkyl} contribution at 200 K stays nearly unchanged. We thus propose that the octyl chains of the $[C_8C_1Im]^+$ cations remain enriched after the first anion exchange process starting from ~135 K. The IL exchange and enrichment of the $[TfO]^-$ anion can also be observed via the increased C_{CF3} signal at 200 K in the C 1s spectrum in Figure S2.

The melting point of bulk [dema][TfO] is 260 K[3a] and the glass transition of [C_8C_1Im][PF_6] occurs at about 195 K.[25] In agreement with the interpretation for other ILs in previous studies,[14c,d,18] we conclude that the phase transition of the IL on top determines the mobility of individual ions in the mixed IL film.

Upon further heating, F_{PF6} shows a next stepwise decrease at ~243 K to a new plateau between 270 and 350 K. The C_{cat} signals also decrease, but over a wider temperature range starting around ~180 K, which is attributed to continuous reorientation effects of the octyl chains at the outer surface.[14c,d] In combination with the 0° data, we attribute this decrease of both signals to the desorption of [dema][PF_6]. The C 1s spectra of the remaining IL at ~300 K (Figure 6-V) shows a C_{alk}/C_{het} ratio of 8.1:3.5 = 2.3 as compared to the nominal ratio of 7:5 = 1.4. This further corroborates the enrichment of octyl chains at the

IL/vacuum interface of the thin film. Notably, the C_{alk}/C_{het} ratio in macroscopic films is 10.0:4.4 = 2.3 for $[C_8C_1Im][PF_6]$ (see Table S1 and Figure S1) and 8.8:4.4 = 2.0 for $[C_8C_1Im][TfO]$ (see Figure S1) in 80°. Together with the conclusions derived from the 0° data, the observed behaviour indicates that between 270 and 350 K the IL film contains only $[C_8C_1Im]^+$ cations with surface-enriched octyl chains (see also results for macroscopic mixtures).

The following stepwise decrease of the F_{PF6} signal at ~385 K occurs similarly to the 0° data, and is due to desorption of $[C_8C_1Im][PF_6]$, leaving only a $[C_8C_1Im][TfO]$ wetting layer at the silver surface. Upon desorption of $[C_8C_1Im][PF_6]$, we also observe a slight increase of the F_{CF3} signal in 80°, which is not visible in 0°. This gain of $[TfO]^-$ at the outer surface is attributed to the fact that in the remaining wetting layer above 385 K, all $[TfO]^-$ anions are necessarily part of the outermost surface layer, whereas below this temperature, also $[PF_6]^-$ anions are present at the IL/vacuum interface. Notably, for the remaining $[C_8C_1Im][TfO]$ wetting layer at ~425 K (Figure 5-VI) at 80° the C_{alk}/C_{het} ratio is 6.8:4.9 = 1.4. This value is very close to the nominal value of 7:5 = 1.4, but is much lower than the value of 2.3 at ~300 K (see above) in Figure 5-V. Possible reasons are loss of order at this elevated temperature due to entropy effects or a different adsorption geometry in the WL (at this temperature).

In line with the 0° data, the decrease of the F_{CF3} signal at ~475 K indicates desorption of $[C_8C_1Im][TfO]$. The minor remaining signal at 550 K could be due to some small amounts of a dissociation product, which is only visible in the very surface sensitive 80° geometry.

As a last point, we want to address the observation that in addition to the discussed changes in peak intensities, we also observe shifts of the F 1s and C 1s peaks upon heating the layered IL film. These shifts are evident in the spectra at 0° (Figure 5, top) but also in the spectra at 80° (Figure 5, bottom). They are assigned to a combination of initial and final state effects as a result of the changing local environment.[14b] From 90 to 200 K, the F_{CF3} and F_{PF6} signals shift to lower binding energy by 0.3 eV, which is attributed to the reorientation and surface enrichment of the alkyl chains at the outermost surface, covering the anions. The shift of the F_{CF3} and F_{PF6} signals by 0.5–0.6 eV to lower binding energy between 200 and 300 K results from the change of the chemical composition of the film due to the desorption of an equivalent of 0.5 ML $[dema][PF_6]$. The same explanation likely holds for the minor shift of all F 1s anion and C 1s cation signals by 0.1–0.2 eV to lower binding energy between 300 and 425 K.

Summary and Conclusions

We investigated the adsorption and thermal evolution of ultrathin mixed films of the protic IL ([dema][TfO]) and the aprotic IL ($[C_8C_1Im][PF_6]$) on Ag(111) by angle-resolved X-ray photoelectron spectroscopy (ARXPS). As first step, we characterized the IL/vacuum interface of ~0.1 mm thick films of various macroscopic mixtures of [dema][TfO] and $[C_8C_1Im][PF_6]$ that serve as a reference for the investigation of the ultrathin films. For each mixture, we find that the $[TfO]^-$ anions and the $[C_8C_1Im]^+$ cations are enriched at the IL/vacuum interface. The latter are also enriched for the neat $[C_8C_1Im][PF_6]$ thin films.

Based on these findings, we then investigated ultrathin mixed IL films. We sequentially deposited 0.5 ML of [dema][TfO] and 1.0 ML $[C_8C_1Im][PF_6]$ on Ag(111) at about 90 K, and heated this film to 550 K while monitoring the film composition by ARXPS. Thereby, bulk-sensitive measurements at 0° allow for determining the overall film composition and changes thereof by selective desorption, while surface-sensitive measurements at 80° provide insight into enrichment and exchange processes at the IL-vacuum and the IL-metal interfaces. Between 135 and 200 K, the exchange of the $[TfO]^-$ anions at the Ag(111) surface by $[PF_6]^-$ anions occurs, yielding an enrichment of the $[TfO]^-$ anions at the IL/vacuum interface together with the $[C_8C_1Im]^+$ cations. Subsequently, $[dema][PF_6]$ selectively desorbs at ~235 K, and $[C_8C_1Im][PF_6]$ at ~380 K. Hereby, a wetting layer of pure $[C_8C_1Im][TfO]$ forms by on-surface metathesis at the IL/metal interface. Finally, this $[C_8C_1Im][TfO]$ layer desorbs more or less completely at ~480 K leaving the Ag(111) surface behind. The here reported enrichment, exchange and desorption processes leading to the on-surface metathesis of ultrathin IL layers on solid supports might open a novel route for the on-surfaces synthesis of new ultrathin coatings with ILs, which cannot be prepared by physical vapor deposition.

Experimental Section

The synthesis and characterization of [dema][TfO] was described in Ref. [54] $[C_8C_1Im][PF_6]$ was purchased from Sigma-Aldrich (purity >95%). Both ILs were carefully degassed in UHV before depositing them via physical vapor deposition (PVD) in UHV from a modified Knudsen cell with a boron nitride crucible. The details of the Knudsen cell have been published in Ref.[14c] [dema][TfO] and $[C_8C_1Im][PF_6]$ were deposited at cell temperatures of 345 and 448 K, respectively. The IL flux was monitored with a quartz crystal microbalance before and after deposition to ensure a constant evaporation rate. In former studies, [dema][TfO][14f] and $[C_8C_1Im][PF_6]$[14a,d,18] showed no signs of decomposition upon deposition on Ag(111) at 90 K.

The Ag(111) single crystal with circular shape and diameter of 15 mm was purchased from MaTeck (purity 99.999%, polished with an alignment better than 0.1° to the (111) plane). It was cleaned by short heating to >500 K and subsequent Ar^+ sputtering (600 V, 8 μA, 30 min) at RT followed by annealing (800 K, 10 min). The temperature was measured using a type K thermocouple put into a 0.5 mm wide pinhole of the single crystal, with an absolute accuracy of ±20 K (500 K) and a reproducibility of ±2 K.

The UHV system for angle-resolved X-ray photoelectron spectroscopy (ARXPS) contains a non-monochromated Al Kα X-ray source (SPECS XR 50, 1486.6 eV, 240 W) and a hemispherical electron analyzer (VG SCIENTA R3000) (described in more detail in Ref.[14e]). A pass energy of 100 eV was applied for all spectra, yielding an overall energy resolution of about 0.9 eV.[14e] The spectra were quantitatively evaluated using CasaXPS V2.3.16Dev6. For the Ag 3d spectra, a Shirley background[26] was subtracted and peaks were fitted with Lorentzian line shapes. For the F 1s, C 1s, O 1s, S 2p and N 1s regions, linear backgrounds were subtracted and the peaks were fitted with Voigt profiles (30% Lorentzian contribution). For the macroscopic $[C_8C_1Im][PF_6]$ and $[C_8C_1Im][TfO]$ films, the XPS binding energy (BE) scale was calibrated by setting C_{alkyl} peak to 285.0 eV,[27] which yielded a BE of F_{CF3} peak of the $[TfO]^-$ anion of 688.5 eV.[17] XP spectra of the macroscopic film of [dema][TfO] were referenced to this value of F_{CF3} at 688.5 eV.[17] Furthermore, all macroscopic mixtures of [dema][TfO] and $[C_8C_1Im][PF_6]$ were referenced to C_{alkyl} at 285.0 eV.[27] The spectra of ultrathin films were referenced to the Fermi edge yielding 368.20 eV for Ag $3d_{5/2}$. In agreement with literature,[14b–e,17b,c,18] we fitted the C 1s components related to the $[dema]^+$ and $[C_8C_1Im]^+$ cations with two contributions, C_{hetero} for the carbon atoms directly bonded to a nitrogen (hetero) atom, and C_{alkyl} for the alkyl carbon atoms further away from the central nitrogen atom. In addition, we applied a constraint for peak widths as used before: $\mathrm{fwhm}(C_{hetero}) = 1.11 \cdot \mathrm{fwhm}(C_{alkyl})$.[14b–e,18] Furthermore, we subtracted a residual carbon contamination signal that could not be removed even after repeated cleaning cycles.

The coverage of [dema][TfO] and $[C_8C_1Im][PF_6]$ on Ag(111) was determined by measuring the attenuation of the Ag 3d substrate signal at an emission angle of $\vartheta = 0°$ according to Lambert-Beer's Law (Eq. (1)), where d is the film thickness, ϑ is the emission angle, λ is the mean free path, I_0 and I_d are the intensity of the clean and IL covered substrate signal, respectively. The interface composition was analysed by comparing 0° and 80° data. By using Kα radiation, the information depth (ID) at an emission angle of $\vartheta = 0°$ is 7–9 nm (depending on the kinetic energy). At $\vartheta = 80°$, the ID reduces to 1–1.5 nm, which means that only the topmost surface layers are probed. The ID is defined as 3 times the inelastic mean free path (λ) of an Ag 3d electron (~1.1 keV) and is 2.5 nm in IL films.[14a,c–e,18]

$$\frac{I_d}{I_0} = e^{-\frac{d}{\lambda \times \cos\vartheta}} \tag{1}$$

We use the definition of a monolayer (1 ML) of IL of a bilayer of cation and anion irrespective of their relative arrangement. The monolayer height h of [dema][TfO] and $[C_8C_1Im][PF_6]$ was calculated from the respective molecular volume based on density values ρ from literature as described previously.[14a,28] We obtain for $[C_8C_1Im][PF_6]$ $h = 0.77$ nm ($\rho = 1.23$ g/cm^3)[23] and for [dema][TfO] $h = 0.67$ nm ($\rho = 1.29$ g/cm^3).[24]

Acknowledgements

S.M., M.L. and H.-P.S. thank the European Research Council (ERC) for support through an Advanced Investigator Grant (ILID 693398) to HPS, and the DFG for support through Collaborative Research Center (CRC)/Sonderforschungsbereich (SFB) 1452. Open Access funding enabled and organized by Projekt DEAL.

Conflict of Interest

The authors declare no conflict of interest.

Data Availability Statement

The data that support the findings of this study are available from the corresponding author upon reasonable request.

Keywords: catalysis · ionic liquids · on-surface metathesis · ultra-thin films · X-ray photoelectron spectroscopy

[1] a) T. Welton, *Chem. Rev.* **1999**, *99*, 2071–2084; b) K. Binnemans, *Chem. Rev.* **2005**, *105*, 4148–4204; c) P. Wasserscheid, T. Welton in: *Ionic Liquids in Synthesis*, *Second Edition* (Eds: P. Wasserscheid, T. Welton), Wiley-VCH Verlag GmbH & Co. KGaA, **2007**; d) K. R. J. Lovelock, I. J. Villar-Garcia, F. Maier, H.-P. Steinrück, P. Licence, *Chem. Rev.* **2010**, *110*, 5158–5190; e) C. Kolbeck, J. Lehmann, K. R. J. Lovelock, T. Cremer, N. Paape, P. Wasserscheid, A. P. Fröba, F. Maier, H. P. Steinrück, *J. Phys. Chem. B.* **2010**, *114*, 17025–17036; f) H.-P. Steinrück, J. Libuda, P. Wasserscheid, T. Cremer, C. Kolbeck, M. Laurin, F. Maier, M. Sobota, P. S. Schulz, M. Stark, *Adv. Mater.* **2011**, *23*, 2571–2587; g) R. Hayes, G. G. Warr, R. Atkin, *Chem. Rev.* **2015**, *115*, 6357–6426.

[2] a) A. Lewandowski, A. Świderska-Mocek, *J. Power Sources* **2009**, *194*, 601–609; b) T. Meng, K.-H. Young, D. F. Wong, J. Nei, *Batteries* **2017**, *3*, 4; c) Q. Yang, Z. Zhang, X.-G. Sun, Y.-S. Hu, H. Xing, S. Dai, *Chem. Soc. Rev.* **2018**, *47*, 2020–2064; d) G. Yang, Y. Song, Q. Wang, L. Zhang, L. Deng, *Mater. Des.* **2020**, *190*, 108563.

[3] a) H. Nakamoto, M. Watanabe, *Chem. Commun.* **2007**, 2539–2541; b) S.-Y. Lee, A. Ogawa, M. Kanno, H. Nakamoto, T. Yasuda, M. Watanabe, *J. Am. Chem. Soc.* **2010**, *132*, 9764–9773; c) T. Yasuda, M. Watanabe, *MRS Bull.* **2013**, *38*, 560–566; d) T. L. Greaves, C. J. Drummond, *Chem. Rev.* **2015**, *115*, 11379–11448.

[4] a) G. Poonam, R. Singh, in: *Applications of Nanotechnology for Green Synthesis* (Eds.: Inamuddin, A. M. Asiri), Springer, Cham, **2020**, p. 41–62; b) S. T. Handy, X. Zhang, *Org. Lett.* **2001**, *3*, 233–236; c) A. D. Sawant, D. G. Raut, N. B. Darvatkar, M. M. Salunkhe, *Green Chem. Lett. Rev.* **2011**, *4*, 41–54.

[5] a) S. Wegner, C. Janiak, in: *Ionic Liquids II* (Eds.: B. Kirchner, E. Perlt), Springer, Cham, **2018**, pp. 153–184; b) K. Richter, P. Campbell, T. Baecker, A. Schimitzek, D. Yaprak, A.-V. Mudring, *Phys. Status Solidi B* **2013**, *250*, 1152–1164; c) T. Sasaki, T. Uematsu, T. Tsuda, S. Kuwabata, *Electrochemistry* **2018**, *86*, 223–225; d) T. Tsuda, T. Kurihara, Y. Hoshino, T. Kiyama, K.-i. Okazaki, T. Torimoto, S. Kuwabata, *Electrochemistry* **2009**, *77*, 693–695.

[6] a) P. Wasserscheid, W. Keim, *Angew. Chem. Int. Ed.* **2000**, *39*, 3772–3789; *Angew. Chem.* **2000**, *112*, 3926–3945; b) S. Breitenlechner, M. Fleck, T. E. Müller, A. Suppan, *J. Mol. Catal. A* **2004**, *214*, 175–179; c) A. Riisager, R. Fehrmann, S. Flicker, R. van Hal, M. Haumann, P. Wasserscheid, *Angew. Chem. Int. Ed.* **2005**, *44*, 815–819; *Angew. Chem.* **2005**, *117*, 826–830; d) U. Kernchen, B. Etzold, W. Korth, A. Jess, *Chem. Eng. Technol.* **2007**, *30*, 985–994; e) P. Virtanen, T. Salmi, J.-P. Mikkola, *Ind. Eng. Chem. Res.* **2009**, *48*, 10335–10342; f) M. Haumann, A. Schönweiz, H. Breitzke, G. Buntkowsky, S. Werner, N. Szesni, *Chem. Eng. Technol.* **2012**, *35*, 1421–1426.

[7] a) K. R. J. Lovelock, *R. Soc. Open Sci.* **2017**, *4*, 171223; b) M. J. Earle, J. M. S. S. Esperança, M. A. Gilea, J. N. Canongia Lopes, L. P. N. Rebelo, J. W. Magee, K. R. Seddon, J. A. Widegren, *Nature* **2006**, *439*, 831–834; c) S. Ravula, N. Larm, M. A. Mottaleb, M. Heitz, G. Baker, *Chem. Eng.* **2019**, *3*, 1–12.

[8] a) Y. Cao, T. Mu, *Ind. Eng. Chem. Res.* **2014**, *53*, 8651–8664; b) C. Maton, N. De Vos, C. V. Stevens, *Chem. Soc. Rev.* **2013**, *42*, 5963–5977; c) Y. Huang, Z. Chen, J. M. Crosthwaite, S. N. V. K. Aki, J. F. Brennecke, *J. Chem. Thermodyn.* **2021**, *161*, 106560; d) C. Cassity, A. Mirjafari, N. Mobarrez, K. Strickland, R. O'Brien, J. Davis, *Chem. Commun.* **2013**, *49*, 7590–7592.

[9] a) K. R. Seddon, *Nat. Mater.* **2003**, *2*, 363–365; b) N. V. Plechkova, K. R. Seddon, *Chem. Soc. Rev.* **2008**, *37*, 123–150.

[10] a) O. Bartlewicz, I. Dąbek, A. Szymańska, H. Maciejewski, *Catalysts* **2020**, *10*, 1227; b) W. Korth, A. Jess, in: *Supported Ionic Liquids* (Eds.: F. Rasmus, A. Riisager, M. Haumann), Wiley-VCH Verlag GmbH & Co. KGaA, **2014**, p. 279–306.

[11] a) S. F. Miller, H. B. Friedrich, C. W. Holzapfel, *ChemCatChem* **2012**, *4*, 1337–1344; b) F. Schwab, N. Weidler, M. Lucas, P. Claus, *Chem. Commun.* **2014**, *50*, 10406–10408; c) G.-R. Zhang, M. Munoz, B. J. M. Etzold, *Angew. Chem. Int. Ed.* **2016**, *55*, 2257–2261; *Angew. Chem.* **2016**, *128*, 2298–2302; d) N. C. Antonels, R. Meijboom, *Catal. Commun.* **2014**, *57*, 148–152.

[12] a) J. K. Smith, in: *Encyclopedia of Catalysis* (Ed.: I. Horáth), John Wiley & Sons, Inc., **2002**; b) J. N. Armor, *Catal. Today* **2011**, *163*, 3–9.

[13] a) C. Austen Angell, Y. Ansari, Z. Zhao, *Faraday Discuss.* **2012**, *154*, 9–27; b) Z. Lei, B. Chen, K. Yoon-Mo, D. R. MacFarlane, *Chem. Rev.* **2017**, *117*, 6633–6635.

[14] a) M. Lexow, F. Maier, H.-P. Steinrück, *Adv. Phys.* **2020**, *5*, 1761266; b) T. Cremer, M. Stark, A. Deyko, H. P. Steinrück, F. Maier, *Langmuir* **2011**, *27*, 3662–3671; c) M. Lexow, B. S. J. Heller, F. Maier, H.-P. Steinrück, *ChemPhysChem* **2018**, *19*, 2978–2984; d) M. Lexow, B. S. J. Heller, G. Partl, R. G. Bhuin, F. Maier, H.-P. Steinrück, *Langmuir* **2019**, *35*, 398–405; e) M. Lexow, T. Talwar, B. S. J. Heller, B. May, R. G. Bhuin, F. Maier, H.-P. Steinrück, *Phys. Chem. Chem. Phys.* **2018**, *20*, 12929–12938; f) S. Massicot, T. Sasaki, M. Lexow, S. Shin, F. Maier, S. Kuwabata, H.-P. Steinrück, *Langmuir* **2021**, *37*, 11552–11560; g) B. Uhl, H. Huang, D. Alwast, F. Buchner, R. J. Behm, *Phys. Chem. Chem. Phys.* **2015**, *17*, 23816–2332; h) F. Buchner, K. Forster-Tonigold, B. Uhl, N. Wagner, H. Farkhondeh, A. Groß, R. J. Behm, *ACS Nano* **2013**, *7*, 7773–7784.

[15] H. Srour, H. Rouault, C. C. Santini, Y. Chauvin, *Green Chem.* **2013**, *15*, 1341–1347.

[16] B. Uhl, T. Cremer, M. Roos, F. Maier, H.-P. Steinrück, R. J. Behm, *Phys. Chem. Chem. Phys.* **2013**, *15*, 17295–17302.

[17] a) R. M. Fogarty, R. P. Matthews, C. R. Ashworth, A. Brandt-Talbot, R. G. Palgrave, R. A. Bourne, T. V. Hoogerstraete, P. A. Hunt, K. R. J. Lovelock, *J. Chem. Phys.* **2018**, *148*, 193817; b) R. M. Fogarty, R. G. Palgrave, R. A. Bourne, K. Handrup, I. J. Villar-Garcia, D. J. Payne, P. A. Hunt, K. R. J. Lovelock, *Phys. Chem. Chem. Phys.* **2019**, *21*, 18893–18910; c) R. M. Fogarty, R. Rowe, R. P. Matthews, M. T. Clough, C. R. Ashworth, A. Brandt, P. J. Corbett, R. G. Palgrave, E. F. Smith, R. A. Bourne, T. W. Chamberlain, P. B. J. Thompson, P. A. Hunt, K. R. J. Lovelock, *Faraday Discuss.* **2018**, *206*, 183–201.

[18] M. Lexow, S. Massicot, F. Maier, H.-P. Steinrück, *J. Phys. Chem. C* **2019**, *123*, 29708–29721.

[19] K. R. J. Lovelock, *Phys. Chem. Chem. Phys.* **2012**, *14*, 5071–5089.

[20] a) B. Heller, C. Kolbeck, I. Niedermaier, S. Dommer, J. Schatz, P. Hunt, F. Maier, H.-P. Steinrück, *ChemPhysChem* **2018**, *19*, 1733–1745; b) B. Heller, M. Lexow, F. Greco, S. Shin, G. J. Partl, F. Maier, H.-P. Steinrück, *Chem. Eur. J.* **2019**, *26*, 1117–1126.

[21] M. G. Freire, P. J. Carvalho, A. M. Fernandes, I. M. Marrucho, A. J. Queimada, J. A. P. Coutinho, *J. Colloid Interface Sci.* **2007**, *314*, 621–630.

[22] W. Martino, J. F. de la Mora, Y. Yoshida, G. Saito, J. Wilkes, *Green Chem.* **2006**, *8*, 390–397.

[23] a) A. Deyko, K. Lovelock, J.-A. Corfield, A. Taylor, P. Gooden, I. Villar-Garcia, P. Licence, R. Jones, V. Krasovskiy, E. Chernikova, L. Kustov, *Phys. Chem. Chem. Phys.* **2009**, *11*, 8544–8555; b) S. Dzyuba, R. Bartsch, *ChemPhysChem* **2002**, *3*, 161–166; c) Z. Gu, J. F. Brennecke, *J. Chem. Eng. Data* **2002**, *47*, 339–345.

[24] a) M. Atilhan, B. Anaya, R. Ullah, L. T. Costa, S. Aparicio, *J. Phys. Chem. C* **2016**, *120*, 17829–17844; b) M. S. Miran, T. Yasuda, R. Tatara, M. Abu Bin Hasan Susan, M. Watanabe, *Faraday Discuss.* **2018**, *206*, 353–364.

[25] J. G. Huddleston, A. E. Visser, W. M. Reichert, H. D. Willauer, G. A. Broker, R. D. Rogers, *Green Chem.* **2001**, *3*, 156–164.

[26] D. A. Shirley, *Phys. Rev. B* **1972**, *5*, 4709–4714.

[27] T. Cremer, C. Kolbeck, K. Lovelock, N. Paape, R. Wölfel, P. Schulz, P. Wasserscheid, H. Weber, J. Thar, B. Kirchner, F. Maier, H.-P. Steinrück, *Chem. Eur. J.* **2010**, *16*, 9018–9033.

[28] T. Cremer, M. Killian, J. M. Gottfried, N. Paape, P. Wasserscheid, F. Maier, H.-P. Steinrück, *ChemPhysChem* **2008**, *9*, 2185–2190.

Manuscript received: January 18, 2022
Accepted manuscript online: April 1, 2022
Version of record online: April 5, 2022

Chemistry–A European Journal

Supporting Information

On-Surface Metathesis of an Ionic Liquid on Ag(111)

Stephen Massicot, Tomoya Sasaki, Matthias Lexow, Florian Maier, Susumu Kuwabata, and Hans-Peter Steinrück*

Table S1: Film composition as measured by XPS at 0° and 80° of macroscopic mixtures of [dema][TfO] and [C$_8$C$_1$Im][PF$_6$] at RT; for [dema][TfO] contents of $x_i = 1.00$ (neat [dema][TfO]$^{\#}$, top), $x_i = 0.85$ (ratio = 5.7:1), $x_i = 0.50$ (1:1), $x_i = 0.20$ (1:4), $x_i = 0.09$ (1:10), and $x_i = 0.00$ (neat [C$_8$C$_1$Im][PF$_6$]$^{\#}$, bottom). Nominal content values are derived from the weighted masses preparing the mixtures.

$^{\#}$ note that data for neat [dema][TfO] and [C$_8$C$_1$Im][PF$_6$] are taken from refs. [1] and [2], respectively:
[1] Massicot *et al. Langmuir* **2021**, 37, 11552-11560,
[2] Lexow *et al. ChemPhysChem* **2018**, 19, 2978-2984.

x_i=1.00 (1:0)	P_{PF6}	S_{SO3}	C_{CF3}	C_{hetero}	C_{alkyl}	N_{dema}	N_{C8C1Im}	O_{SO3}	F_{CF3}	F_{PF6}
Nominal content	0	1	1	3	2	1	0	3	3	0
0°	0	1.0	0.9	3.1	2.0	1.1	0	3.0	3.0	0
80°	0	1.1	1.0	3.1	1.9	1.0	0	2.7	3.3	0

x_i=0.85 (5.7:1)	P_{PF6}	S_{SO3}	C_{CF3}	C_{cat}	N_{cat}	O_{SO3}	F_{CF3}	F_{PF6}
Nominal content	0.15	0.85	0.85	6.1	1.2	2.5	2.5	0.9
0°	0.17	0.88	0.81	6.1	1.2	2.5	2.6	0.8
80°	0.12	0.81	0.82	6.7	1.1	2.3	2.7	0.6

x_i=0.50 (1:1)	P_{PF6}	S_{SO3}	C_{CF3}	C_{cat}	N_{cat}	O_{SO3}	F_{CF3}	F_{PF6}
Nominal content	0.49	0.51	0.51	8.4	1.5	1.5	1.5	2.9
0°	0.51	0.51	0.54	8.8	1.4	1.5	1.5	2.6
80°	0.39	0.57	0.60	9.7	1.2	1.5	1.8	1.7

x_i=0.20 (1:4)	P_{PF6}	S_{SO3}	C_{CF3}	C_{cat}	N_{cat}	O_{SO3}	F_{CF3}	F_{PF6}
Nominal content	0.80	0.20	0.20	10.6	1.8	0.60	0.60	4.8
0°	0.84	0.23	0.31	11.0	1.7	0.66	0.87	4.3
80°	0.66	0.31	0.34	12.8	1.3	0.86	1.14	2.5

x_i=0.09 (1:10)	P_{PF6}	S_{SO3}	C_{CF3}	C_{cat}	N_{cat}	O_{SO3}	F_{CF3}	F_{PF6}
Nominal content	0.91	0.09	0.09	11.4	1.9	0.27	0.27	5.5
0°	0.83	0.11	0.22	11.7	1.8	0.33	0.53	4.9
80°	0.77	0.17	0.27	13.4	1.4	0.48	0.73	3.2

x_i=0.00 (0:1)	P_{PF6}	S_{SO3}	C_{CF3}	C_{hetero}	C_{alkyl}	N_{dema}	N_{C8C1Im}	O_{SO3}	F_{CF3}	F_{PF6}
Nominal content	1	0	0	5	7	0	2	0	0	6
0°	1.0	0.0	0.0	5.1	7.2	0.0	1.9	0.0	0.0	5.7
80°	1.0	0.0	0.0	4.4	10.0	0.0	1.5	0.0	0.0	4.1

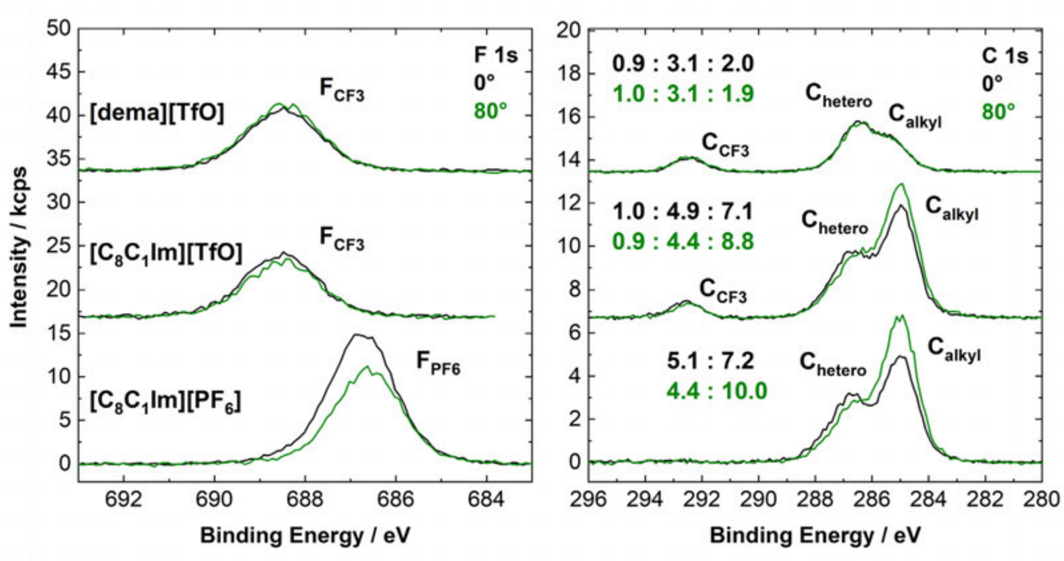

Figure S1: F 1s and C 1s Spectra in 0° and 80° emission of macroscopic samples at RT: [dema][TfO] (top), [C_8C_1Im][TfO] (middle) and [C_8C_1Im][PF_6] (bottom).

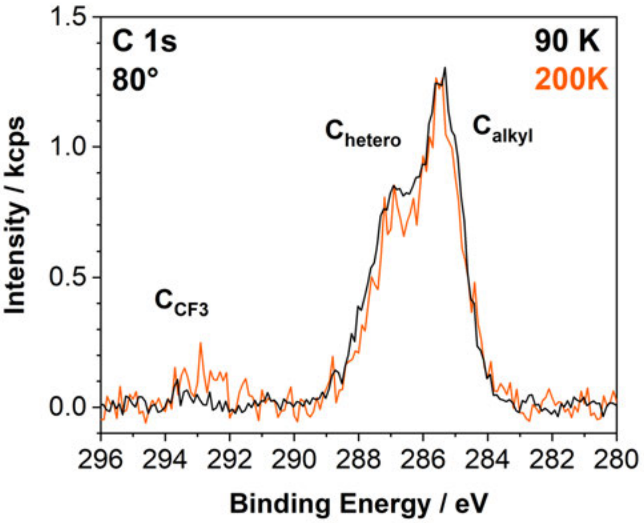

Figure S2: C 1s Spectra in 80° of sequentially deposited 0.5 ML [dema][TfO] and 1.0 ML [C_8C_1Im][PF_6] on Ag (111) at 90 K (black) and 200 K (orange).

[P3]

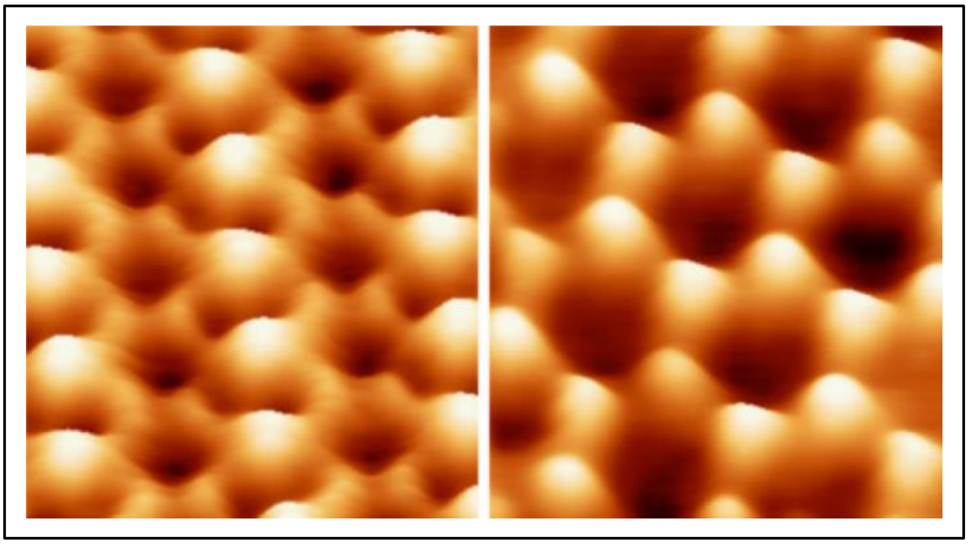

Structure and Reactivity of the Ionic Liquid [C_1C_1Im][Tf_2N] on Cu(111).

R. Adhikari, S. Massicot, L. Fromm, A. Gezmis, M. Meusel, A. Bayer, S. Jaekel, F. Maier, A. Görling, H.-P. Steinrück.

Top Catal **2023**, 66, 1178-1195

DOI: 10.1007/s11244-023-01801-y

Topics in Catalysis (2023) 66:1178–1195
https://doi.org/10.1007/s11244-023-01801-y

ORIGINAL PAPER

Structure and Reactivity of the Ionic Liquid $[C_1C_1Im][Tf_2N]$ on Cu(111)

Rajan Adhikari[1] · Stephen Massicot[1] · Lukas Fromm[2] · Timo Talwar[1] · Afra Gezmis[1] · Manuel Meusel[1] · Andreas Bayer[1] · Simon Jaekel[1] · Florian Maier[1] · Andreas Görling[2] · Hans-Peter Steinrück[1]

Accepted: 2 March 2023 / Published online: 11 April 2023

Abstract

We studied the adsorption and reaction behavior of the ionic liquid (IL) 1,3-dimethylimidazolium bis[(trifluoromethyl)sulfonyl]imide ($[C_1C_1Im][Tf_2N]$) on Cu(111) using non-contact atomic force microscopy (nc-AFM), scanning tunneling microscopy (STM), and angle-resolved X-ray photoelectron spectroscopy (ARXPS) in ultrahigh vacuum as a function of temperature, supported by density-functional theory (DFT) calculations. Our nc-AFM results for sub-monolayer IL films show that at 200 K, the IL self-assembles into highly ordered islands, with cations and anions arranged next to each other in a checkerboard–type phase. After extended annealing at 300 K, the structure transforms first to a hexagonal phase and then to a porous honeycomb phase. Simultaneously, many small, disordered islands are formed. Complementary ARXPS reveals no IL desorption until 300 K. However, a significant fraction of the IL is converted to a new species as deduced from new, strongly shifted peaks that develop in the XP spectra at around 275 K and grow with annealing time at 300 K. We correlate the remaining unshifted peaks to the ordered phases observed in nc-AFM and the shifted peaks to decomposition products, which appear as disordered islands in nc-AFM and STM. Upon further heating to 360 K, about 50% of the anions or their decomposition products desorb from the surface, while cation-related fragments mostly remain on the surface. From DFT, we obtain additional information on the structure of the ordered phases and the interaction of the IL with the substrate.

Keywords $[C_1C_1Im][Tf_2N]$ · Ionic liquids · Cu(111) · Non-contact-atomic force microscopy (nc-AFM) · Scanning tunneling microscopy (STM) · Angle-resolved X-ray photoelectron spectroscopy (ARXPS) · Density functional theory (DFT) calculations

1 Introduction

Ionic liquids (ILs) are composed of molecular ions and have attracted a lot of attention recently because of their unusual properties, such as a wide temperature range of liquid phase, electrochemical stability, very low vapor pressure at room temperature (RT), good ionic heat capacities, and potential as green solvents [1–5]. These properties render them good candidates for applications in a variety of fields [2, 6]. Examples are thermal storage [7, 8], electrochemical applications [9], homogeneous catalysis [1, 2, 10, 11], dye sensitized solar cells [12], lubrication [13–15], fuel cell [16], nuclear energy utilization [17], biomedical sphere [18], and even telescope construction [19] to name only the few. Furthermore, by tailoring their properties with different functional groups one obtains task–specific reaction media [4, 20]. Their specific properties are governed by a complex combination of van der Waals, (unscreened) Coulomb, dipole, and hydrogen bonding interactions, which seldom occur together in other materials [21].

ILs are particularly interesting for catalytic applications. Two concepts have been developed and introduced, that is, the supported ionic liquid phase (SILP) approach [10, 22–24] and the solid catalyst with ionic liquid layer (SCILL) approach [24, 25]. In SILP, an IL film containing dissolved transition metal complexes is coated onto a porous support, whereas in SCILL a thin IL film is coated onto the active metal surface of a heterogeneous catalyst [24]. Both

---

Rajan Adhikari and Stephen Massicot shared first-authorship.

✉ Hans-Peter Steinrück
hans-peter.steinrueck@fau.de

[1] Lehrstuhl für Physikalische Chemie II, Friedrich–Alexander–Universität Erlangen–Nürnberg, Egerlandstr. 3, 91058 Erlangen, Germany

[2] Lehrstuhl für Theoretische Chemie, Friedrich–Alexander–Universität Erlangen–Nürnberg, Egerlandstr. 3, 91058 Erlangen, Germany

SILP and SCILL systems are already in use commercially [26–28]. For example, Petronas employs a SILP system to capture mercury (Hg) from natural gas [29], while Clariant employs SCILL systems for the selective hydrogenation of unsaturated hydrocarbons [30].

In many applications, the interface of the IL with its environment, that is, IL–support [31, 32] and/or IL–vacuum(gas) interfaces, plays a crucial role [33]. The ultimate design, precise control, and understanding of the structural features of ILs at interfaces open the door to manifold applications in batteries, nanoscale tribology, electrical double–layer capacitors, and other fields. In energy storage devices such as lithium ion batteries, a thorough understanding of ionic behavior at the interface is required to understand the formation of the solid–electrolyte interphase. The noble metals gold, silver and copper are essential materials for such energy storage devices. Cu has been used as a current collector in lithium and sodium ion batteries (see ref [34] and references therein). Thus, understanding the nature of the interaction between an IL and the substrate promises a more controlled design and use of ILs for particular applications. This demand resulted in studies of IL–metal interfaces both in situ, under electrochemical conditions [31, 32], and ex situ, under ultraclean ultrahigh vacuum (UHV) conditions [35, 36]. Detailed information on the IL/substrate interface, obtained mostly by angle resolved X–ray photoelectron spectroscopy (ARXPS) and scanning tunneling microscopy (STM) on well–defined single crystal surfaces in UHV, can be found in a review article by Lexow et al. (see Ref. [36] and references therein), and in a number of earlier reviews, which also include data from ultraviolet photoelectron spectroscopy (UPS), inverse photoelectron spectroscopy (IPES), in addition to ARXPS (see Refs. [11, 35, 37–39] and references therein).

Most of the studies by ARXPS and/or STM have been done on inert single crystal surfaces such as Au(111) or Ag(111) [36, 40–42]. In nearly all cases, the formation of a wetting layer was observed, with both anions and cations adsorbed in a checkerboard–like structure in direct contact to the surface. This structure was initially derived from ARXPS, but was later on confirmed by molecularly resolved STM measurements at temperatures well below room temperature. The detailed structure and also stable imaging temperature thereby depended on the particular IL and the substrate. Quite recently, the experimental methods were complemented by non-contact atomic force microscopy (nc-AFM). Meusel et al. demonstrated for [C_1C_1Im][Tf_2N] on Au(111) that with variable temperature nc-AFM highly ordered structures can even be resolved at room temperature and above [43, 44]. At low temperature, they observed the coexistence of a stripe phase and a hexagonal phase—with single molecule thickness—for the first layer on the surface. In this previous study, the individual anions in the wetting layer were identified from their larger height as compared to the flat-lying (and thus invisible) cations [43]. A stripe phase was also resolved for coverages in the multilayer range, where the growth proceeds through bilayer formation, demonstrating the layer-by-layer 2D growth of this IL on the very inert Au(111) surface [44]. Moreover, for certain substrate temperatures, upon deposition metastable 3D droplets were initially formed on top of the wetting layer, which converted into the 2D bilayer structure over time [45].

The aim of this study was to move on to the more reactive Cu(111) surface and investigate the adsorption, thermal evolution and possible reactions of [C_1C_1Im][Tf_2N] on this surface in order to determine potential differences to the Au(111) surface. This topic also appeared quite interesting to us, since in literature there are two studies for related systems, that is, by Biedron et al. for [C_8C_1Im][Tf_2N] on Cu(100) [46] and by Uhl et al. for [BMP][Tf_2N] on Cu(111) [47]. Interestingly, the results seemed to be in conflict with each other, but based on our study a reinterpretation of the data on Cu(111) leads to a consistent picture. We performed our study using in situ ARXPS (100–800 K) and variable temperature nc-AFM/STM (100–350 K). The scheme at the top of Table 1 shows the chemical and molecular structure of [C_1C_1Im][Tf_2N]. The nc-AFM/STM studies with sub–molecular resolution were performed for coverages around 0.15 monolayer (ML) of ion pairs, which corresponds to 30% of a full wetting layer (= 0.30 WL) of [C_1C_1Im][Tf_2N] on Cu(111). To obtain complementary information, ARXPS measurements were performed for 0.3 and 0.5 ML. In addition, DFT calculations provide complementary insight into the structure and the bonding situation of the IL adlayer. To the best of our knowledge, this is the first time that individual ion pairs have been resolved and identified in an IL adlayer on Cu(111) using nc-AFM.

2 Experimental

The ionic liquid [C_1C_1Im][Tf_2N] was either bought from IoLiTec (used in the XPS measurements) or synthesized under ultra-clean conditions described in a previous publication [48] (used in the nc-AFM/STM measurements). It was thoroughly degassed under ultrahigh vacuum (UHV) prior to deposition to remove volatile impurities. In the literature, the cation [C_1C_1Im]$^+$ is also known as [MMIm]$^+$ [49], and the anion [Tf_2N]$^-$ as [NTf_2]$^-$ [50] or [TFSA]$^-$ [51]. The scanning probe microscopy (SPM) and the ARXPS experiments were performed in two separate UHV systems. In both, the

Table 1 Different structures and the corresponding unit cell parameters and unit cell areas, as obtained from nc-AFM and STM

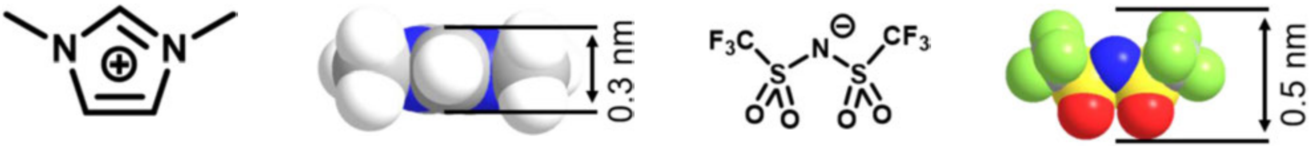

Structure	Unit cell parameters	Matrix notation	Unit cell area [nm^2]	Ion pair density (ρ) [ion pairs/nm^2]
Checkerboard–type (nc-AFM)	$\lvert\vec{a}\rvert=1.90\pm0.08$ nm $\lvert\vec{b}\rvert=0.90\pm0.05$ nm $\gamma=90\pm3°$	$\begin{bmatrix}6&2\\-3&4\end{bmatrix}$ $\gamma=92.2°$	1.71	1.17
Hexagonal–type (nc-AFM)	$\lvert\vec{a}\rvert=\lvert\vec{b}\rvert=2.35\pm0.08$ nm $\gamma=60\pm4°$	$\begin{bmatrix}8&2\\-2&10\end{bmatrix}$ $\gamma=60°$	4.78	1.26
Honeycomb–type (nc-AFM)	$\lvert\vec{a}\rvert=\lvert\vec{b}\rvert=2.35\pm0.08$ nm $\gamma=60\pm4°$ pore diameter ~ 2 nm	$\begin{bmatrix}8&2\\-2&10\end{bmatrix}$ $\gamma=60°$	4.78	1.05
Honeycomb–type (STM)	$\lvert\vec{a}\rvert=\lvert\vec{b}\rvert=2.36\pm0.08$ nm $\gamma=60\pm4°$ pore diameter ~ 2 nm		4.82	1.04

Also given are the unit cell area and the ion pair density, ρ; for details see text. On top of the table the chemical and molecular structure of $[C_1C_1Im][Tf_2N]$ is depicted together with height of the cation (~ 0.3 nm) and anion (~ 0.5 nm); grey: C, white: H, blue: N, red: O, yellow: S, and green: F

clean Cu(111) surface was freshly prepared prior to each IL deposition using sequential cycles of Ar^+ ions bombardment (0.6 to 1 keV) at room temperature followed by a final annealing step at 800 to 900 K for approximately 10 min and consecutive cooling to the desired temperatures. The IL was deposited by physical vapor deposition (PVD) onto the substrate held at different temperatures as denoted using a home-built Knudsen cell [52] with the crucible temperature of 385–398 K. To ensure stable and reproducible evaporation rates, the IL adsorbate flux was monitored with a quartz crystal microbalance (QCM). IL coverages are denoted in ML, where 1 ML corresponds to a complete layer of vertically rented ion pairs. In case of a checkerboard structure with anions and cations adsorbed next to each other in direct contact to the surface, this coverage corresponds to 0.5 ML, which is also denoted as 1 WL (wetting layer).

The variable temperature nc-AFM and STM measurements were carried out in a two-chamber UHV system, using a Scienta Omicron VT-AFM-Q + -XA microscope, with a base pressure in the low 10^{-11} mbar range [43]. Following IL deposition on the sample in the preparation chamber, it was then quickly transferred to the pre-cooled AFM/STM sample stage in the analysis chamber at 110 K for the measurements. All AFM images were obtained in non-contact mode with silicon cantilevers, and the applied frequency shifts Δf in the employed experimental conditions ranged from − 300 to − 650 Hz vs the cantilever's resonance frequency, which is typically around ~ 270 to 300 kHz. The STM images were obtained with a manually cut Pt/Ir tip in constant current mode. The denoted bias voltages refer to voltages applied to the tip relative to the sample potential. The nc-AFM/STM images were processed using the WSxM software [53]. For noise reduction, moderate filtering (background subtraction, Gaussian smoothing) was applied.

The ARXPS measurements were performed in a two-chamber XPS system, which has previously been described in detail elsewhere [54]. The XP spectra were obtained using a non-monochromated Al Kα X–ray source (SPECS XR 50, 1486.6 eV, 240 W) and a hemispherical electron analyzer (VG SCIENTA R3000). For all spectra, a pass energy of 100 eV was used, yielding an overall energy resolution of 0.9 eV [54]. The spectra were quantitatively evaluated using CasaXPS V2.3.16Dev6. For the Cu $2p_{3/2}$ and the Auger-LMM substrate signals, Shirley backgrounds were subtracted and peaks were fitted with Lorentzian line shapes. For the IL-related S 2p, C 1s, N 1s, O 1s and F 1s regions, the positions and widths (fwhm) of the peaks were constrained (see Table S2 in the SI).

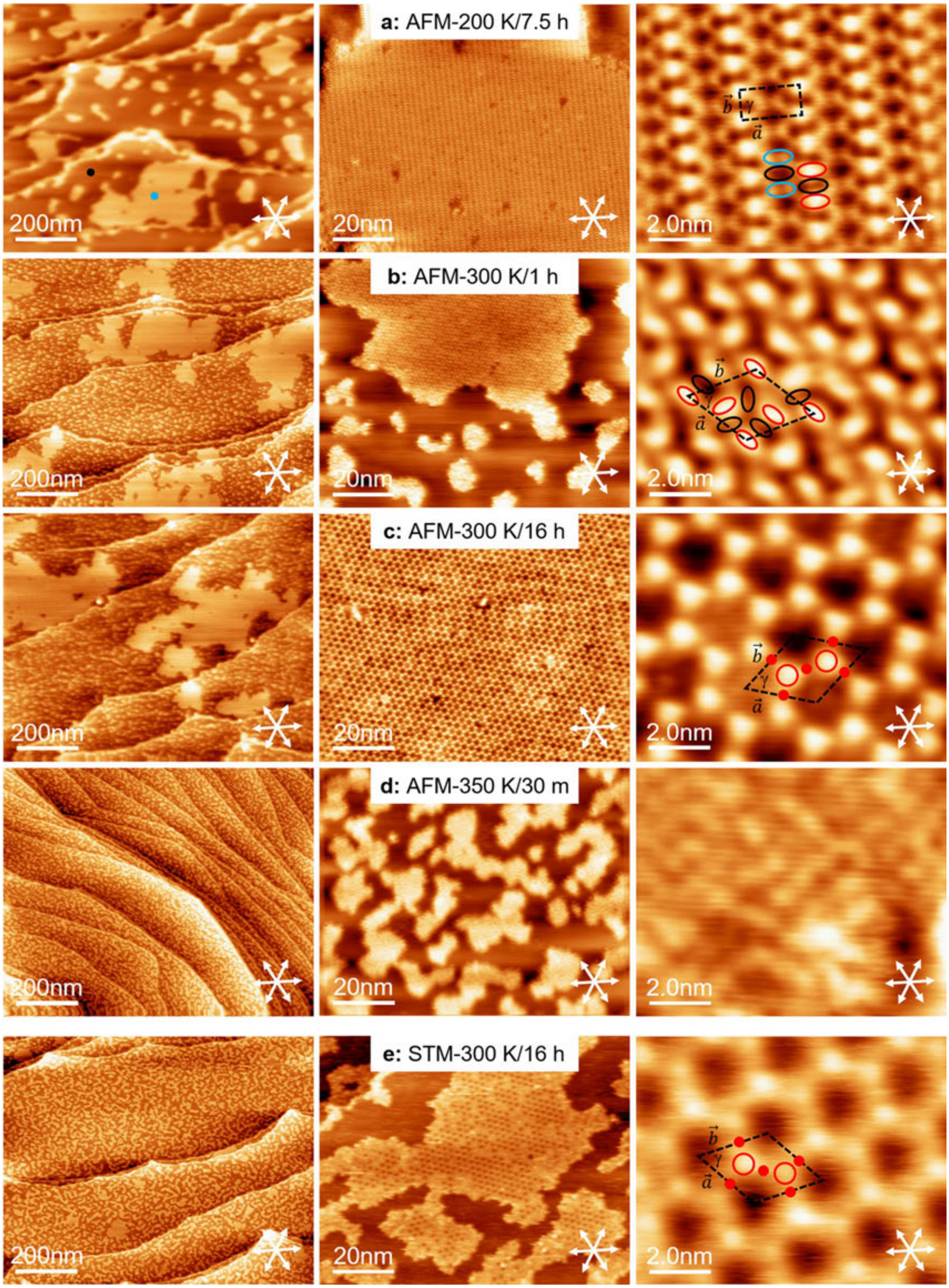

3 Theory

First-principles DFT calculations were performed with the VASP program package (Version 5.4.1) [55–57] using the PBE exchange–correlation functional [58]. The projector augmented wave method (PAW) [59] was used to take into account the core electrons. An energy cutoff of 450 eV was chosen for the plane wave basis. To describe the long-ranged London dispersion interactions the DFT-D3 correction scheme [60] was applied, and a Methfessel-Paxton smearing

◂**Fig. 1** nc-AFM (**a**–**d**) and STM images (**e**) of 0.15 ML $[C_1C_1Im][Tf_2N]$ on Cu(111), as overview (left, 1000×800 nm^2), close-up (middle, 100×80 nm^2), and with high resolution (right, 10×8 nm^2). **a** After annealing at 200 K for 7.5 h, ordered islands with a checkerboard–type structure and a nearly rectangular unit cell are observed; the right image is an average frame of nine consecutively recorded images. **b** After annealing at 300 K for 1 h, disordered small islands coexist with large ordered islands with hexagonal structure. **c** After annealing at 300 K for ~ 16 h, disordered small islands coexist with large IL islands with a highly ordered porous honeycomb structure. **d** After annealing at 350 K for 30 min, only small disordered islands are found. **e** STM images following a different preparation route and annealing at 300 K for ~ 16 h (see text) display the same honeycomb structure as seen in (**c**). The nc-AFM images were measured with $\Delta f = -400$ or -500 Hz, and the STM images with $U_{bias} = 2$ V and I_{set} of 0.2 or 0.4 nA (for details, see Table S4 in the SI); the unit cells are shown as dashed black lines; covered and uncovered areas are denoted by blue and black dots, respectively. For more details see text

[61] with a broadening of 0.2 eV was included. A supercell approach with four layers of Cu atoms was used to model the systems, including a 20 Å layer of vacuum separating periodic images in z-direction. The experimental lattice parameter of 3.58 Å was used for the Cu bulk geometry. The two bottom layers were fixed, while the top two layers were relaxed during the optimizations. The geometry was optimized until all forces were smaller than 0.01 eV/Å. The model for the checkerboard structure with a $\begin{bmatrix} 6 & 2 \\ -3 & 4 \end{bmatrix}$ supercell was calculated with a 2×4 × 1 and the larger hexagonal structures with the $\begin{bmatrix} 8 & 2 \\ -2 & 10 \end{bmatrix}$ supercell with a 2×2 × 1 Gamma centered Monkhorst–Pack [62] k-point mesh. Adsorption energies E_{ads} were calculated as total energy differences between the clean surface unit cell E_{surf} plus the energy of the ions in gas phase $E_{an} + E_{cat}$ minus the total energy of the combined system E_{sys} as $E_{ads} = E_{an} + E_{cat} + E_{surf} - E_{sys}$. Therefore, higher adsorption energies correspond to higher stability. The reference of the ionic liquid are the isolated ions in gas phase and not in the liquid phase. Isolated ions in gas phase represent the most simple and best defined reference. Furthermore, the comparison of different adsorption structures is not affected by the choice of the reference.

4 Results and Discussion

4.1 Atomic Force Microscopy and Scanning Tunneling Microscopy

In a first step, we investigated the adsorption and reaction behavior of 0.15 ML (=0.30 WL) of $[C_1C_1Im][Tf_2N]$ on Cu(111) using nc-AFM. The layers were deposited with the sample at 300 K. After deposition, the sample was immediately transferred to the precooled nc-AFM stage at 110 K within 7 to 10 min, in order to avoid the progress of potential chemical reactions (as it will be shown later, changes at 300 K only occur very slowly over several hours). Thereafter, nc-AFM images were first measured at 110 K, and then the sample was stepwise-annealed for extended times to 200, 250, 300 and 350 K. After each annealing step, the sample was quickly cooled back to 110 K to freeze the present state for imaging.

Figure 1a shows the corresponding images after annealing to 200 K for 7 h 30 min. In the overview image (left), we observe extended IL islands of various sizes (left image, bright areas) at the steps and also on the terraces of the Cu(111) surface; IL-covered areas and large areas of uncovered Cu substrate are indicated by blue and black dots, respectively. Notably, directly after cooling to 110 K, very similar structures are observed, but with a smaller size of the ordered islands and reduced resolution (see SI, Figure S1). The IL islands are observed close to step edges from both the ascending and descending sides of the step edges, implying that the steps are energetically favored adsorption sites that serve as nucleation centers. The close-up in Fig. 1a (middle) shows one representative large island connected to a step edge. This island consists of a highly regular, close-packed phase with only few defects, giving rise to a stripe-like appearance. The high-resolution AFM image of one of the islands in Fig. 1a (right) reveals that the close-packed phase is characterized by molecular rows, that is, stripes with a nearly rectangular unit cell ($\gamma = 90 \pm 3°$), with lattice vectors $\vec{a}$ (1.90 ± 0.08 nm) and $\vec{b}$ (0.90 ± 0.05 nm), and a unit cell area 1.71 nm^2 (see Table 1). From the measured angle of 6° between the unit cell vector $\vec{a}$ and the substrate high symmetry direction, we derive a commensurate $\begin{bmatrix} 6 & 2 \\ -3 & 4 \end{bmatrix}$ superstructure, using standard matrix notation with a unit cell angle of 92.2°. We propose that the unit cell contains 2 ion pairs, yielding a density of 1.17 ion pairs/nm^2. This analysis is based on the comparison to the low-temperature checkerboard–type structures on Au(111), with one ion pair per unit cell, and unit cell areas between 0.74 and 0.85 nm^2 [43]. We assign the very bright oval protrusion (red ellipses) and the two less bright protrusions (blue ellipses) to two differently oriented anions, and the dark areas in between (black ellipses) to the two cations; for more details, see DFT results below. From this consideration, we conclude that the anion to cation ratio is 1:1, that is, the ion pairs on the Cu(111) surface remain intact and are arranged in a checkerboard–type ionic surface tiling without dissociation, self-assembling into stripes. We will address the details of the structure together with the DFT calculations presented later on.

In a next step, we annealed the deposited layer at 250 K and then at 300 K. After annealing to 250 K for 45 min, we again find images with a stripe structure, albeit with a lower resolution of the image (see SI, Figure S2), which likely is due to a different termination of the AFM tip.

After annealing to 300 K for 1 h, we observe a pronounced transformation of the film structure, which is evident from the corresponding nc-AFM images in Fig. 1b. In the overview image (left), large islands are found to coexist with many small islands distributed all over the surface (see also Figure S3 in the SI). The close-up image (middle) reveals long-range order for the large islands, and disorder for the small islands. In the high-resolution nc-AFM image of one of the large islands in Fig. 1b (right), we observe a hexagonal–type lattice with three bright longish protrusions (red ellipses) and three less bright protrusions (black ellipses) per unit cell (dashed black rhombus); the protrusions in the unit cell have different orientation. The unit cell lattice vectors $\vec{a}$and $\vec{b}$ both have a length of 2.35 ± 0.08 nm with $\gamma = 60 \pm 4°$, resulting in a unit cell area of 4.78 nm^2. Assuming that each protrusion now represents an ion pair (see thorough discussion below), we obtain six ion pairs per unit cell. The resulting density of 1.26 ion pairs/nm^2 is quite comparable to that of the stripe phase (see Table 1). The absence of long range order for the small islands is also evident from the high-resolution image shown in Figure S4 (left) in the SI.

After extended annealing to 300 K for 16 h, we see another pronounced change in the structural order of the adsorbed IL layer; see Fig. 1c. In the overview nc-AFM image (left) we again find large islands coexisting with a large number of small islands; the close-up image (middle) shows a highly ordered honeycomb structure of the large islands, while the small islands are again disordered (see also Figure S4 (middle) in the SI). From the high-resolution nc-AFM image of one of the large islands in Fig. 1c (right), we conclude that the unit cell (dashed black rhombus) contains two bright protrusions (red circles) and three less bright protrusions (red dots); we again assume that each protrusion corresponds to one ion pair. The lengths of the lattice vectors $\vec{a}$ and $\vec{b}$ are again 2.35 ± 0.08 nm with $\gamma = 60 \pm 4°$, resulting in a unit cell area of ~ 4.78 nm^2. Assuming five ion pairs per unit cell (see below), we obtain a density of 1.05 ion pairs/nm^2 (see Table 1). From the angle of 12° between the unit cell vectors and the substrate high symmetry directions we derive a $\begin{bmatrix} 8 & 2 \\ -2 & 10 \end{bmatrix}$ superstructure using standard matrix notation, with an angle of 60°, for the porous honeycomb mesh. The pores of the honeycomb mesh have a diameter of roughly 2 nm. Interestingly, the size of the unit cell of the honeycomb structure is identical to that of the hexagonal structure (that is, lattice vector lengths of 2.35 nm), within the experimental uncertainty. Note that the honeycomb structure can be obtained from the overall hexagonal structure by removing one bright protrusion (that is, one ion pair), which results in the pore of the honeycomb structure. Thus, the hexagonal structure can be seen as transition structure from the stripe phase to the honeycomb phase upon annealing the IL layer at 300 K.

Upon further heating to 350 K, the long-range ordered islands disappear, and only small, disordered islands are observed; see Fig. 1d, which is particularly evident from the high-resolution image (right). Interestingly, the appearance of these small islands is very similar to that of the above described small, disordered islands, which coexist with the hexagonal and honeycomb structures at 300 K (see comparison in Figure S4 in the SI).

Notably, we also obtain the honeycomb structure following a different preparation and measurement route. In contrast to the above-described preparation where the IL was deposited at room temperature and quickly cooled down to 110 K, we here deposited 0.15 ML (= 0.30 WL) of $[C_1C_1Im][Tf_2N]$ onto Cu(111) held at low temperature (T < 160 K), and measured at 110 K; here, the measurements were performed by STM and not by nc-AFM. While after adsorption at < 160 K and also after annealing up to 250 K (for 15 min) no ordered IL islands could be found (see Figure S5 in SI), ordering is observed starting after extended annealing for 3–16 h at 300 K. The corresponding STM images after annealing for 16 h are shown in Fig. 1e. The overview image (left) shows the surface homogeneously covered with many small islands. When comparing these STM images with the previous nc-AFM overview images obtained after deposition at 300 K followed by immediate cooling to 110 K and then annealing to 300 K (Fig. 1c), we see much larger islands for the latter, which is attributed to Ostwald ripening during deposition at 300 K. After annealing the < 160 K-deposited layer for 3–16 h at 300 K, we observe again two distinctly different structures coexisting on the surface: The close-up STM image in Fig. 1e (middle) shows a large IL island with a well-ordered inner part surrounded by a disordered rim; in addition, smaller disordered separate islands are seen. The well-ordered inner part of the large island displays the porous honeycomb structure with few defects and additional species in some pores, as deduced from their less-dark appearance. Figure 1e (right) shows the high-resolution STM image of the center of the island, with the primitive unit cell indicated by the dashed black rhombus. The porous honeycomb–type adlayer again has a primitive hexagonal unit cell. The lattice vectors $\vec{a}$ and $\vec{b}$ have an identical length of 2.36 ± 0.08 nm with $\gamma = 60 \pm 4°$, resulting in a pore diameter of ~ 2 nm. The unit cell (area of 4.82 nm^2) again contains two bright (red circles) and 3 less bright (red dots) protrusions, giving a density of 1.04 ion pairs/nm^2; these parameters are identical to those observed using the other preparation route and nc-AFM as imaging technique. The comparison of the close-up images (middle) and high resolution images (right) for the two preparation routes in

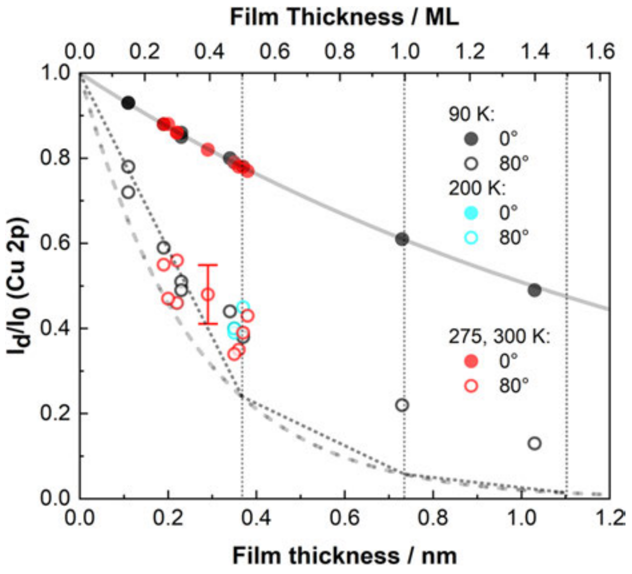

Fig. 2 Dependence of the Cu 2p substrate signal (full symbols for 0° and open symbols for 80° emission) on IL film thickness for $[C_1C_1Im][Tf_2N]$ on Cu(111) at 90, 200, 275 and 300 K. The film thickness of each layer was calculated from the attenuation of the Cu 2p signal at 0°. The solid and long-dashed lines show the exponential decay expected for a uniform increase in layer thickness for emission angles of 0° and 80°, respectively [36], based on the inelastic mean free path λ of 3.0 nm for the Cu 2p peak; the short-dashed lines for 80° are the prediction for perfect 2D layer-by-layer growth (section-wise filling of one layer of flat lying ion pairs after another, each with 0.5 ML coverage, see vertical lines). Up to 0.3 ML, very good agreement of the 80° data with the short-dashed lines is found, indicating the formation of a 2D layer; the fact that between 0.3 and 0.5 ML somewhat larger values are found indicate a small deviation from perfect 2D growth. For larger coverages, pronounced deviations from 2D growth are observed

Fig. 1 reveals a higher degree of order and less defects for the deposition at 300 K followed by fast cooling to 110 K.

4.2 X-ray Photoelectron Spectroscopy

4.2.1 Growth Behavior

Complementing the local scanning probe microscopy data, we also used XPS to follow the overall IL film growth. Figure 2 shows the attenuation of the normalized Cu $2p_{3/2}$ signal I_d / I_0 upon deposition of $[C_1C_1Im][Tf_2N]$ at 90, 200, 275 or 300 K. After each deposition step, we measured the signals at both 0° and 80° emission angle. Under the assumption of perfect 2D growth, one can use the attenuation of the Cu 2p substrate signal at 0°, I_d/I_0, to calculate the mean film thickness d of the IL layer. From this thickness, we can then predict the attenuation at 80° for a two-dimensional IL layer at this thickness: the short-dashed grey lines represent ideal layer-by-layer 2D growth behavior in 80° for the WL (0.5 ML thickness) and another two layers on top (the long-dashed grey line represents exponential decay and agrees with the short dashed lines for each completed layer, e.g. at 0.5 ML; for details of this approach, see refs [36, 63]. A coincidence of the measured 80° data with the predicted short-dashed lines reveals perfect 2D growth; 80° data falling above the lines indicate a deviation from layer-by-layer growth towards island growth (3D growth). Focusing first on low coverages/thicknesses up to 0.5 ML, the 80° data (open symbols) in Fig. 2 fall on or close to the short-dashed line until 0.3 ML, independent of temperature, indicating perfect 2D growth in this coverage regime. Interestingly, between 0.3 and 0.5 ML, all measured data systematically are slightly above the calculated 80° curve, which is attributed to moderate 3D growth. Such a behavior is rather unusual, since 2D growth of the first wetting layer up to 0.5 ML has been observed for a wide variety of ILs on different metal surfaces, independent of the growth mode at higher coverages. Examples are $[C_1C_1Im][Tf_2N]$ on Au(111) [64] and Ag(111) [63], $[C_8C_1Im][Tf_2N]$ on Ag(111) [63] and Au(111) [64] or $[BMP][Tf_2N]$ on Au(111) [41]. The formation of the first flat wetting layer is commonly attributed to strong attractions of the ions towards the metal, e.g. by image dipoles. Above 0.5 ML, the 80° data Fig. 2 fall well above the dashed curve for ideal 2D-growth. This deviation is attributed to island formation in the multilayer regime. Note that such Stranski–Krastanov-type growth behavior is quite commonly observed for ILs with short chains, e.g. for $[C_1C_1Im][Tf_2N]$ on Ag(111) [63] or $[C_2C_1Im][TfO]$ on Au(111) [36, 65].

4.2.2 Adsorption and Thermal Evolution

In order to understand the ongoing surface chemistry of the IL in contact with the Cu(111) surface, we studied the IL layer in the low-coverage regime, during deposition and annealing by XPS. We performed measurements of all relevant IL core levels at selected temperatures, which are characteristic for the changes observed in nc-AFM, that is, 200, 275, 300 and 360 K. We investigated two coverages, namely 0.3 ML and 0.5 ML, which correspond to a partly (0.6 WL) and a more or less fully closed (1.0 WL) wetting layer, respectively; smaller coverages could not be studied reliably, due to poor signal intensities. Nevertheless, the measurements should allow for a comparison to the nc-AFM/STM measurements, which were performed for a 0.15 ML (=0.30 WL) coverage. XP spectra were measured for all core levels at 0° emission angle (and additionally at 80° for 200 K). The corresponding S 2p, C 1s, N 1s, O 1s and F 1s spectra are shown in Fig. 3 (0.5 ML) and Figure S6 (0.3 ML), along with their fits. Data at 0° and 80° are plotted in grey and blue, respectively. In addition, we also measured the corresponding 0° spectra of a multilayer film of 4.6 ML $[C_1C_1Im][TF_2N]$, deposited at 90 K, as reference; these spectra are also included in Figs. 3 and S6 (bottom),

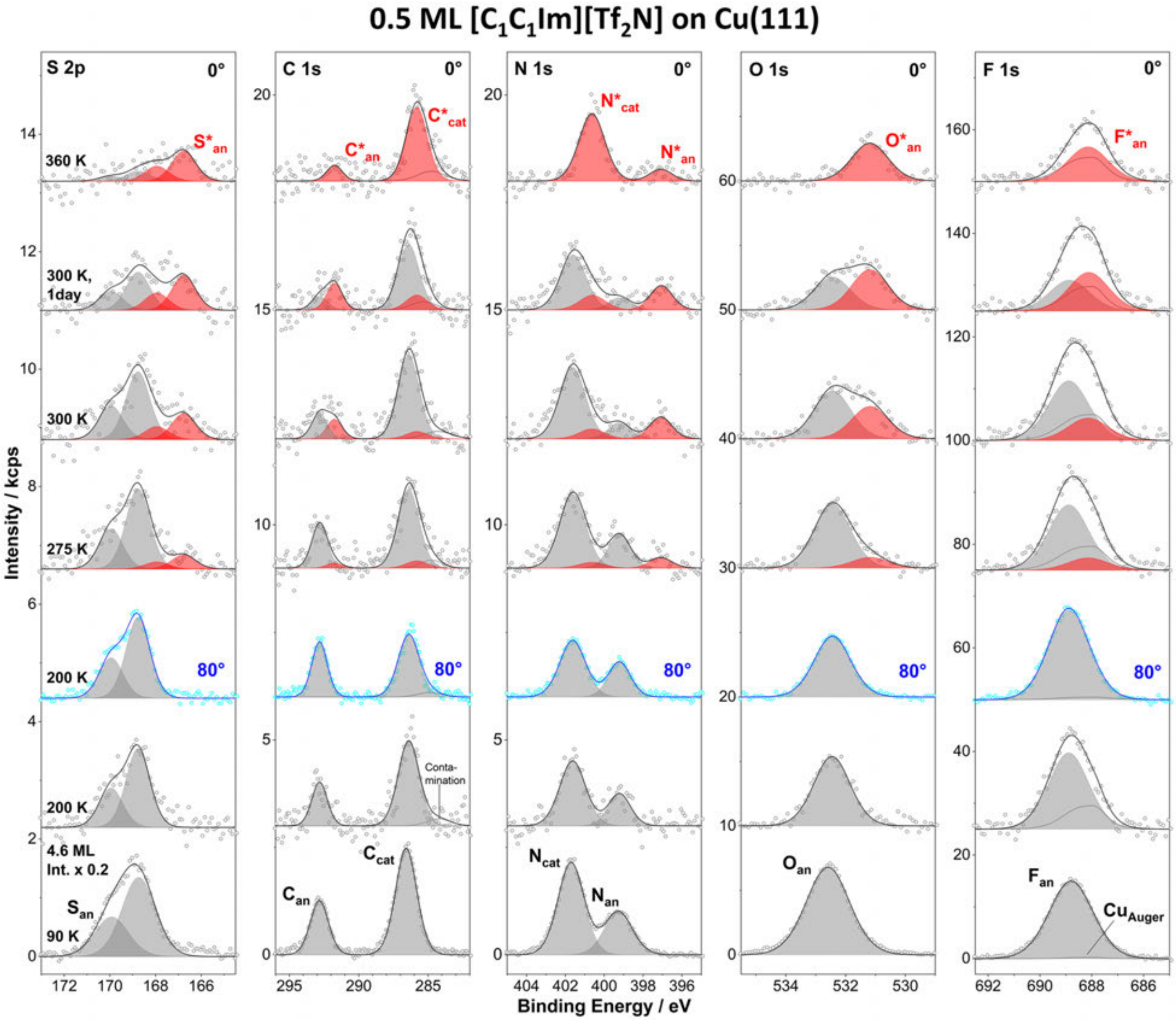

Fig. 3 S 2p, C 1s, N 1s, O 1s and F 1s spectra of 0.5 ML $[C_1C_1Im][Tf_2N]$ on Cu(111) from 200 to 360 K, along with the spectra for 4.6 ML obtained at 90 K as reference for the bulk IL (bottom). For each denoted temperature, a new layer was freshly prepared and measured under normal (0°) and grazing emission (80°; shown only for 200 K in blue). For a better visualization, the 4.6 ML spectra are scaled down by a factor of 0.2. Grey peaks indicate the signals of the intact IL, red peaks denote the peaks of the new species formed upon heating. In the C 1s spectra a small contamination of the surface was taken into account, as indicated exemplarily in the spectrum at 200 K; in the F 1s spectra, the overlapping Cu_{Auger} signal was subtracted (for more details, see experimental section and SI)

downscaled by the factor 0.2 for better visualization. The quantitative analysis of the 0.5 ML spectra is provided in Table 2, and that of the 0.3 ML spectra in Table S1.

We start with discussing the 0° spectra of the 4.6 ML multilayer film at 90 K, as it represents the unperturbed intact IL. The cation displays two distinct peaks in the N 1s and C 1s region. The C_{cat} peak at a binding energy of 286.6 eV is assigned to the three carbon atoms of the imidazolium ring and the two carbon atoms of the methyl groups attached to the nitrogen atoms. The N_{cat} peak at 401.7 eV corresponds to the two nitrogen atoms in the imidazolium ring. For the $[Tf_2N]^-$ anion, the C_{an} peak at 292.8 eV and the F_{an} peak at 688.8 eV are assigned to the carbon and the fluorine atoms of the CF_3 group. The O_{an} peak at 532.6 eV and the S_{an} $2p_{1/2}$ and $2p_{3/2}$ duplet at 169.9 and 168.7 eV originate from the oxygen and sulphur of the sulfonyl-group, respectively, and the N_{an} peak at 399.3 eV stems from the imidic nitrogen. The composition of the 4.6 ML film in Table 2 is in good agreement with the nominal composition within the experimental uncertainty (± 10%), confirming that the IL stays intact in the deposition process, in line with earlier studies [36].

Table 2 Quantitative analysis of the composition of 0.5 ML $[C_1C_1Im][Tf_2N]$ on Cu(111) at different temperatures, as derived from the XP spectra shown in Fig. 3 at 0° (and for 200 K also at 80°) emission angle

Temperature	$S_{an, sum}$	$C_{an, sum}$	$C_{cat, sum}$	$N_{cat, sum}$	$N_{an, sum}$	$O_{an, sum}$	$F_{an, sum}$	Σ
Nominal	**2**	**2**	**5**	**2**	**1**	**4**	**6**	**22**
360 K	0.9	0.7	4.1	1.9	0.3	2.0	3.5	13.3
300 K, 1 day	1.6	1.7	4.6	2.0	0.9	4.0	7.1	22.0
300 K	1.8	1.6	4.6	2.1	0.8	3.8	7.3	22.0
275 K	1.9	1.9	4.7	2.1	1.0	3.5	7.0	22.0
200 K, 80°	1.7	2.3	3.4	1.6	0.9	3.2	8.9	22.0
200 K	1.7	1.8	4.7	1.8	0.8	3.6	7.5	22.0
90 K	1.8	2.0	4.6	2.0	1.0	4.2	6.4	22.0

Bold value are nominal numbers, non-bold values are experimental data

Also given are the results for 4.6 ML deposited at 90 K and measured under 0° emission as reference for the bulk IL. For quantification, the shifted (marked with asterisk) and the unshifted signals of the IL were combined to provide the total atom number for each element

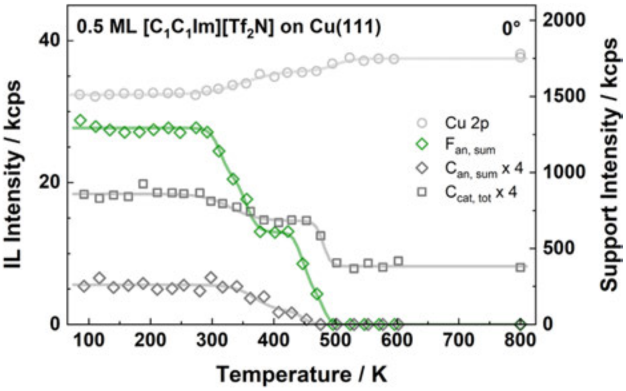

Fig. 4 Thermal evolution of the Cu 2p (open light grey circles), F 1s (green diamonds) and C 1 s (dark grey squares for C_{an}, and dark grey diamonds for $C_{het,comb}$) intensities during heating a 0.5 ML $[C_1C_1Im][Tf_2N]$ film on Cu(111). The IL was first deposited onto the sample at 88 K via PVD; thereafter, XP spectra were recorded while heating with a linear heating rate of 2 K/min up to 600 K; after flashing the sample eventually to 800 K for 5 min, a last data set was also recorded. The intensity scale for the Cu 2p signal is given on the right side and that of the F 1s and C 1s signals on the left. The symbols for the corresponding F and C species represent the sums of the corresponding unshifted and shifted (*) intensities; note that in case of the C_{cation} region, only one broad peak could be used including the minor carbon contamination (see also Fig. 3 and for further details, see text)

The spectra for 0.5 and 0.3 ML $[C_1C_1Im][Tf_2N]$ were recorded for all IL core levels at temperatures, at which we expected characteristic changes based on the thermal evolution observed in Fig. 1 and also Fig. 4 (see below); the full data set required ~ 90/130 min for all core levels of the 0.5/0.3 ML films. To minimize the influence of beam damage, always a new film was freshly prepared and measured at the indicated temperatures of 200, 275 and 300 K, except for the 360 and 500 K films, which were deposited at 300 and 200 K, respectively. Since the behavior is quite similar, the data for 0.5 and 0.3 ML will be discussed together. Thereby, the focus will be on the 0.5 ML films, since the 0.3 ML films are more prone to beam damage, due to the longer measurement times required for the lower coverage.

For 200 K, we address the spectra at 0° (normal emission) and at 80° (grazing emission) in Fig. 3 (0.5 ML) and Figure S6 (0.3 ML), which allow for deriving information on the stoichiometry as well as the orientation of the IL on the surface. The 0° spectra are, apart from their lower intensities, very similar to those of the multilayer. The only difference is a small shift of some levels by up to 0.2 eV to lower binding energy, yielding the cation peaks C_{cat} at 286.4 eV and N_{cat} at 401.6 eV, and the anion peaks C_{an} at 292.8 eV, F_{an} at 688.9 eV, O_{an} at 532.4 eV, N_{an} at 399.2 eV, and the S_{an} duplet at 170.0/168.8 eV (for 0.5 ML); for an overview of the binding energies see Table S2 in the SI. These small shifts are attributed to more efficient screening due to the proximity of the metal surface (final state effect). For the analysis of the F 1 s region, the Cu_{LMM} Auger peak at 688.0 eV, which overlaps with the F_{an} signal of the anion, has to be considered. This is done by using the Auger peak shape of the clean copper surface, downscaling it according to the IL-film related attenuation of the Cu 2p signal. By fitting the F 1 s peak taking into account this downscaled Auger peak, we obtain the correct number of F atoms in Table 2 (note that at elevated temperatures, new species with shifted binding energies appear as discussed below; in Table 2, only the sum for each atom is given). The quantitative analysis of the 0° spectra in Table 2 (0.5 ML) and Table S1 (0.3 ML) yields atom numbers close to the nominal values within the experimental uncertainty (± 10%); the somewhat too large value of the F 1 s signal is attributed to uncertainties in the described Auger peak correction procedure. The very good agreement of XPS quantification in 0° and IL stoichiometry again is a clear indication that the IL adsorbs intact at 200 K.

From the quantitative analysis of the 80° spectra at 200 K in Table 2 and Table S1, we gain insight into the orientation of $[C_1C_1Im][Tf_2N]$ on the Cu(111) surface at this temperature as already done earlier for this IL on Au(111) [64]: An intensity decrease at 80° as compared to 0° for certain IL signals of the two-dimensional WL indicates that the corresponding atoms are close to the metal surface and are attenuated by the atoms above, yielding lower than the nominal atom numbers. On the other hand, enhanced signals at 80° indicate that these atoms are near the vacuum, leading to larger than nominal atom numbers at 80°. At 200 K, $F_{an,sum}$ exhibits a larger than nominal atom number and $O_{an,sum}$ a lower than nominal atom number, indicating that the anion is adsorbed with the oxygen atoms towards the copper surface, while the CF_3 groups preferentially point toward the vacuum, as it is often observed for ILs of this kind [36]. The cation signals $C_{cat,sum}$ and $N_{cat,sum}$ are systematically attenuated in 80° indicating that the imidazolium ring is closer to the surface than the CF_3 groups of the anion. Overall, the adsorption behavior at 200 K thus shows clear similarities to that of comparable ILs on Ag(111) and Au(111) [36, 63, 64]. We therefore conclude also from the XPS data that $[C_1C_1Im][Tf_2N]$ exhibits the checkerboard arrangement at 200 K as it is frequently observed for ILs, in which the anion and cation adsorb alternately next to each other on the surface [36].

We next address the spectra at higher temperatures. At 275 K, new peaks start to appear (marked in red, with an additional asterisk), at the expense of the original peaks (see Figs. 3 and S6), which decrease in intensity. The new peaks all exhibit pronounced shifts towards lower binding energies relative to the peaks of the intact IL at 200 K (see Table S2 in the SI). The anion-related peaks are shifted by − 2.1 eV for N^*_{an}, − 1.3 eV for O^*_{an}, − 1.1 eV for C^*_{an}, − 0.7 eV for F^*_{an} and − 2.0 eV for S^*_{an}, and the cation-related peaks by − 1.0 eV for N^*_{cat} and − 0.6 eV for C^*_{cat}. As already mentioned above, in the quantitative analysis in Tables 2 and S1, only the sum of the shifted (*) and the pristine signals of the IL is given (as indicated with subscript "sum"), in order to provide the total amount for each element.

Upon deposition at 300 K and measuring immediately afterwards, a further increase of the shifted signals and decrease of the unshifted signals is observed in Fig. 3 for 0.5 ML (and in Figure S7 on larger scale), and in Figure S6 for 0.3 ML. This "signal conversion" is even more pronounced when keeping the sample for one day at 300 K after deposition (without X-ray exposure to avoid any beam damage in the meantime), and measuring afterwards. Notably, despite the changes observed for the 275, 300 and 300 K (1 day) spectra, the overall IL composition in 0° (sum of shifted and unshifted signals) is still in good agreement with the nominal values for both investigated coverages (cf. Tables 2 and S1). Thus, no significant loss of individual atoms by desorption occurs up to 300 K (minor deviations might be due to the bad signal-to-noise ratio or indicate changes in ion orientation). The analysis of the XP spectra data for the 0.5 ML film measured immediately after deposition at 300 K in Fig. 3 shows that 39 ± 15% of the original anion peaks at 200 K are converted to the new N^*_{an}, O^*_{an}, C^*_{an}, F^*_{an} and S^*_{an} peaks. For the cation peaks, only a much smaller fraction of 10 ± 2% is converted to N^*_{cat} and C^*_{cat}. After 1 day at 300 K, the total coverage slightly decreased, and the degree of conversion increases to 58 ± 10% of the anions and 20 ± 2% of the cations (with the total anion and cation signals still agreeing with the nominal composition; see Table 2). Note that for the 0.3 ML deposition series (see Figure S6), overall the same trend is observed as for the 0.5 ML discussed here, with the conversion to the (*) species being, however, more pronounced. Most likely, the apparently more reactive situation in case of the 0.3 ML is related to increased beam damage effects since longer measurement times are required at the lower coverage regime to obtain reasonable signals. As will be discussed in detail in the next section, we propose that the unshifted anion and cation signals are due to intact ion pairs on the surface, forming the well-ordered striped phase at 200 K and the hexagonal and honeycomb phases at 300 K. On the other hand, the shifted signals are related to species within the disordered small islands, where cations and anions have partially reacted/decomposed at the copper surface into non-volatile fragments. The smaller fraction of shifted cation signals (as compared to the larger amount of shifted anion signals) is possibly related to the fact that some of the cation fragments still exhibit binding energy values close to the original peaks in contrast to the anion ones (see next section for more details).

At 360 K, the pristine IL signals have virtually disappeared, and only the shifted signals are left (Figs. 3 and S6). In particular, the total amount of $C_{an,sum}$, $O_{an,sum}$, $F_{an,sum}$ and $S_{an,sum}$, that is, all elements involved in the anion, is reduced to ~ 50% compared to the starting point (see Tables 2 and S1). The halving of the anion signals between 300 and 360 K is a strong indication for the desorption of anions or fragments of anions. Notably, this is in line with the in situ temperature-programmed XPS (TPXPS) experiment in Fig. 4 (see below), which also shows a drop of ~ 50% starting from 300 K in the F_{an} signal (as representative for the whole anion). Simultaneously to the decrease of the total anion intensity, we observe the total conversion of the remaining cation signals C_{Cat} and N_{Cat} to the C_{Cat}* and N_{Cat}* species (at lower binding energies by − 0.6 and − 1.0 eV, respectively) along with a small intensity decrease, indicating that also the cation coverage is affected by the ongoing surface processes. Note that this situation at 360 K is likely to represent the one at 350 K in Fig. 1d, where only small disordered islands are observed in nc-AFM (for the initial coverage of 0.15 ML). At 500 K, all anion-derived signals have completely vanished (not shown), and only residual carbon and nitrogen species (with an approximate atomic ratio C_{res}: N_{res} = 5: 1) remain at the copper surface. Moreover, an additional S 2p duplet at 162.4/161.6 is observed at 500 K, which is attributed to atomic sulphur as a remaining decomposition product.

To follow the thermal evolution of the wetting layer more closely, we deposited 0.5 ML of [C_1C_1Im][Tf_2N] on Cu(111) at 88 K and subsequently heated to 600 K with a linear heating ramp of 2 K/min while performing temperature-programmed (TP)-XPS at normal emission. To minimize beam damage, we restricted our analysis to three core levels: Along with the Cu 2p substrate signal (to follow the overall film thickness), we measured only C 1 s and F 1 s spectra. After the ramp was finished, we recorded an additional data set after flashing to 800 K to look for further changes. Figure 4 depicts the quantitative analysis of the Cu 2p substrate signals, the total F 1 s signals $F_{an,sum}$ ($=F_{an}+F_{an}$*), and the C 1 s signals of the anion carbon $C_{an,sum}$ ($=C_{an}+C_{an}$*) and cation carbon $C_{cat,tot}$ (note that due to the reduced signal-to-noise ratio in this TPXPS series, a clear discrimination of C_{cat}, C_{cat}* and at higher temperatures residual carbon was impossible and we thus provide only the total amount using one broad peak for fitting this binding energy range); carbon intensities have been multiplied by factor four for better visualisation. All signals show characteristic intensity changes with temperature, which are in line with the data in Fig. 3. The $F_{an,sum}$ signal stays constant from 100 to ~ 300 K at ~ 28 kcps. At higher temperatures, it decreases by about 50% to reach a plateau at ~ 13 kcps at around 400 K, and finally drops zero at around 500 K. The $C_{an,sum}$ signal shows the same change with temperature, which indicates the loss of CF_3-groups in course of the reaction/fragmentation discussed above. Note that the increase of the shifted F_{an}* and C_{an}* signals at the expense of the unshifted signals is also seen in the data of the TPXPS experiment (not shown), similar to the observations in Fig. 3. In contrast to the anion signals, the cation signal $C_{cat,tot}$ shows much smaller changes in intensity. It initially remains constant until 300 K at ~ 18 kcps, and thereafter only slightly decreases to ~ 15 kcps at 370 K. After a plateau until 450 K, it finally drops to ~ 8 kcps between ~ 460 and 500 K, and then stays constant till 800 K; note that the remaining residual carbon C 1 s peak at 500 and 800 K is much broader compared to the original C_{cat} peak.

4.3 Comparison of nc-AFM/STM and XPS Results

When comparing the nc-AFM images in Fig. 1 and the XPS data in Figs. 3 and S6, we can derive information on the nature of the different surface species at the different temperatures. At 200 K, the adsorbed IL is found in long-range ordered islands, and the very small, disordered islands are absent in nc-AFM. In this temperature range, XPS only detects species with binding energies characteristic of the intact IL. XPS thus corroborates our interpretation of the microscopy data that at this temperature, namely that the deposited IL forms ordered islands consisting of intact ion pairs regularly adsorbed next to each other in the checkerboard arrangement, giving rise to the stripe-like appearance as discussed above. At 300 K, we observe the transformation of the stripe-like island structure first to the hexagonal metastable transition phase and finally to the honeycomb structure. At the same time, we also observe an increasing number of small, disordered islands which coexist with the long-range ordered hexagonal and honeycomb phases. Starting at around 275 K, we also observe pronounced changes in XPS, that is, a partial transformation of the original IL peaks to new chemical shifted (*) peaks. The observed chemical shifts range between 0.7 and 2.1 eV towards lower binding energies for the anion signals and 0.6–1.0 eV for the cation signals. They indicate a chemical reaction with partial decomposition of the IL on the Cu(111) surface. As the formation of the small disordered islands in nc-AFM is observed in the same temperature region as the formation of the new peaks in XPS, we conclude that the small disordered islands are mainly formed by the products of this ongoing reaction, while the remaining unshifted peaks originate from the intact IL ion pairs within the large and well-ordered islands. The small size of the disordered islands indicates that the decomposed species are to some extent mobile on the surface, which allow them to agglomerate into these islands. Notably up to 300 K, no desorption of reaction products occurs, since the sum of IL- and IL*-signals does not change within the margin of uncertainty of the experiments. Upon heating to 350 K, in nc-AFM a complete conversion to small disordered islands occurs, which in XPS goes along with a complete disappearance of the unshifted peaks due to conversion to the shifted peaks. In addition, ~ 50% of the anion signals and 10–20% of the cation signals are lost due to desorption of volatile species.

In the literature, two studies exist on related systems. Biedron et al. performed a detailed comparative XPS, UPS and STM study of [C_8C_1Im][Tf_2N] deposited onto Cu(100) and Au(111) at and above room temperature [46]. They observed that on Au(111), the XPS binding energies of all IL peaks of the layer in direct contact with the surface show only a small uniform shift relative to multilayer spectra. In contrast on Cu(100), they observed that for the first layer, the anion-related signals are shifted to lower binding energy by − 2.0 eV for N^*_{an}, − 1.5 eV for O^*_{an}, − 0.8 eV for C^*_{an}, − 0.6 eV for F^*_{an} and − 1.8 eV for S^*_{an}, as deduced from their spectra (cf. Figure 6 of [46]; the positions of the cation peaks were difficult to discern); these values agree to within max. 0.3 eV with the values observed for the shifted peaks in this study. At the same time, the stoichiometry corresponded to that of an intact IL. Biedron et al. attributed these shifts to a much stronger interaction of the intact IL with the Cu(100) surface, which they also used to explain the more stable imaging conditions at the monolayer coverages on Cu(100) as compared to Au(111).

The second study was performed by Uhl et al. who deposited 1-butyl-1-methylpyrrolidinium bis(trifluoromethylsulfonyl)imide ([BMP][Tf_2N]) on Cu(111) at 80 K in the sub-monolayer range, also using STM and XPS for characterization [47]. While up to 200 K no changes were observed, annealing to 300–350 K yielded pronounced shifts of the anion peaks towards lower binding energy by − 1.1 eV for C^*_{an}, − 0.5 eV for F^*_{an} and − 2.3 eV for S^*_{an}, a decrease of oxygen by 60%, and in addition the formation of atomic sulphur, indicating major structural changes of the IL layer and partial decomposition of the anion at this temperature. The binding energies of the shifted anion signals are similar to those found in this study (deviations between 0.1 and 0.3 eV) and also for [C_8C_1Im][Tf_2N] on Cu(100) by Biedron et al. Interestingly, Uhl et al. report essentially unaffected $[BMP]^+$ -related signals at 300 K, which agrees with the dominance of the unshifted $[C_1C_1Im]^+$ XPS signals of our study at 300 K as shown in Fig. 3: slightly depending on annealing time and initial coverage, only 10–20% of the pristine cation signals are converted at this temperature, in contrast to the much stronger conversion of anion signals.

Based on our results, we are now able to derive a comprehensive understanding of the two studies by Biedron et al. and Uhl et al. and resolve apparent discrepancies [46, 47]. We propose that for all three investigated systems, that is, [C_8C_1Im][Tf_2N] on Cu(100), [BMP][Tf_2N] on Cu(111), and [C_1C_1Im][Tf_2N] on Cu(111) overall the same adsorption and reaction behavior is observed, with some differences in the reaction temperatures: For adsorption at low temperatures (< 200 K), the corresponding IL adsorbs intact and with signatures typically observed for non-reactive surfaces like Au or Ag, in terms of XPS binding energies and formation of a checkerboard structure. Upon heating to or adsorption at room temperature, a very similar behavior is observed in XPS for the three systems studied that is, the $[Tf_2N]^-$ signals exhibit pronounced shifts toward lower binding energies, indicating that for all systems a similar conversion of mainly the anion peaks occurs. In this first step, the cation signals are not (or only moderately) affected. Based on our findings and in contrast to what was proposed by Biedron et al., we assign the observed shifts of the anion peaks not to an enhanced interaction of the pristine IL with the Cu surface, but to a temperature-induced reaction, which progresses with time at 300 K. Above room temperature, in a second step most of the cation signals also show a pronounced shift, while the shifted anion signals remain at the same binding energy, but decrease by 50%. This behavior indicates decomposition of the ILs and/or partial desorption of the ILs or reaction products. After this step, no long-range order can be detected in nc-AFM or STM.

At this point, we have to address the chemical nature of the reaction products formed above 275 K in our sub-ML studies of [C_1C_1Im][Tf_2N] films on Cu(111). We attribute the simultaneous formation of the new peaks observed in XPS and of the disordered islands in nc-AFM to a reaction/decomposition of the IL on the surface yielding new surface species. These might be related to one (or to a combination) of the following three explanations:

Explanation (1), which is most favoured by us, is the partial decomposition of the IL above 275 K to small and non-volatile fragments such as NH_x, SO_x, fluorocarbon species (CF_3), carbene-like and/or other species, which remain in the small disordered islands on the surface at 300 K. The fact that the degree of conversion of the unshifted to the shifted peaks in XPS is different for the anion and cations (~ 40% and 10%, respectively, e.g. for 0.5 ML) could indicate that for the cation several decomposition products with different XPS binding energies are formed, one of which is similar to that of the unshifted peaks of the intact IL. After annealing to 360 K, a part of the anion-related fragments (likely charge neutral) has desorbed, as concluded from the ~ 50% loss of anion signals.

Another decomposition path could be given by explanation (2), where the $[C_1C_1Im]^+$-cations of the IL are deprotonated in C2-position and Cu-carbenes are formed, binding to the Cu(111) surface or to copper adatoms. The protons would be transferred to copper and could react with the anions to form neutral H[Tf_2N], which subsequently desorbs above 350 K. For example, the formation of an organometallic copper dicarbene was observed in STM, XPS and DFT calculations by Jiang et al. [66]: The authors reacted 1,3-Dimethyl-1H-imidazol-3-ium-2-carboxylate with Cu(111), which forms [C_1C_1Im*]Cu[C_1C_1Im*] dimers at the surface after CO_2 elimination ([C_1C_1Im*] is denoted here as the carbene after deprotonation of $[C_1C_1Im]^+$ at position 2). An explanation along these lines can, however, be ruled out, since we observe similar changes in the XP spectra with temperature for the related IL [$C_1C_1C_1$Im][Tf_2N] (Figure S8 and Table S3 in the SI), where the most acidic proton of $[C_1C_1Im]^+$ in position 2 is replaced by a methyl group, and thus deprotonation should not occur (or should occur only at considerably higher temperatures). Furthermore, carbene formation also appears to be very unlikely since for [BMP][Tf_2N]) on Cu(111) overall a very similar thermal evolution to that of [C_1C_1Im][Tf_2N] on Cu(111) is found (see discussion above).

Finally, we cannot completely rule out a third explanation (3), namely that upon heating to 275 K and above, parts of the intact IL reorganize without decomposition, e.g. by interaction with Cu adatoms, forming a specific Cu-IL complex. The complexation would have to affect the electronic structure of the still intact IL such that the corresponding IL signals exhibit the observed strong decreases in binding energy. The formed Cu-IL complex could also be an initial step towards carbene formation, initiating also the decomposition of the IL and the desorption of $H[Tf_2N]$ at 360 K. We consider this last option, however, as rather unlikely.

4.4 Ordered Structures and DFT Calculations

As final step we aim for a more detailed understanding of the ordered structures based on the nc-AFM images in Fig. 1 through corresponding DFT calculations.

4.4.1 Stripe Structure at 200 K

The stripe structure Fig. 1a (right) and Fig. 5a (left) has a rectangular unit cell ($\gamma = 90 \pm 3°$) with vectors $\vec{a}$ (1.90 ± 0.08 nm) and $\vec{b}$ (0.90 ± 0.05 nm), yielding a unit cell area of ~ 1.71 nm^2 (see Table 1). This structure is similar to the stripy structure observed for the same IL on Au(111), with a unit cell area of ~ 0.74 nm^2, and one ion pair per unit cell [43]. If we assume a comparable ion pair density in the wetting layer on both surfaces, this is a strong indication that the unit cell on Cu(111) in Fig. 1 and Fig. 5a (left) contains 2 ion pairs, which yields an ion pair density of 1.17 ion pairs/nm^2. In Fig. 1 (see above), we tentatively assigned the very bright oval protrusion (red ellipses) and the two less bright protrusions (blue ellipses) to two differently oriented anions, and the dark areas in between (black ellipses) to the two cations.

As a next step, we discuss the results from DFT. Because we have a highly ordered structure, we calculated a commensurate structure with a $\begin{bmatrix} 6 & 2 \\ -3 & 4 \end{bmatrix}$ superstructure. The lattice vectors $\vec{a}$ (1.83 nm) and $\vec{b}$(0.92 nm) with an angle γ of 92.2° yield a unit cell area of ~ 1.68 nm^2, which (within the margin of error) very well agrees with the experimental values determined from the nc-AFM images. The resulting structure after geometry optimization is shown in Fig. 5c, d and e (left). It reveals two similarly oriented cations with their plane nearly perpendicular to the surface, and the C2 carbon atom of the imidazolium ring pointing downwards, that is, towards the surface. Interestingly, the two anions have different orientations: one is adsorbed nearly vertically with all four oxygen atoms of the sulfonyl groups pointing downwards in 2–2 orientation adsorption motif, and the six F atoms of the two CF_3 groups pointing away from the surface towards vacuum; the other is adsorbed side-on with only one oxygen atom of each sulfonyl group attached to the surface, that is, in 1–1 orientation adsorption motif, and 3 F atoms pointing towards vacuum. These two different orientations are likely responsible for the different contrast of the anions observed by nc-AFM. The DFT structure is also in line with the overall orientation derived from XPS (see above). The resulting adsorption energy E_{ads}, which is the energy difference between the isolated ion pair in the gas phase and adsorbed in the proposed layer, yields a value of 3.5 eV per ion pair, indicating a very stable structure. One should note here that small modifications to the unit cell yield quite similar results. In an attempt to simulate the nc-AFM images using a simplified approach, we calculated charge density contour plots; the corresponding image is shown in Fig. 5b (left). The agreement with the experimental data is surprisingly good, considering the fact that the contrast strongly depends on the status of the nc-AFM tip and the simplicity of the calculation. One interesting aspect are the different contributions to the calculated total adsorption energy; the detailed analysis shows that the vertical interaction of the ions with the copper surface via their image charges amounts to ~ 1.6 eV, while the lateral Coulomb interaction within the checkerboard wetting layer amounts to ~ 2.0 eV (see Tables S6 and S7 for details on the different contributions to the adsorption energies; the geometries of the different calculated geometries are provided in a separate zip-file).

4.4.2 Honeycomb Structure at 300 K

We next address the honeycomb structure. The lattice vectors $\vec{a}$ and $\vec{b}$ have an identical length of 2.35 ± 0.08 nm, yielding an unit cell area of 4.78 nm^2. It can be described by a $\begin{bmatrix} 8 & 2 \\ -2 & 10 \end{bmatrix}$ superstructure. Based on the significant fraction of unshifted XPS peaks of anions and cations, we attribute the honeycomb structure to intact IL ion pairs. When addressing the number of ion pairs per unit cell, we have to consider the specific properties of the honeycomb lattice. The unit cell of the honeycomb structure in Fig. 1c (right) and Fig. 5a (right) has 2 bright protrusions (indicated as circles) and 3 dimmer ones (dots). If we assume that the bright protrusions are either anion or cation (and not anions and cations that coincidentally exhibit the same brightness), this immediately implies that the bright protrusions cannot be anions and the dimmer ones cations (or vice versa), as this would violate charge neutrality. One solution is that the bright and dim protrusions are oppositely oriented “sandwiches” composed of stacked cations and anions. Based on our assignment of the well-ordered honeycomb-structure to intact IL ion pairs with unshifted XPS peaks (see previous sections), we propose that the XPS binding energies are not affected by the opposite orientation of the sandwiches; we thus observe only one narrow peak for each element. This structure contains 5 ion pairs per unit cell, which yields an ion pair density of 1.05 ion pairs/nm^2, which is slightly smaller than that of the stripe structure. The fact that some of the pores of the honeycomb structure are empty and some have a dim background is attributed to leftovers of the transformation process.

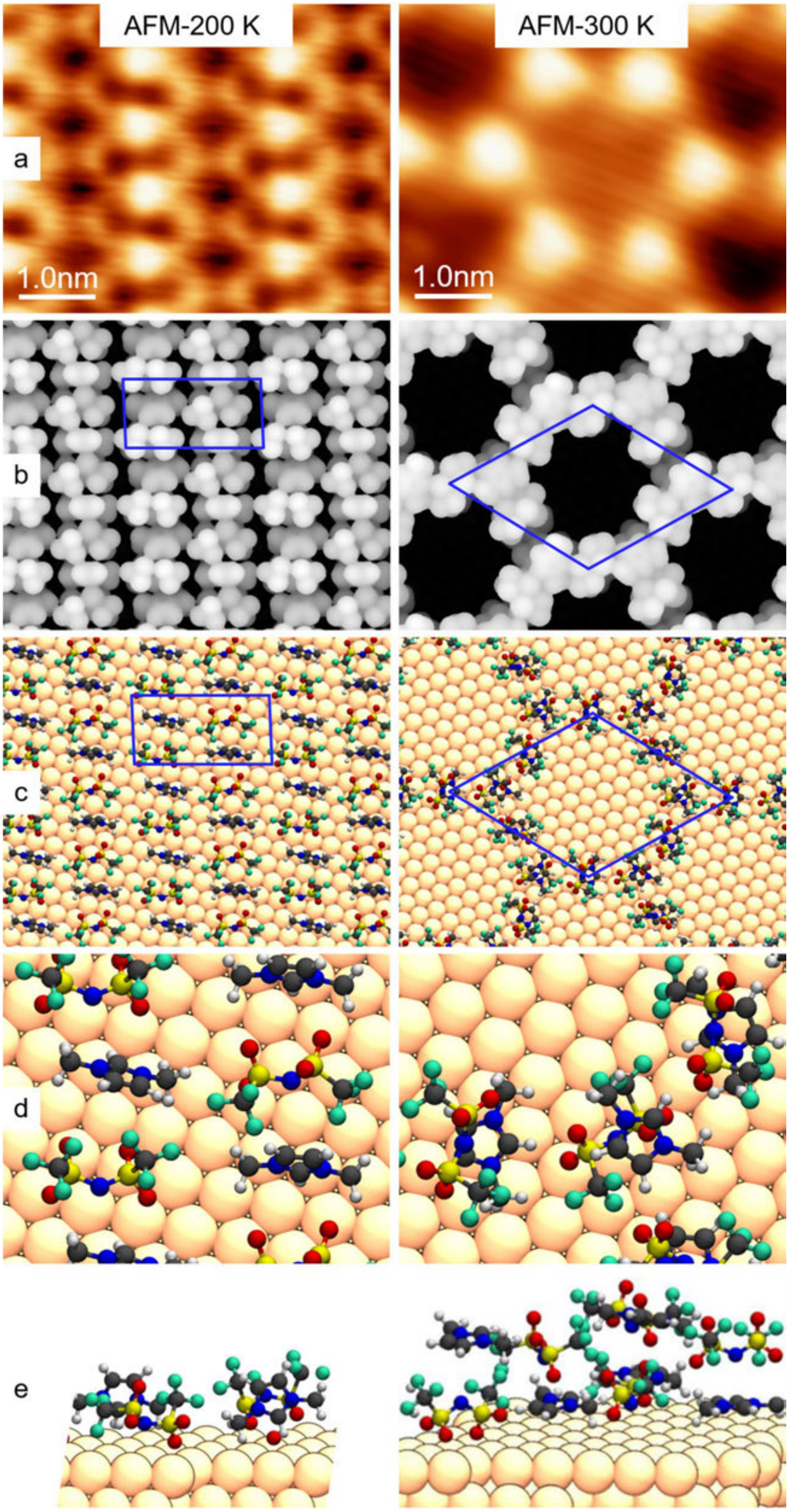

Fig. 5 Surface structure of [C_1C_1Im][Tf_2N] on Cu(111) for the stripe phase (left) and the honeycomb phase (right). **a** nc-AFM images (data from Fig. 1). **b** Charge density plots of the corresponding structures, as derived from DFT calculations. **c** Geometry-optimized structures, as obtained from the DFT calculations. **d** Close-up of the structures shown in (**c**). **e** Side view of the structures shown in (**c**). Graphs (**a**) to (**c**) are shown on the same scale, as indicated by the scale bars in (**a**)

For the honeycomb structure with oppositely oriented sandwiches we also performed DFT calculations. The corresponding structure is shown in Fig. 5c, d and e (right) and the corresponding calculated charge density contour plots in Fig. 5b (right). The structure yields an adsorption energy E_{ads} per ion pair of 3.1 eV, which demonstrates the stability of this porous arrangement. Notably, this adsorption energy value is smaller than the value of 3.5 eV calculated for the nearly rectangular checkerboard–type structure (see above). The reason for the higher adsorption energy of the checkerboard structure is its larger dispersion energy compared to the honeycomb structure; see SI, Table S6. The lower dispersion energy of the honeycomb structure is not surprising because it consists of IL pairs in a sandwich geometry. The top IL molecules of each pair have a larger distance from the metal substrate leading to a smaller dispersion interaction with the substrate. In the checkerboard structure, on the other hand, all IL molecules are in direct contact with the metal substrate structure. One should note that the lower adsorption energy of the honeycomb structure is not expected from the experimental findings, as from a simple consideration one would assume a higher adsorption energy, since upon annealing a transformation towards a more stable structure should occur. Possible reasons are that in the experiment the decomposition of a fraction of the IL layer (yielding the disordered islands) goes along with the formation of the honeycomb structure, and the related energies would have to be included in the total energy balance. An alternative explanation would be that in the calculations, the geometry optimization did not find the global minimum with maximum binding energy. One possible, though unlikely, alternative could be that we actually do not have the structure proposed above, but that a metastable intermediate complex including Cu substrate or adatoms is formed. In particular nitrogen atoms, which are present in the anion and the cation, are known to play an important role in the formation of Cu coordinated frameworks on surfaces [67, 68–70]. The latter considerations are, however, pure speculation.

5 Summary and Conclusions

We investigated the initial formation and thermal stability of sub-monolayer ionic liquid films on Cu(111) as a function of temperature with non-contact atomic force and scanning tunneling microscopy, angle-resolved X-ray photoelectron spectroscopy, and density-functional theory calculations. The IL $[C_1C_1Im][Tf_2N]$ was deposited either at room temperature followed by very fast cooling to 110 K, or directly at low temperatures. Both procedures lead to the adsorption of intact IL on the surface. The thermal evolution of the adsorbate structure and chemical composition was then investigated by stepwise annealing. The nc-AFM and the STM studies were performed for a coverage of 0.15 ML, which corresponds to ~ 30% of the surface being covered with a wetting layer of anions and cations adsorbed next to each other in direct contact with the Cu(111) surface. Due to the low signals, the corresponding XPS studies were performed for coverages of 0.5 and 0.3 ML, which correspond to 100% and 60% of the full wetting layer, respectively.

Annealing to 200 K leads to the formation of large islands. Each island consists of one or more domains of a highly ordered phase characterized by molecular rows, that is, stripes with a nearly rectangular unit cell ($\gamma = 90 \pm 3°$), with lattice vectors of $\vec{a}$ (1.90 ± 0.08 nm) and $\vec{b}$ (0.90 ± 0.05 nm), and a unit cell area of 1.71 nm^2. The checkerboard–type adlayer can be described by a $\begin{bmatrix} 6 & 2 \\ -3 & 4 \end{bmatrix}$ superstructure; the protrusions visible in nc-AFM are assigned to two types of differently oriented anions and the dark spots in-between to the cations. The chemical composition measured by XPS confirms that at 200 K intact anions and cations are indeed adsorbed next to each other. Based on the nc-AFM and XPS results and the DFT calculations, we propose that the unit cell contains 2 ion pairs, yielding a density of 1.17 ion pairs/nm^2. From DFT, we derived an adsorption energy per ion pair of 3.5 eV, which can be decomposed into a contribution of ~ 1.6 eV from the interaction with the substrate and ~ 2.0 eV due to lateral interactions within the IL (see SI, Table S7).

Upon heating to 300 K and annealing at this temperature for hours, we observe a sequence of structural changes in the nc-AFM images which are accompanied by pronounced changes in the XP spectra. In nc-AFM, we observe for the large islands first the transformation of the stripe structure to an overall hexagonal structure and finally to a well-ordered honeycomb-type structure with a pore size of ~ 2 nm, which goes along with the additional appearance of numerous small disordered islands. Simultaneously, a partial conversion of the initial IL peaks towards peaks shifted to lower binding energies is observed in XPS, which is most pronounced for the anions. From the simultaneous appearance of the small disordered islands and the pronounced changes in XPS, we propose that a chemical reaction yielding partial IL decomposition occurs around 300 K, with the reaction products forming the disordered islands. The large islands with the hexagonal and the honeycomb structure still consist of intact ion pairs. Upon further heating to 350 K, only small disordered islands are observed by nc-AFM, and in XPS, the conversion of all anion and cation signals indicates a complete decomposition of the IL on the surface. Notably at this temperature, nearly 50% of the anion-derived reaction products but only 10–20% of the cationic ones left the surface as deduced from the related signal decreases in XPS.

Interestingly, the well-ordered hexagonal and honeycomb structures of the large islands at 300 K have the identical unit cells with lattice vector lengths 2.35 ± 0.08 nm and a unit cell area of ~ 4.78 nm^2; they can be described by a $\begin{bmatrix} 8 & 2 \\ -2 & 10 \end{bmatrix}$ superstructure with an angle of 60°. For the overall hexagonal structure, we assume six ion pairs per unit cell, which yields a density of 1.26 ion pairs/nm^2, and for the honeycomb structure five ion pairs per unit cell, which yields a density of 1.05 ion pairs/nm^2. Notably, the honeycomb structure can be obtained from the overall hexagonal structure by removing one ion pair, which results in the pore of the honeycomb structure. Thus, the hexagonal structure can be seen as metastable transition structure from the stripe phase to the honeycomb phase upon annealing the IL layer at 300 K. From the unit cell area and the number of ion pairs per unit cell, we conclude that in the two structures the IL is not adsorbed in the commonly observed checkerboard arrangement with anions and cation next to each other. We rather propose that they adopt a stacked "sandwich structure" of anions and cations, with the sandwiches adsorbed on the surface alternatingly with opposite orientations. Our DFT calculations indeed show that such a structure is quite stable on the surface with an adsorption energy of 3.1 eV.

To conclude, by a combination of experimental and theoretical methods, we were able to obtain detailed insights into the adsorption and reaction of the IL [C_1C_1Im][Tf_2N] on the Cu(111) surface. In contrast to the adsorption of the same IL on Au(111), a very complex thermal evolution with structural changes and decomposition effects was observed even at room temperature due to the more reactive copper atoms. Moreover, our results allowed for solving apparently conflicting results of two previous studies of related ILs on copper surfaces. We are confident that such model thin film studies under well-defined conditions to gain a molecular understanding into IL-metal interactions at interfaces eventually will allow for a more controlled design and use of ILs for particular applications in many areas.

Supplementary Information The online version contains supplementary material available at https://doi.org/10.1007/s11244-023-01801-y.

Acknowledgements Funded by the Deutsche Forschungsgemeinschaft (DFG, German Research Foundation)—Project-ID 431791331 – SFB 1452 (Catalysis at Liquids Interfaces, CLINT).

Funding Open Access funding enabled and organized by Projekt DEAL. Funding was provided by Deutsche Forschungsgemeinschaft (Project-ID 431791331).

Declarations

Conflict of interest The authors declare no competing interest.

References

1. Welton T (1999) Room-temperature ionic liquids. Solvents for synthesis and catalysis. Chem Rev 99(8):2071–2084
2. Wasserscheid P, Keim W (2000) Ionic liquids—new "solutions" for transition metal catalysis. Angew Chem Int Ed 39(21):3772–3789
3. Wasserscheid P, Welton T (2008) Ionic liquids in synthesis, vol 1. Wiley, New York
4. Plechkova NV, Seddon KR (2008) Applications of ionic liquids in the chemical industry. Chem Soc Rev 37(1):123–150
5. Welton T (2018) Ionic liquids: a brief history. Biophys Rev 10(3):691–706
6. Binnemans K (2005) Ionic liquid crystals. Chem Rev 105(11):4148–4204
7. Crosthwaite JM, Muldoon MJ, Dixon JK, Anderson JL, Brennecke JF (2005) Phase transition and decomposition temperatures, heat capacities and viscosities of pyridinium ionic liquids. J Chem Thermodyn 37(6):559–568
8. Piper SL, Kar M, MacFarlane DR, Matuszek K, Pringle JM (2022) Ionic liquids for renewable thermal energy storage—a perspective. Green Chem 24(1):102–117
9. Endres F, El Abedin SZ (2006) Air and water stable ionic liquids in physical chemistry. Phys Chem Chem Phys 8(18):2101–2116
10. Riisager A, Fehrmann R, Flicker S, van Hal R, Haumann M, Wasserscheid P (2005) Very stable and highly regioselective supported ionic-liquid-phase (SILP) catalysis: continuous-flow fixed-bed hydroformylation of propene. Angew Chem Int Ed 44(5):815–819
11. Steinrück H-P, Wasserscheid P (2015) Ionic liquids in catalysis. Catal Lett 145(1):380–397
12. Pinilla C, Del Pópolo MG, Lynden-Bell RM, Kohanoff J (2005) Structure and dynamics of a confined ionic liquid. Topics of relevance to dye-sensitized solar cells. J Phys Chem B 109(38):17922–17927
13. Zhou F, Liang Y, Liu W (2009) Ionic liquid lubricants: designed chemistry for engineering applications. Chem Soc Rev 38(9):2590–2599
14. Cooper PK, Staddon J, Zhang S, Aman ZM, Atkin R, Li H (2019) Nano-and macroscale study of the lubrication of titania using pure and diluted ionic liquids. Front Chem 7:287
15. Bresme F, Kornyshev AA, Perkin S, Urbakh M (2022) Electrotunable friction with ionic liquid lubricants. Nat Mater 21(8):848–858
16. Avid A, Ochoa JL, Huang Y, Liu Y, Atanassov P, Zenyuk IV (2022) Revealing the role of ionic liquids in promoting fuel cell catalysts reactivity and durability. Nat Commun 13(1):1–13
17. Li R, Zhao Y, Chen Y, Liu Z, Han B, Li Z, Wang J (2018) Imidazolate ionic liquids for high-capacity capture and reliable storage of iodine. Commun Chem 1(1):1–8

18. Tanner EE (2022) Ionic liquids charge ahead. Nat Chem 14(7):842–842
19. Borra EF, Seddiki O, Angel R, Eisenstein D, Hickson P, Seddon KR, Worden SP (2007) Deposition of metal films on an ionic liquid as a basis for a lunar telescope. nature 447 (7147):979–981
20. Seddon KR (2003) A taste of the future. Nat Mater 2(6):363–365
21. Crowhurst L, Lancaster NL, Pérez Arlandis JM, Welton T (2004) Manipulating solute nucleophilicity with room temperature ionic liquids. J Am Chem Soc 126(37):11549–11555
22. Mehnert CP, Cook RA, Dispenziere NC, Afeworki M (2002) Supported ionic liquid catalysis—a new concept for homogeneous hydroformylation catalysis. J Am Chem Soc 124(44):12932–12933
23. Riisagera A, Fehrmanna R, Haumannb M, Wasserscheidb P (2006) Supported ionic liquids: versatile reaction and separation media. Top Catal 40(1):91–102
24. Werner S, Szesni N, Kaiser M, Haumann M, Wasserscheid P (2012) A scalable preparation method for SILP and SCILL ionic liquid thin-film materials. Chem Eng Technol 35(11):1962–1967
25. Zhang GR, Etzold BJ (2021) Emerging applications of solid catalysts with ionic liquid layer concept in electrocatalysis. Adv Func Mater 31(28):2010977
26. Kalb RS (2020) Toward industrialization of ionic liquids. In: Commercial applications of ionic liquids. Springer, New York, pp 261–282
27. Marinkovic JM, Riisager A, Franke R, Wasserscheid P, Haumann M (2018) Fifteen years of supported ionic liquid phase-catalyzed hydroformylation: material and process developments. Ind Eng Chem Res 58(7):2409–2420
28. Naicker L, Schörner M, Kremitzl D, Friedrich HB, Haumann M, Wasserscheid P (2022) Influencing the product distribution in citral hydrogenation using ionic liquid modified Cu catalysts. ChemCatChem 14(19):e202200388
29. Abai M, Atkins MP, Hassan A, Holbrey JD, Kuah Y, Nockemann P, Oliferenko AA, Plechkova NV, Rafeen S, Rahman AA (2015) An ionic liquid process for mercury removal from natural gas. Dalton Trans 44(18):8617–8624
30. Szesni N, Hagemeyer A, Grossmann F, Fischer R, Urbancic M, Lugmair C, Sun M, Hou HC, Lowe DM (2013) Catalyst composition for selective hydrogenation with improved characteristics. Google Patents
31. Endres F, Hoefft O, Borisenko N, Gasparotto LH, Prowald A, Al-Salman R, Carstens T, Atkin R, Bund A, El Abedin SZ (2010) Do solvation layers of ionic liquids influence electrochemical reactions? Phys Chem Chem Phys 12(8):1724–1732
32. Endres F, Borisenko N, El Abedin SZ, Hayes R, Atkin R (2012) The interface ionic liquid (s)/electrode (s): in situ STM and AFM measurements. Faraday Discuss 154:221–233
33. Santos CS, Baldelli S (2010) Gas–liquid interface of room-temperature ionic liquids. Chem Soc Rev 39(6):2136–2145
34. Lahiri A, Borisenko N, Olschewski M, Pulletikurthi G, Endres F (2018) Anomalous electroless deposition of less noble metals on Cu in ionic liquids and its application towards battery electrodes. Faraday Discuss 206:339–351
35. Steinrück HP, Libuda J, Wasserscheid P, Cremer T, Kolbeck C, Laurin M, Maier F, Sobota M, Schulz P, Stark M (2011) Surface science and model catalysis with ionic liquid-modified materials. Adv Mater 23(22–23):2571–2587
36. Lexow M, Maier F, Steinrück H-P (2020) Ultrathin ionic liquid films on metal surfaces: adsorption, growth, stability and exchange phenomena. Adv Phys X 5(1):1761266
37. Lovelock KR, Villar-Garcia IJ, Maier F, Steinrück H-P, Licence P (2010) Photoelectron spectroscopy of ionic liquid-based interfaces. Chem Rev 110(9):5158–5190
38. Steinrück H-P (2010) Surface science goes liquid! Surf Sci 604(5–6):481–484
39. Steinrück H-P (2012) Recent developments in the study of ionic liquid interfaces using X-ray photoelectron spectroscopy and potential future directions. Phys Chem Chem Phys 14(15):5010–5029
40. Buchner F, Forster-Tonigold K, Uhl B, Alwast D, Wagner N, Farkhondeh H, GrossBehm RJr A (2013) Toward the microscopic identification of anions and cations at the ionic liquid| Ag (111) interface: a combined experimental and theoretical investigation. ACS Nano 7(9):7773–7784
41. Uhl B, Cremer T, Roos M, Maier F, Steinrück H-P, Behm RJ (2013) At the ionic liquid| metal interface: structure formation and temperature dependent behavior of an ionic liquid adlayer on Au (111). Phys Chem Chem Phys 15(40):17295–17302
42. Uhl B, Huang H, Alwast D, Buchner F, Behm RJ (2015) Interaction of ionic liquids with noble metal surfaces: structure formation and stability of [OMIM][TFSA] and [EMIM][TFSA] on Au (111) and Ag (111). Phys Chem Chem Phys 17(37):23816–23832
43. Meusel M, Lexow M, Gezmis A, Schötz S, Wagner M, Bayer A, Maier F, Steinrück H-P (2020) Atomic force and scanning tunneling microscopy of ordered ionic liquid wetting layers from 110 K up to room temperature. ACS Nano 14(7):9000–9010
44. Meusel M, Lexow M, Gezmis A, Bayer A, Maier F, Steinrück H-P (2020) Growth of multilayers of ionic liquids on Au (111) investigated by atomic force microscopy in ultrahigh vacuum. Langmuir 36(45):13670–13681
45. Meusel M, Gezmis A, Jaekel S, Lexow M, Bayer A, Maier F, Steinrück H-P (2021) Time-and temperature-dependent growth behavior of ionic liquids on Au (111) studied by atomic force microscopy in ultrahigh vacuum. J Phys Chem C 125(37):20439–20449
46. Biedron AB, Garfunkel EL, Castner EW Jr, Rangan S (2017) Ionic liquid ultrathin films at the surface of Cu (100) and Au (111). J Chem Phys 146(5):054704
47. Uhl B, Buchner F, Gabler S, Bozorgchenani M, Behm RJ (2014) Adsorption and reaction of sub-monolayer films of an ionic liquid on Cu (111). Chem Commun 50(62):8601–8604
48. Lovelock K, Kolbeck C, Cremer T, Paape N, Schulz P, Wasserscheid P, Maier F, Steinrück H-P (2009) Influence of different substituents on the surface composition of ionic liquids studied using ARXPS. J Phys Chem B 113(9):2854–2864
49. Miller SF, Friedrich HB, Holzapfel CW (2012) The effects of SCILL catalyst modification on the competitive hydrogenation of 1-octyne and 1, 7-octadiene versus 1-octene. ChemCatChem 4(9):1337–1344
50. Heinze M, Zill J, Matysik J, Einicke W, Gläser R, Stark A (2014) Solid–ionic liquid interfaces: pore filling revisited. Phys Chem Chem Phys 16(44):24359–24372
51. Hoffmann V, Pulletikurthi G, Carstens T, Lahiri A, Borodin A, Schammer M, Horstmann B, Latz A, Endres F (2018) Influence of a silver salt on the nanostructure of a Au (111)/ionic liquid interface: an atomic force microscopy study and theoretical concepts. Phys Chem Chem Phys 20(7):4760–4771
52. Lexow M, Heller BS, Maier F, Steinrück HP (2018) Anion exchange at the liquid/solid interface of ultrathin ionic liquid films on Ag (111). ChemPhysChem 19(22):2978–2984
53. Horcas I, Fernández R, Gomez-Rodriguez J, Colchero J, Gómez-Herrero J, Baro A (2007) WSXM: a software for scanning probe microscopy and a tool for nanotechnology. Rev Sci Instrum 78(1):013705
54. Maier F, Gottfried JM, Rossa J, Gerhard D, Schulz PS, Schwieger W, Wasserscheid P, Steinrück HP (2006) Surface enrichment and depletion effects of ions dissolved in an ionic liquid: an X-ray photoelectron spectroscopy study. Angew Chem Int Ed 45(46):7778–7780

55. Kresse G, Hafner J (1993) Ab initio molecular dynamics for liquid metals. Phys Rev B 47(1):558
56. Kresse G, Furthmüller J (1996) Efficient iterative schemes for ab initio total-energy calculations using a plane-wave basis set. Phys Rev B 54(16):11169
57. Kresse G, Furthmüller J (1996) Efficiency of ab-initio total energy calculations for metals and semiconductors using a plane-wave basis set. Comput Mater Sci 6(1):15–50
58. Perdew JP, Burke K, Ernzerhof M (1996) Generalized gradient approximation made simple. Phys Rev Lett 77(18):3865
59. Kresse G, Joubert D (1999) From ultrasoft pseudopotentials to the projector augmented-wave method. Phys Rev B 59(3):1758
60. Grimme S, Antony J, Ehrlich S, Krieg H (2010) A consistent and accurate ab initio parametrization of density functional dispersion correction (DFT-D) for the 94 elements H-Pu. J Chem Phys 132(15):154104
61. Methfessel M, Paxton A (1989) High-precision sampling for Brillouin-zone integration in metals. Phys Rev B 40(6):3616
62. Monkhorst HJ, Pack JD (1976) Special points for Brillouin-zone integrations. Phys Rev B 13(12):5188
63. Lexow M, Talwar T, Heller BS, May B, Bhuin RG, Maier F, Steinrück H-P (2018) Time-dependent changes in the growth of ultrathin ionic liquid films on Ag (111). Phys Chem Chem Phys 20(18):12929–12938
64. Cremer T, Stark M, Deyko A, Steinrück H-P, Maier F (2011) Liquid/solid interface of ultrathin ionic liquid films:[C1C1Im][Tf2N] and [C8C1Im][Tf2N] on Au (111). Langmuir 27(7):3662–3671
65. Rietzler F, May B, Steinrück H-P, Maier F (2016) Switching adsorption and growth behavior of ultrathin [C 2 C 1 Im][OTf] films on Au (111) by Pd deposition. Phys Chem Chem Phys 18(36):25143–25150
66. Jiang L, Zhang B, Médard G, Seitsonen AP, Haag F, Allegretti F, Reichert J, Kuster B, Barth JV, Papageorgiou AC (2017) N-Heterocyclic carbenes on close-packed coinage metal surfaces: biscarbene metal adatom bonding scheme of monolayer films on Au. Ag and Cu Chem Sci 8(12):8301–8308
67. Klappenberger F, Weber-Bargioni A, Auwärter W, Marschall M, Schiffrin A, Barth J (2008) Temperature dependence of conformation, chemical state, and metal-directed assembly of tetrapyridylporphyrin on Cu (111). J Chem Phys 129(21):214702
68. Fendt LA, Stöhr M, Wintjes N, Enache M, Jung TA, Diederich F (2009) Modification of supramolecular binding motifs induced by substrate registry: formation of self-assembled macrocycles and chain-like patterns. Chemistry 15(42):11139–11150
69. Lepper M, Schmitt T, Gurrath M, Raschmann M, Zhang L, Stark M, Hölzel H, Jux N, Meyer B, Schneider MA (2017) Adsorption behavior of a cyano-functionalized porphyrin on Cu (111) and Ag (111): from molecular wires to ordered supramolecular two-dimensional aggregates. J Phys Chem C 121(47):26361–26371
70. Adhikari R, Siglreithmaier G, Gurrath M, Meusel M, Kuliga J, Lepper M, Hölzel H, Jux N, Meyer B, Steinrück HP (2020) Formation of highly ordered molecular porous 2D networks from cyano-functionalized porphyrins on Cu (111). Chemistry 26(59):13408–13418

Supporting Information to

Structure and Reactivity of the Ionic Liquid [C_1C_1Im][Tf_2N] on Cu(111)

Rajan Adhikari[1,# ORCID: 0000-0002-3089-8179], Stephen Massicot[1,#,ORCID: 0000-0002-2530-8015], Lukas Fromm[2], Timo Talwar[1], Afra Gezmis[1], Manuel Meusel[1], Andreas Bayer[1, 0000-0002-7353-3532], Simon Jaekel[1, ORCID: 0000-0002-8160-4628], Florian Maier[1, ORCID: 0000-0001-9725-8961], Andreas Görling[2, ORCID: 0000-0002-1831-3318], and Hans-Peter Steinrück[1, *, ORCID: 0000-0003-1347-8962]

[1]Lehrstuhl für Physikalische Chemie II, Friedrich–Alexander–Universität Erlangen–Nürnberg,
Egerlandstr. 3, 91058 Erlangen, Germany

[2]Lehrstuhl für Theoretische Chemie, Friedrich–Alexander–Universität Erlangen–Nürnberg,
Egerlandstr. 3, 91058 Erlangen, Germany

*Corresponding author: hans-peter.steinrueck@fau.de

[#] Shared first-authorship

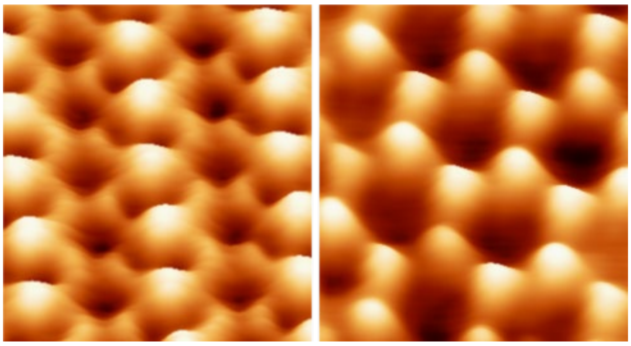

Figure: TOC

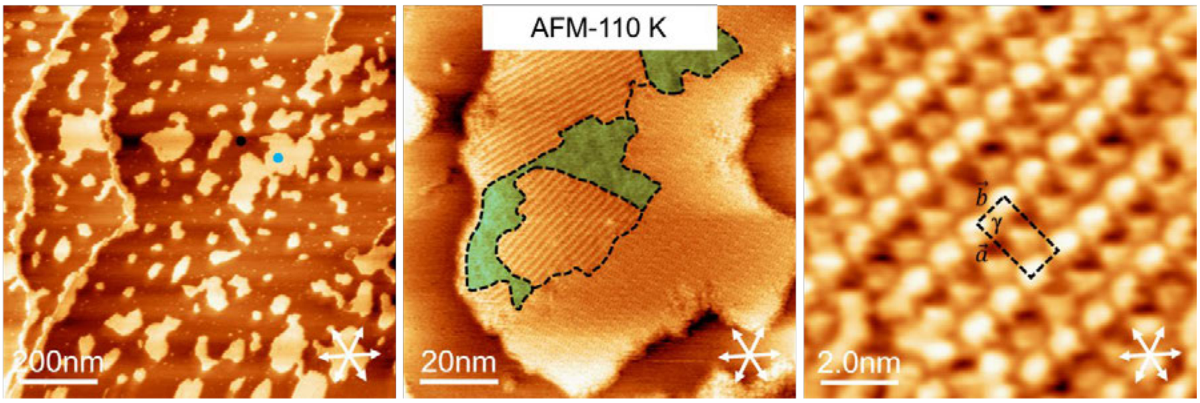

Figure S1. nc-AFM images of $[C_1C_1Im][Tf_2N]$ on Cu(111), deposited at 300 K, quickly cooled down and measured at 110 K. (left) Overview image (1000 x 1000 nm^2) showing IL islands of various shapes and sizes. The blue and black dots indicate IL–covered and IL–free area, respectively. (Middle) Close-up image (100 x 100 nm^2) of an ordered phase of differently oriented domains coexisting with a disordered phase incorporated in–between; boundaries are marked with dashed black lines. (Right) High-resolution image (10 x 10 nm^2) of the ordered phase, which is characterized by molecular rows, that is, stripes with almost a rectangular unit cell ($\gamma = 90 \pm 3°$), with lattice vectors $\vec{a}$ (1.90 ± 0.08 nm) and $\vec{b}$ (0.90 ± 0.05 nm). For details of the phase and the structure, see text. All images were measured with Δf = -400 Hz.

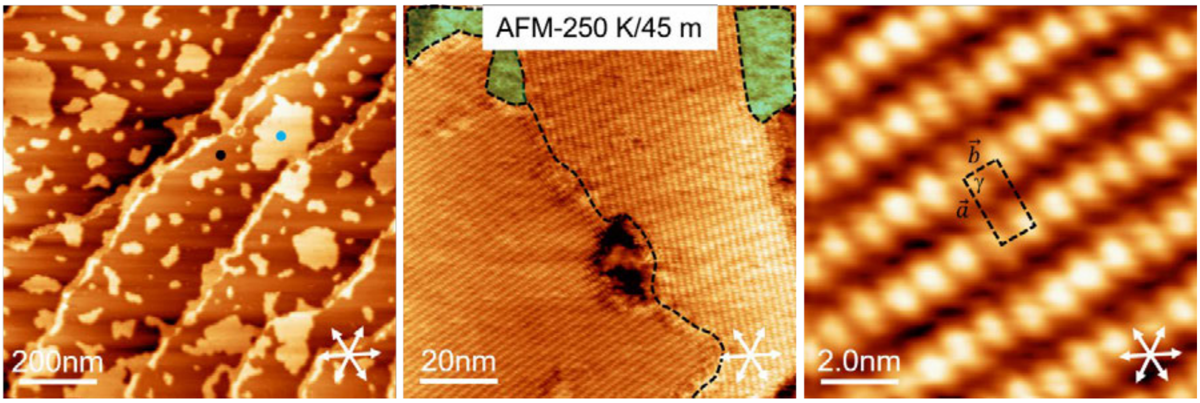

Figure S2. nc-AFM images, measured at 110 K after annealing an adsorbed IL adlayer of $[C_1C_1Im][Tf_2N]$ on Cu(111) at 250 K for 45 min. (left) Overview image (1000 x 1000 nm^2, Δf = -400 Hz) shows IL islands of various shapes and sizes. The blue and black dots indicate IL–covered and IL–free area. (Middle) Close-up image (100 x 100 nm^2, Δf = -600 Hz) depicting an ordered phase of two differently oriented domains with disordered species incorporated in–between; boundaries are marked with broken black lines. (Right) High-resolution image (10 x 10 nm^2, Δf = -400 Hz) of the ordered phase, which is characterized by molecular rows, that is, stripes with a nearly rectangular unit cell ($\gamma = 90 \pm 3°$) with lattice vectors $\vec{a}$ (1.90 ± 0.08 nm) and $\vec{b}$ (0.90 ± 0.05 nm), highlighted with broken black lines. For details of the phase and the structure, see manuscript.

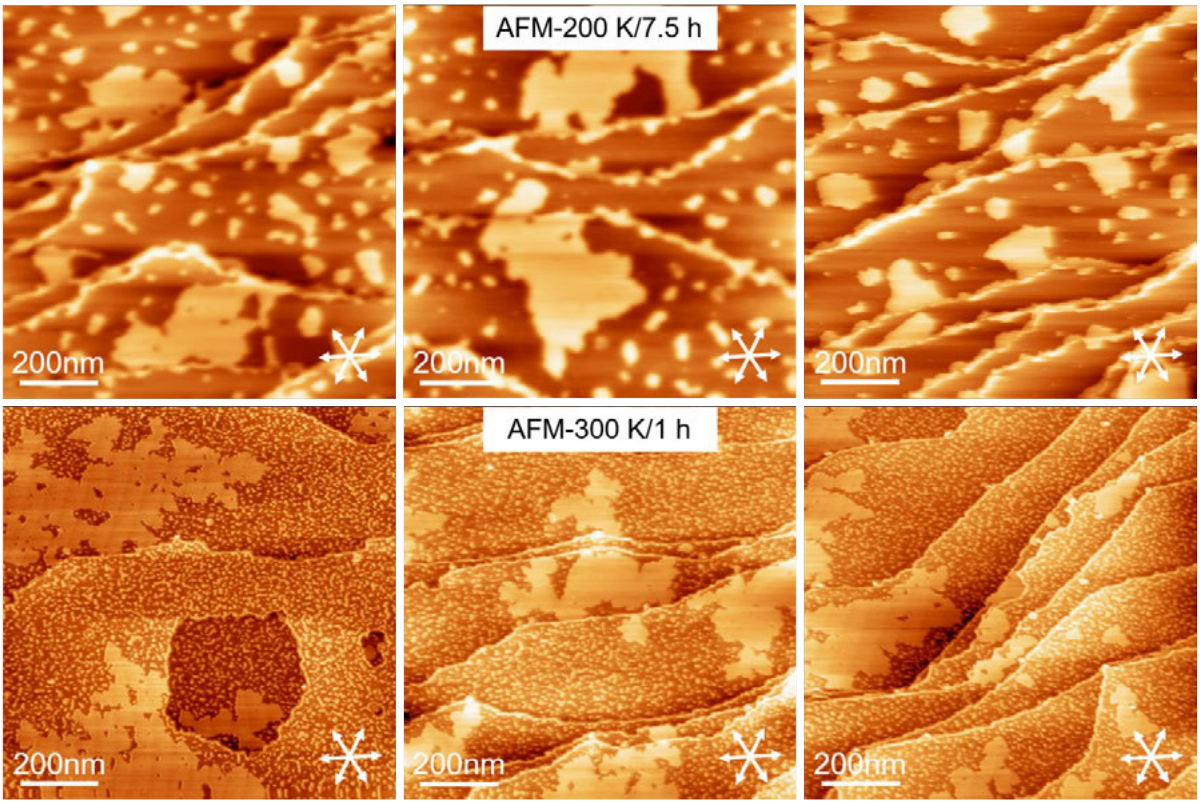

Figure S3. Comparison of a series of nc-AFM overview images (1000 x 1000 nm^2, Δf = -400 Hz) of [C_1C_1Im][Tf_2N] on Cu(111) annealed at 200 K (top) and 300 K (bottom), measured at 110 K. The images clearly show the transformation upon heating, from only large and medium sized islands at 200 K to the coexistence of large and many very small islands at 300 K. High resolution images (Figure 1 in the manuscript) reveal that the large islands are ordered (stripe phase at 200 K, honeycomb phase at 300 K), while the very small islands are disordered (see Figure S4). For details, see manuscript.

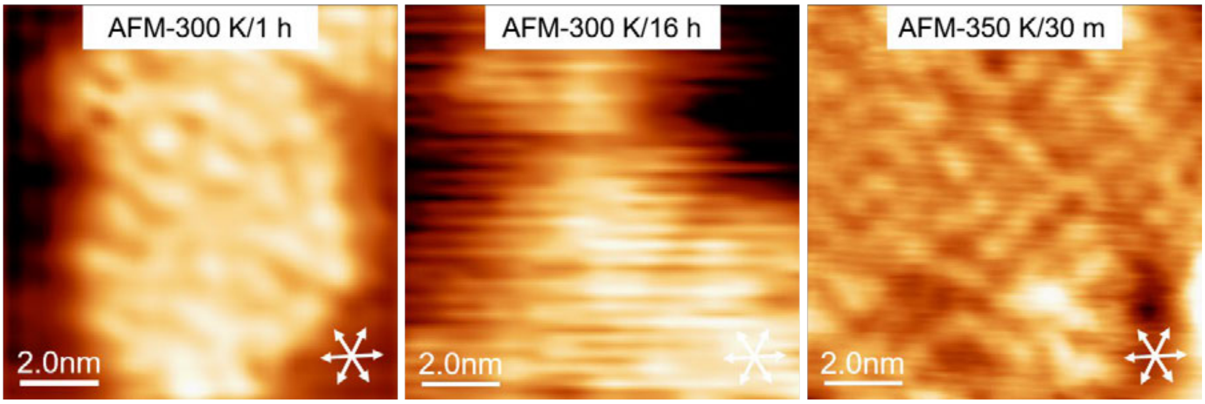

Figure S4. High-resolution nc-AFM images (10 x 10 nm^2, Δf = -500 Hz) of the small islands with disordered internal structure observed after annealing an adsorbed IL adlayer of [C_1C_1Im][Tf_2N] on Cu(111). (Left) At 300 K for 1 h; these islands coexist with large hexagonal–type islands, see Figure 1b. (Middle) At 300 K for 16 h; these islands coexist with large honeycomb-type islands, see Figure 1c. (Right) At 350 K for 30 min; at this temperature, only small disordered islands exist on the surface, see Figure 1d. For details, see manuscript.

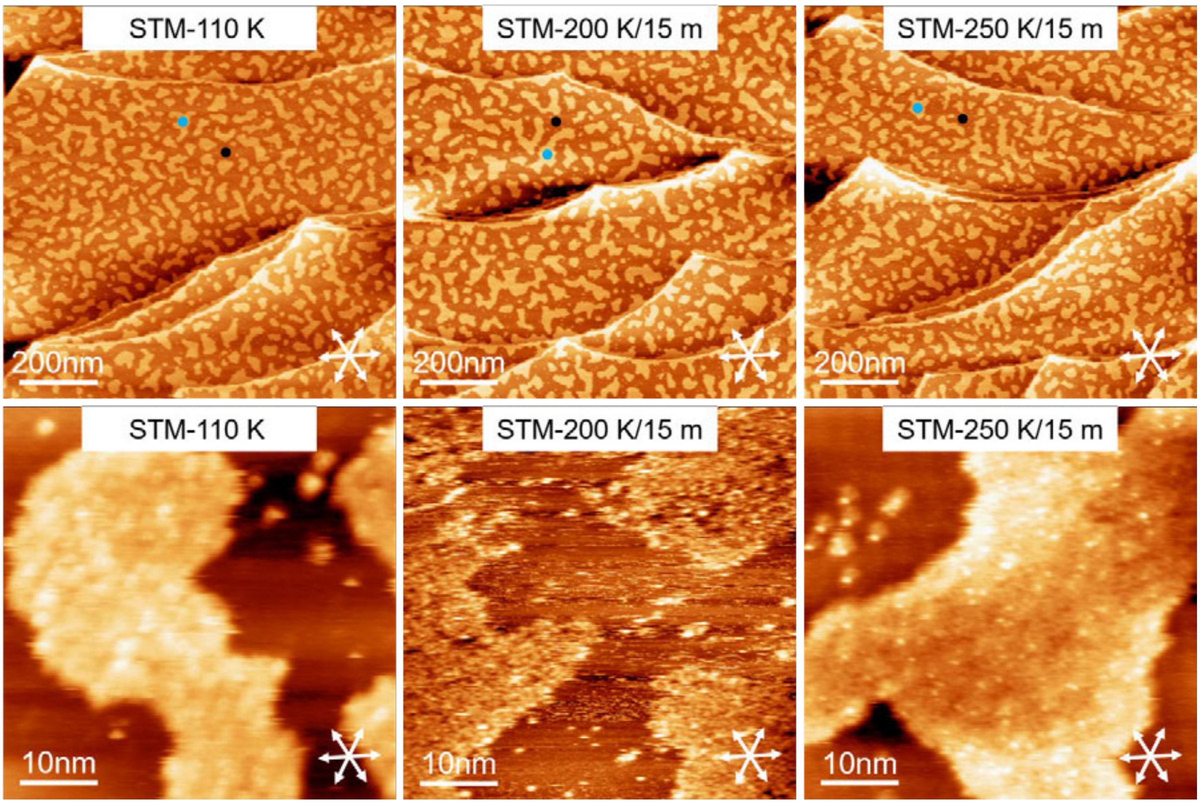

Figure S5. STM images of [C_1C_1Im][Tf_2N] on Cu(111), deposited at <160 K and measured at 110 K (left); the overview image (top, 1000 x 1000 nm^2, U_{bias} = 2 V, I_{set} = 0.5 nA) and the close-up image (bottom, 50 x 50 nm^2, U_{bias} = 2 V, I_{set} = 1.0 nA) show IL islands of various shapes and sizes without long-range order. (Middle) acquired at 110 K after annealing the IL adlayer at 200 K for 15 min; the overview image (top, 1000 x 1000 nm^2, U_{bias} = 2 V, I_{set} = 0.5 nA) also shows IL islands of various shapes and sizes; the close-up image (bottom, 50 x 50 nm^2, U_{bias} = 2 V, I_{set} = 0.6 nA) reveals again the absence of an ordered phase. (Right) STM image acquired at 110 K after annealing the IL adlayer at 250 K for 15 min; the overview image (top, 1000 x 1000 nm^2, U_{bias} = 2 V, I_{set} = 0.2 nA) also shows IL islands of various shapes and sizes, and the close-up image (bottom, 50 x 50 nm^2, U_{bias} = 2 V, I_{set} = 0.6 nA) shows again only a disordered phase. In the overview images, the blue and black dots indicate IL–covered and IL–free areas. For details, see manuscript.

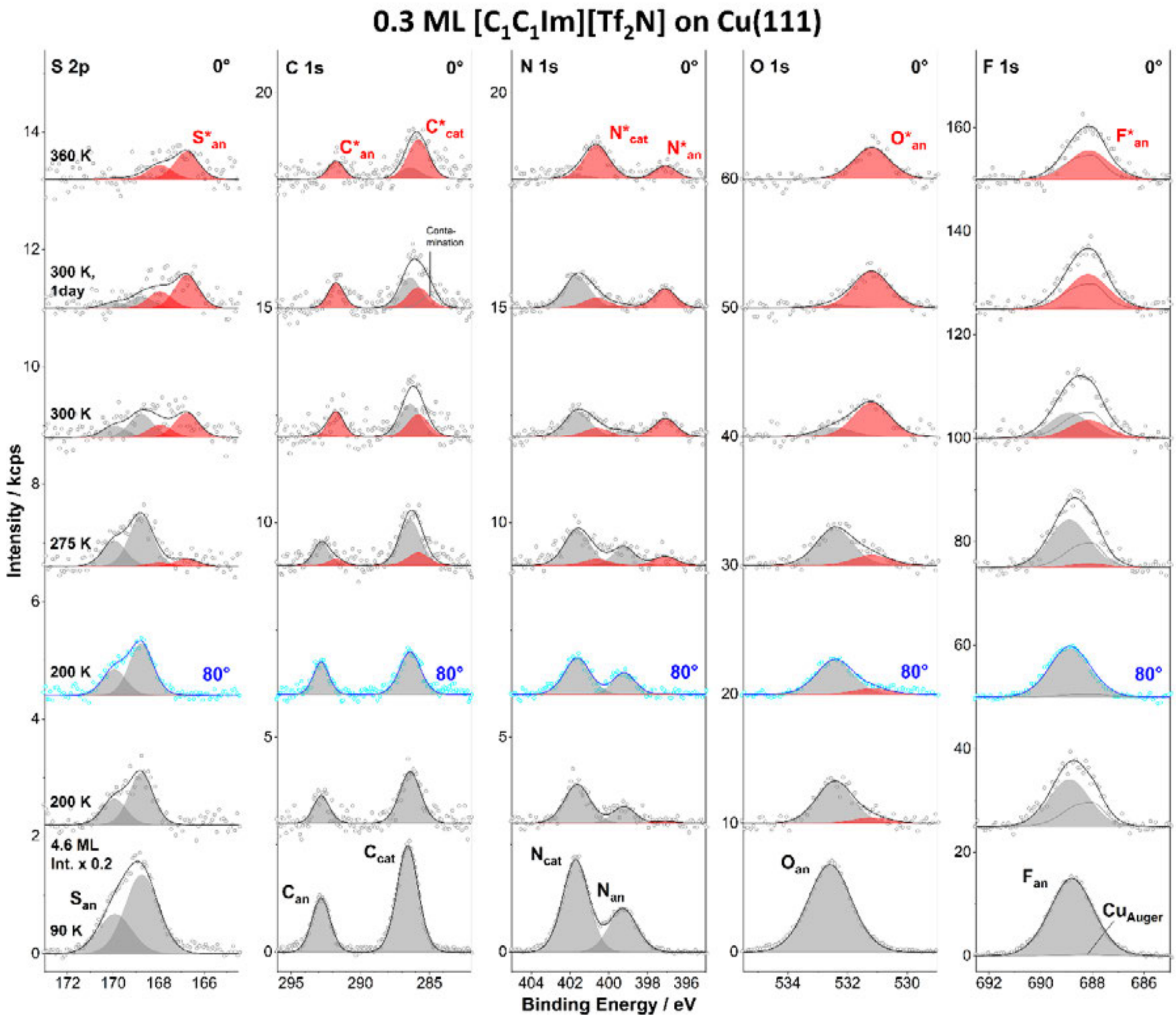

Figure S6. S 2p, C 1s, N 1s, O 1s and F 1s spectra of 0.3 ML $[C_1C_1Im][Tf_2N]$ on Cu(111) from 200 to 360 K, along with the spectra for 4.6 ML obtained at 90 K as reference for the bulk IL (bottom). For each denoted temperature, a new layer were freshly prepared and measured under normal (0°) and grazing emission (80°; shown only for 200 K in blue). For a better visualization, the 4.6 ML spectra are scaled down by a factor of 0.2. Grey peaks indicate the signals of the intact IL, red peaks denote the peaks of the new species formed upon heating. In the C 1s spectra a small contamination of the surface was taken into account, as indicated exemplarily in the spectrum at 200 K; in the F 1s spectra, the overlapping Cu_{Auger} signal was subtracted (for more details, see experimental section and SI).

Table S1. Quantitative analysis of the composition of **0.3 ML** [C_1C_1Im][Tf_2N] on Cu(111) at different temperatures, as derived from the XP spectra shown in Figure S6 at 0° (and for 200 K also at 80°) emission angle. Also given are the results for 4.6 ML deposited at 90 K and measured under 0° emission as reference for the bulk IL. For quantification, the shifted (marked with asterisk) and the unshifted signals of the IL were combined to provide the total atom number for each element.

Temperature	$S_{an, sum}$	$C_{an, sum}$	$C_{cat, sum}$	$N_{cat, sum}$	$N_{an, sum}$	$O_{an, sum}$	$F_{an, sum}$	**Σ**
nominal	**2**	**2**	**5**	**2**	**1**	**4**	**6**	**22**
360 K	1.0	0.9	4.4	1.7	0.5	2.6	4.6	15.7
300 K, 1 day	1.7	1.9	5.1	2.1	1.0	3.7	6.5	21.4
300 K	1.7	1.9	5.1	1.6	1.0	3.7	7.1	22.0
275 K	1.8	1.7	4.7	1.7	1.0	3.6	7.4	22.0
200 K, 80°	1.9	2.2	3.9	1.7	0.9	3.4	7.9	22.0
200 K	1.8	1.9	4.6	1.8	1.3	3.9	7.3	22.0
90 K	1.8	2.0	4.6	2.0	1.0	4.2	6.4	22.0

Subtraction of Auger-LMM and contamination signals

On the (freshly cleaned) Cu(111) surface an Auger-LMM signal and additional small surface contaminations in the C 1s or O 1s region may occur. After film deposition these signals are damped and have to be subtracted for the quantitative analysis of the IL signals. The expected damping factor, I_d/I_0, is calculated via the substrate Cu $2p_{3/2}$ damping by taking into account the different mean free pathes λ_{Cu2p} and $\lambda_{Aug/Cont}$ for Cu $2p_{3/2}$ photoelectrons and Auger electrons/contamination photo-electrons, respectively:

$$\frac{I_{d,\,\mathrm{Auger/cont.}}}{I_{0,\,\mathrm{Auger/cont.}}} = \left(\frac{I_{d,\,Cu\,2p}}{I_{0,\,Cu\,2p}}\right)^{\frac{\lambda_{Cu\,2p}}{\lambda_{Auger/cont.}}}$$

Table S2. Binding energies and fit parameter fwhm used for fitting the different XPS peaks

Signal	S_{an}	S_{an}*	C_{an}	C_{an}*	C_{cat}	C_{cat}*	N_{cat}	N_{cat}*	N_{an}	N_{an}*	O_{an}	O_{an}*	F_{an}	F_{an}*
Binding Energy / eV	168.77	166.77	292.83	291.75	286.40	285.82	401.63	400.64	399.21	397.08	532.44	531.19	688.89	688.15
fwhm / eV	1.23		1.32		1.79		1.56		1.38		1.43		1.45	

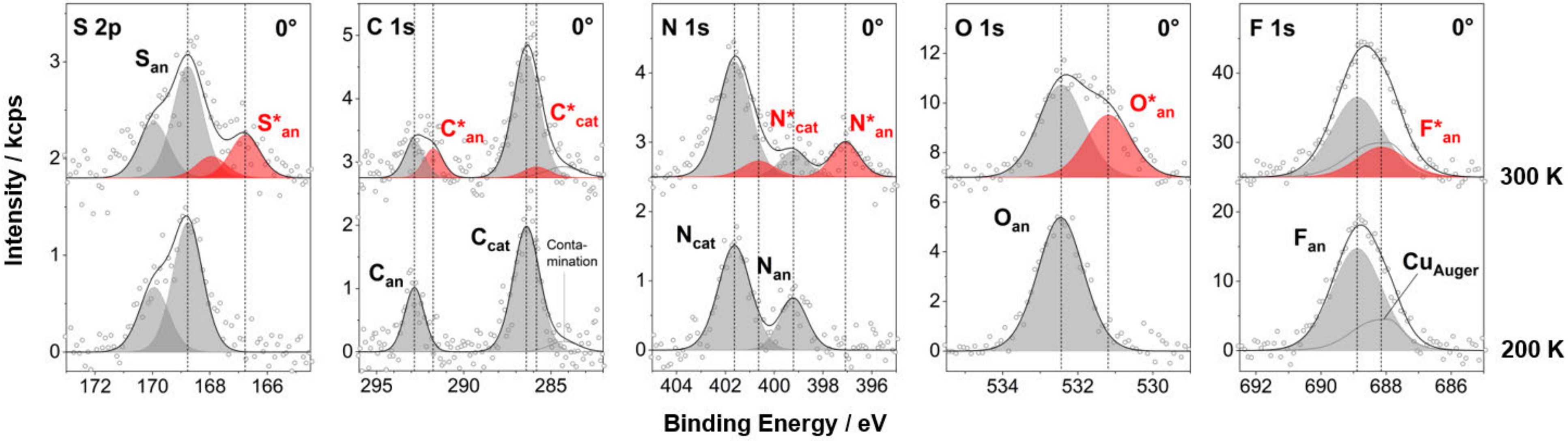

Figure S7. S 2p, C 1s, N 1s, O 1s and F 1s spectra of 0.5 ML $[C_1C_1Im][Tf_2N]$ on Cu(111) at 200 and 300 K; data from Figure 3, but at an enlarged scale. Grey peaks indicate the signals of the intact IL, red peaks denote the peaks of the new species formed upon heating. Vertical lines indicate the peak positions – see Table S2. In the C 1s spectra a small contamination of the surface was taken into account; in the F 1s spectra, the overlapping Cu_{Auger} signal was subtracted.

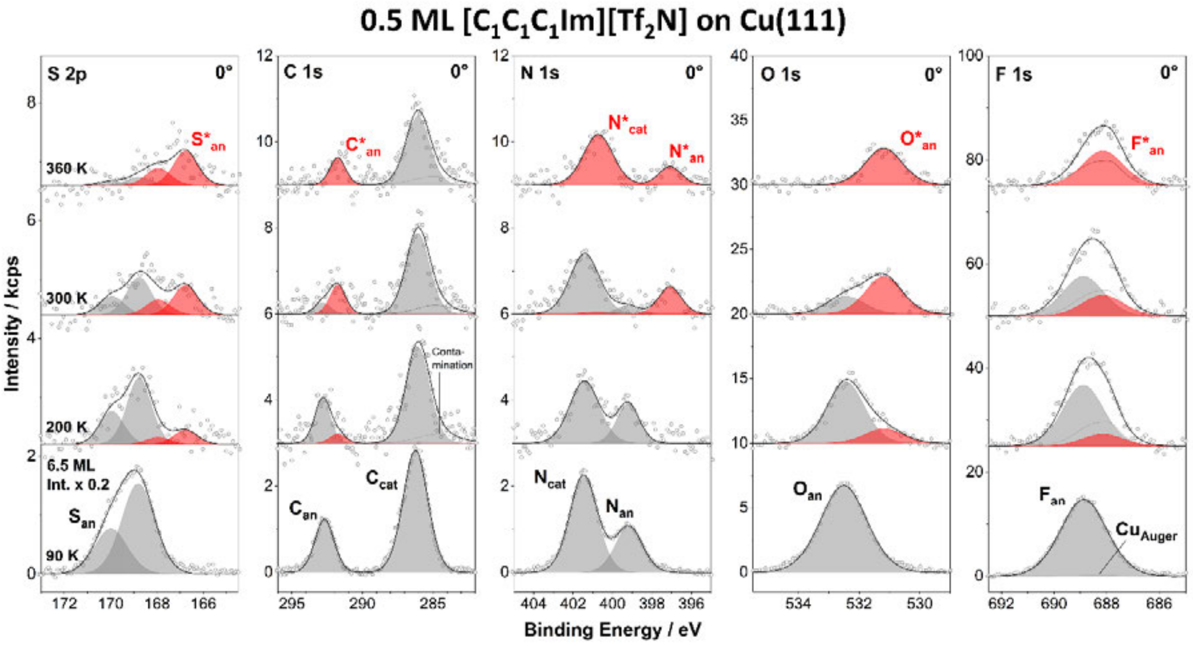

Figure S8. S 2p, C 1s, N 1s, O 1s and F 1s spectra of 0.5 ML [$C_1C_1C_1$Im][Tf_2N] on Cu(111) from 200 to 360 K, along with the spectra for 6.5 ML obtained at 90 K as reference for the bulk IL (bottom). The spectra have been measured for freshly prepared layers (for sample preparation see text) at the denoted temperatures under normal emission (0°). For better visualization, the 6.5 ML spectra are scaled down by a factor of 0.2. Grey peaks indicate the signals of the intact IL, red peaks denote the peaks of new species formed upon heating. In the C 1s spectra a small contamination of the surface was taken into account, as indicated exemplarily in the spectrum at 200 K. In the F 1s spectra, Cu_{Auger} peak was subtracted (for details see experimental section)

Table S3. Quantitative analysis of the composition of **0.5 ML** [$C_1C_1C_1$Im][Tf_2N] on Cu(111) at different temperatures, as derived from the XP spectra shown in Figure S7 at 0° emission angle. Also given are the data for 6.5 ML obtained at 90 K under 0° emission as reference for the bulk IL. For quantification, the shifted (marked with asterisk) and the unshifted signals of the IL were combined to provide the total atom number for each element.

Temperature	$S_{an, sum}$	$C_{an, sum}$	$C_{cat, sum}$	$N_{cat, sum}$	$N_{an, sum}$	$O_{an, sum}$	$F_{an, sum}$	Σ
nominal	**2**	**2**	**6**	**2**	**1**	**4**	**6**	**23**
360 K	0.9	1.1	4.0	1.6	0.4	1.8	3.3	13.2
300 K	1.7	1.9	5.8	2.3	1.0	3.4	6.9	23.0
200 K	1.7	2.1	5.7	1.9	0.9	3.8	6.9	23.0
90 K	1.9	1.9	5.7	2.1	1.0	4.1	6.2	23.0

Table S4. List of nc-AFM and STM images in Figure 1, and Figures S1 - S5, along with their operating conditions and File IDs.

Figures	**Methods**	**nc-AFM set frequency *Δf* [Hz]**	**STM U_{bias} [V], I_{set} [nA]**	**File IDs [YYMMDD_##_##]**
1a (L)	nc-AFM	-400 Hz		20201125_43_1
1a (M)	nc-AFM	-400 Hz		20201126_35_1
1a (R) / 5a (L)	nc-AFM	-400 Hz		20201126_27_3 to 27_11
1b (L)	nc-AFM	-400 Hz		20201130_83_1
1b (M)	nc-AFM	-500 Hz		20201130_52_1
1b (R)	nc-AFM	-400 Hz		20201130_73_1
1c (L)	nc-AFM	-500 Hz		20201201_42_2
1c (M)	nc-AFM	-500 Hz		20201201_47_1
1c (R) / 5a (R)	nc-AFM	-500 Hz		20201201_51_1 to 51_2
1d (L)	nc-AFM	-400 Hz		20210826_44_4
1d (M)	nc-AFM	-400 Hz		20210826_88_1
1d (R)	nc-AFM	-400 Hz		20210826_95_1
1e (L)	STM		2 V, 0.4 nA	20200901_35_1
1e (M)	STM		2 V, 0.4 nA	20200901_36_3
1e (R)	STM		2 V, 0.2 nA	20200831_65_1
S1 (L)	nc-AFM	-400 Hz		20201124_41_1
S1 (M)	nc-AFM	-400 Hz		20201124_95_1
S1 (R)	nc-AFM	-400 Hz		20201124_105_1
S2 (L)	nc-AFM	-400 Hz		20201126_59_2
S2 (M)	nc-AFM	-600 Hz		20201127_30_1
S2 (R)	nc-AFM	-400 Hz		20201126_190_1
S3 (L-T)	nc-AFM	-400 Hz		20201125_43_1
S3 (M-T)	nc-AFM	-400 Hz		20201126_6_1
S3 (R-T)	nc-AFM	-400 Hz		20201125_143_2
S3 (L-B)	nc-AFM	-400 Hz		20201127_75_1
S3 (M-B)	nc-AFM	-400 Hz		20201130_83_1
S3 (R-B)	nc-AFM	-400 Hz		20201201_73_1
S4 (L)	nc-AFM	-500 Hz		20201130_48_1
S4 (M)	nc-AFM	-500 Hz		20201201_38_1
S4 (R)	nc-AFM	-400 Hz		20210826_95_1
S5 (L-T)	STM		2 V, 0.5 nA	20200826_11_21
S5 (M-T)	STM		2 V, 0.5 nA	20200827_66_1
S5 (R-T)	STM		2 V, 0.2 nA	20200829_2_5
S5 (L-B)	STM		2 V, 1.0 nA	20200826_24_3
S5 (M-B)	STM		2 V, 0.6 nA	20200827_39_1
S5 (R-B)	STM		2 V, 0.6 nA	20200829_17_2
L = Left, M = Middle, R = Right, T = Top, and B = Bottom				

Table S5. List of the preparation conditions and File IDs for the XP spectra in Figure 2, 3, 4, S6, S7 and S8.

Figure	Temperature	ID
2	275, 300 K	210512-05 & -08 210623-04 & -06 210804-03 & -04 210804-05 & -06 210908-05 & -07 210910-05 & -06 210930-05 & -07 211111-03 & -04 211118-05 & -06 211123-03 & -04 211215-01 & -02
	200 K	210831-04 & -06 210902-05 & -06 211025-05 & -06 211104-03 & -04
	90 K	210629-03 & -04 210707-04 & -05 210707-06 & -07 210707-08 & -09 210709-03 & -04 210709-05 & -06 210714-03 & -05 210714-06 & -07 210723-04 & -05 210723-06 & -07
3	360 K	210914-05
	300 K, 1 day	210923-01
	300 K	210907-04
	275 K	210928-07
	200 K, 80°	210902-06
	200 K	211112-03
	90 K	210705-05
4	84 K ↓ 800 K	210709-07 ↓ 210709-18
S6	360 K	211029-04
	300 K, 1 day	211130-01
	300 K	211110-04
	275 K	211117-03
	200 K, 80°	211104-04
	200 K	211029-03
	90 K	210705-05
S7	300 K	210907-04
	200 K	211112-03
S8	360 K	221004-04
	300 K	220923-04
	200 K	220918-04
	90 K	220921-05

Table S6: DFT results for the most stable structures; energies given in eV

	total energy	**total disp energy**	**adsorption energy**	**adsorption energy “without disp”**	**disp adsorption energy**	**geometry**
ion pair	-178.99	-0.67	-	-	-	IL_ref
anion	-87.62	-0.25	-	-	-	Anion_ref
cation	-90.08	-0.14	-	-	-	Cation_ref
surf 62	-462.58	-42.79	-	-	-	Surf62_ref
surf 82	-1295.13	-120.31	-	-	-	Surf82_ref
struct1 62	-825.01	-48.05	-3.51	-1.28	-2.24	struct62_1
struct2 62	-824.92	-48.03	-3.47	-1.24	-2.22	struct62_2
struct3 62	-824.88	-48.04	-3.45	-1.22	-2.23	struct62_3
struct4 62	-824.80	-48.11	-3.41	-1.14	-2.27	struct62_4
struct1 82	-2198.97	-130.71	-3.07	-1.38	-1.69	struct82_1
struct2 82	-2198.23	-130.30	-2.92	-1.31	-1.61	struct82_2

The entry ‘struct1 62’ in Table S6 refers to the stripe structure discussed in the main text. The entries ‘struct2 62’, ‘struct3 62’ and ‘struct4 62’ refer to other geometries representing local minima. The entry ‘struct1 82’ refers to the honeycomb structure in the main text. The entry ‘struct2 82’ refers to another geometry representing a local minimum.

Table S7: Decomposition of DFT energies in horizontal interactions present already in a freestanding IL layer and vertical interactions with the substrate emerging after placing the IL layer on the substrate; energies in eV. For a description of the considered stripe and honeycomb structure see text right after Table S6.

	total energy freestanding IL	**total disp energy freestanding IL**	**horizontal interaction**	**vertical interaction**	**disp horizontal interaction**	**disp vertical interaction**
struct1 62 (2 ion pairs)	-359.31	-1.77	-1.96	-1.56	-0.49	-1.74
struct1 82 (5 ion pairs)	-898.36	-4.63	-1.97	-1.10	-0.53	-1.15
struct2 82 (5 ion pairs)	-898.64	-4.53	-2.03	-0.89	-0.51	-1.09

[P4]

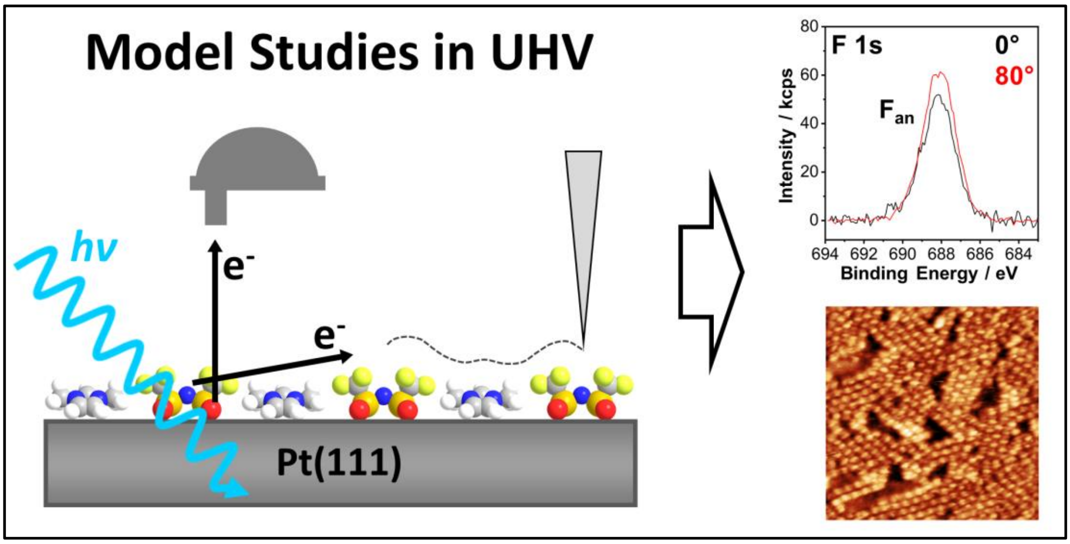

Adsorption and Thermal Evolution of $[C_1C_1Im][Tf_2N]$ on Pt(111).

S. Massicot, A. Gezmis, T. Talwar, M. Meusel, S. Jaekel, R. Adhikari, L. Winter, C. C. Fernández, A. Bayer, F. Maier, H.-P. Steinrück:

Phys. Chem. Chem. Phys. **2023**, 25, 27953-27966

DOI: 10.1039/d3cp02743k

Volume 25
Number 41
7 November 2023
Pages 27895–28542

PCCP

Physical Chemistry Chemical Physics

rsc.li/pccp

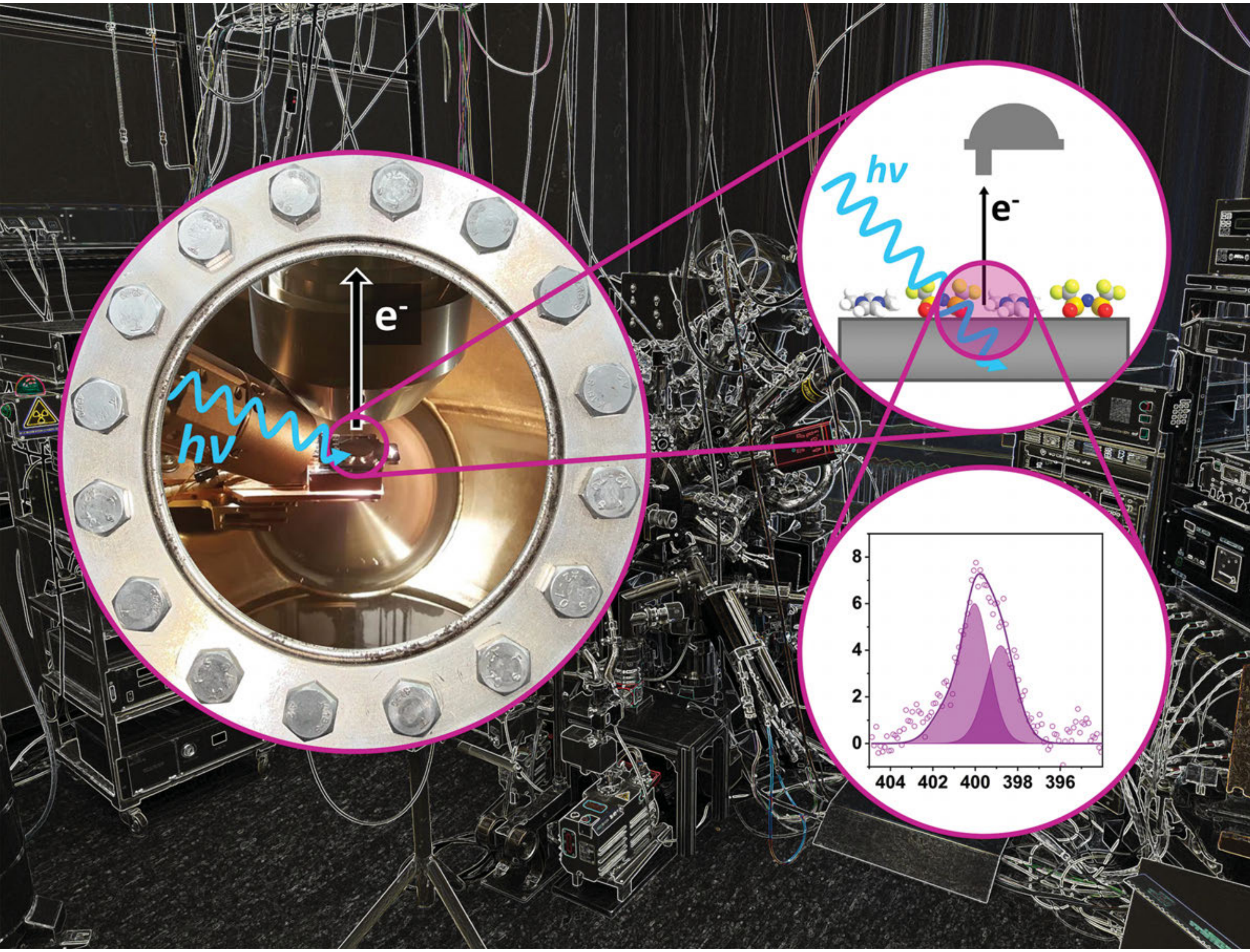

ISSN 1463-9076

ROYAL SOCIETY
OF CHEMISTRY

PAPER
Hans-Peter Steinrück *et al.*
Adsorption and thermal evolution of $[C_1C_1Im][Tf_2N]$ on Pt(111)

PCCP
Owner Societies

PCCP

ROYAL SOCIETY OF CHEMISTRY

PAPER

Check for updates

Cite this: *Phys. Chem. Chem. Phys.*, 2023, **25**, 27953

Adsorption and thermal evolution of $[C_1C_1Im][Tf_2N]$ on Pt(111)†

Stephen Massicot, Afra Gezmis, Timo Talwar, Manuel Meusel, Simon Jaekel, Rajan Adhikari, Leonhard Winter, Cynthia C. Fernández, Andreas Bayer, Florian Maier and Hans-Peter Steinrück*

In the context of ionic liquid (IL)-assisted catalysis, we have investigated the adsorption and thermal evolution of the IL 1,3-dimethylimidazolium bis(trifluoromethylsulfonyl)imide ($[C_1C_1Im][Tf_2N]$) on Pt(111) between 100 and 800 K by angle-resolved X-ray photoelectron spectroscopy and scanning tunneling microscopy. Defined amounts of IL in the coverage range of a complete first wetting layer were deposited at low temperature (100–200 K), and subsequently heated to 300 K, or directly at 300 K. At 100 K, the IL adsorbs as an intact disordered layer. Upon heating to 200 K, the IL stays intact, but forms an ordered and well-oriented structure. Upon heating to 250 K, the surface order increases, but at the same time STM and XPS indicate the onset of decomposition. Upon heating to 300 K, decomposition progresses, such that 50–60% of the IL is decomposed. The anion-related reaction products desorb instantaneously, and the cation-related products remain on the surface. Thereby, the surface is partly passivated, enabling the remaining IL to still be adsorbed intact at 300 K. For IL deposition directly at 300 K, a fraction of the IL instantaneously decomposes, with the anion-related products desorbing, opening free space for further deposition of IL. Hence, cation-related species accumulate at the expense of anions, until one fully closed wetting layer is formed. As a consequence, a higher dose is required to reach this coverage at 300 K, compared to 100–200 K.

Received 12th June 2023,
Accepted 18th August 2023

DOI: 10.1039/d3cp02743k

rsc.li/pccp

Introduction

Catalytic processes in modern industry are in some way involved in the processing of over 80% of all manufactured products.[1] Particularly in the chemical industry, catalysts are even used for the production of about 90% of all chemicals.[2] Pushing towards a more sustainable chemical industry, "greener" and more efficient catalyst technologies have to be developed. In this context, ionic liquids (ILs) have been applied in industrial processes on the large scale.[3–5] ILs are a class of compounds that consist solely of cations and anions and exhibit melting points typically well below 100 °C. Novel catalytic concepts based on ILs were developed like the SCILL (solid catalyst with ionic liquid layer) approach.[6–9] In SCILL, a thin IL film is added to a solid catalyst material – often metal nanoparticles dispersed on a porous support. In the course of the catalytic turnover, the reactants have to pass through the IL layer in order to reach the active sites of the solid catalyst, where the actual chemical conversion takes place. By exploiting differences in the solubility and diffusion rate of competing reactants (and products), the concentration and reactivity close to the active metal sites can be tuned. More importantly, the IL also interacts directly with the solid catalyst.[10–13] Hereby, the IL can modify sites by ligand-like interactions or block less selective sites of the solid catalyst and thus increase the selectivity of the catalytic process. Such SCILL systems are already commercially available by Clariant for the selective hydrogenation of unsaturated hydrocarbons.[14] In 2017, the Dow Chemical Company started up a new world-scale production site using a SCILL catalyst for the ultra-selective hydrogenation of acetylene to form ethylene, which is a crucial feedstock for the production of a variety of polymers.[15]

Despite successful applications of ILs in the chemical industry, a thorough understanding of SCILL catalysts on the molecular scale is still lacking, particularly with respect to the interface formed between the IL and the solid catalyst, which plays a crucial role as the chemical conversion happens there. Thus, fundamental knowledge about the film growth, wetting, thermal behavior and orientation of the ions at this interface is crucial for SCILL catalysis. These properties can be addressed by detailed surface science studies of thin IL films on metallic substrates as model catalysts. However, mostly less reactive surfaces, like Au(111) or Ag(111), have been investigated so

---

Lehrstuhl für Physikalische Chemie II, Friedrich-Alexander-Universität Erlangen-Nürnberg, Egerlandstraße 3, 91058 Erlangen, Germany.
E-mail: hans-peter.steinrueck@fau.de

† Electronic supplementary information (ESI) available. See DOI: **https://doi.org/10.1039/d3cp02743k**

far,[16–20] and only a few studies exist on more reactive surfaces such as Cu(111),[21,22] Ni(111),[23] Pd(111)[24,25] or Pt(111).[26,27] The latter is particularly interesting since ILs were reported to promote platinum-based fuel cell catalysts,[28] particularly by improving the oxygen reduction reaction.[29,30]

With this work, we aim to thoroughly investigate a more application-relevant IL/metal model system. We chose the IL 1,3-dimethylimidazolium bis(trifluoromethylsulfonyl)imide ([C_1C_1Im][Tf_2N], see top of Fig. 1) since this IL was already well characterized in surface science studies on Au(111), Ag(111) and Cu(111) in our group.[20,21,23,31–35] As model catalyst, we selected the Pt(111) single crystal surface, as platinum-based catalysts are widely used in the chemical industry. Moreover, evaporated IL films of the very similar IL [C_2C_1Im][Tf_2N] on Pt(111) had already been studied by means of infrared spectroscopy.[26,27] We will compare our results to this study, and provide additional insights also for this system. For our model catalytic approach, we used *in situ* physical vapor deposition (PVD) to prepare ultrathin films of [C_1C_1Im][Tf_2N] on Pt(111). These films were then studied by scanning tunneling microscopy (STM) and angle-resolved X-ray photoelectron spectroscopy (ARXPS).

Experimental

The ionic liquid [C_1C_1Im][Tf_2N] was either bought from IoLiTec (used in the XPS measurements) or synthesized under ultraclean conditions described in a previous publication (used in the STM measurements).[36] The cation [C_1C_1Im]$^+$ is also known as [MMIm]$^+$ in literature,[37] and the anion [Tf_2N]$^-$ as [NTf_2]$^-$[38] or [TFSA]$^-$.[39] The IL was thoroughly degassed under ultrahigh vacuum (UHV) prior to deposition to remove volatile impurities. The STM and the ARXPS experiments were performed in two independent UHV systems with base pressures below 2×10^{-10} mbar. Using a home-built Knudsen cell, the IL was deposited onto the Pt(111) crystal at different temperatures by physical vapor deposition (PVD),[40] with the crucible temperature between 385–398 K. It has been shown before that this IL can be evaporated intact.[16] IL coverages are denoted in ML, where 1 ML corresponds to a complete layer of vertically oriented ion pairs with an ion density as in the bulk. For a complete first wetting layer in a checkerboard-like arrangement with anions and cations adsorbing next to each other in direct contact to the surface, this coverage corresponds to 0.5 ML. One should note that the real IL coverage required to form a closed wetting layer at the metal surface can deviate from this 0.5 ML value due to the specific ion/substrate interactions, the resulting adsorption geometry and long-range ordered structures.

All STM measurements were performed using a Scienta Omicron VT-AFM-Q + -XA microscope in a two-chamber UHV system. The Pt(111) surface was cleaned by Ar$^+$ ion sputtering (1 keV), annealing at 1100 K for 10 min, an oxidizing step at 1×10^{-6} mbar O_2 pressure for 10 min at 800 K, and a final annealing/oxygen desorption step at 1100 K for 10 min. The IL doses were calibrated with a quartz crystal microbalance in close proximity to the sample in the preparation chamber. After IL deposition on the sample at 157 K, the sample was then quickly transferred within 4–8 min to the pre-cooled AFM/STM sample stage in the analysis chamber at 110 K for the measurements. After annealing at selected temperatures for a given time in the analysis chamber, STM images were then again recorded at 110 K using a tungsten tip in constant current mode. The images were processed with Gwyddion software and moderate filtering. The processing included background subtraction and 2D FFT filtering. For a consistent scaling, some images were cut in Gwyddion and/or CorelDraw software, which was used to prepare the figures.

ARXPS measurements were done in a different two-chamber XPS system equipped with a non-monochromated Al Kα X-ray source (SPECS XR 50, 1486.6 eV, 240 W) and a hemispherical electron analyzer (VG SCIENTA R3000); for details see ref. 33. The Pt(111) surface was cleaned by Ar$^+$ ion sputtering (600 eV), annealing at 1100 K for 10 min, oxidizing for 10 min at 800 K at 1×10^{-7} mbar, and a final annealing/desorption step at 1000 K for 10 seconds. For all spectra, a pass energy of 200 eV was used, yielding an overall energy resolution of ~1 eV. The spectra were evaluated quantitatively using CasaXPS V2.3.16Dev6. The intensity of the Pt 4f signal was obtained by numerical integration from 77.0 to 66.0 eV binding energy after subtraction of a constant background adjusted at low binding energy. This method proved to be more robust towards adsorbate-induced changes in the Pt 4f satellite structure than subtraction of a Shirley or linear background. For the IL-related S 2p, C 1s, N 1s, O 1s and F 1s regions, linear backgrounds were subtracted and the peaks were fitted with Voigt profiles (30% Lorentzian contribution). Additionally, the widths (fwhm) and some positions of the peaks were constrained (see Table S4 in the ESI†). All spectra were referenced to the Fermi edge yielding 71.2 eV for the Pt $4f_{7/2}$ signal.

Results and discussion

Structure and growth behavior

To start with, we investigated the adsorption of [C_1C_1Im][Tf_2N] on Pt(111) at low temperature using scanning tunneling microscopy (STM). Fig. 1 shows the corresponding images of a nearly closed wetting layer (~0.5 ML) at different temperatures. All layers were prepared by evaporating the IL onto the Pt(111) surface in the preparation chamber, with the surface at a temperature of 157 K. The sample was then quickly transferred within a few minutes to the STM chamber and cooled to 110 K, where all STM measurements have been performed. Fig. 1 shows images recorded directly after sample transfer (with 157 K as maximum temperature), and after stepwise heating to 200, 250 and 300 K, in each case at this temperature for 10 min. For each temperature, three representative images are shown at different scales of (left) 100 × 100 nm^2, (middle) 50 × 50 nm^2, and (right) 20 × 20 nm^2.

Upon deposition at 157 K and subsequent measurement at 110 K, a disordered, nearly closed 2D layer is formed (Fig. 1a–c). We can identify individual protrusions, which we tentatively

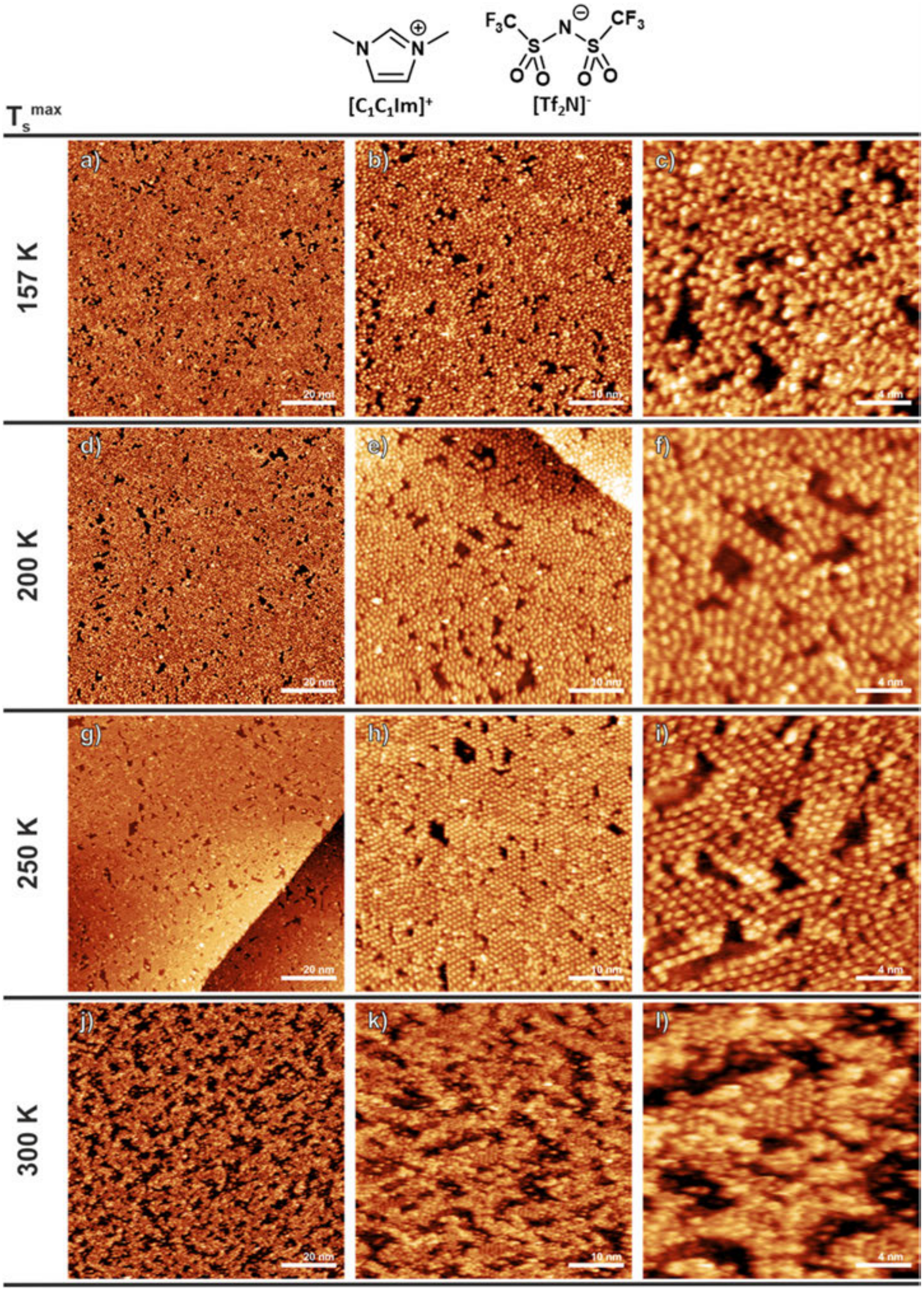

Fig. 1 STM images of a nearly closed [C_1C_1Im][Tf_2N] wetting layer (∼0.5 ML; originally deposited at 157 K) on Pt(111) at different scales: (left) 100 × 100 nm^2, (middle) 50 × 50 nm^2, and (right) 10 × 10 nm^2. (a)–(c) Measured after deposition, (c)–(f) after annealing to 200 K for 10 min, (d)–(f) after annealing to 250 K for 10 min, and (j)–(l) after annealing to 300 K for 10 min. Brighter features correspond to higher elevation. All STM images were measured after cooling back to 110 K with U_{bias} = 1.2 V and I_{set} of 0.2 to 0.5 nA (for details, see Table S5 in the ESI†). At the top of the figure the chemical structure of [C_1C_1Im][Tf_2N] is shown.

assign to the [Tf_2N]$^-$ anions. While this assignment is not unequivocal, it is based on the adsorption geometry derived from ARXPS (see below): The anions have a much higher elevation due to their adsorption in *cis* conformation, with the CF_3 groups pointing away from the surface, while the cations lie flat on the surface. Overall, the different protrusions have very similar brightness, with only a few being brighter than the others. Annealing to 200 K for 10 min induces ordering in the adsorbed layer, which indicates an enhanced mobility of the IL ions on the surface at this temperature. In Fig. 1d–f, highly ordered regions with stripe-like or hexagonal local structure can be observed. Again, most of the protrusions have very similar brightness, and only a few are brighter than the others. Upon heating to 250 K (Fig. 1g–i), the surface order further increases, now displaying larger regions with mostly hexagonal order and homogeneously bright protrusions. At the same time, however, the number of individual brighter features has significantly increased (best seen at the 50 × 50 nm^2 scale in Fig. 1h). Obviously, other processes in addition to ordering occur at this temperature, which will later be identified as the onset of decomposition of the IL (see below). Upon heating to 300 K, dramatic changes are observed (Fig. 1j–l). The ordered regions have strongly decreased in number, but can still be recognized, being indicative of intact IL on the surface. In addition, large areas show a disordered appearance with a broad variation in brightness, in particular, the number of very bright (and fuzzy) features has strongly increased. We attribute these observations to the decomposition of the IL (see below).

The appearance of the ordered regions in Fig. 1 is similar to structures that were recently observed on Au(111) by our group.[35] They are attributed to a checkerboard-like structure of intact IL, in which the cations and anions adsorb alternatingly next to each other. This type of behavior has been observed for many ILs on different metal surfaces and is governed by strong attraction of the ions towards the metal.[16]

In addition to the STM experiments, we also studied the initial growth behavior of $[C_1C_1Im][Tf_2N]$ on Pt(111) by ARXPS, after depositing increasing amounts of IL by PVD at sample temperatures of 100, 180 and 200 K, where the IL is intact (see also below). To deduce the growth mode, we analyzed the attenuation of the Pt 4f substrate signal, $I_d/I_{d=0}$, at $\theta = 0°$ (normal) and $\theta = 80°$ (grazing) emission as a function of the nominal thickness of the deposited IL film, using our previously established approach, see Fig. 2.[16] Thereby, for each deposition experiment, the mean thickness d of the film is first determined from $I_d/I_0 = \exp(-d/\lambda\cos\theta)$ for $\theta = 0°$, that is, in the bulk-sensitive geometry. Thereby, λ is the inelastic mean free path length of the Pt 4f photoelectrons within the IL (extrapolated to be 3.10 nm at 1415 eV kinetic energy[33]). With the obtained d value, we can then predict the attenuation at 80° for a two-dimensional IL layer at this thickness (for details of this approach, see ref. 16,33): the short-dashed grey lines represent ideal layer-by-layer 2D growth; deviations lying above the curve indicate a three-dimensional (3D) film morphology. For the here-studied system, the 80° data follows the prediction for ideal layer-by-layer growth up to ~1.0 ML (~0.7 nm for $[C_1C_1Im][Tf_2N]$[33]), indicating that at low coverages initially a closed wetting layer forms, where all ions are in direct contact with the metal surface in a checkerboard arrangement, which is in line with the observations by STM (see above). This 2D growth continues up to a coverage of 1 ML, which indicates that above the wetting layer, another 2D IL layer on top forms with the same thickness. Above this 1 ML coverage, the 80° data fall above the prediction for ideal layer-by-layer growth. Such a behavior has been observed before for other ILs on different metals and indicates the growth of ''moderate'' 3D islands on top of the initially formed 2D layers.[16] Notably, the initial 2D growth and subsequent 3D growth occurs similarly at 100, 180 and 200 K.

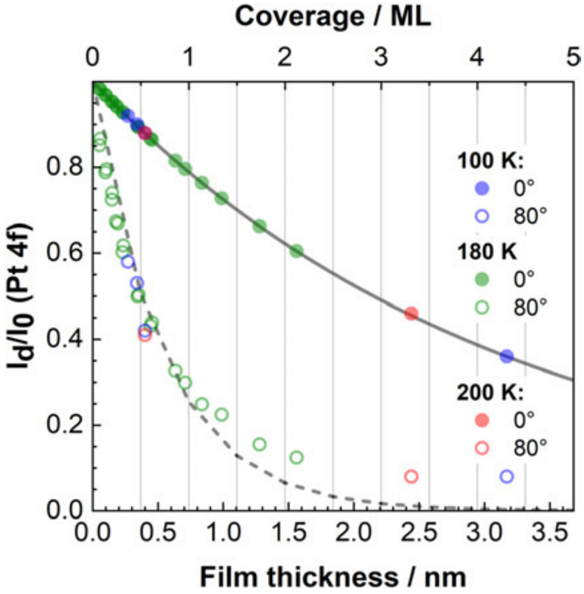

Fig. 2 Dependence of the Pt 4f substrate signal (full symbols for 0° and open symbols for 80° emission) on IL film thickness for $[C_1C_1Im][Tf_2N]$ on Pt(111) at 100, 180 and 200 K. The film thickness of each layer was calculated from the attenuation of the Pt 4f signal at 0°. The solid and dashed lines show the exponential decay expected for a uniform increase in layer thickness for emission angles of 0° and 80°, respectively,[16] based on the inelastic mean free path λ of 3.1 nm for the Pt 4f peak. Up to ~1.0 ML, very good agreement of the 80° data with the dashed lines is found, indicating the formation of a 2D layer. For larger coverages, pronounced deviations from 2D growth are observed (for details see text).

Chemical composition at low temperature

To study the interaction of the IL with the Pt(111) surface, we investigated nominal coverages of 0.4 and 0.5 ML, which are below and close to the completion of the wetting layer, respectively, by ARXPS of all relevant core levels (note that the coverages of different preparations varied from 0.47–0.52 ML for the ''0.5 ML'' spectra and from 0.35–0.39 ML for the ''0.4 ML'' spectra; for details, see Table S6, ESI†). The sub-wetting layer coverage data (0.4 ML) were measured to rule out multilayer features in the spectra; due to their better signal-to-noise ratios, the discussion will mostly focus on the 0.5 ML data in the following. For comparison, we also measured spectra of a 3.3 ML (2.4 nm) thick film, which serve as reference for the measurements of the thinner films. We start with discussing the data of the 3.3 ML (multilayer) film at 200 K, which was evaporated onto the surface at this temperature. The corresponding S 2p, C 1s, N 1s, O 1s and F 1s spectra were collected at an emission angle of 0° (normal emission) and are shown in Fig. 3a. Two of the observed signals are assigned to the $[C_1C_1Im]^+$ cation: The C_{cat} peak at 286.4 eV stems from the three carbon atoms of the imidazolium ring and the two carbon atoms of the methyl groups attached to the nitrogen atoms. The N_{cat} peak at 401.9 eV corresponds to the two nitrogen atoms in the imidazolium ring. The remaining signals are assigned to the $[Tf_2N]^-$ anion: The C_{an} peak at 292.6 eV and the F_{an} peak at 688.5 eV originate from the carbon and the fluorine atoms of the CF_3 group, respectively. The O_{an} peak at 532.4 eV and the

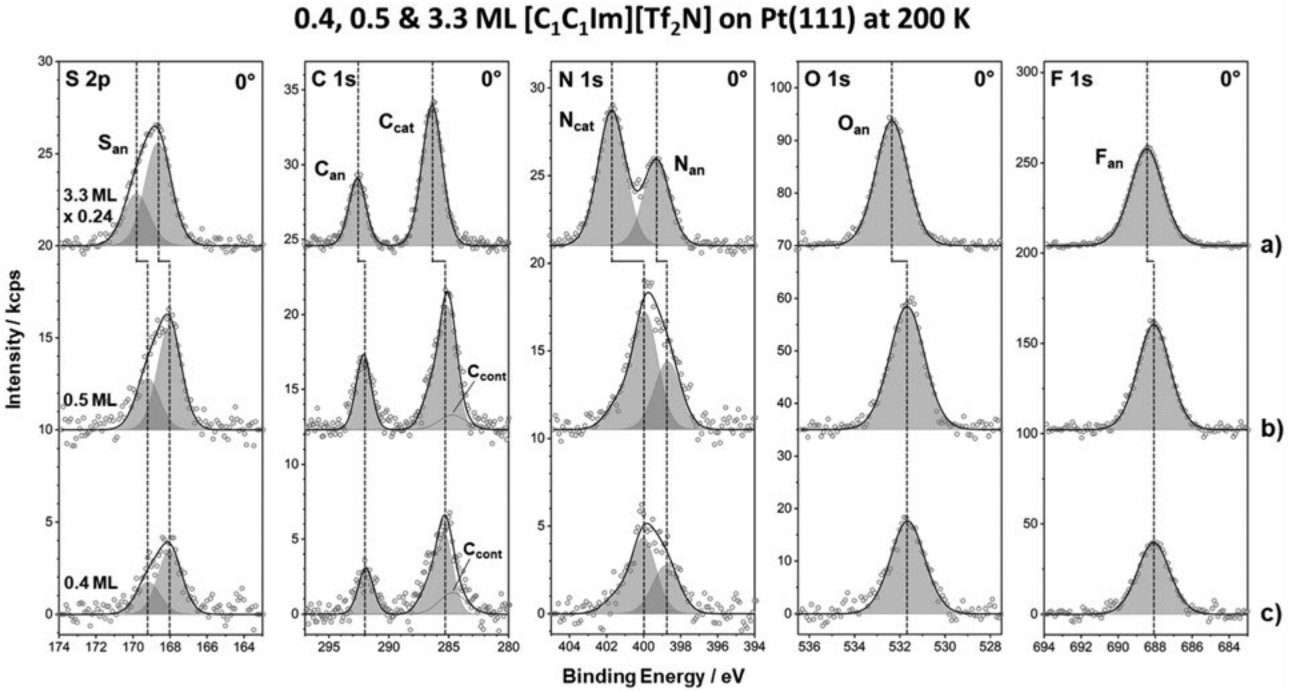

Fig. 3 S 2p, C 1s, N 1s, O 1s and F 1s spectra of $[C_1C_1Im][Tf_2N]$ on Pt(111). (a) 3.3 ML deposited at 200 K and measured at 200 K; (b) 0.5 ML deposited at 200 K and measured at 200 K, and (c) 0.4 ML deposited at 100 K and measured at 200 K. For a better visualization, the spectra in (a) are scaled down by a factor of 0.24. All spectra were fitted, and the corresponding results are shown as grey-shaded peaks (for peak assignment details, see text); dashed lines indicate the peak positions. In the C 1s spectra, a minor surface carbon contamination of the crystal (C_{cont}) was additionally taken into account for (b) and (c).

S_{an} $2p_{1/2}/2p_{3/2}$ doublet at 169.8/168.6 eV are assigned to the oxygen and sulfur atoms of the sulfonyl-group, respectively. Finally, the N_{an} peak at 399.3 eV stems from the central imidic nitrogen. The quantitative analysis of the data is shown in Table 1, together with the nominal IL stoichiometry. The deduced atom numbers agree to the nominal values within the experimental uncertainty (±10%), which unequivocally proves that the IL evaporates as intact ion pairs and adsorbs intact at 200 K on Pt(111).

The spectra for films in the wetting layer coverage range are shown in Fig. 3b for 0.5 ML and Fig. 3c for 0.4 ML. The 0.4 ML film was deposited at 100 K and heated to 200 K while the 0.5 ML film was deposited at 200 K. Overall, the spectra for the two coverage regimes are very similar. The binding energies of the various core levels are given in Table 2, along with the corresponding values for the 3.3 ML film. To enable a better comparison, the 3.3 ML spectra in Fig. 3a were downscaled by a factor of 0.24. Apart from their lower intensity, all anion signals of the 0.4 and 0.5 ML films are overall similar as those of the 3.3 ML film. The shifts by 0.4–0.7 eV to lower binding energies of the different levels are attributed to a more efficient screening of the excited core holes in the vicinity of the platinum surface, as compared to the situation in the IL bulk.[31] For the cation signals of the 0.4 and 0.5 ML films, however, the situation is

Table 1 Quantitative composition analysis of 0.5 ML $[C_1C_1Im][Tf_2N]$ films on Pt(111): after deposition at low temperatures (100 or 200 K) and subsequent heating to 200, 250 and 300 K (spectra shown in Fig. 3b and 5 bottom), and also after direct deposition at 300 K (spectra of Fig. 5 top). In addition, the results for a 0.4 ML film (deposited at 100 K) and a 3.3 ML film (deposited at 200 K) are provided (spectra of Fig. 3a and c, respectively). The numbers for anion atoms shown in brackets are re-normalized to the sum 15 for intact $[Tf_2N]^-$. Note that for each measurement temperature, a new layer was freshly prepared. For details, see text

	S_{an}	C_{an}	C_{cat}	N_{cat}	N_{an}	O_{an}	F_{an}	Σ
Nominal	2 (2)	2 (2)	5	2	1 (1)	4 (4)	6 (6)	22 (15)
3.3 ML@200 K								
Measured at 200 K	1.9	2.0	4.9	2.1	1.2	3.7	6.2	22
0.5 ML@300 K								
300 K	1.1 (1.6)	1.3 (1.9)	7.0	3.6	0.6 (0.9)	2.5 (3.7)	4.5 (6.9)	20.5 (15)
0.5 ML@100/200 K								
300 K	0.8 (1.5)	1.0 (1.9)	4.4	2.2	0.5 (1.0)	1.8 (3.4)	3.8 (7.2)	14.5 (15)
250 K	1.4 (1.6)	1.7 (2.0)	4.3	1.9	0.9 (1.0)	3.3 (3.8)	5.7 (6.6)	19.3 (15)
200 K	1.8 (1.7)	2.0 (1.9)	4.5	2.0	1.0 (1.0)	4.0 (3.9)	6.7 (6.5)	22 (15)
100 K	1.7 (1.6)	2.0 (1.9)	4.2	1.8	1.1 (1.0)	4.5 (4.2)	6.7 (6.3)	22 (15)
0.4 ML@100 K								
200 K	1.6	1.8	4.4	1.9	1.1	4.4	6.8	22

Table 2 Binding energies of the different core levels for 0.5 ML [C_1C_1Im][Tf_2N] on Pt(111). The 100 K film was deposited at 100 K, the other films at 200 K; derived from the XP spectra shown in Fig. 3b and 5 (bottom). In addition, also the results for the 0.4 ML film (deposited at 100 K) and the 3.3 ML film (deposited at 200 K) in Fig. 3a and c, respectively, are provided

	S $2p_{3/2an}$ [eV]	C $1s_{an}$ [eV]	C $1s_{cat}$ [eV]	N $1s_{cat}$ [eV]	N $1s_{an}$ [eV]	O $1s_{an}$ [eV]	F $1s_{an}$ [eV]
3.3 ML							
200 K	168.6	292.6	286.4	401.9	399.3	532.4	688.5
0.5 ML							
300 K	168.1	292.2	285.1	400.1	398.9	531.7	688.2
250 K	168.1	292.1	285.1	400.0	398.8	531.7	688.2
200 K	168.0	292.1	285.1	399.9	398.7	531.7	688.1
100 K	168.3	292.2	285.4	400.0	398.8	532.0	688.2
0.4 ML							
200 K	168.0	291.9	285.4	400.0	398.8	531.7	688.1

quite different, as is evident from the peak fitting in Fig. 3b and c. The C_{cat} peak at 285.1 eV and the N_{cat} peak at 399.9 eV (for 0.5 ML) display much larger shifts towards lower binding energies, by 1.3 and 2.0 eV, respectively (the shifts for 0.4 ML are by 0.1–0.3 eV smaller). In addition, we observe a weak shoulder at higher binding energy in both regions (close to the positions of the 3.3 ML bulk film). Notably, we fitted the cation signals in the C 1s and N 1s spectra for 0.4 and 0.5 ML in Fig. 3 considering this high binding energy shoulder, which leads to a strongly asymmetric line shape. We propose that these line shapes originate from cations in the wetting layer, which are adsorbed flat on the Pt(111) surface with strong covalent bonding interactions involving charge transfer between the π-orbitals of the imidazolium and platinum. We attribute these to IL in the ordered phases observed in the STM images in Fig. 1.

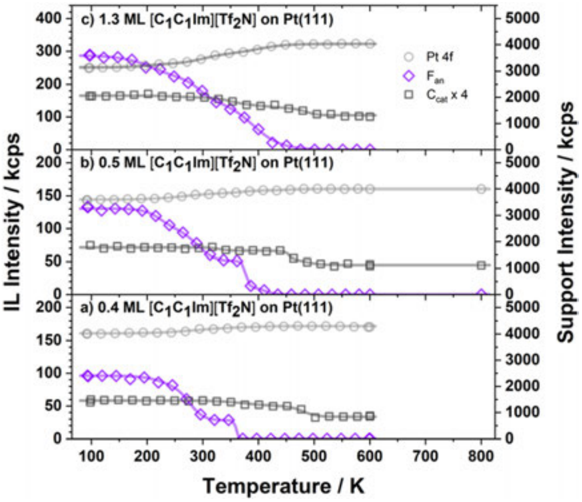

Fig. 4 Thermal evolution of the Pt 4f (light grey circles), F_{an} (violet diamonds) and C_{cat} (dark grey squares) intensities during heating of [C_1C_1Im][Tf_2N] films on Pt(111): (a) 0.4 ML, (b) 0.5 ML, and (c) 1.3 ML. The IL was first deposited onto the sample at low temperature *via* PVD; thereafter, XP spectra were recorded while heating with a linear heating rate of 2 K min^{-1} up to 600 K; after a final flash heating of the 0.5 ML sample to 800 K for about 1 min, a last data set was also recorded at 600 K. The intensity scale for the Pt 4f signal is given on the right side and that of the F_{an} and C_{cat} signals on the left.

Thermal evolution

The stability and thermal evolution of [C_1C_1Im][Tf_2N] films on Pt(111) was studied *in situ* by temperature-programmed XPS (TPXPS). 0.4, 0.5 and 1.3 ML thick films were each prepared at 100 K and heated to 600 K with a constant heating rate of 2 K min^{-1}. Simultaneously, the Pt 4f, F 1s and C 1s regions were measured at 0°. Thereafter, the 0.5 ML sample was flash-heated to 800 K for about 1 min, and spectra were measured at 600 K. We consider the F_{an} and C_{cat} peaks as representative for the anion and cation coverage, respectively, and use them to follow the thermal evolution; notably, all other anion and cation signals were not measured for time reasons and to minimize beam damage in the TPXPS series (a detailed analysis at selected temperatures is provided below). In Fig. 4a–c, the temperature-induced intensity changes are shown for the F_{an} (violet diamonds), C_{cat} (dark grey squares; note that fitting of the C_{cat} signal with its low signal-to-noise ratio in TPXPS was simplified using only one broad peak instead of the shape described above using a main line plus high binding energy shoulder) and Pt 4f signals (light grey circles). In this type of plot, a decrease of IL-related signals indicates desorption of anion- or cation-related species from the surface, which is accompanied by an increase in the Pt 4f substrate signal due to the corresponding decrease in surface coverage.

Fig. 4a and b show that the 0.4 and 0.5 ML films behave very similar, apart from the lower signals of the former due to its lower initial coverage. Both show constant Pt 4f, C_{cat} and F_{an} intensities between 100 and ~200 K, which indicates that the IL films stays chemically intact in this temperature window. Above 200 K, the F_{an} intensity, indicative of the adsorbed anions, continuously decreases by ~60% to reach a plateau between ~300 and ~375 K, with ~40% of the original intensity. At the same time, the C_{cat} intensity, indicative of adsorbed cations, remains constant until ~300 K, and thereafter shows a minor decrease (by less than 10%) to reach a plateau between ~375 and ~450 K. Upon further heating, the anion intensity drops rapidly to zero at ~385 K, while the cation intensity stays constant. Finally, starting at ~450 K, the cation intensity decreases by another 30%, to reach a plateau at ~475 K, with ~60% of its original intensity. In the absence of any anion signal, this signal is attributed to a residual carbon species, which is remaining at the Pt surface even up to 800 K. Simultaneously to the decrease of the IL-related signals, the Pt 4f substrate signal increases accordingly, reflecting the coverage decrease due to desorption of anion- and cation-related species.

We propose the following interpretation of these TPXPS experiments. For coverages up to the full wetting layer and temperatures below 200 K, the IL is fully intact with anions and cations in direct contact with the Pt(111) surface. Upon further heating, the IL starts to decompose above 200 K. The anion-related reaction products are volatile and leave the surface, as reflected in the decrease in F_{an} signal until a plateau is reached between ∼300 and ∼375 K, at around 40% of its original intensity. For charge neutrality reasons, we assume that a similar fraction of the cations also undergoes decomposition. In contrast to the desorbing anion decomposition products, the decomposed cation fragments remain at the surface exhibiting similar C 1s and N 1s binding energies as the intact cations. We also propose that the remaining 40% of anion and also cation signals within the plateau between ∼300–375 K correspond to still intact IL (see below). This scenario implies that in course of the ongoing IL decomposition, the surface becomes less and less reactive due to an increasing amount of cation-derived decomposition products. When a certain coverage of decomposition products is reached, further IL decomposition is suppressed, and still intact IL remains stable, until desorption or further decomposition occurs above 375 K. The remaining carbon signals seen at higher temperatures in Fig. 4 thus originate from the cation decomposition process.

As the film thickness might play an important role for the performance of SCILL catalysts, we also studied the thermal evolution of an IL coverage of 1.3 ML, which corresponds to a full wetting layer plus IL multilayers on top of it. The corresponding data are shown in Fig. 4c (note the changed IL intensity range as compared to Fig. 4a and b). The anion

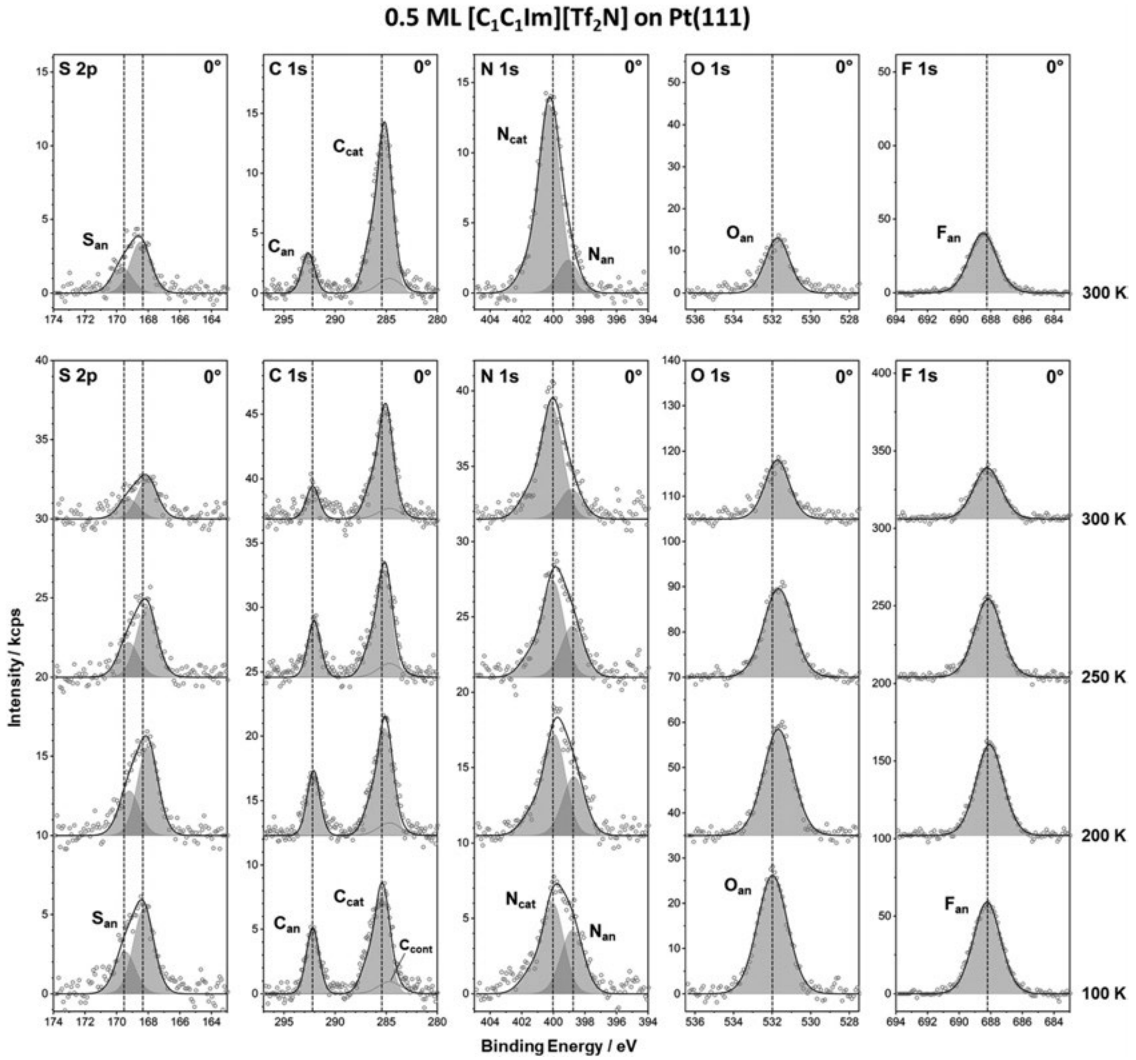

Fig. 5 S 2p, C 1s, N 1s, O 1s and F 1s spectra of $[C_1C_1Im][Tf_2N]$ on Pt(111). (Bottom part) After low temperature deposition of 0.5 ML and heating to the denoted temperatures (the 100 K film was deposited at 100 K, the other films at 200 K); for each temperature, a new layer was freshly prepared (the exact coverages of the individual layers varied between 0.47 and 0.52 ML; see Table S6, ESI†). (Top row) IL deposition at 300 K up to a total film thickness equivalent to 0.5 ML intact IL. All spectra were fitted, and the corresponding results are shown as grey-shaded peaks. In the C 1s spectra, a small contamination of the surface (C_{cont}) was taken into account. The dotted lines indicate the binding energy positions of the film at 100 K. Note that the spectra for 0.5 ML at 200 K are the same as the spectra in Fig. 3b.

intensity decreases continuously starting at around ∼175 K and vanishes at ∼450 K, which is about 75 K higher than for the low coverages. The evolution of the cation intensity is similar to that of the 0.4 and 0.5 ML films. The smaller Pt 4f intensity at 100 K is due to the stronger damping by the thicker IL layer. The observed behavior can be understood considering that for the 1.3 ML film ions on top of the wetting layer are not in direct contact with the Pt(111) surface. Hence, the interface-related decomposition, desorption and surface passivation processes at the IL-metal interface likely are superimposed by additional exchange processes between multilayer (which desorbs at 345 K[16]) and wetting layer: Surface sites emptied by desorption of the anion-related decomposition products can be refilled by intact IL, which partly decomposes again and partly is stable up to 450 K, due to an increasing degree of passivation by the cation decomposition products. In line with this interpretation, the remaining carbon intensity above 500 K, which is higher for the 1.3 ML film than for the 0.5 and 0.4 ML films (note the different scale), indicates that overall more IL ions underwent decomposition upon heating.

Characterization at selected temperatures

For a more detailed characterization of the thermally induced processes, we performed isothermal measurements of all relevant IL core levels of 0.5 ML and 0.4 ML films at 100, 200, 250 and 300 K. Note that each temperature set represents a freshly prepared film on the clean Pt(111) surface to avoid accumulation of beam damage effects (individual deposition temperatures and coverage values are given in the corresponding figure captions). After deposition or after heating to the indicated temperatures, a full set of ARXP spectra was measured. The corresponding spectra along with their fits in 0° emission are shown in Fig. 5 (bottom part) and Fig. S1 (ESI†) for 0.5 ML, and Fig. S2 (ESI†) for 0.4 ML; notably, the 200 K data are the same as shown in Fig. 3. The quantitative analyses are summarized in Table 1 and Tables S1, S2 (ESI†), respectively. The more surface sensitive spectra measured at 80° (Fig. 6 and Fig. S1, S2, ESI†) will be discussed later. Since the 0.5 and 0.4 ML films behave qualitatively the same at all temperatures, we focus the following discussion on the 0.5 ML films due to the better signal-to-noise ratios.

The 100 and 200 K spectra for the 0.5 ML films in Fig. 5 look very similar. The overall intensities and the resulting atom numbers (Table 1) agree with each other and with the nominal values within the experimental uncertainty of ±15% (the somewhat larger deviation for the S_{an} signal is due to some uncertainties in the background subtraction). The good agreement for all core levels again confirms intact IL in contact with Pt(111) up to 200 K, in line with the TPXPS experiments discussed in Fig. 4. The small peak shifts towards lower binding energy (−0.3 eV) at 200 K, mainly seen for the S 2p and O 1s anion peaks, are likely due to a reorganization of the ions at the surface: Due to the low mobility at temperatures well below 200 K, the IL adsorbs in different adsorption geometries, as witnessed by the disorder observed in the STM images (see Fig. 1a–c, deposited at 157 K and measured at 110 K). At 200 K, the increased thermal energy allows for obtaining the energetically more favorable adsorption geometry, that is, a checkerboard-type arrangement, with the SO_2 groups of the anion preferentially pointing downwards, which is typically observed for other metal surfaces.[18,19,21,25–27,31,33,40–47] This orientation at 200 K is also confirmed by our 80° spectra (see below). The close proximity of the SO_2 groups to the metal surface allows for a better core hole screening of the S and O atoms of the anion, leading to the observed small shifts.[31] The C_{cat} and N_{cat} peaks also show minor changes concerning binding energy and intensity (note that the C 1s and N 1s peaks of the cation are fitted with the same shoulder as used in Fig. 3, yielding the same asymmetric line shapes), reflecting some reorganization of the cations as well at 200 K.

For higher temperatures, the TPXPS experiments in Fig. 4 indicated desorption and/or decomposition of the IL, while in STM we observed an increased formation of disordered regions. Indeed, also the XP spectra at 250 K in Fig. 5 display a decrease of the anion signals by ∼15%, compared to the 200 K spectra, while the intensities and binding energy positions of the cation signals remain virtually unchanged. At 300 K, the anion signals have decreased by ∼50% as compared to 200 K, while the cation signals still remain unaffected. For both anion and cation signals, the binding energies undergo minor shifts (up to 0.2 eV) to higher binding energy. The loss of anions from the surface as compared to 100 K is also reflected from the atomic numbers in Table 1 (note that the total atom number, given in the last column Σ has been adapted to account for the desorbing anion fragments). The observed behavior indicates that up to 300 K ∼50% of the anion-related species desorb from the surface while the amount of cation-related species remains more or less constant up to 300 K. At this temperature, the STM data shown in Fig. 1 reveal the formation of the disordered phase at the expense of the ordered islands.

In the following, we provide evidence that the remaining S_{an}, C_{an}, N_{an}, O_{an} and F_{an} signals at 250 and 300 K originate from intact IL on the surface, and that all anion-related decomposition products have desorbed. In Table 1 all anion values given in brackets are re-normalized to the sum of atoms of $\Sigma = 15$ for an intact $[Tf_2N]^-$ anion. The deviations of the measured values from the stoichiometry are quite small ($<20\%$), which is in line with intact anions present at the surface at 250 and 300 K. Thus, the isothermal measurements strongly support our above-proposed behavior upon linear heating, namely that at 300 K a significant fraction of the adsorbed IL decomposes, and the undecomposed IL fraction remains on the surface. The anion-related decomposition products are volatile above 200 K and desorb from the surface while the cation-related decomposition products remain on the surface and have similar binding energy positions as the intact IL cations. This self-passivation allows for maintaining non-decomposed IL anions and cations in the wetting layer even at 300 K. The decrease of the anion signal to ∼40% in the TPXPS experiment as compared to ∼50% in the isothermal 300 K measurements is likely due to the fact that the plateau at 40% is not yet fully reached at 300 K (see Fig. 4). The STM data are also in line with this interpretation, as upon heating the ordered phase increasingly converts to a disordered phase assigned to intact IL coexisting with cation-related disordered decomposition products.

To evaluate possible decomposition mechanisms of the IL, we additionally studied the thermal evolution of 0.5 ML of the trimethylated [$C_1C_1C_1$Im][Tf_2N]. The motivation for this measurement is that decomposition of the IL above 200 K could start with partial deprotonation of the imidazolium cation forming a strongly bound carbene at the Pt-surface. The proton could then react with the anions to form neutral bistriflimidic acid (Tf_2NH), which subsequently desorbs above 200 K. The additional methyl group in [$C_1C_1C_1$Im][Tf_2N] protects the most acidic C_2 carbon atom of the cation, where deprotonation should start.[48,49] The TPXPS data in Fig. S3a (ESI†), and the isothermal XPS data in Fig. S4 (ESI†) along with the quantitative analysis in Table S3 (ESI†) show that the anion and cation signals of this IL evolve virtually identical to those of the di-methylated [C_1C_1Im][Tf_2N]. The unchanged thermal behavior strongly indicates that deprotonation of the C_2 carbon most likely is not the initial decomposition step for the wetting layer of [C_1C_1Im][Tf_2N] on Pt(111). We refrain from further speculating on the nature of the observed decomposition process since its products are difficult to assess. The anions could decompose to volatile fragments like NH_x, SO_x and CF_x species, similar as proposed for the same IL on Cu(111).[21] Ideally, temperature programmed desorption experiments would be helpful, but are out of the scope of this work. The nature of the cation-related species also cannot be identified from the C 1s and N 1s peaks.

Orientation of the IL in the wetting layer regime

In a next step, we address the orientation of the anions and cations in the wetting layer regime. This information can be derived by comparing the spectra of all relevant core levels at 0° and 80° emission of our ARXP spectra: Thereby, a larger signal of a specific atom at 80° (as compared to 0°) indicates that this atom is located closer to the vacuum side of the ultrathin IL film, and *vice versa*, a smaller signal indicates that this atom is closer to the Pt(111) surface. In Fig. 6, the corresponding spectra of the 0.5 ML films are shown (0°: black; 80°: red); note that the 0° spectra are the same as those already shown in Fig. 5 (bottom). In addition, the fitted spectra along with the quantitative analysis are provided in Fig. S1 and Table S1 (ESI†). The corresponding data for the 0.4 ML films are shown in Fig. S2 and Table S2 (ESI†). In our analysis, we focus on the changes in intensity with emission angle of the F_{an} signal (representative of the CF_3 group of the anion), the O_{an} signal (SO_2 group of the anion) and the C_{cat} signal. The C_{an} and N_{cat} signals behave qualitatively the same as the F_{an} and C_{cat} signal, respectively. Note that the S_{an} signal has a larger uncertainty due to challenges with background subtraction. As the behavior for 0.4 ML and 0.5 ML is very similar, we concentrate discussing the behavior of the latter.

At 100 K, the F_{an} signal at 80° in Fig. 6 is significantly larger than at 0°, and the O_{an} signal significantly smaller. This behavior is also reflected in the quantitative analysis provided

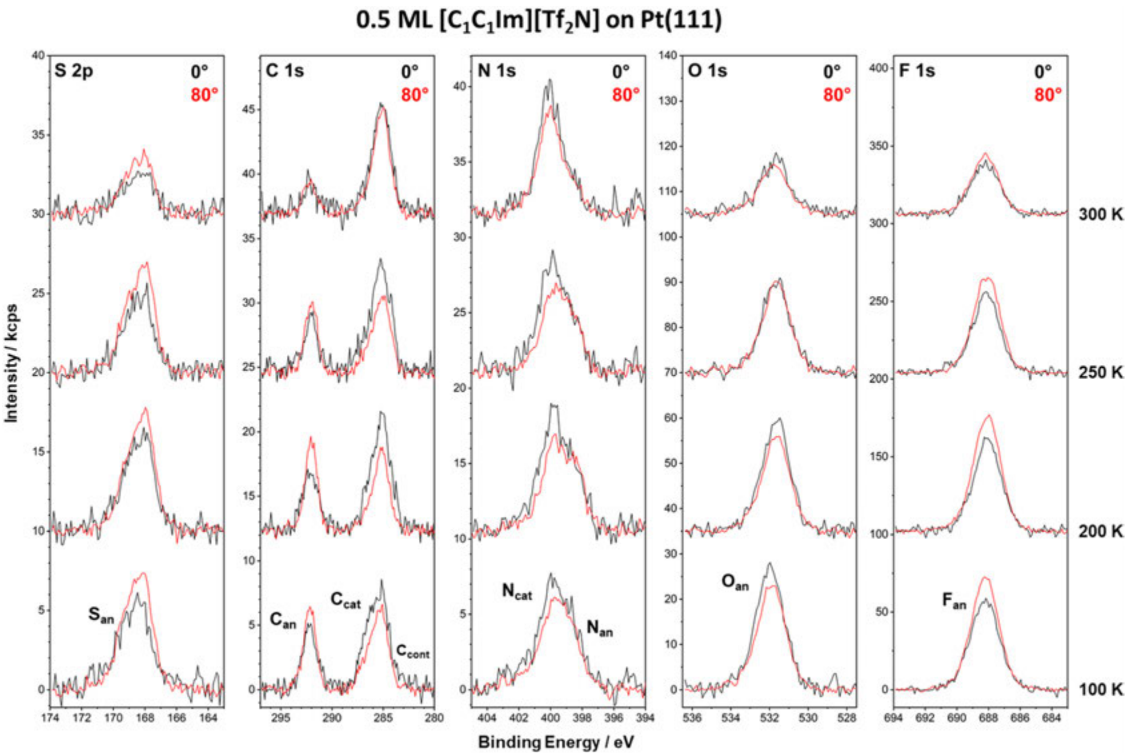

Fig. 6 S 2p, C 1s, N 1s, O 1s and F 1s spectra of 0.5 ML [C_1C_1Im][Tf_2N] on Pt(111) after low temperature deposition and heating to the denoted temperatures (the 100 K film was deposited at 100 K, the other films at 200 K); for each temperature, a new layer was freshly prepared (the exact coverages of the individual layers varied between 0.46 and 0.54 ML; see Table S6, ESI†) and measured under normal (0°; black) and grazing emission (80°; red). Note that the spectra in 0° are the same as shown in Fig. 5 (bottom).

in Table S1 (ESI†), where the atom number for F_{an} at 80° is larger than the nominal one (8.1 *vs.* 6) and for O_{an} lower than the nominal one (3.7 *vs.* 4). For the N_{an} atoms (which are in the center of the anion) no angle dependence was seen. These observations indicate that the anion is orientated with the CF_3 groups preferentially pointing towards the vacuum side and the SO_2 groups towards the metal surface. This characteristic orientation has been observed for similar systems with similar anions.[18,19,21,25–27,31,33,40–47] For the C_{cat} signal, we measure a decrease at 80° in Fig. 6, which goes along a with a lower than nominal atom number C_{cat} at 80° in Table S1 (ESI†) (3.3 *vs.* 5), which is in line with the cation ring lying flat in close proximity to the metal surface.

At 200 K, the F_{an} signal further increases (8.4 *vs.* 6, at 80°), while the O_{an} (3.4 *vs.* 4) and C_{cat} (3.1 *vs.* 5) signals further decrease. This effect is attributed to the increased mobility at this temperature, which enables the IL to obtain its optimum adsorption geometry. At 100 K, the IL has low mobility, yielding a moderate preferential orientation. At 200 K, the IL film is better equilibrated, yielding a higher, more uniform degree of orientation. This interpretation is in line with our STM results in Fig. 1, where at 200 K highly ordered IL islands are observed. Notably, the orientation effects are to some extent also reflected in the bulk sensitive 0° measurements, as it was also observed for other (sub-)wetting layer IL systems.[18,21] This effect is most prominent for the F_{an} signal at 200 K (6.7 *vs.* 6; see Table S1, ESI†).

At 250 and 300 K, the differences between 0 and 80° in Fig. 6 become increasingly less pronounced. We attribute this behavior to a lower degree of order, since above 200 K decomposition of the IL sets in with desorption of anion-related decomposition products (see above). The remaining IL is coadsorbed with the cation-related decomposition products, which could lead to different, less well-oriented adsorption geometries, which might particularly affect the order and the orientation of the remaining anions. Further, entropic effects (*e.g. cis–trans* isomerization of $[Tf_2N]^-$) also could contribute to the less pronounced orientation at the higher temperatures.

Our findings for $[C_1C_1Im][Tf_2N]$ on Pt(111) are compatible to results published by Hohner *et al.* for a closely related system, that is, $[C_2C_1Im][Tf_2N]$ on Pt(111).[26] The only difference of the two ILs is an ethyl group instead of a methyl group in the cation, and thus, one would expect a similar adsorption behavior (note that the authors use a different coverage definition, that is, 1 ML as full wetting layer coverage in their study, which corresponds to 0.5 ML in our study; further, they use an alternative name for $[Tf_2N]$, namely $[NTf_2]$). Hohner *et al.* exposed the Pt(111) surface to $[C_2C_1Im][Tf_2N]$ at 200 and 300 K, and analyzed the geometry of the $[Tf_2N]^-$ anion in the (sub-)wetting layer regime using infrared absorption spectroscopy (IRAS) at 200 and 300 K in combination with DFT calculations.[26] For both temperatures, IRAS indicates a coverage dependence of the molecular orientation in the wetting layer range. At low coverages, the $[Tf_2N]^-$ anion predominantly adsorbs with the S–N–S bonds parallel to the surface: the CF_3 groups point towards the vacuum side while the SO_2 groups point towards the metal surface in a 2–1 bonding motif, that is, one SO_2 group binds *via* one oxygen atom and the other SO_2 group binds *via* both oxygen atoms to the metal. Interestingly, the authors rule out a 2–2 bonding motif (all oxygen atoms of both SO_2 groups point towards the metal) due to missing peaks in the IRAS spectra. We want to note, however, that a mixture of anions coadsorbed in 2–2 or 2–1 motif is still compatible with their data, in particular, since the DFT-derived adsorption energies even favor the former (2.74 eV for 2–2 *vs.* 2.51 eV for 2–1). Reaching wetting layer saturation, Hohner *et al.* proposed a change of the adsorption motif towards an upright standing species that binds only *via* both oxygen atoms of one SO_2 group, while the other SO_2 group is lifted from the surface (so-called 2–0 *cis* motif); notably, this adsorption motif is found to be not stable in their DFT calculation.[26] Independent of coverage, the $[C_2C_1Im]^+$ cations are proposed to adopt an orientation with the imidazolium ring parallel to the metal surface.

While the IRAS data by Hohner *et al.*[26] and our ARXPS data for wetting layers of $[C_2C_1Im][Tf_2N]$ and $[C_1C_1Im][Tf_2N]$, respectively, on Pt(111) are more or less consistent, our interpretation is, however, different: From ARXPS, we know that a $[C_1C_1Im][Tf_2N]$ wetting layer deposited at 100 K decomposes to 50–60% upon heating to 300 K, with the anion-related reaction products desorbing instantaneously and the cation-related products remaining on the surface. Thereby, the surface is partly passivated, enabling the remaining IL to still be adsorbed intact at 300 K. Notably, IRAS is not sensitive to flat-lying cations or decomposition products without a dipole moment perpendicular to the surface, due to the metal-surface selection rule.[26] Therefore, Hohner *et al.* did not consider any influence of the described decomposition and surface passivation process on their IRAS data.

Adsorption at 300 K

As a last step, we investigated the adsorption of $[C_1C_1Im][Tf_2N]$ on Pt(111) directly at 300 K; notably in our above-described experiments, 0.5 ML IL films were deposited at 100 or 200 K, and then further heated to 300 K. Interestingly, when deposition is done at 300 K, the dose required to reach a surface coverage of 0.5 ML (as deduced from the attenuation of the Pt 4f signal) was about twice as large as the one required at 100 K. The corresponding XP spectra at 0° in Fig. 5 (top part) can be directly compared to the spectra measured at 100 K (Fig. 5, bottom) and after annealing to 300 K (Fig. 5, bottom). The quantitative analysis is provided in Table 1. After deposition at 100 K, the atomic numbers were in line with the nominal values (within ±10%), reflecting the adsorption of the intact IL. After heating to 300 K, the cation intensities in Fig. 5 (bottom) were unchanged, but those of the anion decreased to ∼50% due to IL decomposition and desorption of the anion-related products. After direct deposition at 300 K, the situation is quite different: The cation signals in Fig. 5 (top) are much larger than after annealing to 300 K, while the anion signals have an intensity between those obtained after deposition at 100 K and after annealing to 300 K, indicative of massive IL decomposition. These observations can be understood based on our explanation proposed above: during deposition at 300 K, a fraction of the anions decomposes and instantaneously desorbs opening free space for further adsorption of IL, where again

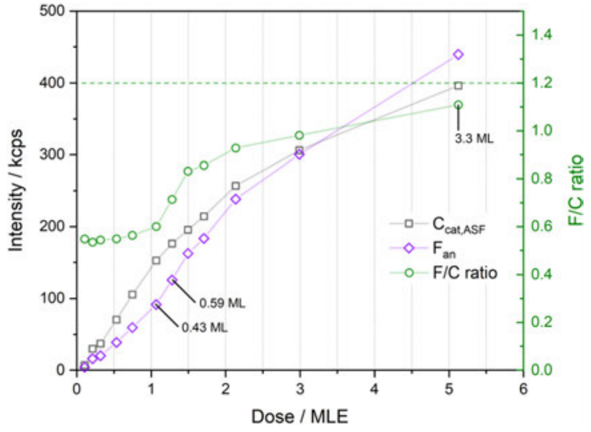

Fig. 7 Intensity of the C_{cat} signal (grey) and F_{an} signal (violet) of $[C_1C_1Im][Tf_2N]$ on Pt(111), as a function of IL dose at 300 K. Both signals are corrected by the respective atomic sensitivity factors to allow for a direct quantitative comparison of their absolute intensities. In addition, also the $F_{an}:C_{cat}$ ratio is depicted (green; scale on the right side); the dashed horizontal line indicates the nominal ratio $F_{an}:C_{cat} = 6:5 = 1.2$, reflecting the six F_{an} atoms and five C_{cat} atoms of the intact IL.

anions partly decompose, with the products desorbing. Hence, cation-related species accumulate at the expense of anions until one fully closed wetting layer is formed (=0.5 ML of decomposition products plus IL). This explains the higher dose required to reach an equivalent 0.5 ML coverage at 300 K as compared to 100 K. Due to the higher dose, more intact IL can adsorb on the surface, which explains the larger anion signal for deposition at 300 K as compared to annealing to 300 K. The quantification of the anion signals in Table 1 reveals atom numbers close to the nominal values, indicating that the remaining IL is indeed intact.

To study the behavior from sub-wetting layer coverages up to the multilayer range at room temperature, we sequentially deposited at 300 K increasing amounts of $[C_1C_1Im][Tf_2N]$ on Pt(111) and measured the Pt 4f, F_{an} and C_{cat} signals each time. In Fig. 7, the F_{an} (violet diamonds) and C_{cat} (grey squares) signal intensities are plotted against the dose in MLE; thereby 1 MLE (monolayer equivalent) is the dose required to obtain a coverage of 1 ML at 100 K. Additionally, the $F_{an}:C_{cat}$ ratio for each dose (green circles) is shown, along with the nominal ratio $F_{an}:C_{cat} = 6:5 = 1.2$ of an intact IL (green dashed horizontal line). At low doses, the $F_{an}:C_{cat}$ ratio is $\sim$0.55, which is less than half of the nominal value, which reflects the desorption of anion-related decomposition products. This ratio remains more or less constant up to doses $\sim$1 MLE, where the surface at 300 K is actually covered only by 0.43 ML of decomposition products plus IL, which is close to the nominal coverage of one closed layer of 0.5 ML. At higher doses, the F_{an} signal increases strongly and the $F_{an}:C_{cat}$ ratio finally approaches the nominal value of 1.2. This indicates that after forming one closed layer composed of decomposition products plus IL, the Pt(111) surface is passivated and IL can co-adsorb intact without decomposition. At high doses, the slopes of the C_{cat} and also the F_{an} curves decrease, due to self-damping in the thin IL layer.

At this point, we come back to the study by Hohner *et al.* for $[C_2C_1Im][Tf_2N]$ on Pt(111).[26] The authors also observed that a considerably higher IL dose was required to reach a closed first layer (wetting layer) at 300 K as compared to deposition at 200 K. Moreover, they assumed a change in anion orientation in this layer when reaching the full wetting layer coverage at 300 K. As mentioned above, Hohner *et al.* did not consider any decomposition effects at this temperature. They attributed the required higher dose to a smaller sticking coefficient, and the change in orientation to lateral interactions within the IL layer and not to the coadsorption of decomposition products. We therefore propose that their interpretation should be reconsidered. Moreover, our ARXPS results might also explain the discrepancy concerning the upright adsorption geometry of the IL for the full wetting layer with the DFT calculations in the study by Hohner *et al.*[26]

Conclusions

We have investigated the adsorption and thermal evolution of the ionic liquid $[C_1C_1Im][Tf_2N]$ on Pt(111) in the temperature range from 100 to 800 K. Information about adsorbate structure, growth behavior, and chemical composition as function of temperature was obtained from angle-resolved X-ray photoelectron spectroscopy and scanning tunneling microscopy. Our measurements concentrated on the coverage required to achieve a fully covered surface, the so-called wetting layer. 0.5 and 0.4 ML of the IL were deposited at low temperature (100 or 200 K), followed by heating to 250/300 K, or directly at 300 K.

Upon IL deposition and adsorption at 100/157 K, initially an intact, disordered layer is formed. At 200 K, long range order, as deduced from STM, and molecular orientation, as deduced from ARXPS, become more pronounced; the IL still is fully intact, adsorbed in a checkerboard-type structure with anions and cations in direct contact with the Pt(111) surface. Upon heating to 250 K, the surface order further increases, but simultaneously indications of IL decomposition are seen in both STM and XPS. Further heating to 300 K leads to enhanced IL decomposition of 50–60% of the IL. The anion-related reaction products are volatile and leave the surface, as reflected in the decrease in F_{an} signal until a plateau is reached between $\sim$300 and $\sim$375 K, at around 40% of its original intensity. For charge neutrality reasons, we assume that a similar fraction of the cations also undergoes decomposition. In contrast to the desorbing anion fragments, the cation fragments remain at the surface exhibiting similar C 1s and N 1s binding energies as the intact cations. We propose that the remaining 40% of anion and also cation signals within the plateau between $\sim$300–375 K correspond to still intact IL. This scenario implies that in the course of the ongoing IL decomposition, the surface becomes less and less reactive due to an increasing amount of cation-derived decomposition products. When a certain coverage of decomposition products is reached, further IL decomposition is suppressed, and still intact IL remains stable until desorption or further decomposition occurs above 375 K. The remaining carbon signals seen at higher temperatures originate from the cation decomposition process.

Comparing our results to an earlier IRAS study for the closely related system $[C_2C_1Im][Tf_2N]$ adsorbed on Pt(111),[26] we found similar orientation effects for the intact IL in the wetting layer; however, Hohner *et al.* were not aware of decomposition effects occurring at room temperature due to the reduced spectral sensitivity with respect to the cations and remaining decomposition products. In any case, we propose that the observed decomposition and resulting partial surface passivation might play an important role to understand observed selectivity effects in SCILL catalysis.

Our findings show the complexity of the processes occurring at the IL/metal interface of our model SCILL system, which are relevant for real SCILL systems in general. Strong covalent interactions of the IL with the platinum surface – as witnessed by the pronounced chemical shifts found for the imidazolium cation signals – modify catalytic sites and hence, might promote or suppress their catalytic behavior. In course of a surface passivation, very reactive but unselective sites that even lead to the decomposition of the IL are likely blocked by strongly adsorbed decomposition products (originating from the imidazolium cations in our case) and thus, could increase the selectivity of the catalytic process. Moreover, these IL-derived decomposition products might also be beneficial in the context of platinum-based fuel cell catalysis using ionic liquid coatings.[28] An understanding of these types of phenomena at the IL/metal interface on the molecular level might indeed help to understand the catalytic behavior of real systems on the macroscopic scale.

Author contributions

Conceptualization, S. M., F. M., H.-P. S.; methodology, S. M., T. T., L. W., C. C. F. (XPS), A. G., M. M., S. J., R. A., A. B. (STM); validation, S. M., A. G., A. B., F. M., H.-P. S.; formal analysis, S. M., A. G.; investigation, S. M., T. T., L. W., C. C. F. (XPS), A. G., M. M., S. J., R. A. (STM); resources, H.-P. S.; data curation, S. M. (XPS), A. G. (STM); writing – original draft preparation, S. M., A. G.; writing – review and editing, S. M., F. M., H.-P. S.; visualization, S. M., A. G.; supervision, F. M., H.-P. S.; project administration, F. M., H.-P. S.; funding acquisition, H.-P. S., C. C. F. All authors have read and agreed to the published version of the manuscript.

Conflicts of interest

There are no conflicts to declare.

Acknowledgements

Funded by the Deutsche Forschungsgemeinschaft (DFG, German Research Foundation) – Project-ID 431791331 – SFB 1452 (Catalysis at Liquids interfaces, CLINT). C. C. F. thanks the Alexander von Humboldt Foundation for a research fellowship.

References

1 C. R. Catlow, M. Davidson, C. Hardacre and G. J. Hutchings, Catalysis making the world a better place, *Philos. Trans. R. Soc., A*, 2016, **374**(2061), 20150089.

2 J. Hagen, *Industrial Catalysis: A Pratical Approach*, Wiley-VCH Verlag GmbH & Co. KgaA, 2005.

3 N. V. Plechkova and K. R. Seddon, Applications of ionic liquids in the chemical industry, *Chem. Soc. Rev.*, 2008, **37**(1), 123–150.

4 K. R. Seddon, A taste of the future, *Nat. Mater.*, 2003, **2**(6), 363–365.

5 A. J. Greer, J. Jacquemin and C. Hardacre, Industrial Applications of Ionic Liquids, *Molecules*, 2020, **25**(21), 5207.

6 U. Kernchen, B. Etzold, W. Korth and A. Jess, Solid Catalyst with Ionic Liquid Layer (SCILL) – A New Concept to Improve Selectivity Illustrated by Hydrogenation of Cyclooctadiene, *Chem. Eng. Technol.*, 2007, **30**(8), 985–994.

7 W. Korth and A. Jess, Solid Catalysts with Ionic Liquid Layer (SCILL), in *Supported Ionic Liquids*, ed. F. Rasmus, A. Riisager and M. Haumann, Wiley-VCH Verlag GmbH & Co. KGaA, 2014, pp. 279–306.

8 H.-P. Steinrück and P. Wasserscheid, Ionic Liquids in Catalysis, *Catal. Lett.*, 2015, **145**(1), 380–397.

9 O. Bartlewicz, I. Dąbek, A. Szymańska and H. Maciejewski, Heterogeneous Catalysis with the Participation of Ionic Liquids, *Catalysts*, 2020, **10**(11), 1227.

10 M. Sobota, M. Happel, M. Amende, N. Paape, P. Wasserscheid, M. Laurin and J. Libuda, Ligand Effects in SCILL Model Systems: Site-Specific Interactions with Pt and Pd Nanoparticles, *Adv. Mater.*, 2011, **23**(22–23), 2617–2621.

11 J. Arras, E. Paki, C. Roth, J. Radnik, M. Lucas and P. Claus, How a Supported Metal Is Influenced by an Ionic Liquid: In-Depth Characterization of SCILL-Type Palladium Catalysts and Their Hydrogen Adsorption, *J. Phys. Chem. C*, 2010, **114**(23), 10520–10526.

12 L. Naicker, M. Schörner, D. Kremitzl, H. B. Friedrich, M. Haumann and P. Wasserscheid, Influencing the Product Distribution in Citral Hydrogenation Using Ionic Liquid Modified Cu Catalysts, *ChemCatChem*, 2022, **14**(19), e202200388.

13 T. Barth, W. Korth and A. Jess, Selectivity-Enhancing Effect of a SCILL Catalyst in Butadiene Hydrogenation, *Chem. Eng. Technol.*, 2017, **40**(2), 395–404.

14 N. Szesni, R. Fischer, A. Hagemeyer, F. Großmann, J. Boyer, H. C. Hou, D. M. Lowe, C. Lugmair, M. Sun and M. Urbancic, *Catalyst composition for selective hydrogenation with improved characteristics*, *European Patent Application*, EP2583751B1, 2013.

15 Clariant OleMax® 260: New acetylene selective hydrogenation catalyst starts strong at Dow, **https://www.clariant.com/en/Corporate/News/2018/05/Clariant-Olemax-260-new-acetylene-selective-hydrogenation-catalyst-starts-strong-at-DOW** (accessed 09.05.2023).

16 M. Lexow, F. Maier and H.-P. Steinrück, Ultrathin ionic liquid films on metal surfaces: adsorption, growth, stability and exchange phenomena, *Adv. Phys.: X*, 2020, **5**(1), 1761266.

17 H.-P. Steinrück, Recent developments in the study of ionic liquid interfaces using X-ray photoelectron spectroscopy and potential future directions, *Phys. Chem. Chem. Phys.*, 2012, **14**(15), 5010–5029.

18 S. Massicot, T. Sasaki, M. Lexow, S. Shin, F. Maier, S. Kuwabata and H.-P. Steinrück, Adsorption, Wetting, Growth, and Thermal Stability of the Protic Ionic Liquid Diethylmethylammonium Trifluoromethanesulfonate on Ag(111) and Au(111), *Langmuir*, 2021, **37**(39), 11552–11560.

19 B. Uhl, H. Huang, D. Alwast, F. Buchner and R. J. Behm, Interaction of ionic liquids with noble metal surfaces: structure formation and stability of [OMIM][TFSA] and [EMIM][TFSA] on Au(111) and Ag(111), *Phys. Chem. Chem. Phys.*, 2015, **17**(37), 23816–23832.

20 M. Meusel, A. Gezmis, S. Jaekel, M. Lexow, A. Bayer, F. Maier and H.-P. Steinrück, Time- and Temperature-Dependent Growth Behavior of Ionic Liquids on Au(111) Studied by Atomic Force Microscopy in Ultrahigh Vacuum, *J. Phys. Chem. C*, 2021, **125**(37), 20439–20449.

21 R. Adhikari, S. Massicot, L. Fromm, T. Talwar, A. Gezmis, M. Meusel, A. Bayer, S. Jaekel, F. Maier, A. Görling and H.-P. Steinrück, Structure and Reactivity of the Ionic Liquid [C_1C_1Im][Tf_2N] on Cu(111), *Top. Catal.*, 2023, DOI: 10.1007/s11244-023-01801-y.

22 B. Uhl, F. Buchner, S. Gabler, M. Bozorgchenani and R. J. Behm, Adsorption and reaction of sub-monolayer films of an ionic liquid on Cu(111), *Chem. Commun.*, 2014, **50**(62), 8601–8604.

23 T. Cremer, L. Wibmer, S. Krick Calderón, A. Deyko, F. Maier and H.-P. Steinrück, Interfaces of ionic liquids and transition metal surfaces—adsorption, growth, and thermal reactions of ultrathin [C_1C_1Im][Tf_2N] films on metallic and oxidised Ni(111) surfaces, *Phys. Chem. Chem. Phys.*, 2012, **14**(15), 5153–5163.

24 R. Eschenbacher, S. Trzeciak, C. Schuschke, S. Schötz, C. Hohner, D. Blaumeiser, D. Zahn, T. Retzer and J. Libuda, Thermal Stability and CO Permeability of [C_4C_1Pyr][NTf_2]/Pd(111) Model SCILLs: from UHV to Ambient Pressure, *Top. Catal.*, 2023, DOI: 10.1007/s11244-023-01798-4.

25 T. Bauer, S. Mehl, O. Brummel, K. Pohako-Esko, P. Wasserscheid and J. Libuda, Ligand Effects at Ionic Liquid-Modified Interfaces: Coadsorption of [C_2C_1Im][OTf] and CO on Pd(111), *J. Phys. Chem. C*, 2016, **120**(8), 4453–4465.

26 C. Hohner, L. Fromm, C. Schuschke, N. Taccardi, T. Xu, P. Wasserscheid, A. Görling and J. Libuda, Adsorption Motifs and Molecular Orientation at the Ionic Liquid/Noble Metal Interface: [C_2C_1Im][NTf_2] on Pt(111), *Langmuir*, 2021, **37**(43), 12596–12607.

27 D. Blaumeiser, C. Schuschke, L. Fromm, N. Taccardi, S. Schötz, R. Eschenbacher, H. Bühlmeyer, T. Xu, T. Bauer, P. Wasserscheid, A. Görling and J. Libuda, CO Permeability and Wetting Behavior of Ionic Liquids on Pt(111): An IRAS and PM-IRAS Study from Ultrahigh Vacuum to Ambient Pressure, *J. Phys. Chem. C*, 2021, **125**(28), 15301–15315.

28 A. Avid, J. L. Ochoa, Y. Huang, Y. Liu, P. Atanassov and I. V. Zenyuk, Revealing the role of ionic liquids in promoting fuel cell catalysts reactivity and durability, *Nat. Commun.*, 2022, **13**(1), 6349.

29 H. Wang, Y. Wang, C. Li, Q. Zhao and Y. Cong, Introduction of Surface Modifiers on the Pt-Based Electrocatalysts to Promote the Oxygen Reduction Reaction Process, *Nanomaterials*, 2023, **13**(9), 1544.

30 T. Sasaki, R. Izumi, T. Tsuda and S. Kuwabata, Innovative Approach for Preparing a CNT-Supported Pt Nanoparticle Functional Electrocatalyst Using Protic Ionic Liquids, *ACS Appl. Energy Mater.*, 2021, **4**(7), 7298–7308.

31 T. Cremer, M. Stark, A. Deyko, H.-P. Steinrück and F. Maier, Liquid/Solid Interface of Ultrathin Ionic Liquid Films: [C_1C_1Im][Tf_2N] and [C_8C_1Im][Tf_2N] on Au(111), *Langmuir*, 2011, **27**(7), 3662–3671.

32 F. Rietzler, J. Nagengast, H.-P. Steinrück and F. Maier, Interface of Ionic Liquids and Carbon: Ultrathin [C_1C_1Im][Tf_2N] Films on Graphite and Graphene, *J. Phys. Chem. C*, 2015, **119**(50), 28068–28076.

33 M. Lexow, T. Talwar, B. S. J. Heller, B. May, R. G. Bhuin, F. Maier and H.-P. Steinrück, Time-dependent changes in the growth of ultrathin ionic liquid films on Ag(111), *Phys. Chem. Chem. Phys.*, 2018, **20**(18), 12929–12938.

34 M. Meusel, M. Lexow, A. Gezmis, A. Bayer, F. Maier and H.-P. Steinrück, Growth of Multilayers of Ionic Liquids on Au(111) Investigated by Atomic Force Microscopy in Ultrahigh Vacuum, *Langmuir*, 2020, **36**(45), 13670–13681.

35 M. Meusel, M. Lexow, A. Gezmis, S. Schötz, M. Wagner, A. Bayer, F. Maier and H.-P. Steinrück, Atomic Force and Scanning Tunneling Microscopy of Ordered Ionic Liquid Wetting Layers from 110 K up to Room Temperature, *ACS Nano*, 2020, **14**(7), 9000–9010.

36 K. R. J. Lovelock, C. Kolbeck, T. Cremer, N. Paape, P. S. Schulz, P. Wasserscheid, F. Maier and H.-P. Steinrück, Influence of Different Substituents on the Surface Composition of Ionic Liquids Studied Using ARXPS, *J. Phys. Chem. B*, 2009, **113**(9), 2854–2864.

37 S. F. Miller, H. B. Friedrich and C. W. Holzapfel, The Effects of SCILL Catalyst Modification on the Competitive Hydrogenation of 1-Octyne and 1,7-Octadiene versus 1-Octene, *ChemCatChem*, 2012, **4**(9), 1337–1344.

38 M. T. Heinze, J. C. Zill, J. Matysik, W. D. Einicke, R. Gläser and A. Stark, Solid–ionic liquid interfaces: pore filling revisited, *Phys. Chem. Chem. Phys.*, 2014, **16**(44), 24359–24372.

39 V. Hoffmann, G. Pulletikurthi, T. Carstens, A. Lahiri, A. Borodin, M. Schammer, B. Horstmann, A. Latz and F. Endres, Influence of a silver salt on the nanostructure of a Au(111)/ionic liquid interface: an atomic force microscopy study and theoretical concepts, *Phys. Chem. Chem. Phys.*, 2018, **20**(7), 4760–4771.

40 M. Lexow, B. S. J. Heller, F. Maier and H.-P. Steinrück, Anion Exchange at the Liquid/Solid Interface of Ultrathin Ionic Liquid Films on Ag(111), *ChemPhysChem*, 2018, **19**(22), 2978–2984.

41 S. Schernich, D. Kostyshyn, V. Wagner, N. Taccardi, M. Laurin, P. Wasserscheid and J. Libuda, Interactions Between the Room-Temperature Ionic Liquid [C_2C_1Im][OTf] and Pd(111), Well-Ordered Al_2O_3, and Supported Pd Model Catalysts from IR Spectroscopy, *J. Phys. Chem. C*, 2014, **118**(6), 3188–3193.

42 S. Schernich, V. Wagner, N. Taccardi, P. Wasserscheid, M. Laurin and J. Libuda, Interface Controls Spontaneous Crystallization in Thin Films of the Ionic Liquid [C_2C_1Im][OTf]

on Atomically Clean Pd(111), *Langmuir*, 2014, **30**(23), 6846–6851.

43 S. Mehl, T. Bauer, O. Brummel, K. Pohako-Esko, P. Schulz, P. Wasserscheid and J. Libuda, Ionic-Liquid-Modified Hybrid Materials Prepared by Physical Vapor Codeposition: Cobalt and Cobalt Oxide Nanoparticles in [C_1C_2Im][OTf] Monitored by In Situ IR Spectroscopy, *Langmuir*, 2016, **32**(34), 8613–8622.

44 C. Schuschke, L. Fromm, J. Träg, C. Stumm, C. Hohner, R. Eschenbacher, S. Grau, D. Zahn, A. Görling, T. Bauer and J. Libuda, A Molecular View of the Ionic Liquid Catalyst Interface of SCILLs: Coverage-Dependent Adsorption Motifs of [C_4C_1Pyr][NTf_2] on Pd Single Crystals and Nanoparticles, *J. Phys. Chem. C*, 2021, **125**(24), 13264–13272.

45 B. Uhl, F. Buchner, D. Alwast, N. Wagner and R. J. Behm, Adsorption of the ionic liquid [BMP][TFSA] on Au(111) and Ag(111): substrate effects on the structure formation investigated by STM, *Beilstein J. Nanotechnol.*, 2013, **4**, 903–918.

46 B. Uhl, T. Cremer, M. Roos, F. Maier, H.-P. Steinrück and R. J. Behm, At the ionic liquid|metal interface: structure formation and temperature dependent behavior of an ionic liquid adlayer on Au(111), *Phys. Chem. Chem. Phys.*, 2013, **15**(40), 17295–17302.

47 A. B. Biedron, E. L. Garfunkel, E. W. Castner and S. Rangan, Ionic liquid ultrathin films at the surface of Cu(100) and Au(111), *J. Chem. Phys.*, 2017, **146**(5), 054704.

48 A. J. Arduengo III, R. L. Harlow and M. Kline, A stable crystalline carbene, *J. Am. Chem. Soc.*, 1991, **113**(1), 361–363.

49 S. T. Handy and M. Okello, The 2-Position of Imidazolium Ionic Liquids: Substitution and Exchange, *J. Org. Chem.*, 2005, **70**(5), 1915–1918.

Electronic Supplementary Material (ESI) for Physical Chemistry Chemical Physics.

Supporting information

Adsorption and Thermal Evolution of $[C_1C_1Im][Tf_2N]$ on Pt(111)

Stephen Massicot, Afra Gezmis, Timo Talwar, Manuel Meusel, Simon Jaekel,
Rajan Adhikari, Leonhard Winter, Cynthia C. Fernández, Andreas Bayer, Florian Maier
and Hans-Peter Steinrück

Lehrstuhl für Physikalische Chemie II, Friedrich-Alexander-Universität Erlangen-Nürnberg,
Egerlandstraße 3, 91058 Erlangen, Germany

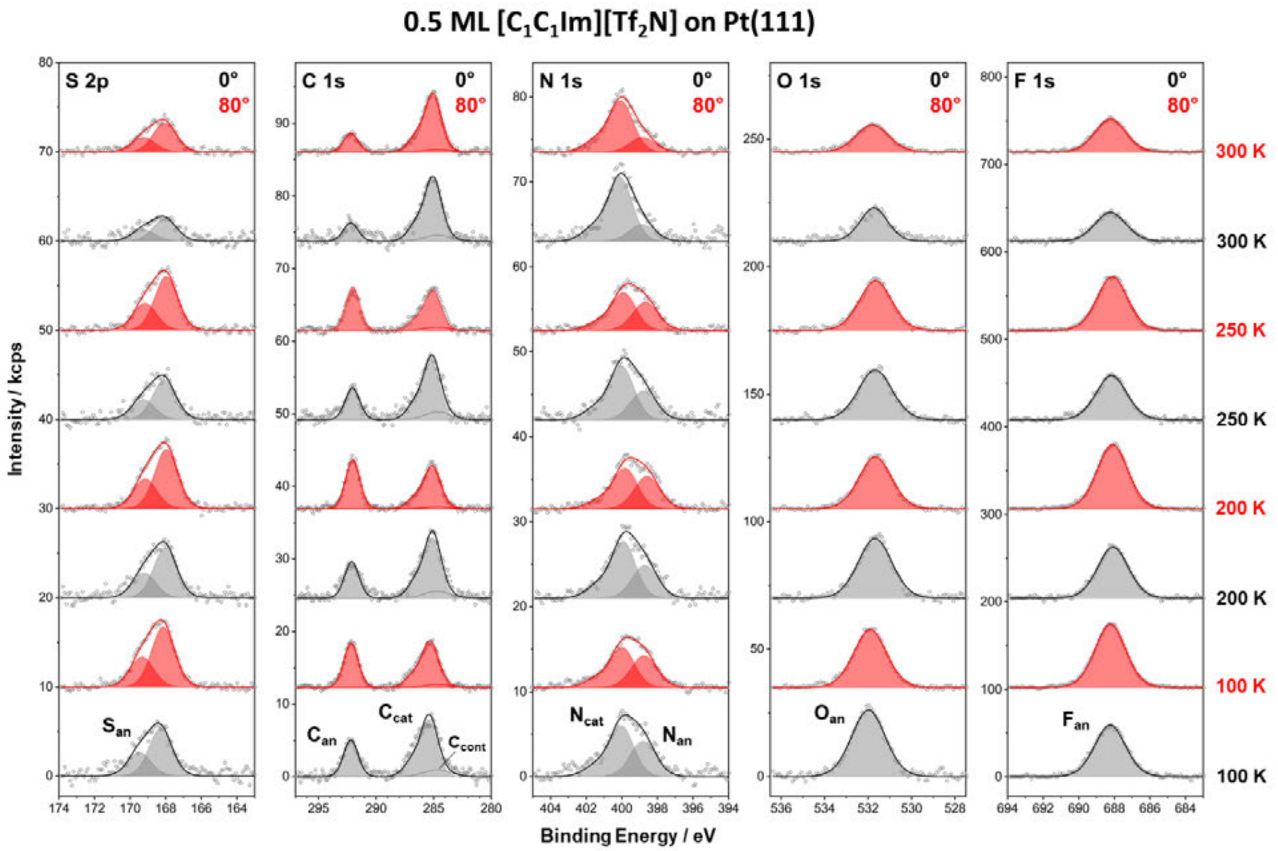

Figure S1: S 2p, C 1s, N 1s, O 1s and F 1s spectra of **<u>0.5 ML</u>** [C_1C_1Im][Tf_2N] on Pt(111), including peak fitting. Measured at 0° (black) and 80° (red) emission angle, after low temperature deposition and heating to the denoted temperatures (the 100 K film was deposited at 100 K, the other films at 200 K); for each temperature, a new layer was freshly prepared (the exact coverages of the individual layers varied between 0.46 and 0.54 ML; see Table S6). In the C 1s spectra, a small contamination of the surface (C_{cont}) was taken into account. Note that the spectra are the same as shown in Figure 6 without fitting.

Table S1: Quantitative analysis of the composition of **<u>0.5 ML</u>** [C_1C_1Im][Tf_2N] on Pt(111) at different temperatures, as derived from the XP spectra shown in Figure S1 at 0° (black) and 80° (red) emission angle.

	S_{an}	C_{an}	C_{cat}	N_{cat}	N_{an}	O_{an}	F_{an}	Σ
nominal	**2**	**2**	**5**	**2**	**1**	**4**	**6**	**22**
300 K, 80°	1.0	1.0	4.1	1.8	0.5	1.8	4.4	14.5
300 K, 0°	0.8	1.0	4.4	2.2	0.5	1.8	3.8	14.5
250 K, 80°	1.9	2.1	3.1	1.3	0.9	3.2	6.9	19.3
250 K, 0°	1.4	1.7	4.3	1.9	0.9	3.3	5.7	19.3
200 K 80°	2.1	2.7	3.1	1.4	1.0	3.4	8.4	22
200 K, 0°	1.8	2.0	4.5	2.0	1.0	4.0	6.7	22
100 K, 80°	2.1	2.4	3.3	1.4	1.0	3.7	8.1	22
100 K, 0°	1.7	2.0	4.2	1.8	1.1	4.5	6.7	22

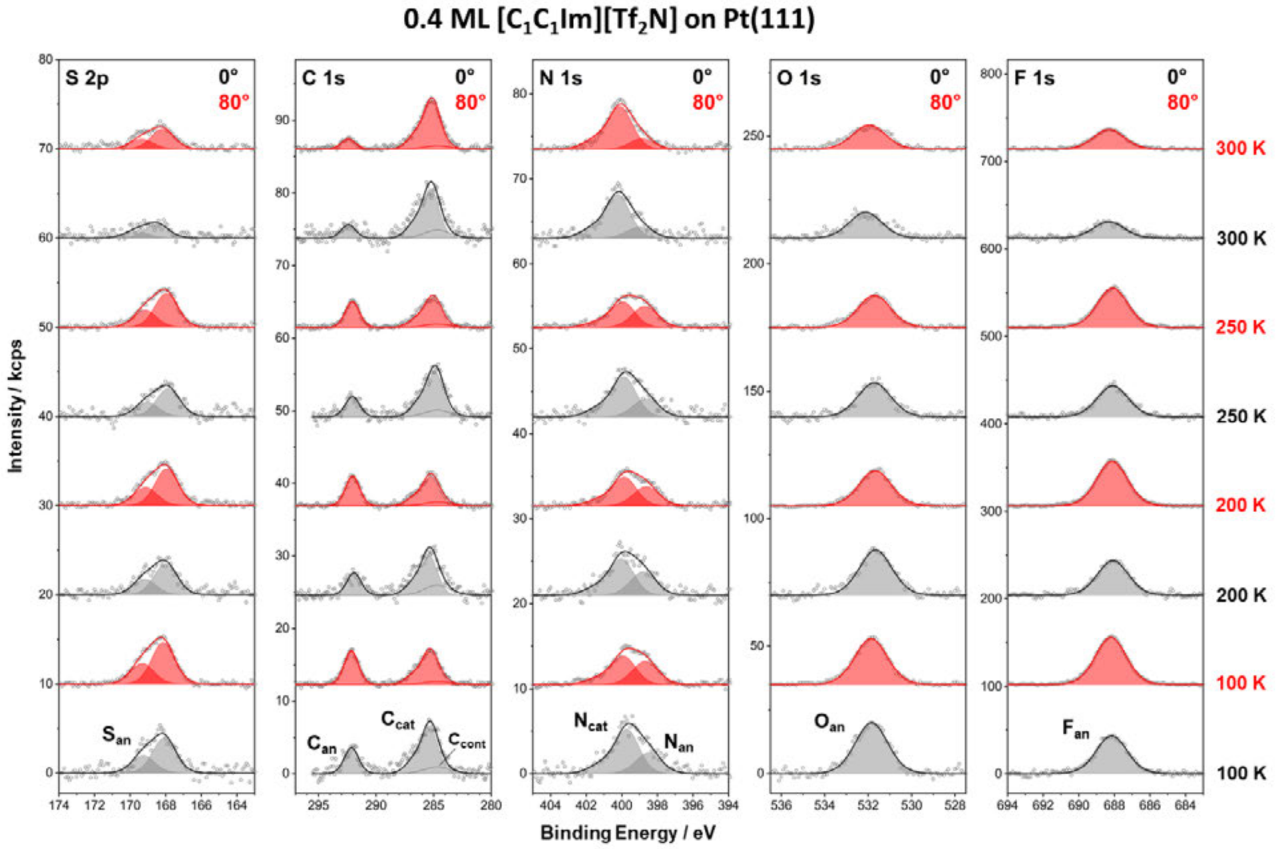

Figure S2: S 2p, C 1s, N 1s, O 1s and F 1s spectra of **<u>0.4 ML</u>** [C_1C_1Im][Tf_2N] on Pt(111), including peak fitting. Measured at 0° (black) and 80° (red) emission angle, after deposition at 100 K and heating to the denoted temperatures; for each temperature, a new layer was freshly prepared (the exact coverages of the individual layers varied between 0.35 and 0.39 ML; see Table S6). In the C 1s spectra, a small contamination of the surface (C_{cont}) was taken into account. Note that the spectrum at 200 K (0°) is the same as shown in Figure 3c.

Table S2: Quantitative analysis of the composition of **<u>0.4 ML</u>** [C_1C_1Im][Tf_2N] on Pt(111) at different temperatures, as derived from the XP spectra shown in Figure S2 at 0° (black) and 80° (red) emission angle.

	S_{an}	C_{an}	C_{cat}	N_{cat}	N_{an}	O_{an}	F_{an}	Σ
nominal	**2**	**2**	**5**	**2**	**1**	**4**	**6**	**22**
300 K, 80°	0.9	0.7	4.7	1.9	0.4	2.0	3.3	14.0
300 K, 0°	0.7	1.0	4.9	2.0	0.5	2.2	2.9	14.0
250 K, 80°	1.6	1.9	2.9	1.2	0.9	2.8	6.8	18.0
250 K, 0°	1.3	1.4	4.4	1.8	0.7	2.9	5.4	18.0
200 K 80°	1.9	2.4	3.2	1.5	0.9	3.4	8.7	22
200 K, 0°	1.6	1.8	4.4	1.9	1.1	4.4	6.8	22
100 K, 80°	1.9	2.4	3.3	1.3	1.0	3.9	8.2	22
100 K, 0°	1.6	1.9	4.6	2.0	0.9	4.4	6.6	22

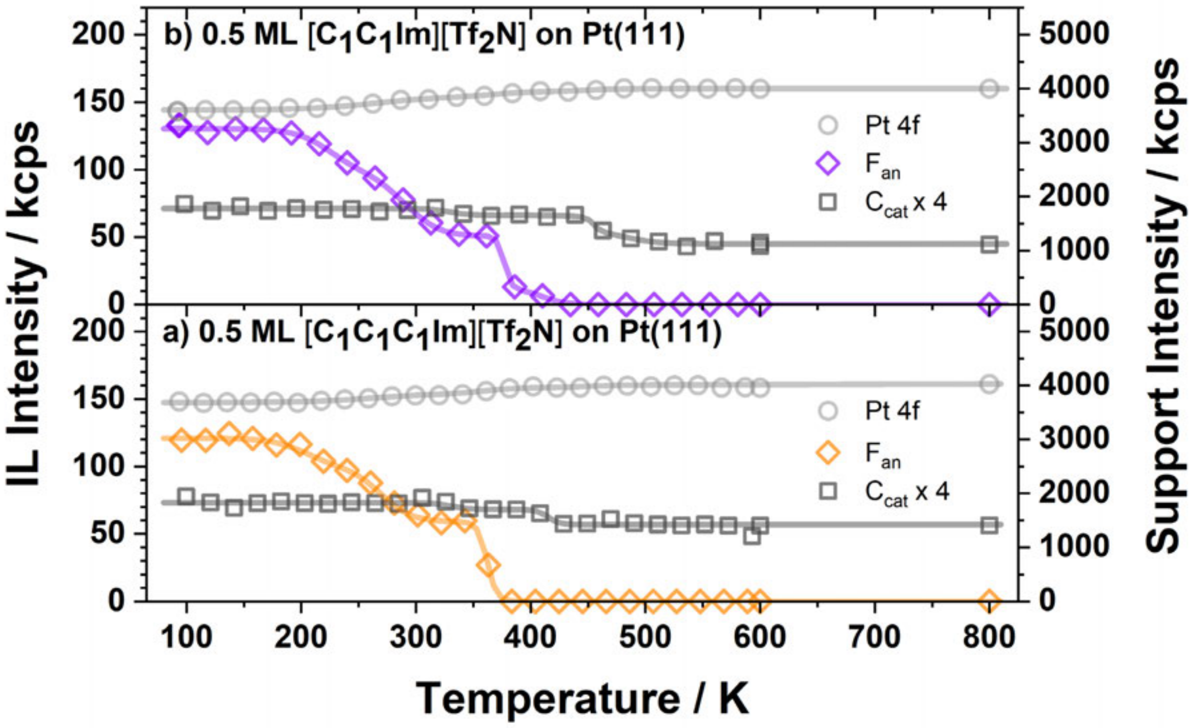

Figure S3: Comparison of the thermal evolution of (a) 0.5 ML $[C_1C_1C_1Im][Tf_2N]$ and (b) 0.5 ML $[C_1C_1Im][Tf_2N]$ on Pt(111), for the Pt 4f (light grey circles), F_{an} (orange (a) and violet (b) diamonds) and C_{cat} (dark grey squares) intensities during heating on Pt(111). The IL films were first deposited onto the sample at 100 K via PVD; thereafter, XP spectra were recorded while heating with a linear heating rate of 2 K/min up to 600 K; after flashing the samples to 800 K, a last data set was also recorded. The intensity scale for the Pt 4f signal is given on the right side and that of the F_{an} and C_{cat} signals on the left. Note that the data for $[C_1C_1Im][Tf_2N]$ (b) correspond to those in Figure 4b.

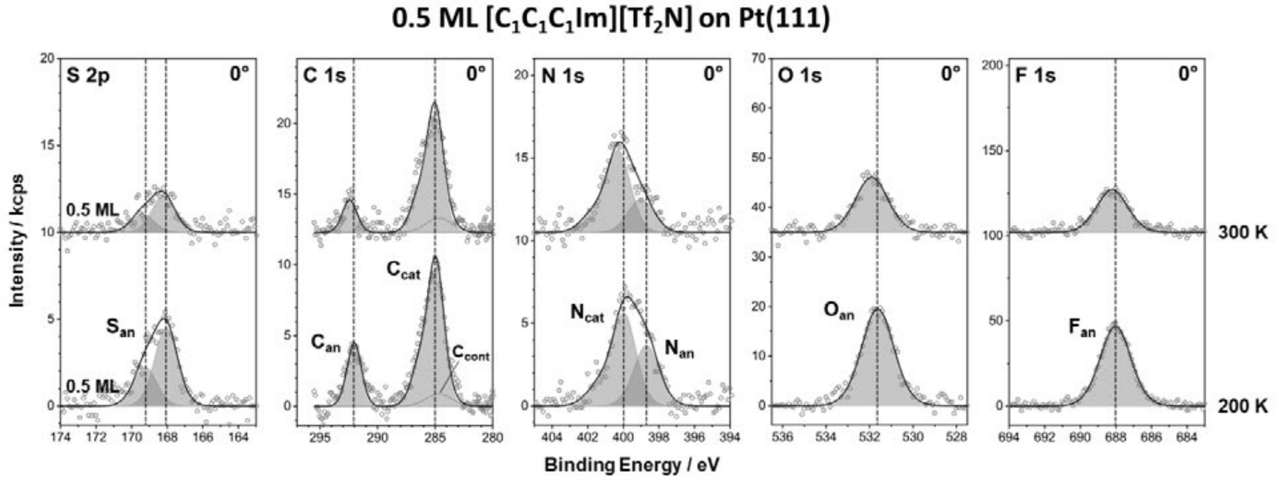

Figure S4. S 2p, C 1s, N 1s, O 1s and F 1s spectra of 0.5 ML $[C_1C_1C_1Im][Tf_2N]$ on Pt(111) at 200 K (deposited at 200 K) and 300 K (deposited at 100 K, followed by heating to 300 K). The exact coverages are 0.48 and 0.46 ML for 200 and 300 K, respectively, see Table S6. In the C 1s spectra, a small contamination of the surface (C_{cont}) was taken into account. The dotted lines indicate the binding energy positions of the film at 200 K.

Table S3: Quantitative analysis of the composition of **0.5 ML** $[C_1C_1C_1Im][Tf_2N]$ on Pt(111) at 200 and 300 K, as derived from the XP spectra shown in Figure S4.

	S_{an}	C_{an}	C_{cat}	$N_{cat, sum}$	N_{an}	O_{an}	F_{an}	Σ
nominal	**2** **(2)**	**2** **(2)**	**6**	**2**	**1** **(1)**	**4** **(4)**	**6** **(6)**	**23** **(15)**
300 K, 0°	0.7 (1.5)	1.0 (2.0)	4.8	1.6	0.6 (1.2)	2.0 (4.0)	3.1 (6.3)	13.7 (15)
200 K, 0°	1.7 (1.7)	2.1 (2.1)	6.2	1.9	1.1 (1.1)	3.7 (3.8)	6.3 (6.3)	22 (15)

Table S4: Fitting parameters for 0.4/0.5 ML thick films of $[C_1C_1Im][Tf_2N]$ and $[C_1C_1C_1Im][Tf_2N]$ on Pt(111). The S 2p doublet is separated by 1.18 eV, and the N_{cat} and N_{an} signals are separated by 1.21 eV. The C_{cat} signal was fitted with an additional shoulder at 1.52 eV higher binding energy (BE), with 25 % intensity of the main peak, and the N_{cat} signal with an additional shoulder at 1.50 eV higher BE, with 20 % intensity (10 % intensity for the film deposited at 300 K) of the main peak; this procedure reproduces the asymmetric line shapes of the cation signals. The absolute BEs in eV are not constrained and are given in Table 2.

0.4/0.5 ML	S_{an}	C_{an}	C_{cat}	N_{an}	N_{cat}	O_{an}	F_{an}
Fwhm /eV	1.53	1.48	1.67	1.70	1.60	1.75	2.04

Table S5: Summary of preparation conditions and file IDs for the shown STM images. After deposition of 0.5 ML IL at T_{prep}, onto clean Pt(111) and an optional annealing step to T_{max}, the sample was imaged at T_{meas}. The tunneling bias (U_{bias}) is applied to the substrate.

Figure	**T_{meas}**	**T_{max}**	**T_{prep}**	**U_{bias}**	**I_{set}**	**File_ID** [YYMMDD_##-##]
1a	110 K	157 K	157 K	1.2 V	0.3 nA	20210901_57-2
1b	110 K	157 K	157 K	1.2 V	0.3 nA	20210901_58-1
1c	110 K	157 K	157 K	1.2 V	0.4 nA	20210901_40-2
1d	110 K	200 K	157 K	1.2 V	0.3 nA	20210901_131-1
1e	110 K	200 K	157 K	1.2 V	0.3 nA	20210901_175-1
1f	110 K	200 K	157 K	1.2 V	0.3 nA	20210901_175-1
1g	110 K	250 K	157 K	1.2 V	0.5 nA	20210903_203-1
1h	110 K	250 K	157 K	1.2 V	0.2 nA	20210903_123-1
1i	110 K	250 K	157 K	1.2 V	0.3 nA	20210903_194-1
1j	110 K	300 K	157 K	1.2 V	0.3 nA	20210903_236-1
1k	110 K	300 K	157 K	1.2 V	0.2 nA	20210903_294-1
1l	110 K	300 K	157 K	1.2 V	0.2 nA	20210903_294-1

Table S6: Overview of the preparation/measuring conditions and file IDs for all XP spectra.

Figure		**File_ID** [YYMMDD-##]	**Coverage / ML**
2	100 K	221221-08 & -07 220628-07 & -08 230210-04 & -05 230206-04 & -05	4.3 0.37 0.46 0.54
	180 K	220711-06 to -25 220712-05 to -24	0.07 – 1.7 0.08 – 2.1
	200 K	230111-05 & -06 230207-04 & -05	3.3 0.54
3	a)	230111-05	3.3
	b)	230124-04	0.51
	c)	220614-03	0.35
4	c) 1.3 ML	220726-04 to -06	1.3
	b) 0.5 ML	230213-04 to -06	0.51
	a) 0.4 ML	220622-04 to -06	0.39
5	300 K, top	230321-05	0.47
	300 K	230126-03	0.49
	250 K	230125-04	0.50
	200 K	230124-04	0.51
	100 K	230127-03	0.52
6 & S1	300 K, 80°	230209-07	0.46
	300 K, 0°	230126-03	0.49
	250 K, 80°	230208-06	0.48
	250 K, 0°	230125-04	0.50
	200 K, 80°	230207-05	0.54
	200 K, 0°	230224-04	0.51
	100 K, 80°	230210-05	0.46
	100 K, 0°	230127-03	0.52
7		230313-03 to -14	0 – 3.3

S2	300 K, 80°	220705-07	0.39
	300 K, 0°	220519-04	0.39
	250 K, 80°	220704-05	0.37
	250 K, 0°	220601-03	0.37
	200 K, 80°	220629-06	0.36
	200 K, 0°	220614-03	0.35
	100 K, 80°	220628-08	0.37
	100 K, 0°	220524-05	0.38
S3	b)	230213-04 to -06	0.51
	a)	221026-03 to -05	0.46
S4	300 K	221020-06	0.46
	200 K	221019-04	0.48